

# Middlesex University Research Repository

An open access repository of

Middlesex University research

<http://eprints.mdx.ac.uk>

Lei, Daiqing (1999) Multi-chip module interconnections at microwave frequencies: electromagnetic simulation and material characterisation. PhD thesis, Middlesex University.  
[Thesis]

This version is available at: <https://eprints.mdx.ac.uk/13417/>

## Copyright:

Middlesex University Research Repository makes the University's research available electronically.

Copyright and moral rights to this work are retained by the author and/or other copyright owners unless otherwise stated. The work is supplied on the understanding that any use for commercial gain is strictly forbidden. A copy may be downloaded for personal, non-commercial, research or study without prior permission and without charge.

Works, including theses and research projects, may not be reproduced in any format or medium, or extensive quotations taken from them, or their content changed in any way, without first obtaining permission in writing from the copyright holder(s). They may not be sold or exploited commercially in any format or medium without the prior written permission of the copyright holder(s).

Full bibliographic details must be given when referring to, or quoting from full items including the author's name, the title of the work, publication details where relevant (place, publisher, date), pagination, and for theses or dissertations the awarding institution, the degree type awarded, and the date of the award.

If you believe that any material held in the repository infringes copyright law, please contact the Repository Team at Middlesex University via the following email address:

[eprints@mdx.ac.uk](mailto:eprints@mdx.ac.uk)

The item will be removed from the repository while any claim is being investigated.

See also repository copyright: re-use policy: <http://eprints.mdx.ac.uk/policies.html#copy>

## **Middlesex University Research Repository:**

an open access repository of  
Middlesex University research

<http://eprints.mdx.ac.uk>

Lei, Daiqing, 1999.  
Multi-chip module interconnections at microwave frequencies:  
electromagnetic simulation and material characterisation.  
Available from Middlesex University's Research Repository.

---

### **Copyright:**

Middlesex University Research Repository makes the University's research available electronically.

Copyright and moral rights to this thesis/research project are retained by the author and/or other copyright owners. The work is supplied on the understanding that any use for commercial gain is strictly forbidden. A copy may be downloaded for personal, non-commercial, research or study without prior permission and without charge. Any use of the thesis/research project for private study or research must be properly acknowledged with reference to the work's full bibliographic details.

This thesis/research project may not be reproduced in any format or medium, or extensive quotations taken from it, or its content changed in any way, without first obtaining permission in writing from the copyright holder(s).

If you believe that any material held in the repository infringes copyright law, please contact the Repository Team at Middlesex University via the following email address:  
[eprints@mdx.ac.uk](mailto:eprints@mdx.ac.uk)

The item will be removed from the repository while any claim is being investigated.

# **Multi-chip Module Interconnections at Microwave Frequencies: Electromagnetic Simulation and Material Characterisation**

**Daiqing Li**

**Communication Research Group  
School of Computing Science  
Middlesex University**

**January 1999**

**A thesis submitted to Middlesex University in partial fulfilment  
of the requirements for the degree of Doctor of Philosophy**

## Abstract

In this work both the interconnections and materials used in multi-chip modules (MCMs) at microwave frequencies have been investigated. The electrical behaviour of the interconnections was studied using commercially available 2.5D and 3D electromagnetic simulators (HFSS<sup>TM</sup>, MDS<sup>TM</sup> and Momentum<sup>TM</sup>). State-of-the-art conductive and dielectric film materials used in the fabrication of multi-layer MCM structures were characterized using microstrip/waveguide resonator techniques.

The models chosen for simulation of interconnections are commensurate with those in current use in MCM technology. Crosstalk between microstrip conductors in multi-layer MCM structures was simulated and new knowledge leading to new design rules was obtained. Typical elements in MCM interconnect structures, such as vias, bends and airbridges were also investigated. The principal features of these elements were simulated and the results were obtained in S-parameter form. Based on the simulated results, these parasitic elements were modelled in terms of their equivalent circuits which can be used in circuit simulators to aid more rigorous MCM circuit design.

A microstrip ring resonator, fabricated using the newly developed conductive material from Heraeus, was employed to measure the line loss.

New techniques have been developed to measure the permittivity and loss tangent of thin dielectric films. In the previous methods for the measurement of these films, the accuracy in measuring the relative permittivity is limited and there is no available technique to measure the loss tangent. A novel cavity perturbation method was developed to accurately measure both the relative permittivity and loss tangent of the films deposited on a supporting substrate. An additional independent technique, derived from transmission line theory, for measuring the relative permittivity of dielectric film was also established. A particular feature of the new

techniques, which led to high accuracy in measuring dielectric constant and loss tangent was the positioning of the dielectric film in the region of maximum electric field strength, thereby ensuring maximum interaction between the electric field and the film material. A rigorous error analysis was performed on the new techniques, which led to the establishment of practical measurement correction factors.

A simple and rigorous method has also been developed to accurately measure the loss tangent of dielectrics with known dielectric constant using a resonant cavity. The novel method eliminates the need for any physical measurement of the dielectric sample. The new technique should permit the development of techniques for very high frequency characterisation of dielectric materials.

## **Acknowledgements**

I thank my supervisors, Dr. Charles E. Free, Dr. Peter Barnwell and Keith E. G. Pitt for their encouragement and guidance during my research.

I am also grateful to Heraeus Inc. for their financial support, sample preparation and technical information.

Thanks also to my colleague K. P. Tang for his support in using CAD software and helpful discussions.

I thank Martin Scott, Donald Thorpe, Pathma Gunasingham and Dave Court for their assistance in preparing samples and using clean room facilities.

# Table of contents

<b>Abstract</b>	ii
<b>Acknowledgements</b>	iv
<b>Overview of thesis</b>	xi
<b>Chapter 1 Introductions and literature review</b>	1
1.1 Overview of multi-chip modules(MCMs) used at high frequencies	1
1.2 The aim of this study and the approaches adopted	4
1.2.1 Simulation and modelling of interconnections in MCMs	4
1.2.2 Characterisation of MCM materials at the microwave frequencies	5
<b>Chapter 2 Crosstalk between microstrip lines in multi-chip modules(MCMs)</b>	12
2.1 Introduction	12
2.2 The classification of MCM technologies	14
2.3 Microwave theory for parallel-coupled microstrip lines	17
2.4 Simulation techniques	19
2.5 Structures investigated using HFSS™	22
2.6 Simulation and results	25
2.7 Conclusions	32

<b>Chapter 3 Simulation and modelling of vias in MCMs and high density packaging in microwave frequencies</b>	<b>35</b>
3.1 Introduction	35
3.2 Structures under Investigation	36
3.3 Comparison between simulated and experimental results for a grounding via	42
3.4 Simulation of cylindrical, square and wedge-shaped vias	43
3.4.1 Simulated S-parameters of vias	43
3.4.2 Simulated phase change from vias	48
3.5 Modelling of vias by equivalent circuit	52
3.6 Conclusions	55
 <b>Chapter 4 Interactions between discontinuities in proximity in MCM interconnection in microwave frequencies</b>	 <b>58</b>
4.1 Introduction	58
4.2 Simulation and modelling of microstrip bends in MCM interconnection	59
4.2.1 HP Momentum : a 2.5-D multi-layer planar electromagnetic field solver	59
4.2.2 Simulation and modelling of a single microstrip bend	60
4.2.3 Two offset microstrip bends	63
4.2.4 Crosstalk between two microstrip bends	65
4.2.5 Summary for simulation and modelling of microstrip bends	69
4.3 Interaction between vias in MCM interconnection at microwave frequencies	70
4.3.1 Simulation of a standard cylindrical grounding via	70
4.3.2 Simulation of a 35 $\mu\text{m}$ cylindrical via	72



4.3.3 Investigation of a 35 $\mu\text{m}$ cylindrical via connected by microstrip lines with Different angles	75
4.3.4 Two offset vias	79
4.3.5 Crosstalk between two individual vias in proximity	82
4.3.6 Summary for simulation of interaction between vias	84
4.4 Simulation of airbridge in high frequency, high density packaging	85
4.4.1 The effect of airbridge height on transmission behaviour	85
4.4.2 Characteristic impedance and phase constant of airbridge line	89
4.4.3 Simulated results for airbridge	92
4.4.4 Crosstalk between airbridge lines in proximity	96
4.4.5 Summary for simulation of airbridge lines	100
<b>Chapter 5 Design rules for interconnections in mutichip modules</b>	102
5.1 Design rules for the minimisation of crosstalk between conductor lines	102
5.2 Design rules for interconnect vias in multi-layer MCM structures	103
5.3 Design rules for airbridge line in MCM interconnections	104
5.4 Design rules for interaction between discontinuities in proximity in multi-layer MCM interconnections	104
<b>Chapter 6 Characterisation of conductive materials using a ring resonator</b>	106
6.1 Theory of microstrip ring resonator	106
6.2 Optimisation of coupling gap for microstrip ring resonator	109
6.3 Test results for attenuation of microstrip line fabricated using a novel conductive paste	112
6.4 conclusions	113

<b>Chapter 7 Characterisation of microwave dielectric materials using resonant cavities</b>	<b>115</b>
7.1 Introduction	116
7.2 Advanced thick film technologies from Heraeus	118
7.3 Permittivity measurement of film materials in a resonant cavity using transmission line theory	125
7.3.1 Basic relations in a rectangular waveguide	125
7.3.2 Theoretical treatment of a resonant cavity loaded with dielectric samples	127
7.3.3 Experimental details of the measurement	141
7.4 Cavity perturbation method for the characterisation of dielectric film materials	150
7.4.1 Introduction	150
7.4.2 Quality factors: basic relationships and measurement	151
7.4.3 General principles of the cavity perturbation method	155
7.4.4 Application of the perturbation method in a rectangular-shaped resonant cavity loaded with a two-layer specimen	160
7.4.5 Measurement results using the perturbation method	168
7.5 Further studies into the cavity perturbation method employing a circular waveguide and high Q mode	171
7.6 Error investigation in the measurement of permittivity and loss tangent	176
7.6.1 Identification of error sources for permittivity measurement	177
7.6.2 The effect of the clearance gap between the dielectric sample and waveguide walls on the shift of resonant frequency	178

7.6.3 Correction algorithm for the clearance gap between broad side of sample and waveguide wall	184
7.6.4 Numerical calculation of error range in permittivity measurement	187
7.6.5 Error range calculation for loss tangent measurement	189
7.7 Conclusions	191
 <b>Chapter 8 Further advances in the dielectric characterisation techniques at microwave frequencies</b>	 193
8.1 Introduction	193
8.2 Theory	193
8.3 Experimental results and discussion	196
8.4 Conclusion	198
 <b>Chapter 9 Conclusions and suggestions for the future work</b>	 200
9.1 Summary and conclusions of the work carried out in this study	200
9.2 Implication of this study	202
9.3 Suggestions for future work	203
9.3.1 Interconnections using coplanar waveguide structures	204
9.3.2 Packaging effects in microwave circuit design	205
9.3.3 Other options for cavity techniques	206

# **Chapter 1 Introduction and literature review**

In this study, the newly developed conductive and dielectric film materials from Heraeus Inc. for high speed interconnections and microwave devices were evaluated. The characterisation of dielectric films was carried out using the theory and techniques developed in the present work. The crosstalk between conductive tracks and the microwave behaviour of parasitic elements, such as vias, bends and airbridges and the interactions between them were investigated using electromagnetic simulators.

## **1.1 Overview of multi-chip modules(MCMs) used at high frequencies**

Current very large scale integration (VLSI) circuit techniques are developing so rapidly that the performance of high-speed digital circuits is often dominated by packaging and interconnections external to VLSI circuits. This has resulted in emphasis being placed on the development of interconnection and packaging technologies that minimise interdevice spacing, signal paths, crosstalk and parasitic capacitance and inductance. Traditionally the silicon chips are packaged individually on printed circuit board (PCB), which is a packaging format known as single chip module (SCM). When SCM packaging is used, if the PCB were completely covered with chip carriers, the board area would only have at most 30% of silicon area. It means that 70% or more of the board space would be wasted and unavailable to active silicon and this would also contribute to increased signal delay at the same time. To meet the packaging demand and overcome the previous problems limiting the system performance, multi-chip module (MCM) packaging technology has emerged, which provides a very high level of system integration, with hundreds of bare integrated circuit (IC) chips that are placed very close to each other on a single substrate. MCMs have the advantages of smaller size, reduced weight, higher reliability and smaller signal delay leading to improved performance. If very large quantities of MCM circuits are demanded, the technology could offer reduced packaging cost in comparison with conventional hybrid packaging technology.

Research on MCMs is an exciting interdisciplinary engineering field which embraces analogue, digital, RF/Microwave techniques, thermal and mechanical engineering, computer-aided design, testing, manufacturing and material sciences for conductive and dielectric materials. The key point in the design and fabrication of MCMs is the interconnection between chips. Two aspects have to be addressed for a specific type of interconnection in MCMs. The first one is concerned with the physical structure of the interconnection; the second one is about the selection of the appropriate materials for the interconnection. The layout of MCM interconnection necessarily involves multi-layer structures routed through by vias. At microwave frequencies, the extent of crosstalk noise between adjacent conductors has to be understood to determine how tight a MCM layout can be designed and produced within the fabrication limits. While the interconnect conductor tracks can be viewed and modelled as transmission lines at high frequency, the vias and bending part of the conductor track can only be treated as discontinuities to the propagation of microwave. They need to be characterised and modelled either through experiment or through rigorous electromagnetic simulation. As for materials aspects of MCM interconnections, the choice of materials can sometimes become vital in both the performance and the cost competitiveness of products. For example, there are three generic MCM approaches, MCM-L, -C and -D. MCM-D is a thin film technique which provides the highest performance of the three [1-4], but at the same time MCM-D is also the most expensive way of making MCM circuits. If thin film techniques could be replaced by thick film technique, MCM-C, the cost of products would be drastically reduced. MCM-L is based on printed circuit technologies and is not considered further here.

Heraeus Inc. have recently developed an advanced thick film MCM technology [5,6] based on etched printed gold conductors and a new kind of printable thick film dielectric material to achieve a performance almost equivalent to deposited thin film MCM technology [7] but with much lower cost. The newly developed thick film dielectrics have extremely low losses and therefore can be used in low-frequency and high-frequency MCM structures or alternatively in microwave integrated circuits (MIC).

In state-of-the-art MCM structures, high packaging density and high clock rate are needed to give high performance. In order to realise the optimum circuit design, a circuit designer should have a thorough understanding of the behaviour of the interconnections between different elements of the circuit, since the pulse distortion caused by signal delay, high levels of crosstalk, discontinuities and switching-induced noise may significantly degrade the overall performance. Because the existing interconnection models for both VLSI and PCB are no longer valid in high-frequency MCM circuits, a new approach from first principles has to be employed. A number of techniques have been developed to investigate the properties of various interconnections in MCMs [8-16]. These techniques can be divided into two groups: frequency-domain S-parameter based characterisation [8-12] and time-domain characterisation [13-16]. The former is often used to extract frequency dependent transmission parameters at high frequencies; while the latter is more useful in estimating the effect of interconnection discontinuities and its effect on signal integrity.

Computer-aided analysis of the MCM interconnection and its comparison with experimental data will provide a theoretical basis for the electrical design of MCMs. Since only limited experimental data on MCM interconnections is available in the literature due to the difficulties involved in the measurement of multi-layer circuit structures at microwave frequencies, the development of a more efficient simulation and modelling technique is needed to obtain more comprehensive and more accurate data for MCM interconnections.

Currently the MCM technology is still developing towards the direction of low cost, small size and high performance. In the wireless communication area, MCM technology not only provides a interconnect mechanism for digital and RF applications, but also includes a unique feature of building embedded components [17-22]. For example a voltage controlled oscillator, low noise amplifier and HIPERLAN radio front end can be realised using MCM-D technology [23]. It is expected that the MCM technology will be more widely used in areas like wireless communication, high performance computers, military warfare etc. Extensive research into MCMs has to be carried out to match this fast growing area.

## **1.2 The aim of this study and the approaches adopted**

Objectives of this project and their implementation:

- 1) To develop an accurate and efficient approach in the frequency domain to accurately characterise the behaviour of MCM interconnections in the microwave region.
- 2) To develop several more rigorous experimental approaches to accurately characterise dielectric film materials used in MCM structures and microwave circuits.

### **1.2.1 Simulation and modelling of interconnections in MCMs**

MCMs form a new packaging approach in which multiple bare chips are mounted and interconnected on a substrate. Their emergence bridged the gap between high performance VLSI technology on chip level and that of PCB which involves the interconnection of individually packaged chips on a board. As a new methodology of high density packaging, MCMs provide a new route for interconnections between functional chips or dice and thus allow a dramatic reduction in the propagation delay of signals in comparison with traditional PCB and hybrid technologies. This results in greatly enhanced performance. As far as production cost is concerned, which is often critical in today's competitive electronic market, the size of the individual chip or die can be kept small by limiting its functionality, which in turn allows increased yield and reduced cost. In addition the individual die can be sourced from different semiconductor manufacturers, so allowing the optimum mix of technologies throughout. Since the MCM substrate has substantially finer conductor lines, smaller dielectric thickness, and a denser via grid than a PCB, they are no longer subject to the conventional PCB design rules and assembly restrictions. At the same time, the geometric size and interconnection length of VLSI circuits on the chip is even smaller than in MCM

structures, consequently, the established rules for VLSI design are also not applicable for MCM design. A new, independent and rigorous approach has to be developed for MCM design. Generally interconnections in MCM structures have to be treated as transmission lines involving multi-layer structures routed through by vias, which all need to be characterised. The fine geometries and complex configurations of MCM interconnections are also out of the range of validity for conventional microstrip formulae, which makes a rigorous electromagnetic simulation from first principle the only viable theoretical approach towards the characterisation of MCM interconnections at microwave frequency range.

This thesis describes new approach which has been developed to extend the established microwave S-parameter modelling techniques to high density digital circuit environments within MCMs. During the project the interconnections, and particularly the inter-layer vias, have been simulated and modelled using state-of-the-art field simulation packages (HP HFSS™, HP Momentum™ and HP MDS™) from Hewlett Packard. The discontinuities, such as bends and airbridge in MCM interconnections have been investigated. The crosstalk between microstrip conductors and discontinuities in proximity in multi-layer MCM structures has also been simulated to provide the knowledge for layout in MCM interconnections. The simulation and modelling has been supported by experimental results taken either from our own measurements or from the test results found in the literature.

### **1.2.2 Characterisation of MCM materials at microwave frequencies**

As mentioned before, materials play a vital role in MCM circuit design at high frequencies. In general, the material properties will change with frequency. The choices of conductive and dielectric materials for high frequency applications and for models in computer-aided circuit design, depend on rigorous material characterisation. Without this, the physical layout, attenuation and dispersion etc. of the microwave circuit can not be accurately designed. For the characterisation of conductive materials, the standard ring resonator method [24] was used to measure the frequency dependence of the ohmic losses of standard 50Ω microstrip line fabricated on a alumina substrate using Heraeus high quality gold paste. Although the



techniques for the characterisation of bulk dielectric materials are mature [25-30], the rigorous characterisation of dielectric film materials is always a challenge because they are very thin and need a rigid substrate for support, i.e. a two-layer sample has to be used for measurement. If a two-layer sample is inserted in cavity resonator the effect of the dielectric film on the resonant frequency and the cavity Q-factor has to be separated from the effect due to the supporting substrate. Earlier attempts have been made to characterise the dielectric film materials. Huang et al [31] developed a cavity technique based on Janezic's method [32] to measure the dielectric constant of the film materials. However, there are two disadvantages in Huang's method. One is that the loss tangent of the material can not be measured with his approach; the other is that the sample has to be loaded at the end of the cavity. The latter restricts the resolution and sensitivity of the test system. Recently Amey et al [33] adopted a new approach by using a T-pattern microstrip resonator to characterise both bulk and film dielectric materials. They pointed out that this method, also, can only be used to measure the dielectric constant of the dielectric film materials. As the available thickness of the thick film is usually restricted to less than 150  $\mu\text{m}$ , the conductor track width for a 50  $\Omega$  line on the dielectric film substrate will be very narrow and the narrow track will dominate the total loss, making the separation of the dielectric loss from total loss very difficult. As a result of high conductor loss, the loss tangent of a dielectric film can not be measured accurately. As far as dielectric constant measurement is concerned in this method, the inevitable correction of the discontinuities involved in a T-pattern microstrip resonator will introduce further errors in dielectric constant data. For example the available formulae used for the correction of an open circuit microstrip discontinuity are only accurate within five percent.

To address the problems encountered in the previous measurement techniques and to meet the growing need for the accurate characterisation of dielectric thick film materials in microwave and millimetre frequency ranges, a new and more rigorous approach has to be developed. To this end, the project has concentrated on the use of a cavity resonator because the dielectric samples are enclosed in the cavity to avoid radiation and the field pattern in the waveguide constituting the cavity resonator is also well understood. What is needed is to find the relationship between the material properties (permittivity and loss tangent) and measurable quantities (resonant

frequency and loaded Q values). Appropriate derivations will be described which enable us to find this relationship. In general the test sample was a two-layer type with dielectric film printed on a rigid substrate. It was realised that the accuracy of the measurement would be greatly improved if the dielectric film layer could be positioned in a high field region to ensure an adequate interaction between the electric field and film materials so that the changes in measurable quantities solely due to the film materials are maximised. Later chapters describe in detail how these areas of the project were carried out.

## References

- [1] C. Truzzi, E. Beyne, and E. Ringoot, "Electrical performance of high speed digital systems on thin film MCM", Proceedings of the 3rd ESA Electronic Component Conference - EECC '97. ESA/ESTEC, 1997. pp. 171-176. (ESA SP; Vol. 395). STEC, Noordwijk, The Netherlands, April 1997
- [2] P. Pieters, S. Brebels, and E. Beyne, "Integrated microwave filters in MCM-D", Proceedings 1996 IEEE Multi-Chip Module Conference (MCMC '96), IEEE Computer Society, pp. 61-66, 1996
- [3] C. Truzzi, E. Beyne, and E. Ringoot, "MCM-D switching units for interconnection technology validation", Proceedings of the IEEE Multi-Chip Module Conference MCMC'96), pp. 132-137, Santa Cruz, CA, USA, February 1996
- [4] Philip Pieters, Steven Brebels, Walter De Raedt, Eric Beyne, "Passive distributed RF structures in MCM-D", 12th European Microelectronics & Packaging Conference, Harrogate, Yorkshire, England, June 1999
- [5] Peter G. Barnwell, "A thick film technology combining microwave and MCM applications", ISHM'96 microelectronics symposium, Proceedings, pp340-343, Minneapolis, Minnesota, USA, October, 1996
- [6] Peter G. Barnwell and Jim Wood, "Advanced thick film technology-the new generation", 11th European Microelectronics Conference, Proceeding, pp221-226, Venice, Italy, May, 1997.
- [7] Naveed Sherwani, Qiong Yu, and Sandeep Badida, "Introduction to multichip modules", John Wiley & Sons, Inc., USA, 1995.
- [8] C.E. Free, K.P. Tang, D. Li, K.E.G. Pitt, P. Barnwell, "High frequency interconnections and crosstalk on MCM structures", ISHM'96 microelectronics symposium, Proceedings, pp522-525, Minneapolis, Minnesota, USA, October, 1996
- [9] T.R. Haller, B.S. Whitmore, P.J. Zabinski, and B.K. Gilbert, "High frequency performance of GE high density interconnect modules", IEEE Trans. Comp., Hybrid, Manuf., Technol. vol.15, no1, pp21-27, 1993

- [10] Y. Eo and W.R. Eisenstadt, "High-speed VLSI interconnect modeling based on S-parameter measurements", IEEE Trans. Comp., Hybrid, Manuf., Technol., vol.16, no.5, pp.555-562, Aug., 1993
- [11] D. G. Swanson, "Grounding microstrip lines with via holes", IEEE Trans, 1992, MTT-40, (8), pp1719-1721
- [12] E. Pillai, F. Rostan , and W. Wiesbeck, "Derivation of equivalent circuits for via holes from full wave models", Electron. Lett., 1993, vol 29, no11, pp1026-1028
- [13] J. Jong, B.J. Rabin and V. Tripathi, "Equivalent circuit modeling of interconnections from time-domain measurements", IEEE Trans, Comp., Hybrid, Manuf., Technol., Vol.16, no.1, pp119-125, Feb, 1993.
- [14] S. Maeda, T. Kashiwa, and I. Fukai, "Full wave analysis of propagation characterization of a through hole using the finite-different time-domain method", IEEE Trans. MTT-39, No12, pp2154-2159, Dec., 1991.
- [15] W. D. Becker, P.H. Harms and R. Mittra, "Time-domain electromagnetic analysis of interconnects in a computer chip package", IEEE Trans MTT-40, no12, pp2155-2163, Dec., 1992
- [16] W.J.R. Heofer, "Time domain electromagnetic simulation for microwave CAD applications", IEEE Trans. MTT-40, no7, pp1517-1527, July,1992
- [17] J. Burghartz, M. Soyuer, and K. Jenkins, "Microwave inductors and capacitors in standard multilevel interconnect silicon technology", IEEE Transactions on Microwave Theory and Techniques, vol 44, no1, pp100-104, January, 1996.
- [18] Y. L. Low and R. C. Frye, "The impact of miniaturization and passive component integration in emerging MCM applications", IEEE Multi-chip Module Conference, Santa Cruz, CA, USA, February, 1996.
- [19] T. Lenihan, L. Schaper, Y. Shi, G. Morcan and J. Parkerson, "Embedded thin film devices in flexible polyimide films", Proceedings of 46th Electronic components Technology Conference, pp.119-124, May, 1996.
- [20] T. Lenihan, L. Schaper, Y. Shi, G. Morcan and K. Fairchild, "Embedded thin film resistors, capacitors and inductors in flexible polyimide films", International Electronics Packaging Conference, pp. 192-202, September, 1996.

- [21] J. Parkson, L. Schaper, G. Morcan and T. Lenihan, "Product design using integrated passive components", Proceedings of International Conference on FLEX Circuits, pp. 83-93, October, 1996.
- [22] R.C. Frye, "Passive components in electronic applications: requirements and prospects for integration", Microcircuits & Electronic Packaging, vol. 19, no 4, pp. 483-489, 1996.
- [23] R. G. Arnold, C. C. Faulkner and D. J. Pedder, "Silicon MCM-D technology for RF integration", Proceedings of 6th International Conference on Multichip Modules, pp. 340-344, April, 1997.
- [24] T. Edwards, "Foundations for Microstrip Circuit Design", John Wiley & Sons, second edition, 1992.
- [25] M. Sucher and J. Fox, Handbook of Microwave Measurements. Polytechnic Press of the Polytechnic Institute of Brooklyn, Vol.II, 1963
- [26] A. M. Nicolson and G. F. Ross, "Measurement of the intrinsic properties of materials by time-domain techniques", IEEE Trans. Instrum. and Measurem., Vol. IM-19, No. 4, pp377-382, Nov., 1970.
- [27] P. K. Kadaba, "Simultaneous measurement of complex permittivity and permeability in the millimeter region by a frequency-domain technique", IEEE Trans. Instrum. and Measurem., Vol. IM-33, No. 4, pp336-340, Dec., 1984.
- [28] F. I. Shimabukuro and C. Yeh, "Attenuation measurement of very low loss dielectric waveguides by the cavity resonator method applicable in the millimeter/submillimeter wavelength range", IEEE Trans. MTT-36, No7, pp1160-1166, July, 1988.
- [29] D. K. Ghodgaonkar, V. V. Varadan, V. K. Varadan, "A free-space method for measurement of dielectric constants and loss tangents at microwave frequencies", IEEE Trans. Instrum. and Measurem., Vol. IM-37, No. 3, pp789-793, June, 1989.
- [30] K. E. Dudeck and L. J. Buckley, "Dielectric material measurement of thin samples at millimeter wavelengths", IEEE Trans. Instrum. and Measurem., Vol. IM-41, No. 5, pp723-725, Oct., 1992.
- [31] H. Huang, C. E. Free, K. E. G. Pitt, A. R. Berzins and G. P. Shorthouse, "Relative permittivity measurement of thick-film dielectrics at microwave frequencies," Electronics Lett., pp. 1812-1814, 1995.

- [32] M. D. Janezic and J. H. Grosvenor, "Improved technique for measuring permittivity of thin dielectrics with a cylindrical resonant cavity," IEEE Int. Conf. Instrument and Measurement, pp. 580-584, 1991.
- [33] D. I. Amey and S. J. Horowitz, "Microwave material characterization," ISHM'96 Proceedings, pp. 494-499, October, 1996.

# **Chapter 2 Crosstalk between microstrip lines in multi-chip modules (MCMs)**

- 2.1 Introduction
  - 2.2 The classification MCM technologies
  - 2.3 Microwave theory for parallel-coupled microstrip lines
  - 2.4 Simulation techniques
  - 2.5 Structures investigated using HFSS™
  - 2.6 Simulation and results
  - 2.7 Conclusions
- 

## **2.1 Introduction**

The development of integrated circuit (IC) technology has reached the stage of very large scale integration (VLSI) and the circuit structure is still becoming more and more complex and dense. As a result, printed circuit boards (PCBs), the conventional electronic packaging and interconnection technology, which can only provide at most 6% active silicon area efficiency [1], becomes unsuitable for VLSI technology. The consequence of using PCB technology to realise the interconnection between chips is that its interconnect length is extremely long compared with that on silicon. This introduces large signal propagation delays and therefore limits the system performance promised by the active VLSI technology. Another drawback of PCB packaging technology is that the area of the circuit layout is so big that it can not provide the compact product size necessitated in many applications, such as mobile communication. Even surface-mount technology (SMT) is still inefficient and can not match the VLSI chip technology. From a packaging point of view, wafer scale integration (WSI), the technology of fabricating an entire system on a single wafer, should be ideal because it has the highest packaging level and can provide the smallest size for the complete system and the shortest interconnect distance to deliver the best possible performance. However WSI is limited by yield and cost and it is also not flexible in mixing different technologies in one system.

Multi-chip module (MCM) technology can provide a solution to all of the above problems. Multi-chip modules (MCMs) have a very high level of system integration in which multiple bare chips are mounted and interconnected on a substrate. There are several advantages in using MCM technology. Firstly, it eliminates chip packages and offers a cost effective solution to achieve high system performance. Secondly, higher density packaging obviously allows significant miniaturisation and reduces the size and weight of the devices. Finally, the increase in the level of packaging can increase the reliability of the system. MCM design necessarily involves multi-layer structures with tracks which have fine geometries and small spacings [2-4]. The current trend in MCM development is the continuing shrinkage in circuit size to improve performance and to meet the specific demand of a competitive market, such as mobile communications, military equipment etc. At the same time, both the digital data rate to be transmitted and analogue working frequencies keep increasing. A major implication of combining high interconnection density and high frequency of the transmitted signal is the necessity of addressing the crosstalk noise between adjacent lines and the electrical effect of discontinuities all of which are frequency dependent and may increase dramatically as a result of miniaturisation and increased working frequency [5-7]. The crosstalk noise level and discontinuities need to be quantified for accurate electrical design of MCMs.

In the literature when the question of crosstalk has been discussed, analysis has been based on closed-form microstrip expressions [8]. These equations are usually restrictive in the range of line geometries to which they apply. Since MCM interconnections have very different line geometries from conventional microstrip line and since the formulae for calculation of crosstalk between adjacent lines on different layers is not yet available, a new and more comprehensive approach is needed. In our study, a simulation technique based on finite element analysis is used to provide a rigorous electromagnetic field simulation of multi-conductor, multi-layer structures. The crosstalk effects were then extracted from the field simulation in terms of S-parameters.



## 2.2 The classification MCM technologies

Since our simulation in this chapter and in others throughout this thesis is mainly concerned with MCM structures, it is necessary to understand the physical structure and the fabrication process of the MCM circuits. There are three available MCM technologies which have both their advantages and disadvantages.

### a. MCM-L technology

MCM-L technology is based on laminated, multilayer PCB ( printed circuit board) technology, which employs the manufacturing process and materials used in PCBs. It can be considered as fine-line PCB technology. To fabricate a MCM-L circuit, first a dielectric sheet covered with conductive material is etched to a certain pattern to form a layer with signal paths on it. This process is repeated to prepare several required layers. Then these layers are bonded together with heat and pressure to form a sublaminate. After a sublaminate has been formed, through-holes are drilled and plated to form buried vias. By repeating the procedure mentioned above until all the sublaminate are formed, these sublaminate are laminated together to form the substrate on which the through-holes are drilled and plated to form the through-vias. Finally the chips can be attached to the substrate using wire bonding or flip-chip technologies.

The advantages of MCM-L technology are its low cost, parallel fabrication process, assemblies with components on both sides, well established infrastructure and ease of repairing or reworking individual layers. The disadvantages of the technology are low performance, low wiring density, poor thermal conductivity of the substrate, significant mismatch of CTE (coefficient of thermal expansion) between the substrate and the silicon chips, moisture sensitivity of the materials and high crosstalk noise. Although MCM-L is not

suitable for high performance applications, it is a cost effective packaging technology for most high volume and portable electronic systems, such as communications, computer, automotive and test equipment. It is very widely used industrially for suitable, i.e. less critical, applications.

#### b. MCM-C technology

MCM-C technology is usually based on co-fired multilayer ceramic structures. Some versions are based on co-fired or glass-ceramic technology. A version based on the Dupont green tape® materials is summarised here [8,9,10]. The fabrication procedure of MCM-C consists of formation of green tape®, via drilling, screen printing of conductive material, and, finally stacking and co-firing all the layers to form a complete interconnect structure. The green tape® is formed by casting a liquid slurry into solid. The liquid slurry is formed from ceramic particles and organic binders. The via holes are drilled on the green tape sheets. Then a screening printing process is carried out to form the conductive pattern and fill the via holes in the green tape whose other side is held by a vacuum to suck the conductive paste into the holes. Finally, all the green tapes with formed conductive patterns on them are stacked directly on top of each other and co-fired to form a complete structure of interconnections.

The advantages of MCM-C technology are high wiring capacity, better electrical conductivity, better thermal conductivity, flexible choice of packaging, superior strength and rigidity, and parallel process in fabrication. The disadvantages include lower wiring density than MCM-D, shrinkage of the substrate during co-firing process, high dielectric constant of the substrate material, and CTE mismatch between substrate materials and die material. The perception for this technology is that it is mainly used for high performance mainframe computers fabricated by the big companies like IBM, NEC and Mitsubishi.

#### c. MCM-D technology

MCM-D is a thin film technology directly employing IC technology and equipment for the fabrication of thin film interconnections. It is a process of depositing thin film metal conductors and un-reinforced polymer dielectrics alternately on a base substrate which can be silicon, ceramic, metal or PCB laminate. In addition to deposition method in creating thin film materials on a base substrate, thermal growth, ion implantation and diffusion are often also used for this purpose. The pattern on each layer of conductive or dielectric materials can be defined using photolithography technology combined with chemical etching. Because MCM-D is a VLSI based technology, it offers high performance, high wiring density, low dielectric constant, and good electrical properties. The line pitch and via size is much smaller than for MCM-L and MCM-C technologies. The high cost and the lack of availability of known good dice are major problems. It is used in mainframe computers, high capacity and high speed telecommunication switching and transmission systems.

Table 2.1 Comparison between different MCM technologies [1]

Parameters	MCM-L	MCM-C	MCM-D
Minimum line width ( $\mu\text{m}$ )	60-100	75-100	8-25
Minimum line pitch ( $\mu\text{m}$ )	625-2250	50-450	25-75
Dielectric constant	3.7-5	5-9	2.4-4
Via diameter ( $\mu\text{m}$ )	150-500	50-100	8-25
Via grid ( $\mu\text{m}$ )	1250	125-450	25-75
Maximum number of layers	46	63	8
Wiring density ( $\text{cm}/\text{cm}^2$ )	30	20-40	200-400
Repair/rework	Easy	Easy	Difficult
Relative cost	1	1.5-2.0	2-10

Sometimes in order to achieve high performance at an economical cost, hybrid approaches such as MCM-DL and MCM-DC are used. For example, MCM-DC refers to the technology of deposition of thin film on the co-fired ceramic substrate, which contains interconnections for the power, ground, and some signals. The comparison of three basic MCM technologies are given in table 2.1 [1]. Comparing table 2.1 with table 7.1 (to be presented later in chapter 7) shows that Heraeus KQ® novel material system corresponds to MCM-C technology but provide the performance comparable with MCM-D. That means the dramatic reduction in cost can be achieved in the fabrication of high performance interconnections using KQ® technology. Our simulation models in this chapter are also based on this material system.

## 2.3 Microwave theory for parallel-coupled microstrip lines

While the main topic of this chapter is to deal with crosstalk in the interconnections in MCM structures, it is necessary to first examine the available analytical formulae for the calculation of crosstalk between conductors in a multilayer environment. The availability of analytical formulae is restricted to parallel-coupled microstrip lines on the same substrate without overlay shown in figure 2.1. The frequency-dependent coupling coefficient of this simple structure is given as [11]

$$C(\theta) = C(j\omega) = \frac{jC \sin \theta}{\sqrt{1 - C^2} \cos \theta + j \sin \theta} \quad (2-1)$$

where

$$C = \frac{Z_{0e} - Z_{0o}}{Z_{0e} + Z_{0o}} \quad (2-2)$$

In equation 2-2,  $Z_{0e}$  and  $Z_{0o}$  are even-mode and odd-mode characteristic impedances respectively.  $C$  is the mid-band coupling factor and  $\theta = \beta l = 2\pi l / \lambda_g$ , where  $\theta$  is electrical

angle,  $\beta$  is phase constant,  $l$  is the coupling length between two microstrip lines, and  $\lambda_g$  is guide wavelength.  $\lambda_g$  is usually taken as the mean of the even-mode and odd-mode guide wavelength, i.e.

$$\lambda_g = \frac{\lambda_{ge} + \lambda_{go}}{2} \quad (2-3a)$$

where

$$\lambda_{ge} = \frac{\lambda_0}{\sqrt{\epsilon_{effe}}} \quad (2-3b)$$

$$\lambda_{go} = \frac{\lambda_0}{\sqrt{\epsilon_{effo}}} \quad (2-3c)$$

in which  $\lambda_0$  is the wavelength in air and  $\epsilon_{effe}$  and  $\epsilon_{effo}$  are even and odd-mode effective microstrip permittivities respectively. Equation (2-1) combined with equations (2-2) and (2-3) can be used to calculate the crosstalk between two microstrip lines on the same substrate. The limitation of equation 2-1 is that it can not deal with the conductors on

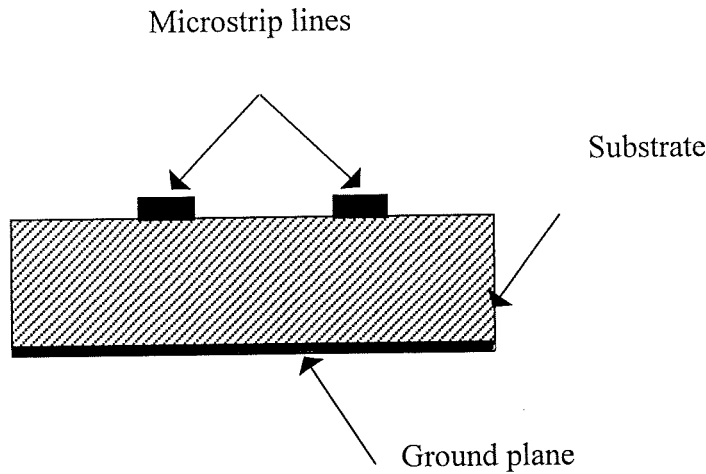


Figure 2.1 Parallel-coupled microstrip lines

different layers in a multi-layer structure and the collective effect of multi-conductors also can not be calculated. In addition, the available formulae for the calculation of the effective

permittivities are obtained through curve-fitting with experimental data from conventional microstrip structures. The effect due to the miniaturisation of the MCM structures with respect to standard/typical microwave structure dimensions may not be accurately taken into account in these formulae. Therefore a totally different and more general approach, using 3-D electromagnetic simulation, was chosen in order to characterise the electrical behaviour of the conductors in MCMs.

## **2.4 Simulation techniques**

The simulations were performed using HFSS™, an electromagnetic field simulator from Hewlett Packard, which numerically solves Maxwell's equations under boundary conditions suitable to the structures we have chosen, and provides a thorough understanding of the electromagnetic properties of the structures. The simulation technique effectively divides the structure into a number of three-dimensional finite element meshes which consist of thousands of tetrahedra. In each tetrahedron the electromagnetic field is represented with a local function and in this way the wave equation derived from Maxwell's equations can be transformed into a matrix equation that is solved using traditional numerical methods. The final results in our case are in the form of an S-parameter matrix, thus reducing the three-dimensional electromagnetic behaviour of transmission structures to a set of high frequency circuit parameters. Clearly some care must be taken in selecting the mesh size for the simulation in order to achieve an accurate result compatible with realistic computing time. In the present work, the finite element meshes are generated and optimised at the top end of the frequency range being investigated, thereby ensuring accurate results over the whole frequency range. An adaptive procedure shown in figure 2.2 is used for the generation and optimisation of the finite element meshes. After each adaptive process, the finite element meshes will be refined further. The number of adaptive processes is determined by the required accuracy of the S-parameters. After the adaptive solution is complete, the resulting finite element meshes can be used to produce frequency sweep, as shown in figure 2.3, to generate the frequency response of the simulated structure.

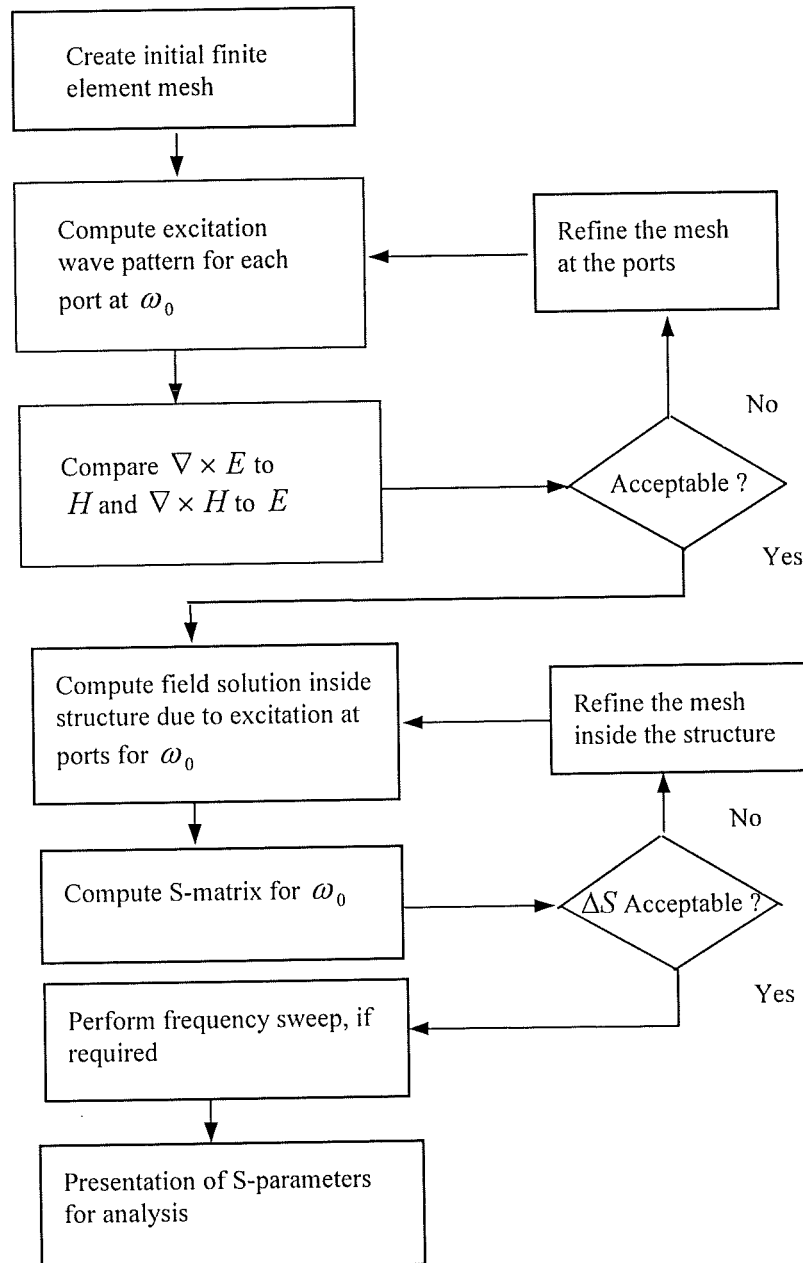


Figure 2.2 Adaptive procedure for the generation and optimisation of the finite element meshes

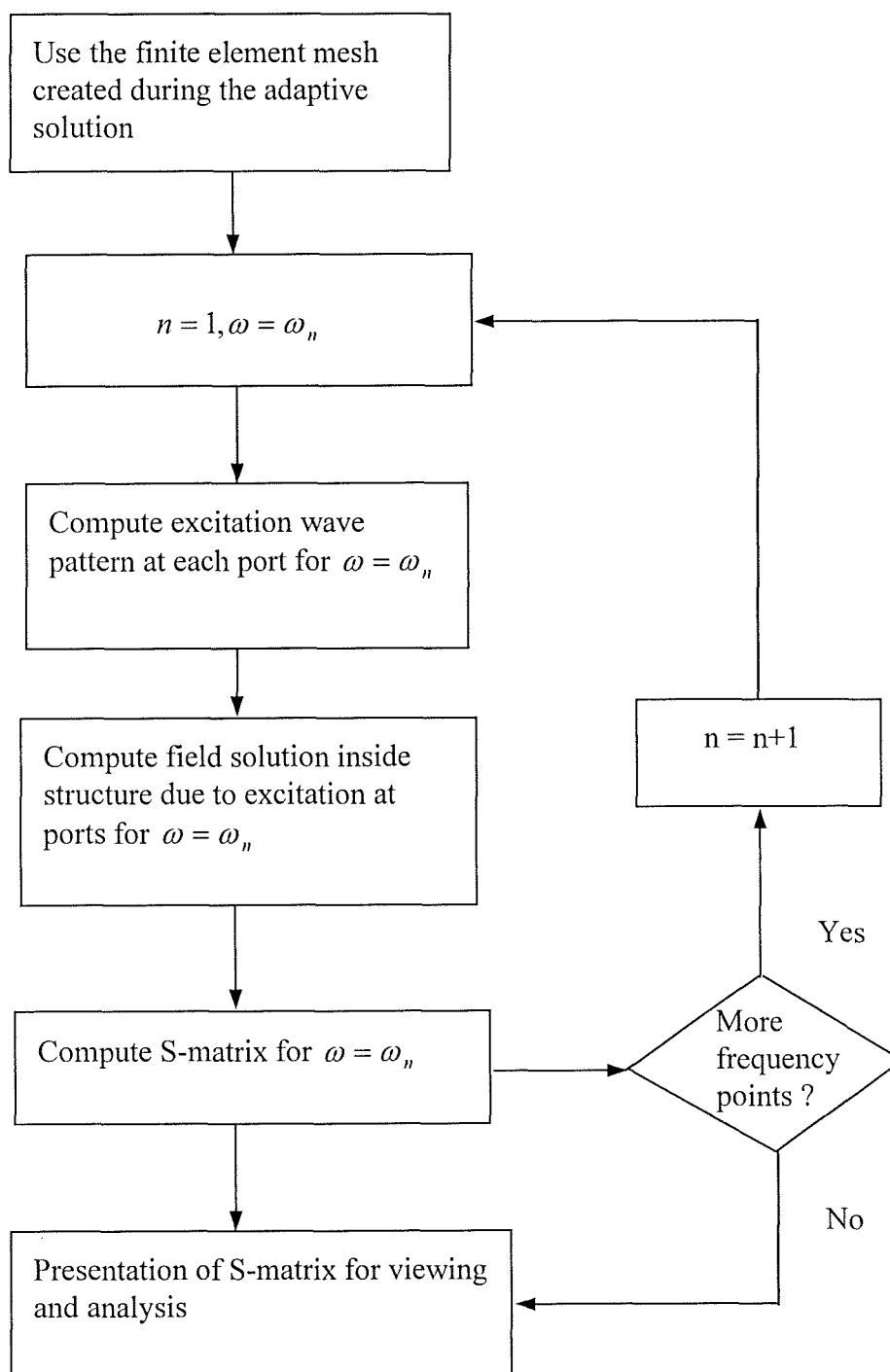
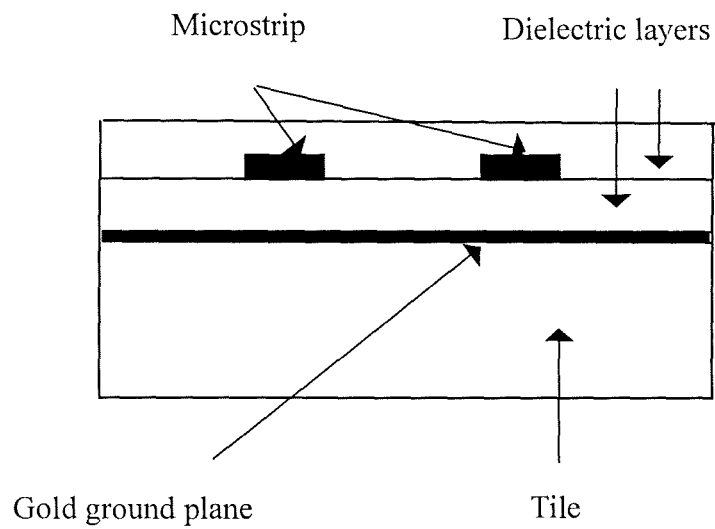


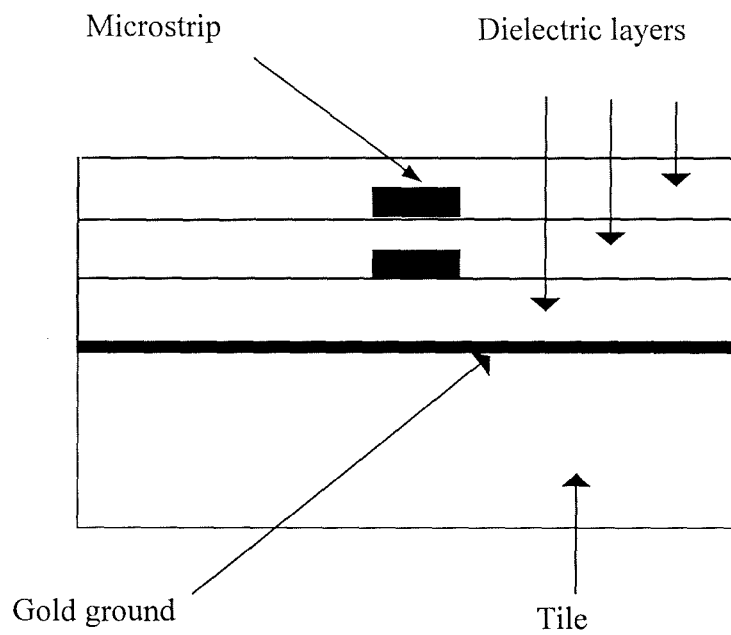
Figure 2. 3 Frequency sweep in HFSS™ around an adaptively solved frequency point.



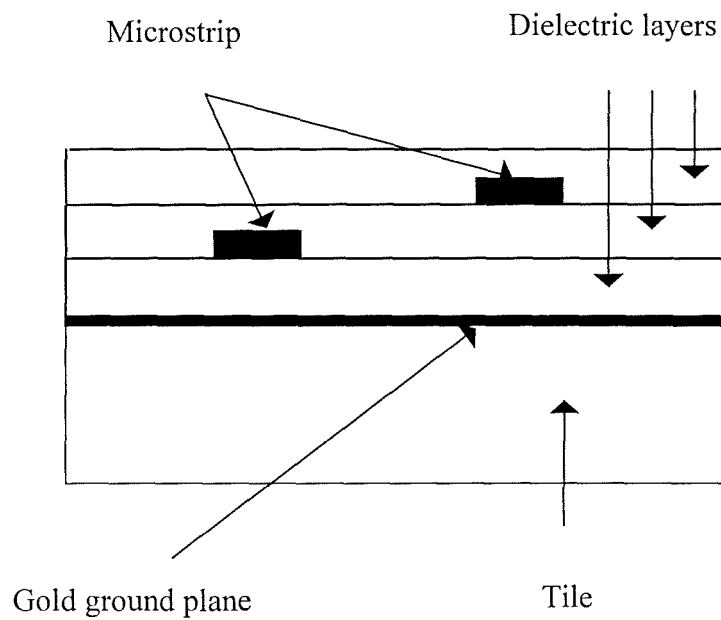
## 2.5 Structures investigated using HFSS™



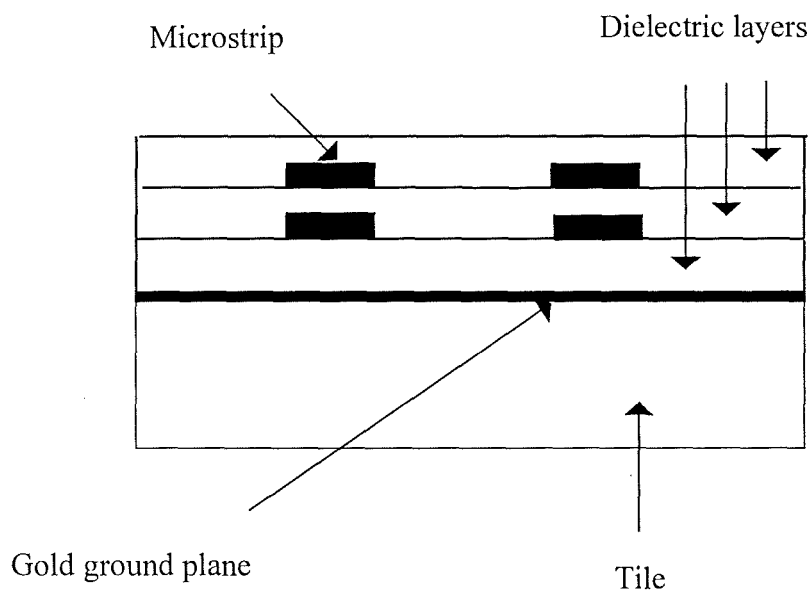
(a) Parallel lines with overlay



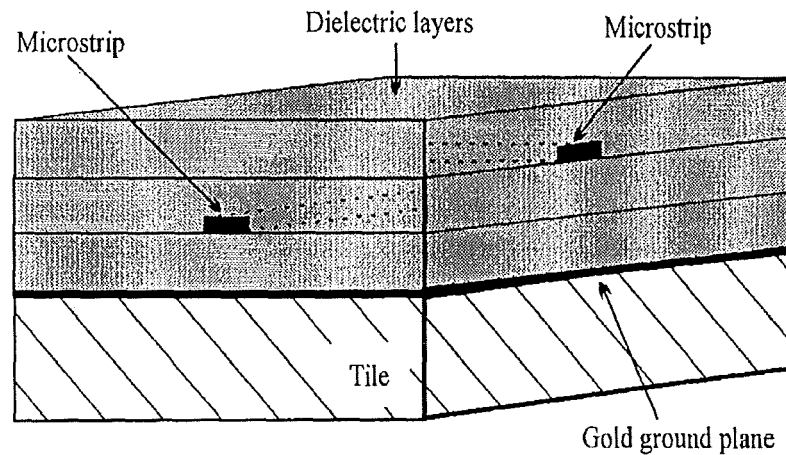
(b) Vertically stacked lines



(c) Displaced lines



(d) Four lines arrangement



(e) Crossover lines

Figure 2.4 Cross section of five structures used in simulation.

Five structures, representative of the transmission line interconnections found in MCM devices, were chosen for simulation; these are shown in figure 2.4. Figure 2.4 a is a simple parallel line arrangement, with a dielectric overlay on top of the conductors. This can be used for investigating crosstalk between lines on the same layer. It can be seen from figure 2.4 a that the ground plane is located on top of a dielectric substrate. This latter layer is merely a dielectric tile used to provide rigidity and support, and does not enter into the simulation. Figure 2.4 b shows two conductors vertically stacked on different layers and is used to investigate multi-layer coupling. In the figure 2.4 c, a staggered line arrangement is given. Figure 2.4 d shows an arrangement of four conductors, which enables single and multi-layer coupling to be investigated in the presence of additional conductors. Lastly a crossover connection is shown in figure 2.4 d, to enable crosstalk arising from this common structure to be quantified. In all of the five structures, the width, length and spacing of the lines are taken

as 20, 1080 and 20  $\mu\text{m}$  respectively. The individual dielectric layer has a thickness of 20  $\mu\text{m}$ , and a relative permittivity of 4. It should be noted that the dimensions of the conductor tracks, and their horizontal and vertical separations were chosen to be consistent with the geometries available from current, high-quality photo-processible materials and technologies, such as those from Heraeus.

## 2.6 Simulation and results

Initially, in order to verify the HFSS™ model that had been created, simulations were performed on a standard microstrip parallel-line coupler with alumina as substrate over the frequency range 8-12GHz. The results of simulation were then compared with measurement to verify the simulation technique. Before we present the simulated results, the port definition will be given first. Figure 2.5 defines the ports for an electrical structure with two conductors which is applicable for the microstrip couplers to be simulated. The wave or energy is assumed to be launched from port 1. In figure 2.6 the ports for an electrical structure with four conductors are defined.

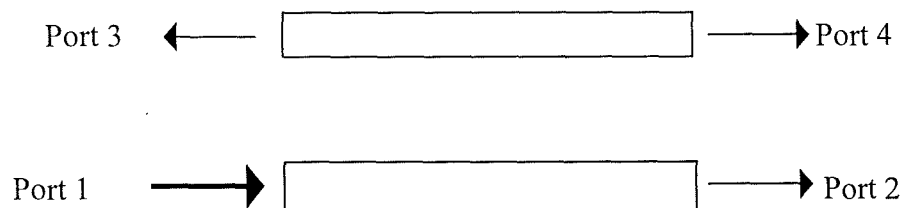


Figure 2.5 Port definition for electrical structure with two conductors

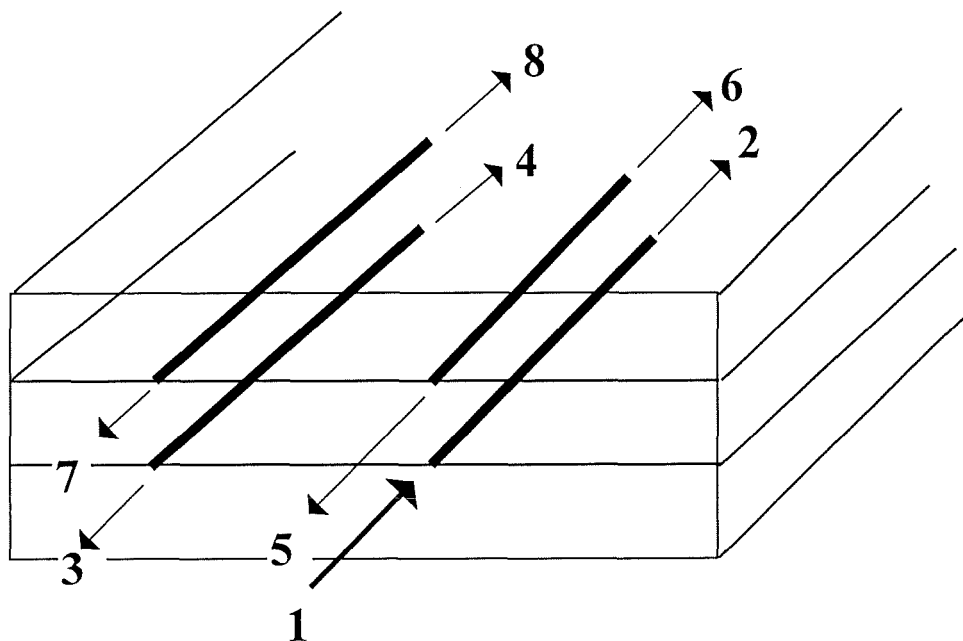


Figure 2.6 Port definition for electrical structure with four conductors

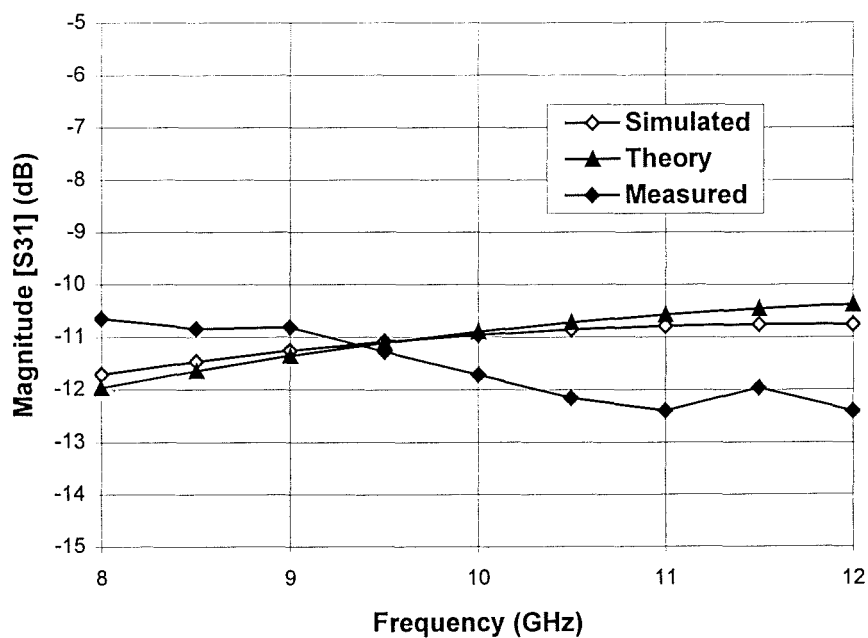


Figure 2.7 Comparison of results between HFSS™ simulation, microstrip theory and experiment for a general coupler with alumina substrate

Following the port definition, the simulated results for the standard coupler is presented in figure 2.7 which show very good agreement between measured and simulated data and hence verify the HFSS™ model being used. In addition, the simulation results show excellent agreement with the results using conventional microstrip theory [11].

As a result the simulation for several fine line geometric models found in MCM structures was carried out. In figure 2.8 the simulated crosstalk expressed in S-parameter, S<sub>31</sub>, for fine geometric parallel-coupled conductors without overlay is presented. The crosstalk for the same structure is also calculated using the standard microstrip coupler theory presented previously. The frequency range was chosen to be 1-5GHz, to be commensurate with the spectral frequencies of current high data rate systems. It can be observed from figure 2.8 that, unlike the excellent agreement in figure 2.7 between the simulated results and those

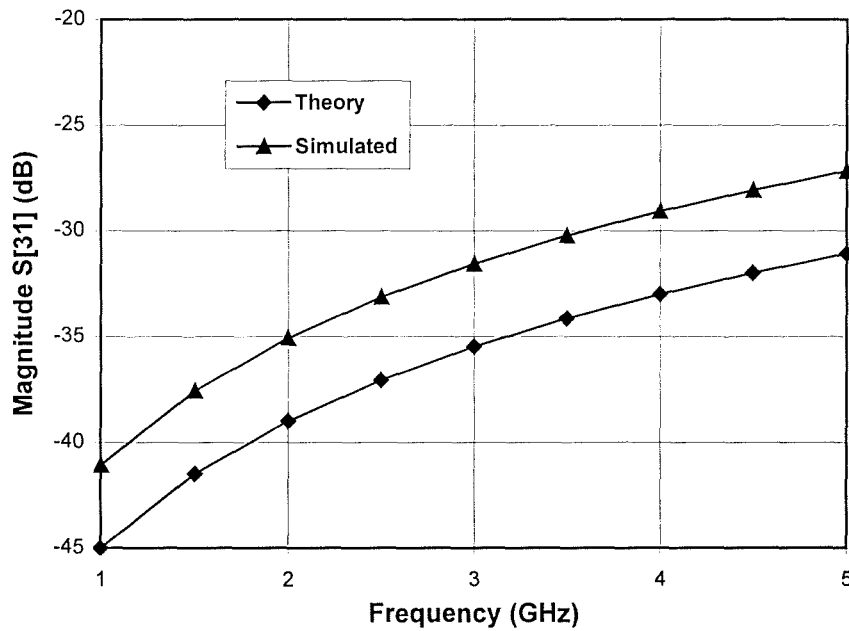


Figure 2.8 Crosstalk for fine line geometric parallel-coupled conductors without overlay, simulated and based on microstrip theory.

obtained from microstrip coupler theory for a general coupler, there is a 3dB difference between them for a fine line geometric coupler with much thinner substrate and narrower conductor tracks. Although the shape of the response is essentially the same in both cases, the conventional microstrip theory delivered an underestimation of the coupling between conductors. Whilst this is not a large difference, it could be significant in terms of achieving maximum packing density on an MCM structures or MIC. It certainly indicates that the application of microstrip design expressions to structures with very different dimensions from one of standard microstrip, should be used with caution.

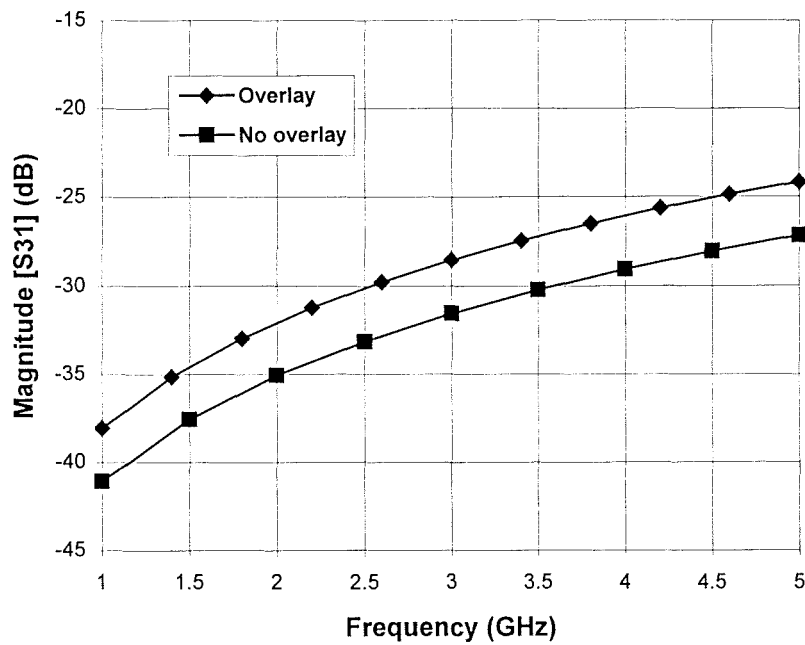


Figure 2.9 Crosstalk for fine geometric parallel-coupled lines with and without dielectric overlay

The effect of overlay on the crosstalk for the fine geometric coupler described in figure 2.4 a is shown in figure 2.9. As expected, the crosstalk is enhanced by the overlay because the

coupling capacitance between the conductors is increased by the presence of the dielectric overlay.

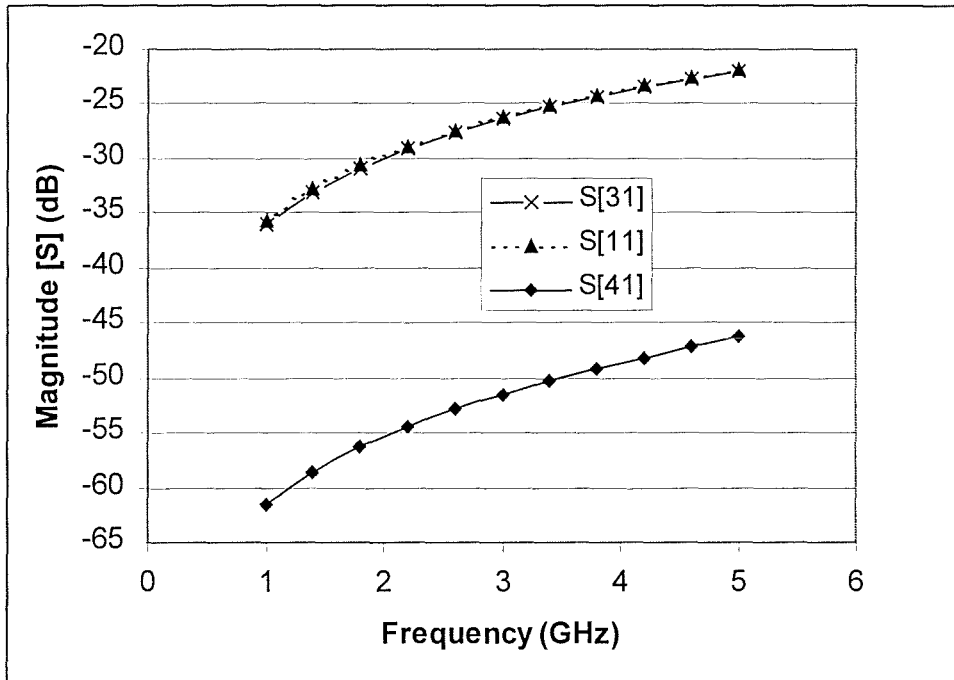


Figure 2.10 Crosstalk between displaced lines on different layers

The coupling between conductor lines displaced on adjacent dielectric layers is shown in figure 2.10. In addition to S31, the backward wave coupling, S11 and S41 are also presented. It can be seen that the wave reflection (expressed in S11) from the launching port, caused by the presence of the adjacent conductor, is nearly equal to the crosstalk S31 in the frequency range investigated. The very small magnitude of S41 indicates that, similar to a microstrip coupler with the conductors on the same layer, port 4 can be considered as the isolation port.

Figure 2.11 shows the crosstalk for stacked line geometry. The coupling between the two lines in this case is much larger than in the previous cases. As far as two conductors are



concerned, this is probably the worst case in producing crosstalk. The two conductors now form a capacitor which maximises the inductance and capacitance between them. In the practical layout of high frequency, high density packaging, the arrangement of lines like this should be avoided. For comparison, the crosstalks S31 for stacked, displaced lines and coupler structure with overlay are presented in figure 2.12. The comparison shows that the coupler structure has the minimum crosstalk.

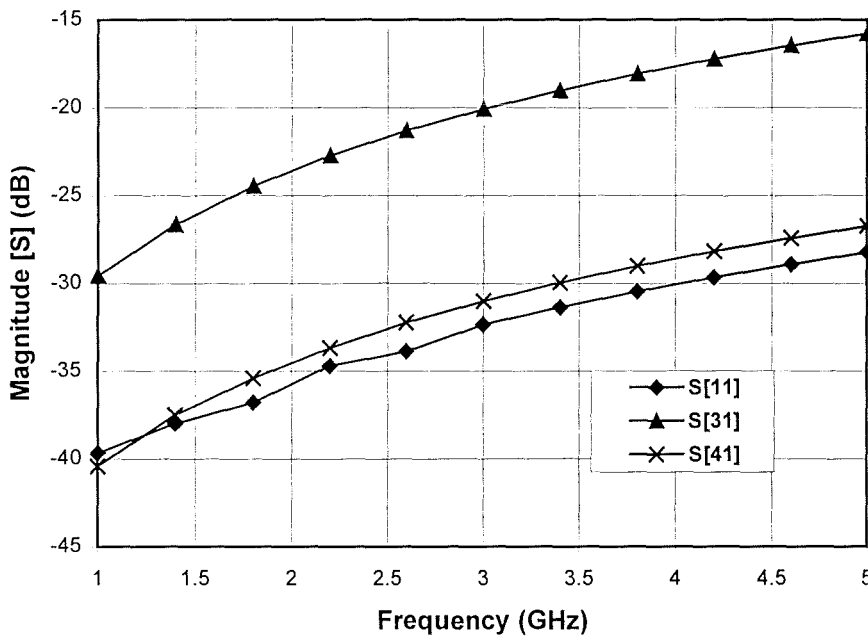


Figure 2.11 Crosstalk between stacked lines on different layers

Crosstalk in the four-line structure is shown in figure 2.13. It is interesting to compare these results with the corresponding values in figure 2.12, where the same structure exists, but without the additional two lines. The difference between them provides a clear indication that the way

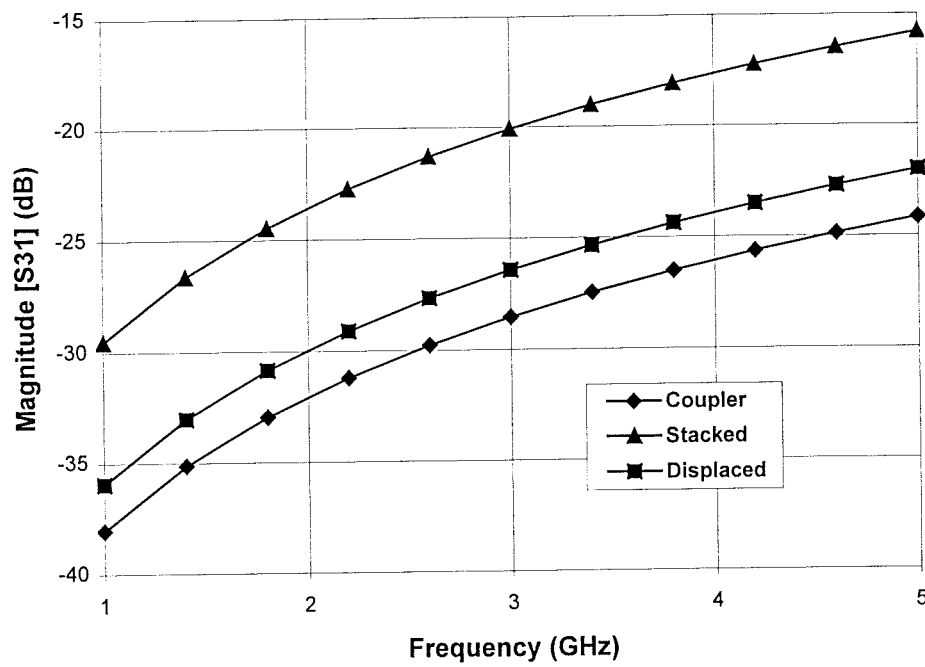


Figure 2.12 Comparison of crosstalk between stacked, displaced lines and coupler structure with overlay

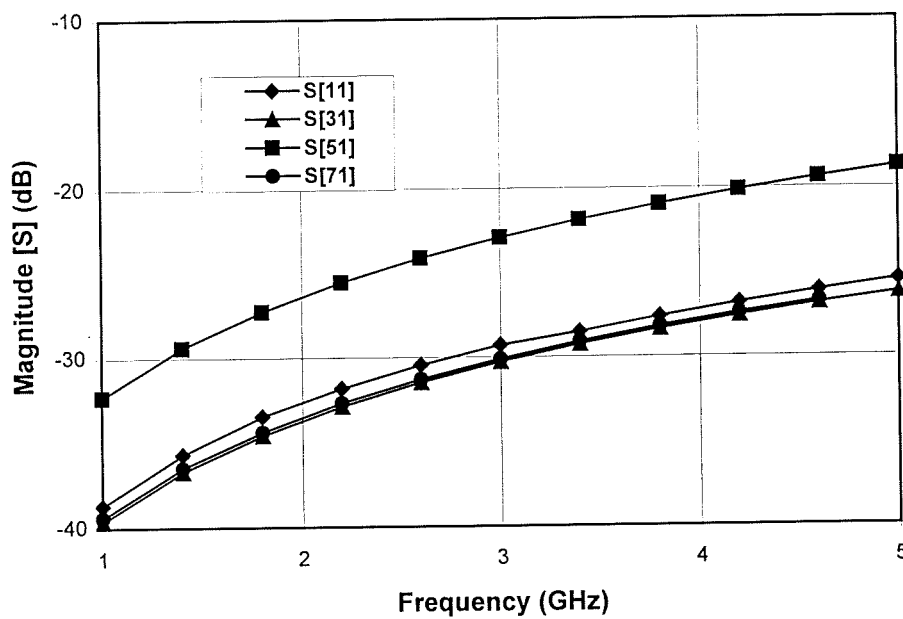


Figure 2.13 Crosstalk in four-line structure

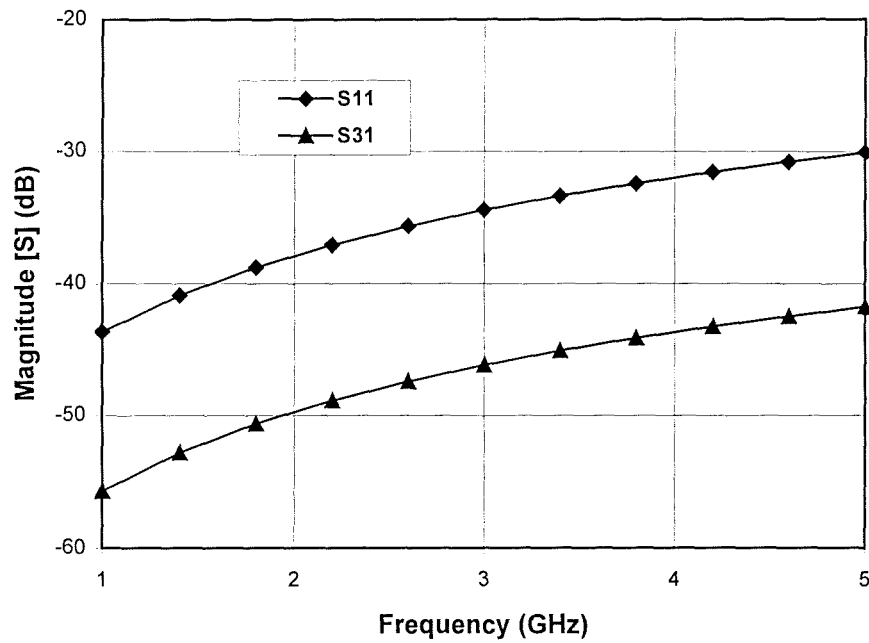


Figure 2.14 Crosstalk between crossover lines

the conductors are arranged has to be considered to give a rigorous understanding of the behaviour of multi-conductor interconnections at high frequencies.

Finally, in figure 2.14, the effects of crosstalk due to a crossover are shown. This result tends to support the argument that the coupling at a crossover is small simply because the coupling volume is small. Clearly the effects of coupling between parallel lines are of much greater significance.

## 2.7 Conclusions

The use of electromagnetic simulators provides a powerful tool in obtaining a rigorous understanding of the high-frequency behaviour of MCM interconnection structures. The work has shown that traditional microstrip design equations must be used with some caution when usually the small dimensions are used. Moreover, because many of the complex

transmission line structures encountered in MCM work do not have microstrip equivalents, a field theory simulation, based on first principles provides the only viable method of approach.

## References

- [1] Naveed Sherwani, Qiong Yu, and Sandeep Badida, "Introduction to multichip modules", John Wiley & Sons, Inc., USA, 1995.
- [2] Frye, R.C., and Tai, K.L., "Interconnection lines for wafer-scale-integrated assemblies", U.S. Patent 4,703,288, 1987.
- [3] Shao-fang Gong, Jan Strandberg, Heike Thiede, Hans Hentzell, Hjalmar Hesselbom, and Weine Karner, "Investigation of high-speed pulse transmission in MCM-D", IEEE Trans. Components, Hybrids and Manufact. Techn., vol 16, no7, pp735-741, Nov., 1993.
- [4] Guang-wen Pan, Jeffrey A. Prentice, Sharon K. Zahn, Andrew J. Staniszewski, Wayne L. Walters, and Barry K. Gilbert, "The simulation of high-speed, high-density digital interconnects in single chip packages and multichip modules", IEEE Trans. Components, Hybrids and Manufact. Techn., vol 15, no4, pp465-477, Aug., 1992.
- [5] Kobayashi, M., "A dispersion formula satisfying recent requirements in microstrip CAD", IEEE Trans. MTT-36, pp. 1246-1250, Aug. 1988.
- [6] Kirschning, M., and Jansen, R.H., "Accurate wide-range design equations for the frequency-dependent characteristic of parallel coupled microstrip lines", IEEE Trans. MTT-32, No. 1, pp.83-89, Jan. 1984.
- [7] Huang, H., Free, C., Pitt, K., Berzins, A., and Shorthouse, G., "High Frequency Measurements on Modern MCM Structures", Journal of Microcircuits and Electronic Packaging, vol. 18, No. 4, pp. 357-362, 1995.
- [8] Tummala, R. P. and Rymaszewski, E. J., "Microelectronics Packaging Handbook", Van Nostrand Reinhold, 1989.
- [9] Horowitz, S. J., Needs, C. R. S., "Smart Materials for Hybrid Circuits and Multichip Modules", Proc. Japan IEMT Symposium, 1995.
- [10] Amey, D. I. and Horowitz, S. J., "High Frequency Performance of Ceramic and Printed Wiring Materials under Varying Temperature and Humidity Conditions", Proc. EMC97, 11th European Microelectronics Conference, Venice, Italy, 269-276, 1997.
- [11] Edwards, T. "Foundations for Microstrip Circuit Design", John Wiley & Sons, second edition, 1992

## **Chapter 3 Simulation and modelling of vias in MCMs and high density packaging at microwave frequencies**

### 3.1 Introduction

### 3.2 Structures under Investigation

### 3.3 Comparison between simulated and experimental results for a grounding via

### 3.4 Simulation of cylindrical, square and wedge-shaped vias

### 3.5 Modelling of vias by equivalent circuit

### 3.6 Conclusions

---

### **3.1 Introduction**

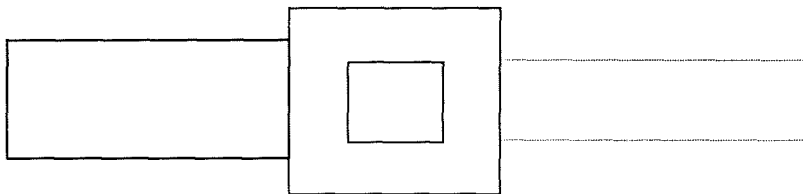
The current trend towards high density packaging in multilayer MCM and MMIC structures, combined with high data rate operation, has created a demand for accurate high-frequency models of complex interconnection structures for optimal circuit design. Among the interconnect issues in addition to crosstalk between the adjacent conductors, which has been addressed in the last chapter, discontinuities, such as vias, bonding wires and T-junctions etc., inevitably have a great frequency-dependent effect on the performance of the circuit. A complete understanding of these interconnection discontinuities can be achieved in two ways; one is experimental characterisation [1], the other is electromagnetic simulation by software based on the solution of Maxwell's equations in time-domain [2] or in frequency-domain. The disadvantage of experimental characterisation is that it is not cost effective. In addition, if the geometric size of the circuit is very small, the task of accurate measurement would become quite difficult. In contrast, the simulation method is both accurate and flexible. After the procedures of simulation and optimisation the results can be loaded into a circuit simulator for high frequency circuit design [3]. The simulated results can also be used to create a passive element library. In this chapter we will mainly deal with the simulation and modelling of vias, which is a new requirement brought about by the rapid expansion in the design and application of high frequency multi-layer interconnection system.

In previous studies of vias, quasi-static analysis was used to derive their equivalent circuits [4,5]. The advantage of the quasi-static analysis is that it is straightforward and easy in numerical computation. However, at higher frequencies (above 10 GHz) it is not accurate enough and a more fundamental approach is necessary. Subsequently full wave approaches have been proposed to characterise vias. In references [6-7] the integral equations describing the current distribution in a via and the microstrip lines connecting it were solved to obtain S-parameters by applying the method of moments. In [8-10] the finite-difference time-domain (FDTD) method was also used for the analysis of vias. In this method, Maxwell's curl equations are expressed in discretised space and time domains and used to simulate the propagation of an initial excitation to finally obtain the S-parameters. In addition, the full-wave mode matching technique has also been used to simulate the electromagnetic behaviour of vias [11]. There is one common problem for all these previous methods, i.e. the difficulty in dealing with complex via geometries, such as wedge-shaped vias, or even irregular shaped vias, which are often encountered in the practical fabrication of microelectronic circuits. As a result, most of the previous studies are only concerned with cylindrical vias, which are relatively easy to treat analytically. Recently the finite element method (FEM) has been used to simulate vias [12]. FEM is not only an alternative to the previous methods but is more versatile in dealing with complex geometries and, hence, more suitable for the analysis of vias. This method has been chosen for use in this investigation for the analysis of vias with varied shapes.

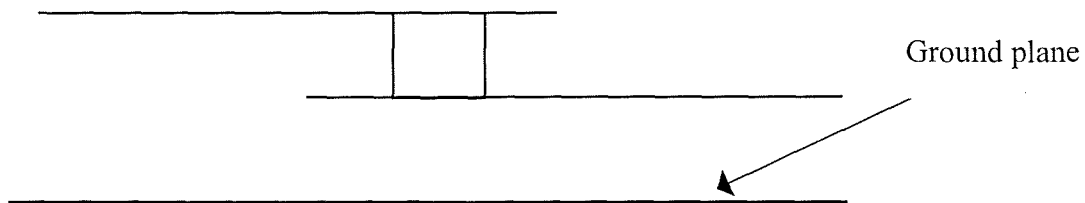
### **3.2 Structures under investigation**

In order to obtain more information on the geometric effect of the vias on their microwave performance, wedge-shaped vias were studied to complement the simpler cylindrical and square shapes. Figure 3.1 (a-f) shows diagrams of these three kinds of vias with and without via pads (corresponding to normal and ideal via geometry respectively). To demonstrate further the details of vias, three-dimensional square vias are shown in figure 3.2. In all via structures, the thickness of the dielectric layers (20 $\mu$ m) and the cross dimension of the vias are

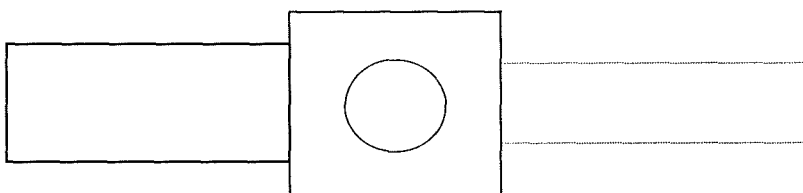
commensurate with the KQ-technology of Heraeus Inc. It should be noted that in previously published studies the geometric size of the vias examined are only applied to PCB technology, whereas the via sizes considered here are representative of modern MCM interconnections. For all structures investigated here, the microstrip lines are assumed to have zero thickness and to be perfect conductors. Since the KQ-dielectric materials have very low loss ( $\tan\delta \sim 0.0001$ ), the dielectric losses are also neglected. (In addition, the very small geometric size of vias also makes it justifiable to neglect the conductor and dielectric losses). Based on the HFSS<sup>TM</sup> simulation, equivalent circuit models of vias are derived which can be used in a circuit simulator for MCM design.



(a1) Top view of square via with via pad

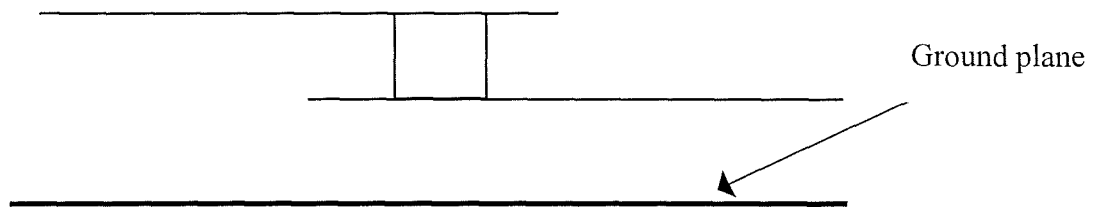


(a2) Side view of square via with via pad

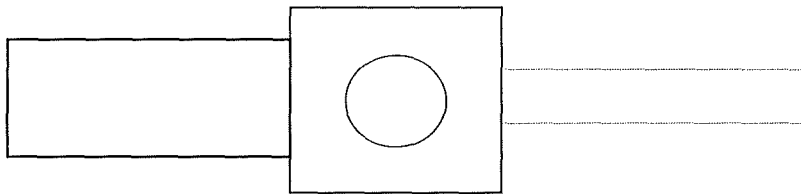


(b1) Top view of cylindrical via with via pad

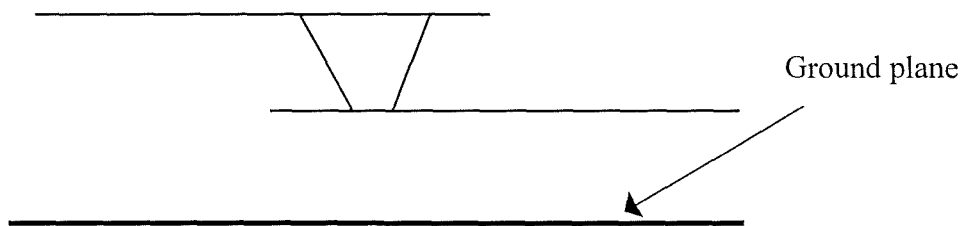




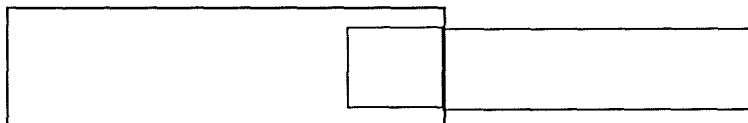
(b2) Side view of cylindrical via with via pad



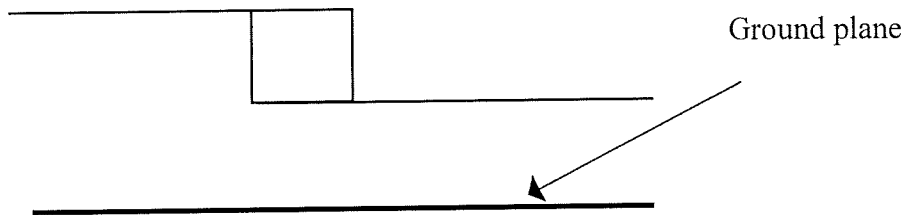
(c1) Top view of wedge-shaped via with via pad



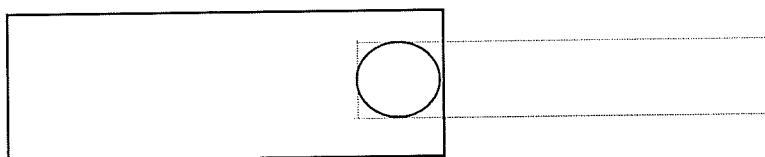
(c2) Side view of wedge-shaped via with via pad



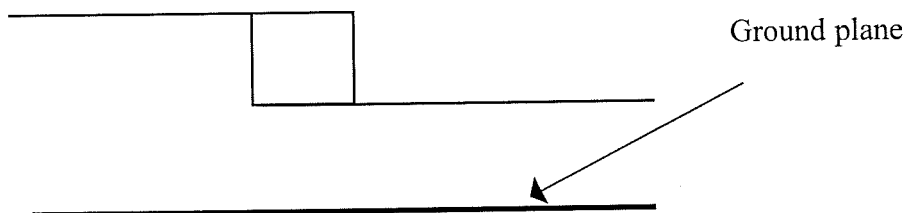
(d1) Top view of square via with ideal geometry



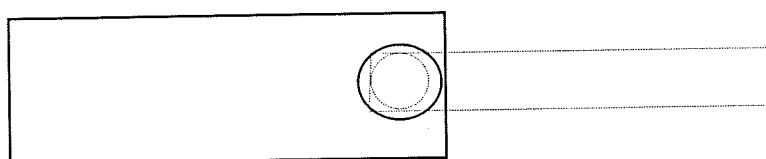
(d2) Side view of square via with ideal geometry



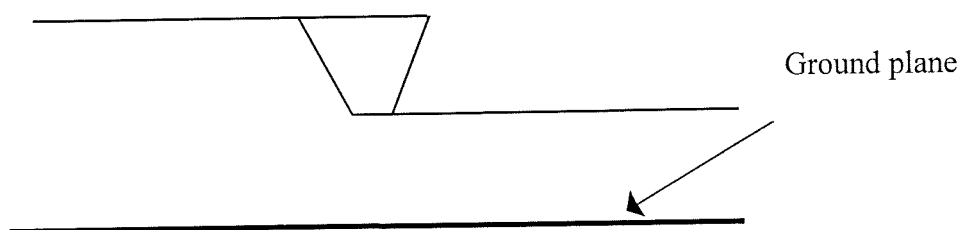
(e1) Top view of cylindrical via with ideal geometry



(e2) Side view of cylindrical via with ideal geometry

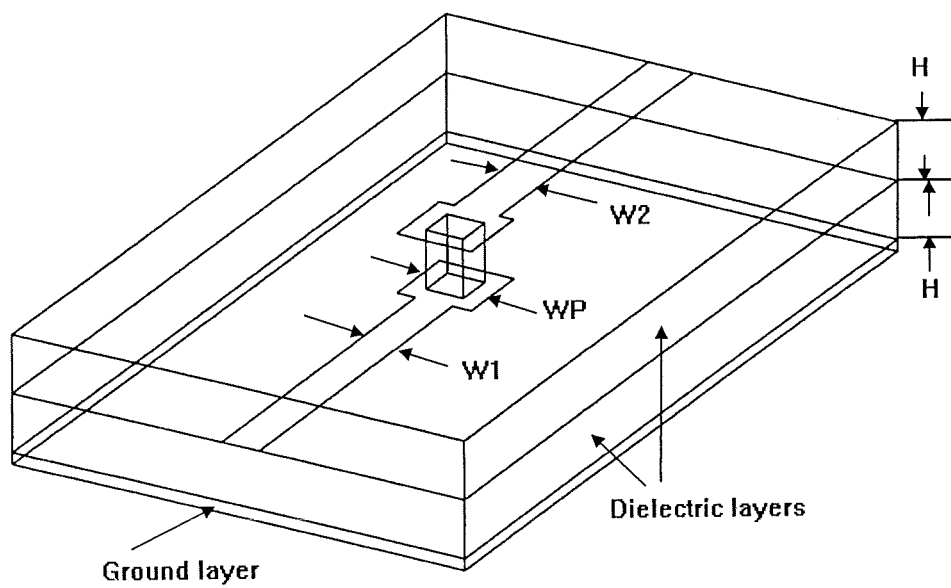


(f1) Top view of wedge-shaped via with ideal geometry

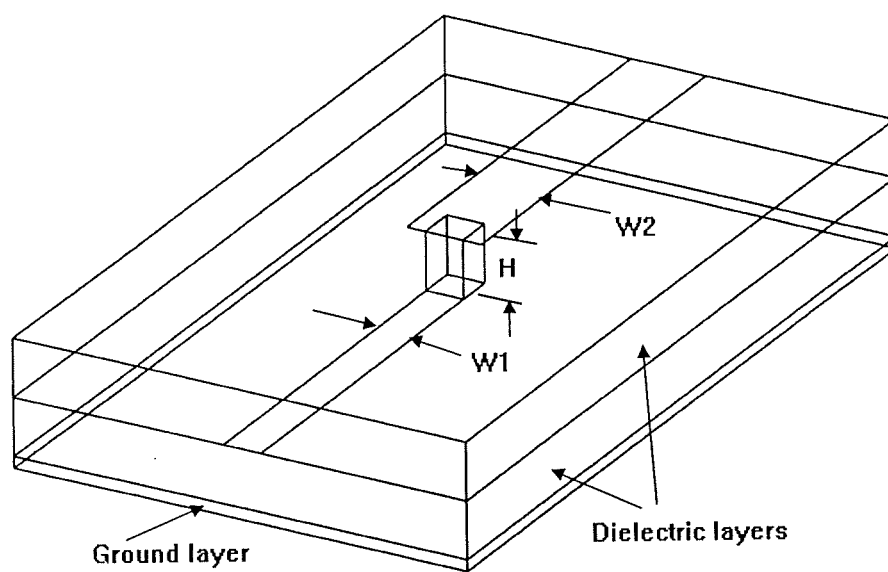


(f2) Side view of wedge-shaped via with ideal geometry

Fig. 3.1 Diagrams of square, cylindrical and wedge-shaped vias. Fig.3.1 (a, b, c) are normal via geometries with square via pads on both ends of the via. Fig.3.1(d, e, f) are vias with ideal geometries with minimum discontinuity.



(a)



(b)

Figure 3.2 Three-dimensional diagrams of square vias with normal (a) and ideal (b) geometry.

### 3.3 Comparison between simulated and experimental results for a grounding via

In order to confirm the validity of the simulation process, a simulation was performed on a via whose experimental results had been published. A cylindrical microstrip ground via (diameter = 0.6 mm, conductor track width = 2.3 mm, dielectric thickness = 0.794 mm,  $\epsilon_r = 2.32$ ) was simulated and a comparison made between our simulated results and experimental ones given in the literature by Sorrentino et al[11]. The comparison is given in figure 3.3 and inspection shows that there is very good agreement between our simulated and their experimental data. The accuracy and reliability of the simulation technique are demonstrated again.

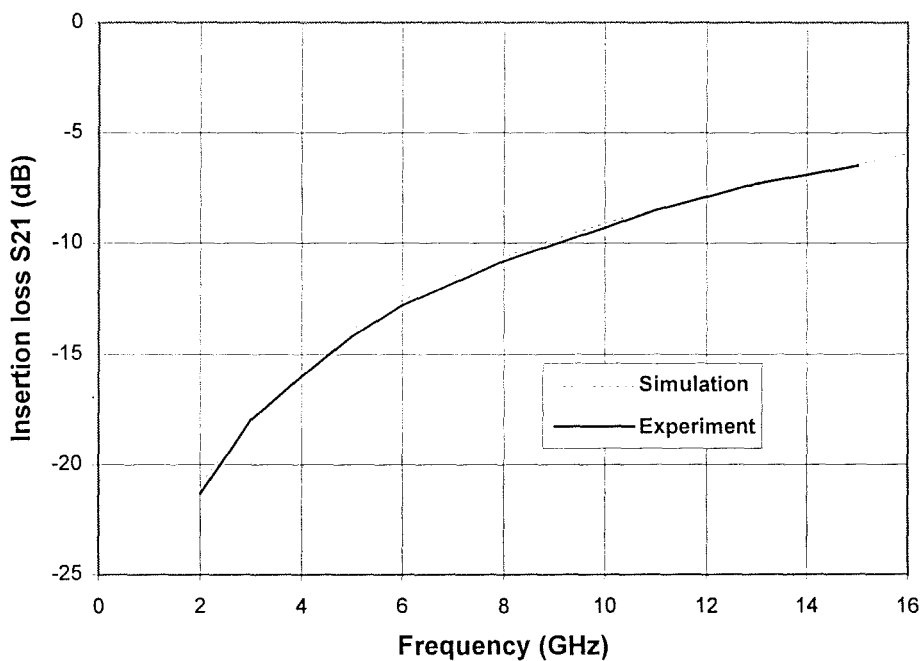


Figure 3.3 Comparison between simulated and experimental data for a cylindrical grounding via.

### 3.4 Simulation of cylindrical, square and wedge-shaped vias

#### 3.4.1 Magnitude of S-parameters for simulated vias

In order to avoid mismatches due to different characteristic impedances of the lower and upper transmission lines connected to the via under investigation, HFSS<sup>TM</sup> was used to optimise the width of the conductor track on the two layers to give equal characteristic impedance. The “port only function” in HFSS<sup>TM</sup> makes this process of optimisation very quick and accurate. For the 50 $\mu\text{m}$  square and cylindrical vias (50 $\mu\text{m}$  represents the diameter of the cross-section for a cylindrical via or the lateral length of the cross-sectional square shape for square via), the widths of the lower and upper conductor tracks were 50 $\mu\text{m}$  and 112 $\mu\text{m}$  respectively. Similarly, for the 100 $\mu\text{m}$  square and cylindrical vias, the conductor widths were 100 $\mu\text{m}$  and 211 $\mu\text{m}$  respectively. Two kinds of wedge-shaped vias were investigated. One is a 50 $\mu\text{m}$  wedge-shaped via with top and bottom diameters of 50 $\mu\text{m}$  and

Table 3.1 Dimensions of the simulated structures

Via structures	Via size ( $\mu\text{m}$ )	Upper track width ( $\mu\text{m}$ )	Lower track width ( $\mu\text{m}$ )
Cylindrical	50	112	50
Cylindrical	100	211	100
Square	50	112	50
Square	100	211	100
Rectangular	150x50	112	50
Wedge-shaped	50/30 top/bottom	72	30
Wedge-shaped	100/60 top/bottom	133	60

30  $\mu\text{m}$  respectively, which is connected by upper and lower conductor tracks with the width of 72 $\mu\text{m}$  and 30 $\mu\text{m}$  respectively. The other is 100 $\mu\text{m}$  wedge-shaped via with top and bottom diameters of 100 $\mu\text{m}$  and 60 $\mu\text{m}$ , and 133 $\mu\text{m}$  and 60 $\mu\text{m}$  for the widths of the upper and lower conductor tracks. The thickness of any single dielectric layer for all vias simulated here is 20 $\mu\text{m}$ . For a clear and convenient reference, the widths of the conductors on the two layers for several different kinds of vias are listed in Table 3.1. Fig.3.4 (a-c) show the return loss (or reflection coefficient) for 50 $\mu\text{m}$  square, cylindrical and wedge-shaped vias. The size of the square via pads (figure 3.2a) is set as either 150 $\mu\text{m}$  or 120 $\mu\text{m}$ . As anticipated, the vias with the smaller pads always yield higher return loss or better performance. It follows that increasing the pad area reduces the return loss. The ideal geometries of vias without via pads set the highest limit of the return loss or performance since, in this situation, in addition to the elimination of discontinuities between microstrip line and via pad, the discontinuities between vias and pads are also minimised. The comparison between the vias with different geometries shows that the cylindrical via has the highest return loss, while the wedge-shaped one demonstrates the worst performance (i.e. the least return loss). In order to compare the differences due to the via size, the simulation is also performed for 100 $\mu\text{m}$  square, cylindrical and wedge-shaped vias with ideal geometry shown in figure 3.1. The simulation results are shown in figure 3.5 and it clearly indicates that the cylindrical via still has the best performance and the return losses for smaller vias are lower than that for bigger vias irrespective of geometry, i.e. the performance of the bigger vias is better than smaller ones. This is due to a relative increase in the significance of the fringing field component around smaller vias. It should be noted that the simulated results can be equivalently presented as transmission loss, S<sub>21</sub>. The S-parameters can also be normalised to any port impedance, for example 50 ohm.

The simulation was also carried out for rectangular vias because this kind of via is sometimes used in MCM structures. The only difference between the rectangular via and

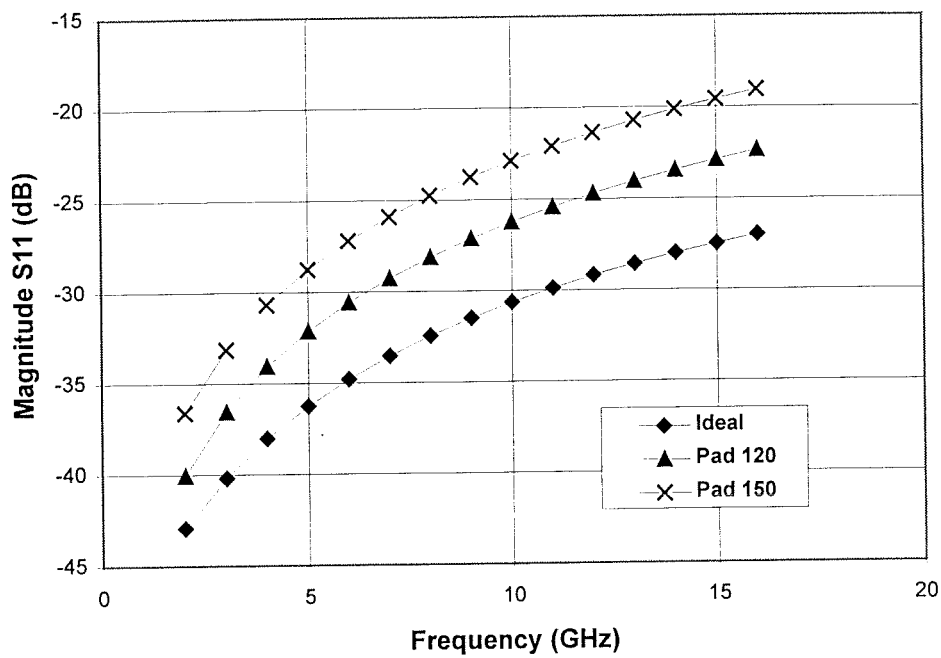


Figure 3.4 (a) 50 $\mu$ m cylindrical via

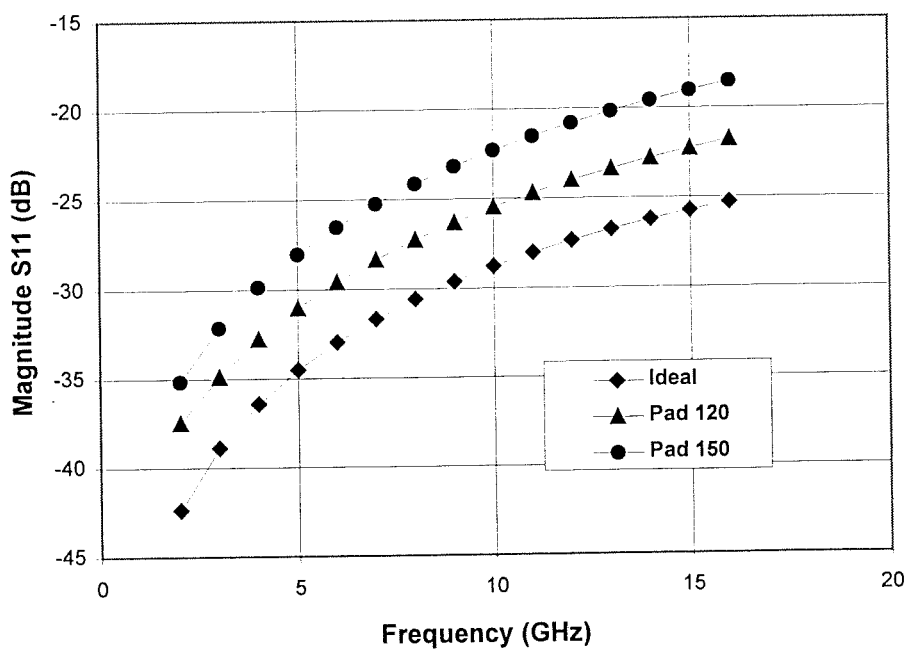
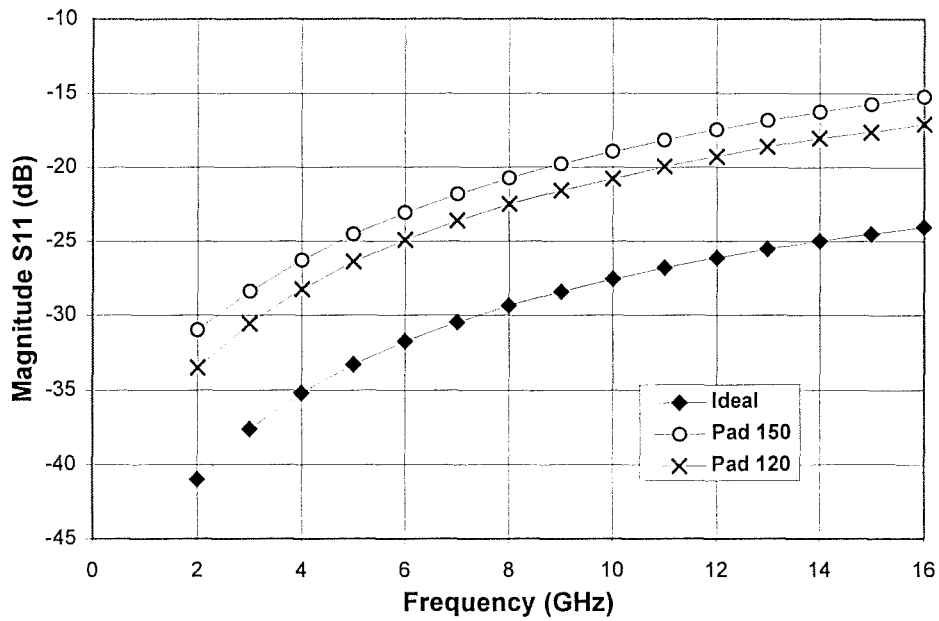


Figure 3.4(b) 50  $\mu$ m square via





(c) 50  $\mu\text{m}$  wedge-shaped via

Figure 3.4 Simulated reflection coefficient, S11, for 50 $\mu\text{m}$  cylindrical (a), square (b) and wedge-shaped vias (c).

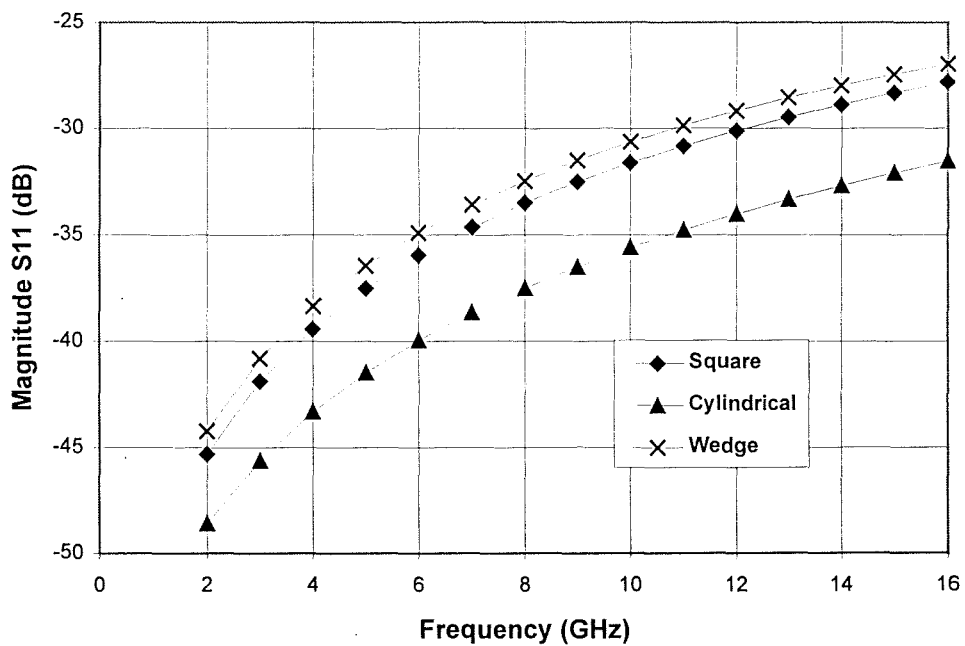
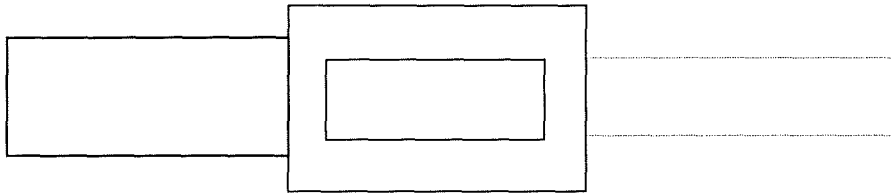
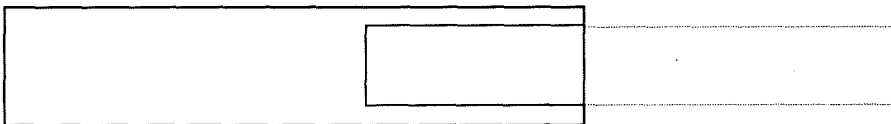


Figure 3.5 Simulated results for 100 $\mu\text{m}$  cylindrical, square and wedge-shaped vias.

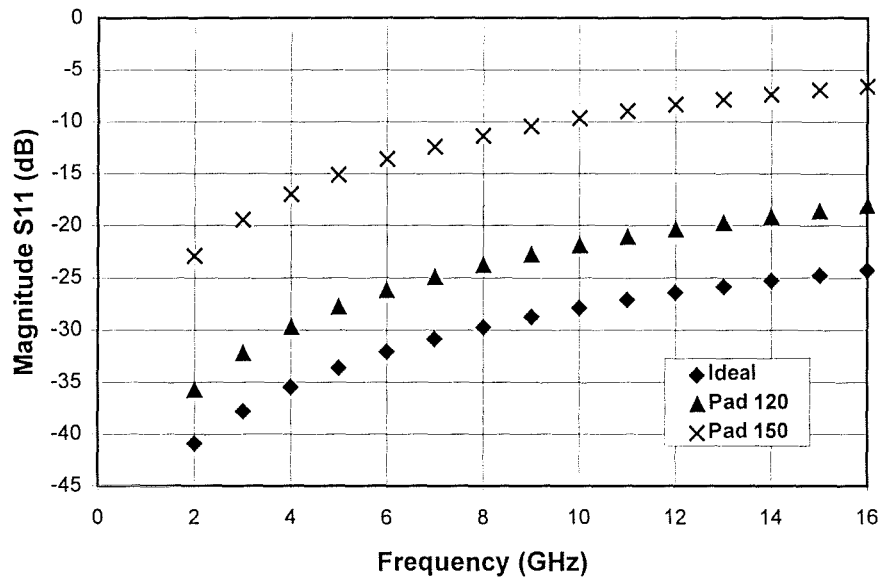
square via is that the former is three times longer than the latter. The physical size of a square via is  $W \times L \times H = 50 \times 50 \times 20 \mu\text{m}$  while the physical size of a rectangular via is  $W \times L \times H = 50 \times 150 \times 20 \mu\text{m}$ .  $L$  is the length of a via which is the dimension along the microstrip line;  $W$  is the width of the via and  $H$  represents the height of a via which equals the thickness of each dielectric layer. The via pads for a rectangular via are either  $120 \times 230 \mu\text{m}$  (pad 120) or  $150 \times 230 \mu\text{m}$  (pad 150) with the shorter side of the via pad facing the direction of the propagating wave and the longer side of the via pad along the direction of propagating wave. Figure 3.6 shows the diagrams and simulated results for rectangular via with via pads or with ideal geometry and it clearly indicates that the performance of a rectangular via is much more dependent on the via pads than a square via. The minimisation of via pads is necessary to reduce the discontinuity introduced by the rectangular via.



(a)



(b)



(c)

Figure 3.6 Diagrams and simulated results for rectangular vias. (a) Top view of rectangular via with rectangular via pad; (b) Top view of rectangular via with ideal geometry; (c) Simulated reflection coefficient  $S_{11}$  for rectangular vias with via pads.

### 3.4.2 Simulated phase change from vias

Phase change due to vias for the transmitted and reflected waves is another important factor for the electromagnetic characterisation of vias. Since a via is a discontinuity in the transmission route rather than a piece of transmission line, it is important to quantify the phase change after the signal is transmitted through the via. The phase change for a reflected wave could also be very important if multi-vias are employed in the same route.

Shown in figure 3.7 is the de-embedded phase change caused by 50 $\mu$ m square, cylindrical and wedge-shaped vias with ideal geometry. Extra phase change has been introduced by the presence of a via in the transmission route. For example, the phase delay at 10GHz for a piece of microstrip line connecting via on upper or lower layer with 50  $\mu$ m in length will give a phase change of about 1.1°. After de-embedding, the absolute phase changes through the square, cylindrical and wedge-shaped vias are 2.52°, 2.74° and 2.71° respectively. Shown in figure 3.8 and 3.9 are the phase changes due to the 50 $\mu$ m vias with 120 $\mu$ m and 150 $\mu$ m square via pads respectively. Obviously the via pad introduces more phase change, especially for a wedge-shaped via. Figure 3.10 is the phase change of the reflected waves for 50 $\mu$ m cylindrical, square and wedge-shaped vias with ideal geometries. The significant difference in reflection phase change between cylindrical via and square or wedge-shaped via is attributed to the smaller parasitic capacitance and inductance for the former (sharp edges removed in comparison with square via, and less restriction to current flow compared with wedge-shaped via).

In the practical microwave circuit design, sometimes the excess phase introduced by a parasitic element such as a via, microstrip bend or bonding wire etc. has to be calculated and compensated. The excess phase arises, in general, where there is a field discontinuity in a transmission route which causes a change in the transmission phase through the discontinuity, greater than that simply calculated in terms of the electrical length of the discontinuity. This excess phase may be small, but where there are a number of vias in cascade, the cumulative effect of the excess phase can be very significant. This becomes important for the circuit designer, particularly where there may be unequal numbers of vias in the routes interconnecting ICs. The excess phase can be determined in a straightforward manner by taking the difference between the measured or simulated transmission phase through a discontinuity and the phase calculated using the electrical length of the structure. For the case of a cylindrical via, the excess phase is calculated and presented in figure 3.11. The excess phase is increased by the presence of the via pad, as might be expected from considerations of fringing capacitance. The values, although small, are by no means insignificant, and certainly when there are a number of

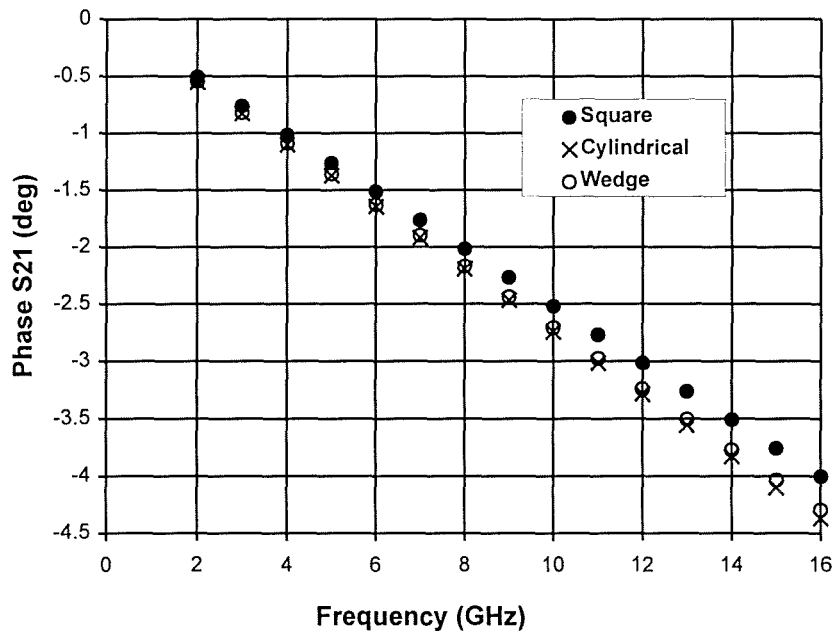


Figure 3.7 De-embedded phase change after transmission through square, cylindrical and wedge-shaped vias with ideal geometry.

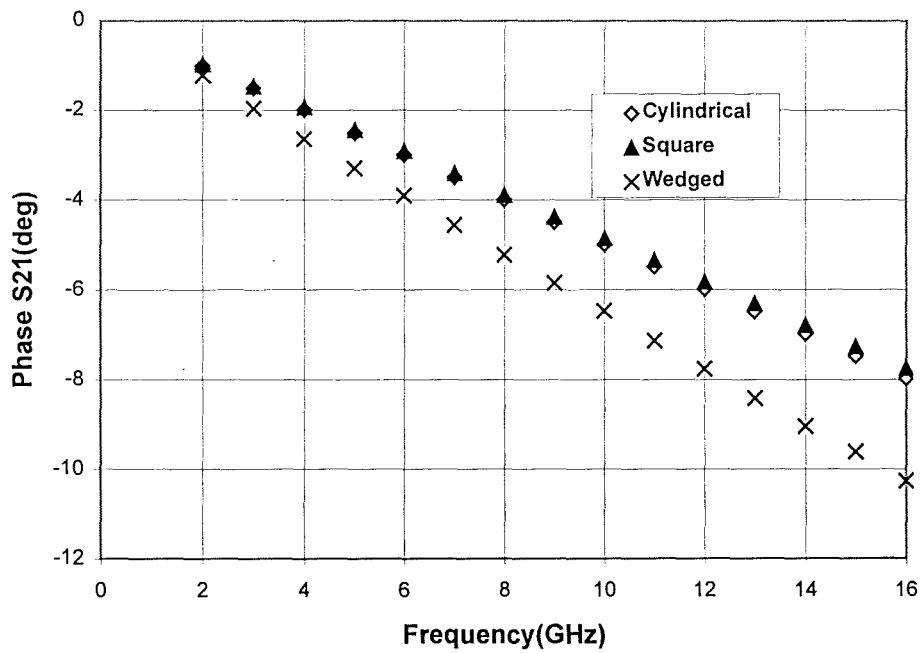


Figure 3.8 De-embedded phase change after transmission through square, cylindrical and wedge-shaped vias with 120 $\mu$ m via pad.

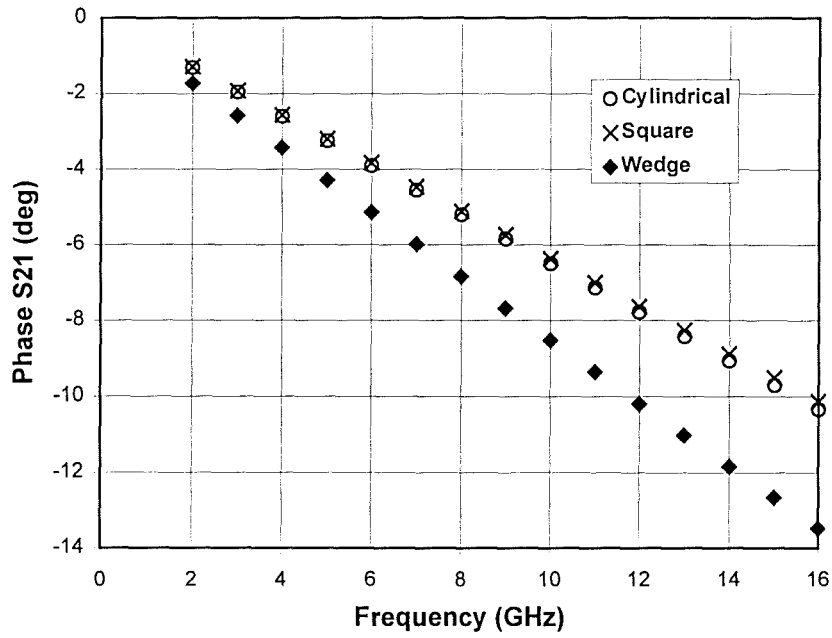


Figure 3.9 De-embedded phase change after transmission through Square, cylindrical and wedge-shaped vias with 150 $\mu$ m via pad.

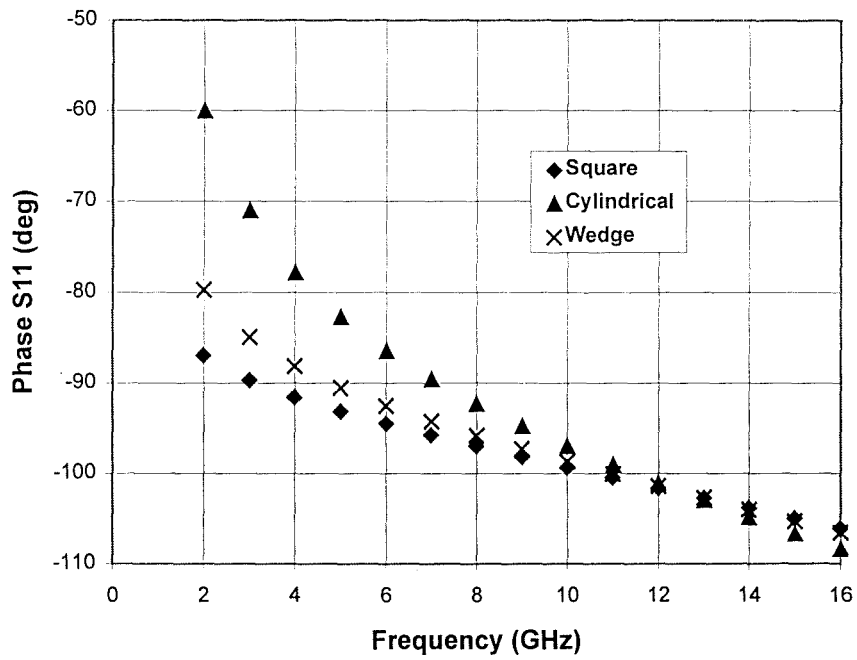


Figure 3.10 De-embedded phase change of reflected waves for 50 $\mu$ m square, cylindrical and wedge-shaped vias with ideal geometry.

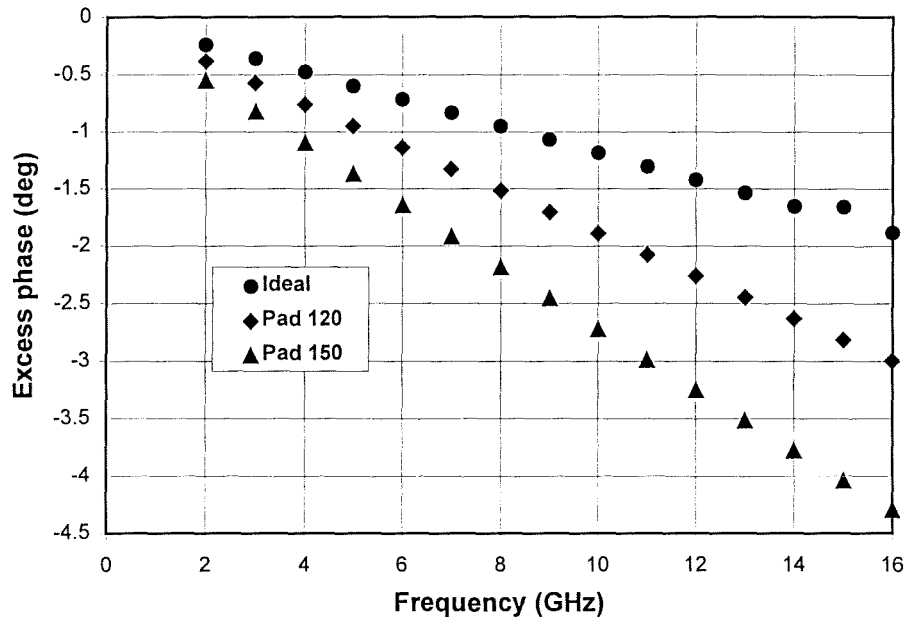


Figure 3.11 Excess phase for cylindrical vias with square pads

vias in cascade that could represent a major source of error. This identifies an important design parameter, and shows clearly that it is not sufficient merely to consider the electrical length of the via when calculating the total phase change through an MCM interconnect.

### 3.5 Modelling of vias by equivalent circuit

A via is a kind of discontinuity exhibiting frequency-dependent behaviour which can be used for interconnections in multi-layer electronic circuits. For the practical use of the simulated results, it would be ideal to have a physical model to describe the electromagnetic characteristics of the vias. This would make the circuit design more rigorous. To this end, based on electromagnetic simulation by the finite element method, the equivalent circuits of

Table 3.2 Component values of  $\pi$ -type equivalent circuit for vias with different geometric shapes

Vias	Via pad	L(nH)	C(pF)
50 $\mu\text{m}$ cylindrical vias	Ideal geometry	0.010	0.0155
	120 $\mu\text{m}$ pad	0.023	0.026
	150 $\mu\text{m}$ pad	0.027	0.036
50 $\mu\text{m}$ square vias	Ideal geometry	0.0058	0.0159
	120 $\mu\text{m}$ pad	0.018	0.0288
	150 $\mu\text{m}$ pad	0.021	0.038
50 $\mu\text{m}$ wedge-shaped vias	Ideal geometry	0.0050	0.0134
	120 $\mu\text{m}$ pad	0.014	0.031
	150 $\mu\text{m}$ pad	0.022	0.041
100 $\mu\text{m}$ vias with ideal geometry	cylindrical	0.0158	0.023
	square	0.012	0.026
	wedge-shaped	0.0145	0.0185

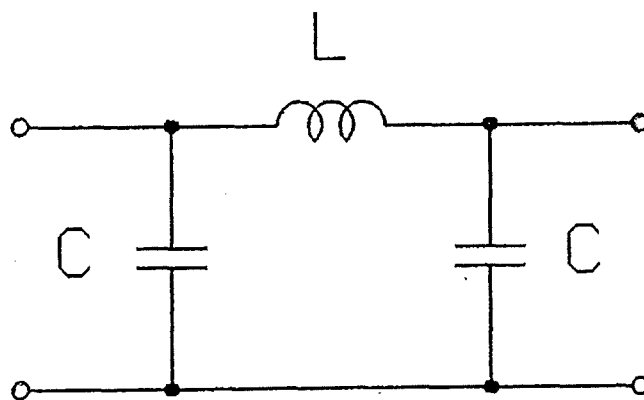
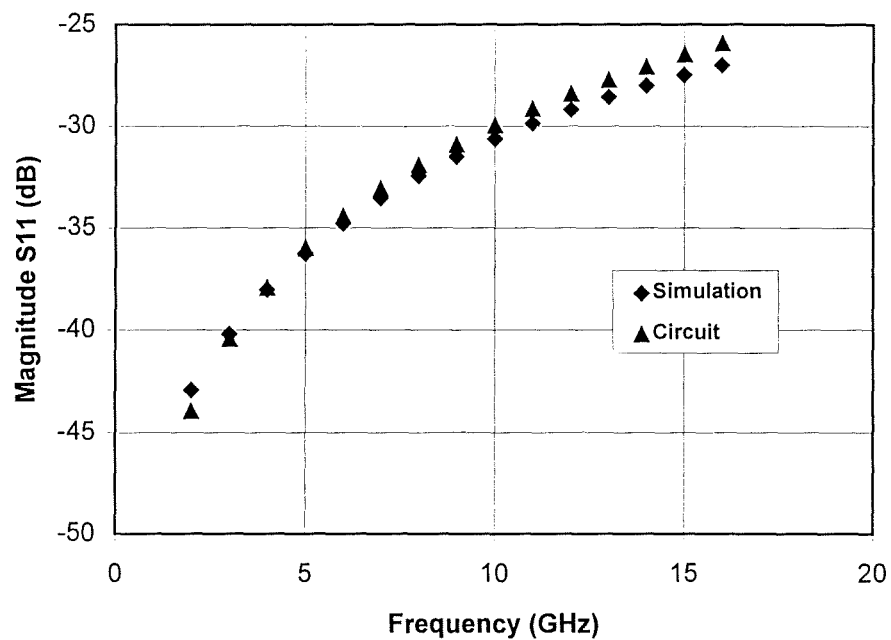
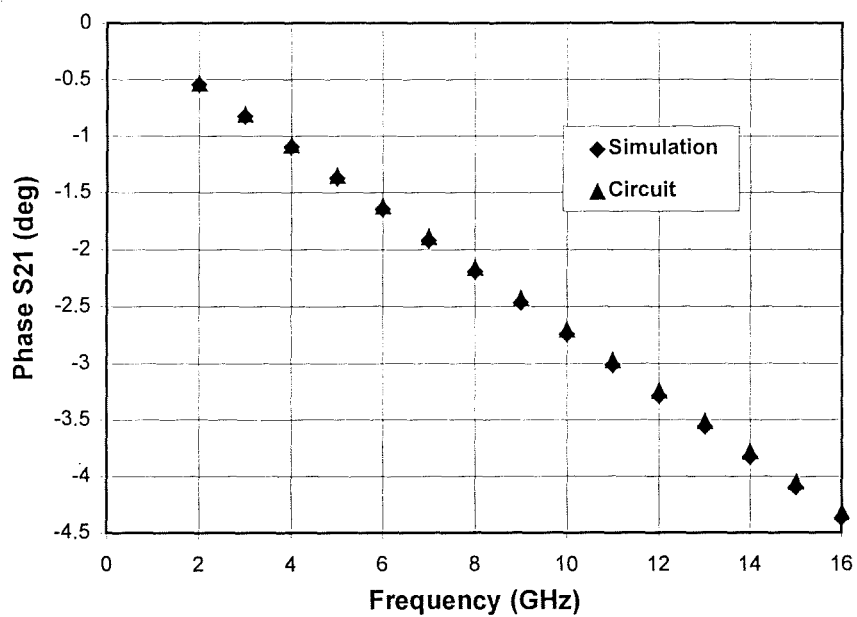


Figure 3.12  $\pi$ -type equivalent circuit used to model the transmission behaviour of vias.





(a)



(b)

Figure 3.13 Fitting of S-parameter in magnitude (a) and phase (b) between the simulation and  $\pi$ -type equivalent circuit for cylindrical via.

the vias are obtained from fitting the S-parameters of the equivalent circuits with those from simulation.  $\pi$  type equivalent circuits were adopted for all of the vias because it is simple yet gives a fairly good fitting. The basic structure of the  $\pi$ -type equivalent circuit is shown in figure 3.12. The components of the equivalent circuits are listed in Table 3.2. It was found that the  $\pi$ -type circuit provides an excellent fitting with the simulated results. Figure 3.13 (a), (b) show the agreement in the fitting regarding to the magnitude and phase of S-parameter for 50  $\mu\text{m}$  cylindrical via. The reason why a single stage  $\pi$ -type equivalent circuit can give a good description of a via is that the via simulated here is physically very small compared with the guide wavelength and the distributed behaviour of it can therefore be neglected, leaving the use of the lumped component accurate enough for most applications.

### 3.6 Conclusions

A new electromagnetic approach to the analysis of vias in multi-layer MCM structures has been shown to yield useful circuit design information. The cylindrical via exhibits the least discontinuity of the structures studied, while the wedge-shaped via presents the highest discontinuity. The size of the pad associated with a via can significantly change its transmission behaviour. Moreover, the work has shown that an accurate analysis of the characteristic impedance of the planar transmission line elements of a multi-layer interconnection structure is required to achieve acceptable return losses. The results obtained here show that this new approach using finite element simulation can provide a design methodology which gives precise data for the design of MCMs and also for the development of packaging for very high speed integrated circuits. Since vias are very small with respect to line length, it has been shown also that it is legitimate to use a lumped component equivalent for vias within circuit design.

## References

- [1] P. A. Kok and D. D. Zutter, "Least-square estimation of the equivalent circuit parameters of a via-hole from a TDR reflectogram, including on-board rise time and delay estimation", IEEE Trans. Composite, Hybrid, and Manufact. Tech., vol 16, No. 3, May 1993.
- [2] N. Jain and P. Onno, "Methods of using commercial electromagnetic simulators for microwave and millimeter-wave circuit design and optimisation", IEEE Trans. Microwave Theory Tech., Vol. 45, No. 5, pp724-746, May, 1997.
- [3] J. Gipprich, J. Faulkner, M. Pingor, J. Masti and M. Hershfeld, "A 16 watt, 8.0-10.5 GHz power amplifier using HFET MMICs and a compact LTCC splitter/combiner network", ISHM'96 microelectronics symposium, Proceedings, pp508-510, Minneapolis, Minnesota, USA, October, 1996
- [4] T. Wang, J.F.Mautz, and R.F. Harrington, "The excess capacitance of a microstrip via in a dielectric substrate", IEEE Trans. Computer-aided Design, vol. 9, No.1, pp48-56, Jan., 1990.
- [5] P. Kok, and D.D. Zutter, "Capacitance of a circular symmetric model of a via hole including finite ground plane thickness", IEEE Trans. Microwave Theory Tech., Vol. 39, No. 7, pp1229-1234, July, 1991.
- [6] S. Hsu, and R. Wu, "Full-wave characterisation of a through hole via using the matrix-penciled moment method", IEEE Trans. Microwave Theory Tech., Vol. 42, No. 8, pp1540-11547, August, 1995.
- [7] A.S. Theodorou, and N.K. Uzunoglu, "Transition properties of a vertical conductor connecting two microstrip lines at different planes", IEEE Trans. Microwave Theory Tech., Vol.42, No. 12, pp2277-2284, Dec., 1994
- [8] S. Maeda, T. Kashiwa, and I. Fukai, "Full wave analysis of propagation characteristics of a through hole using the finite-difference time-domain method", IEEE characteristics of a through hole using the finite-difference time-domain method", IEEE Trans. Microwave Theory Tech., Vol. 39, No.12, pp 2154-2159, Dec., 1991

- [9] W.D. Becker, P.H. Harms, and R. Mittra, "Time-domain electromagnetic analysis of interconnects in a computer chip package", IEEE Trans. Microwave Theory Tech., Vol. 40, No. 12, pp 2155-2163, Dec., 1992.
- [10] E. Pillai, and W. Wiesbeck, "Derivation of equivalent circuits for multilayer printed circuit board discontinuities using full wave models", IEEE Trans. Microwave Theory Tech., Vol. 42, No. 9, pp1774-1783, Sept., 1994.
- IEEE Trans. Microwave Theory Tech., Vol. 42, No. 9, pp1727-1736, Sept., 1994.
- [11] R. Sorrentino, F. Alessandri, M. Mongiardo, G. Avitabile, and L. Roselli, "Full-wave modelling of via hole grounds in microstrip by three-dimensional mode matching technique", IEEE Trans. Microwave Theory Tech., Vol. 40, No. 12, pp 2228-2233, Dec., 1992.
- [12] J. Yook, N.I. Dib, and L.P.B. Katehi, "Characterisation of high frequency interconnects using finite difference time domain and finite element methods", IEEE Trans. Microwave Theory Tech., Vol. 42, No9, pp1727-1736, September, 1994.

# **Chapter 4 Interactions between discontinuities in proximity in MCM interconnection in microwave frequencies**

## **4.1 Introduction**

## **4.2 Simulation and modelling of microstrip bends in MCM interconnection**

## **4.3 Interaction between vias in MCM interconnection at microwave frequencies**

## **4.4 Simulation of airbridge in high frequency, high density packaging**

---

Chapters 2 and 3 have respectively looked at two major aspects of 'real' MCM structures, crosstalk between conductor tracks at the same or different levels and the effects of a passive component, the via between layers of a multilayer structure. In MCMs these effects are joined by proximity effects due to the need to accommodate geometrical or electrical demands. This chapter discusses in detail how the discontinuities interact with each other when they are in proximity and the implications in the MCM design due to the interactions.

## **4.1 Introduction:**

The current development of MCM and MMIC is towards higher packaging density and higher frequency of operation, leading to more compact and versatile commercial products. The high packaging density demands the miniaturisation of interconnection between chips and passive elements, and in tight layout. The tight layout results in undesirable interaction or crosstalk between interconnect lines and interconnect components. In addition, the extent of discontinuities in MCM interconnection and interaction between discontinuities must be understood for a satisfactory electrical design. For example in the design of high performance RF IC, such as local oscillators, mixers and low noise amplifiers, the crosstalk between interconnection lines and parasitic discontinuities has to be addressed.

It is well known that the coupling between closely spaced conductors is frequency dependent, and that this coupling increases as the frequency increases. The type of interconnection structure encountered in three-dimensional MCM and MMIC devices is sometimes non-standard (bends, vias, bondwire and air bridges etc. are examples of non-standard structures) and previous work (by the authors) [1,2] has shown full electromagnetic simulations are needed to adequately represent the microwave behaviour of these interconnection elements. Such simulations yield useful high-frequency information, both for the individual interconnection elements and for the interaction between them. The 3-D full electromagnetic simulation, compared with quasi-static techniques which simulate the discontinuities in the transmission route by lumped elements and interaction between interconnection elements by mutual inductance and capacitance [3-5], is not only more rigorous and accurate but also more flexible and versatile in producing electrical information and providing more in-depth understanding of the electromagnetic characteristics of the interconnection structures involved for both passive and active circuit design employing high density packaging. In this chapter we extend the previous work on a single via structure and the coupling between interconnection lines to include the effects of coupling between interconnect discontinuities of bends, vias and air bridges to provide more insight into the high frequency behaviour of densely packed interconnection structures. The individual elements of discontinuities are also simulated and modelled, the results of which can be used in a circuit simulator.

## **4.2 Simulation and modelling of microstrip bends in MCM interconnection**

### **4.2.1 HP Momentum™ : a 2.5-D multi-layer planar electromagnetic field solver**

In chapters 2 and 3 we have already carried out electromagnetic simulation using HP HFSS™, a true three dimensional (3-D) electromagnetic simulator. Whilst the versatility of HFSS™ in simulating the electromagnetic structure with almost any kinds of geometries is

readily available, there is always a limitation imposed by computer resources. In HFSS™ the three-dimensional structures have to be meshed using tetrahedra, the resulting matrix equation are usually very large and the time needed for the simulation at a given accuracy could be very long. In practice most of the interconnections encountered in MCM and MMIC structures are planar ones, which can be more conveniently solved by a two and a half dimensional (2.5-D) electromagnetic simulator based on a method of moments (MoM) solution of the mixed potential integral equations. This chapter describes the use of HP Momentum™ to simulate bends, vias and airbridges, and their interactions. Since the meshes are only generated on conductors, the size of the resulting matrix equation will be much smaller than that generated by HFSS™, and consequently the solution time can be reduced dramatically. This would be more practical and economical for the design of real MCM and MMIC circuits.

HP Momentum™ carries an adaptive solution that automatically creates and refines the meshes in regions where needed to satisfy an accuracy predefined by the users. Conductor loss, dielectric loss and radiation effects can also be included in the simulation. The conductors can lie either on or within layered dielectric substrates. Standard planar and multi-layer structures can be quickly produced from built-in models. The drawing interface also allows users to draw their own structures.

#### **4.2.2 Simulation and modelling of a single microstrip bend**

For a thorough understanding of interaction between microstrip bends, and of implication arising from the miniaturisation of interconnections in high frequency and high density packaging, we start from the simulation and modelling of a single microstrip bend. The structure and reference planes for a single microstrip bend are shown in figure 4.1. The dimensions chosen for the all bend structures in this chapter were commensurate with those corresponding to KQ-technology from Heraeus. Each dielectric layer was 20  $\mu\text{m}$  in thickness and had a relative permittivity of 4. The conductor track width was calculated to be 41  $\mu\text{m}$  in

order to give a characteristic impedance of  $50\Omega$  for the microstrip lines. The frequency range for the simulation is from 1 GHz to 20 GHz. All of the simulated structures are meshed at the highest frequency point in the simulation range throughout this chapter to create dense meshes and to ensure the high accuracy of the simulation. Figure 4.2 shows the transmission loss and phase change for a single microstrip bend. It can be seen that there is a significant difference between the simulated results using Momentum™ and that obtained using the Gupta model which is widely quoted in the literature [6]. Using the conventional T-model employed by Gupta as an equivalent circuit for microstrip bend, as shown in figure 4.3, the element values in the T-model were refined to give a good fit to the simulated data. The original and refined element values are shown in table 4.1. It can be seen that the differences are significant and this reflects the need to modify conventional microstrip design equations when dealing with the very small conductor geometries associated with MCM structures.

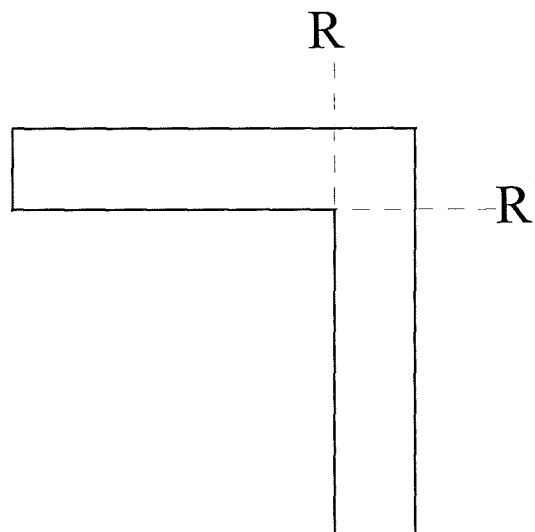
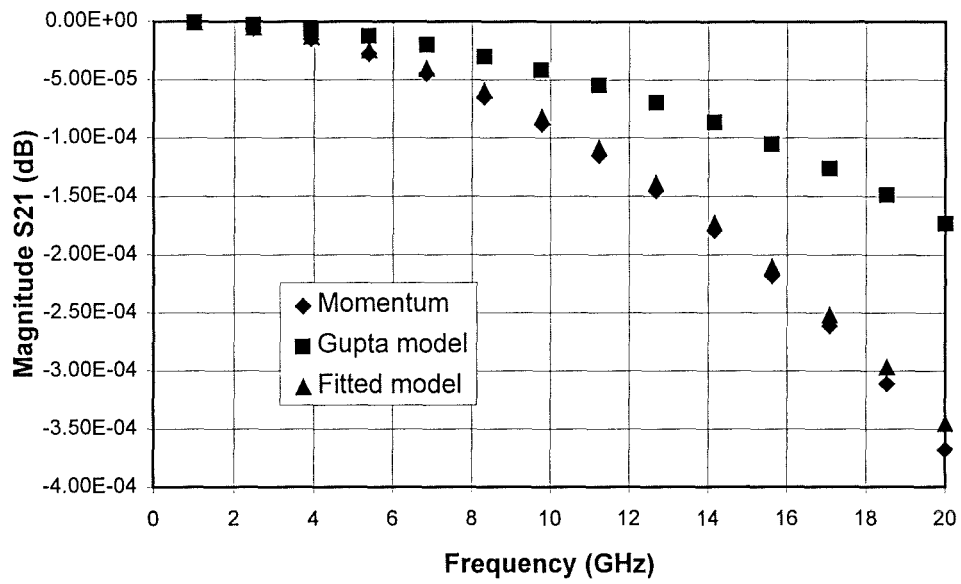
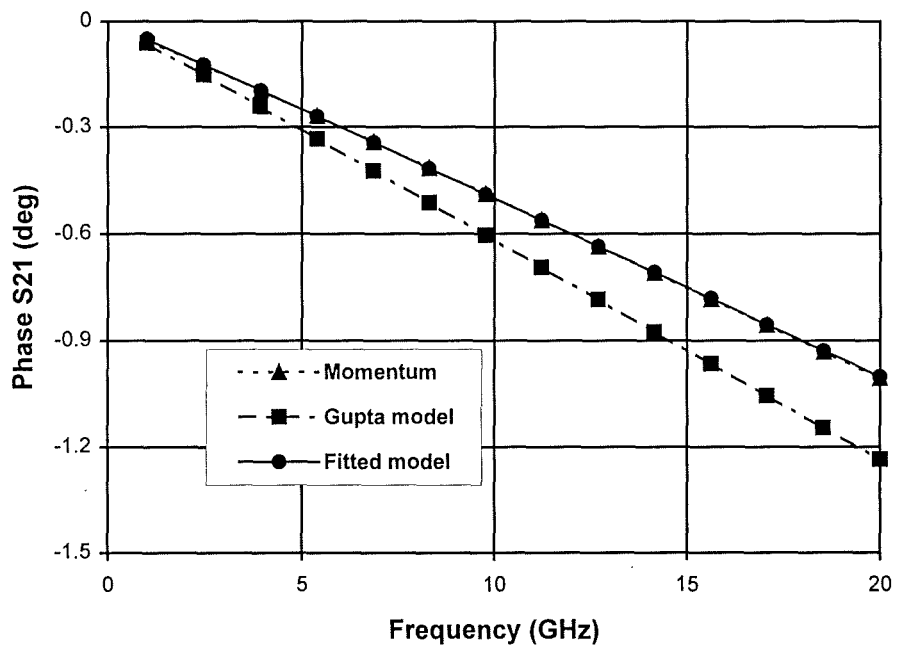


Figure 4.1 Structure and reference planes (R, R') for a single microstrip bend





(a)



(b)

Figure 4.2 Transmission loss (a) and phase change (b) for a single microstrip bend.

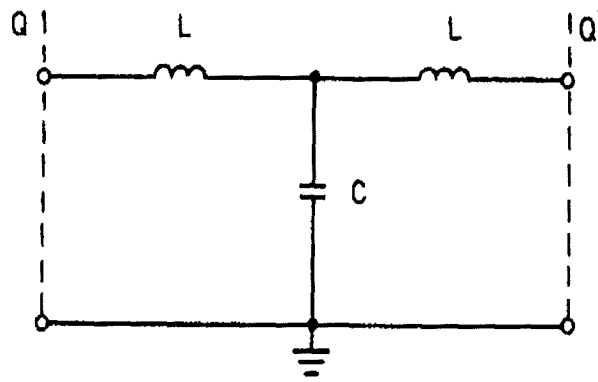


Figure 4.3 Equivalent circuit of a single microstrip bend presented as a T-model.

Table 4.1 Component values of T-model for a single microstrip bend.

T-model element	L (nH)	C (pF)
Gupta model	0.003034	0.004439
Fitted model	0.0017	0.0042

### 4.2.3 Two offset microstrip bends

Figure 4.4 shows two offset bends on the same level. The physical parameters of the offset bends are the same as those for the single microstrip bend. The magnitude and phase of the transmission coefficient for two offset bends on the same level are shown in figure 4.5. What is significant here is the effect of the spacing(s) between the bends. The figure shows the values of the transmission coefficient after the transmission through the offset length has been removed. Thus the graphs show the true effect of the interaction between the bends. From figure 4.5 it can be seen that for a smaller offset the transmission loss is also smaller than that for a larger offset.

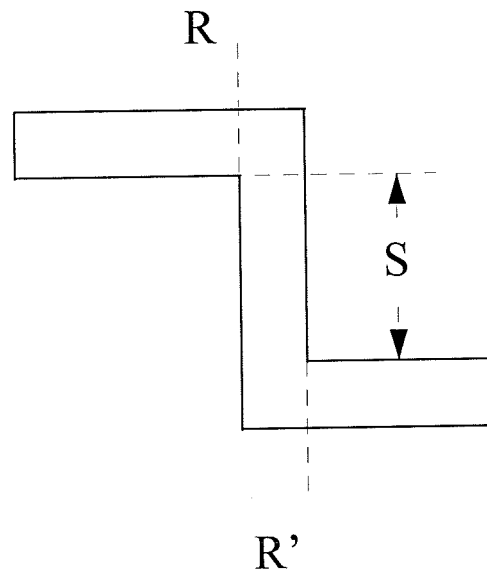
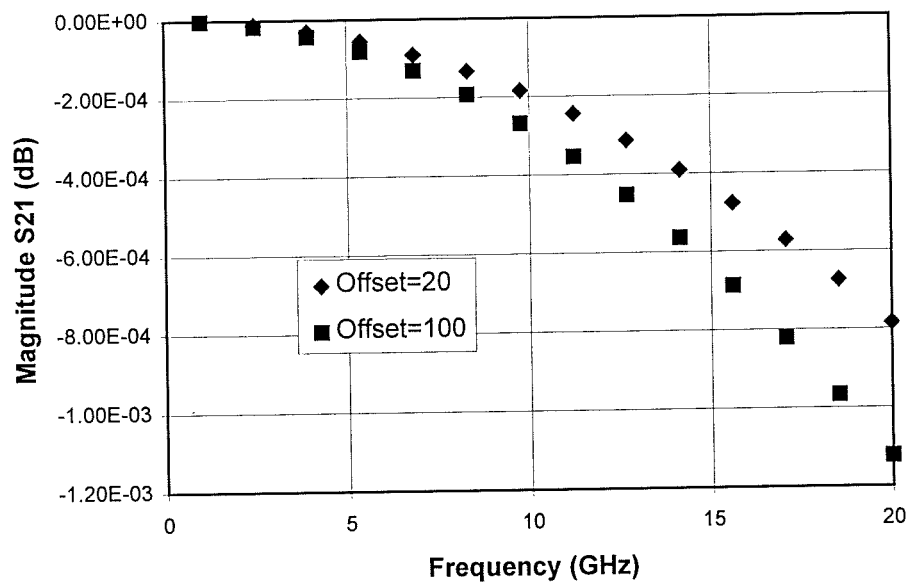
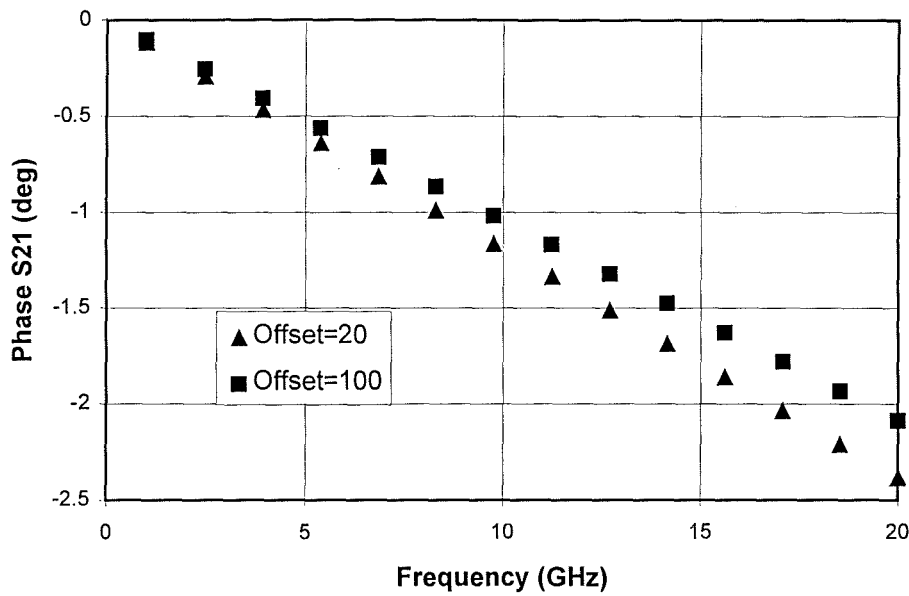


Figure 4.4 Two offset bends on the same level. Track width  $w = 41\mu\text{m}$ ; dielectric layer thickness  $h = 20\mu\text{m}$ ; permittivity  $\epsilon_r = 4$ .



(a)



(b)

Figure 4.5 Transmission loss (a) and phase change (b) for two bends with offset

The phase delay for a smaller offset, however, is bigger than that for a larger offset. This is an indication of electromagnetic interaction between two offset bends in proximity. The bends with smaller offset will be more efficient in guiding the wave through the whole structure because the transmission loss is smaller for this situation. The large phase delay for the situation of smaller offset is due to the bigger inductance associated with two bends.

#### 4.2.4 Crosstalk between two microstrip bends

Figure 4.6 is the diagram for two microstrip bends on the same level. The dielectric layer has a thickness of 20  $\mu\text{m}$  with a permittivity of 4. The microstrip width is still 41  $\mu\text{m}$ . When a dielectric overlay with a thickness of 20  $\mu\text{m}$  is placed on the top of the microstrip bends, the

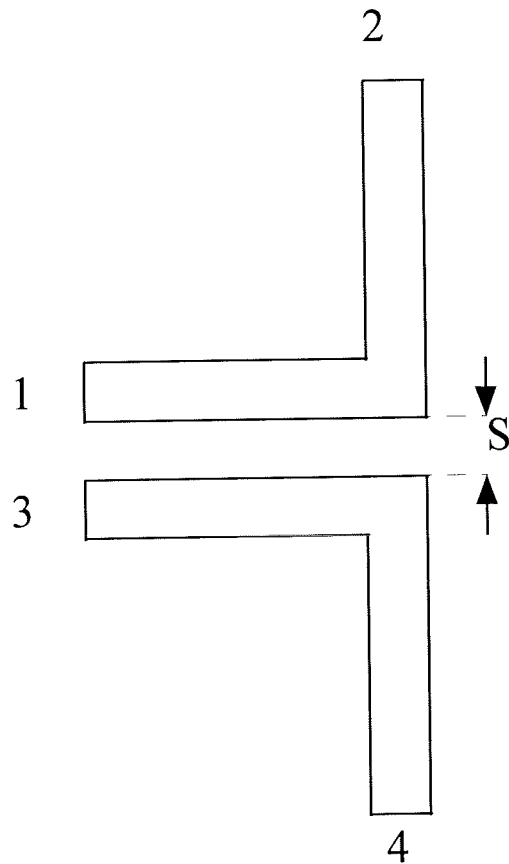


Figure 4.6 Coupled microstrip bends on the same level.

microstrip width is calculated as  $35\ \mu\text{m}$  to give, again, a characteristic impedance of 50 ohms. The crosstalk between two microstrip bend on the same layer is shown in figure 4.7. The crosstalk is that due only to the bend, after the effect of the coupled lines has been removed. It can be seen that the effect is small enough to be neglected with most practical spacings. In figure 4.8 the effect of a dielectric overlay is shown, and the crosstalk is increased by around 7%. The increase in crosstalk caused by the overlay is due to enhanced capacitance between the two microstrip bends.

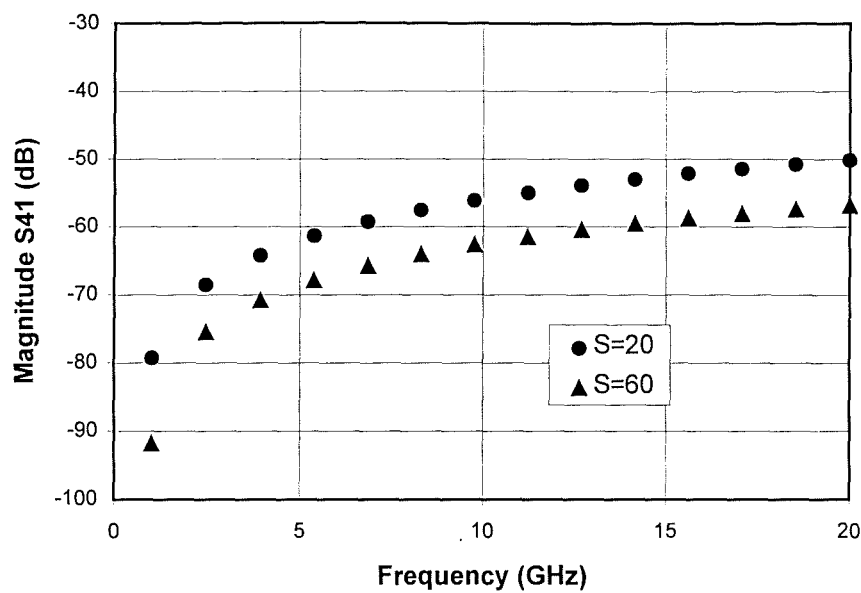


Figure 4.7 Crosstalk between two microstrip bends on same level with different separation. (20 and 60  $\mu\text{m}$  )

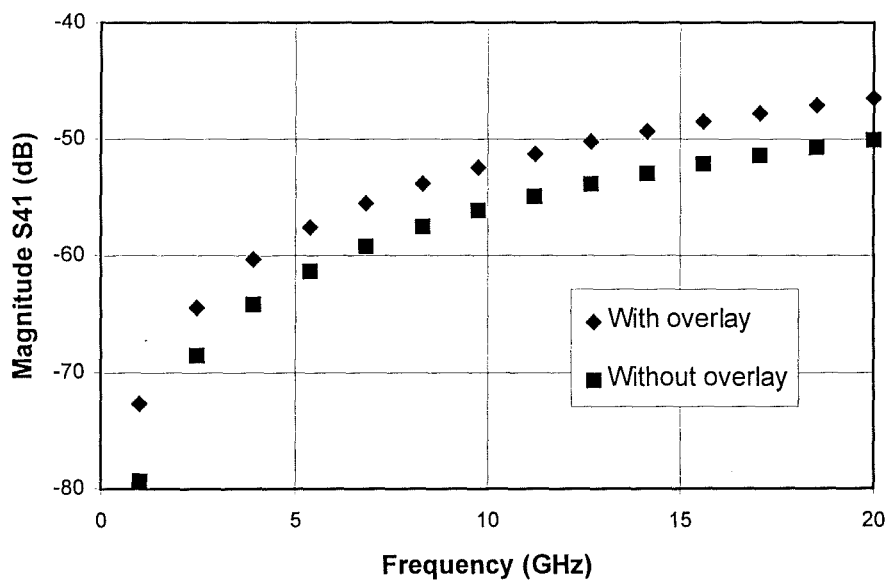


Figure 4.8 Crosstalk between two microstrip bends on the same level with overlay. The separation between bends are 20  $\mu\text{m}$ .

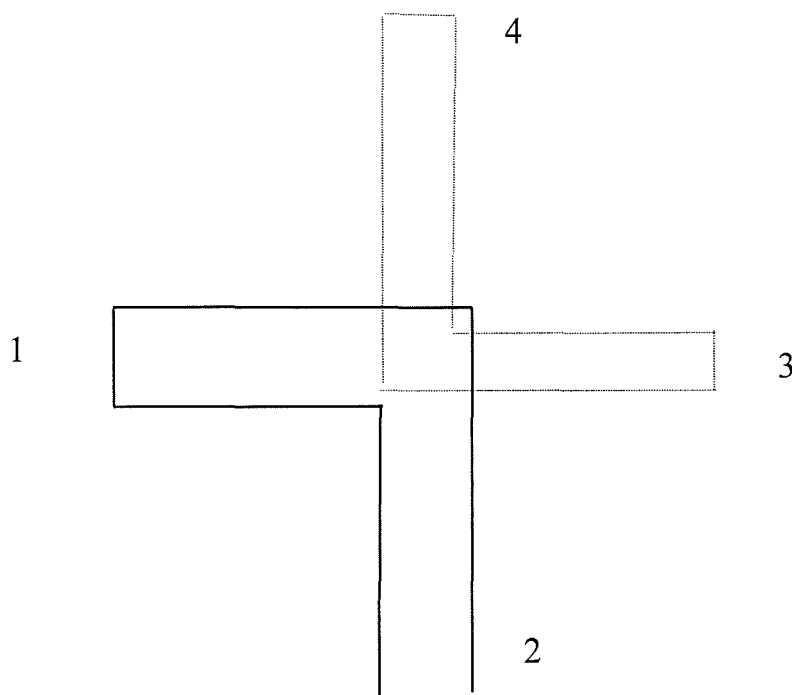


Figure 4.9 Coupled microstrip bends on adjacent levels.

Figure 4.9 shows the structure of vertically stacked bends on adjacent layers. The thickness of each layer is  $20\text{ }\mu\text{m}$  respectively. The width of the microstrip line comprised of the bend on the lower level is  $35\text{ }\mu\text{m}$ . While the width of that on the upper level is  $81\text{ }\mu\text{m}$  which corresponds to a characteristic impedance of 50 ohms. The effect of having two microstrip bend discontinuities one above the other is shown in figure 4.10. The effect is generally consistent with microstrip behaviour, with dominant backward-wave coupling, but the responses show that there is also significant coupling in the forward direction. Comparison with crosstalk for the microstrip bends on the same level reveals that the electromagnetic coupling between the two vertically stacked microstrip bends is much stronger. This indicates that caution has to be taken in generating layout where microstrip bends on different levels are involved.

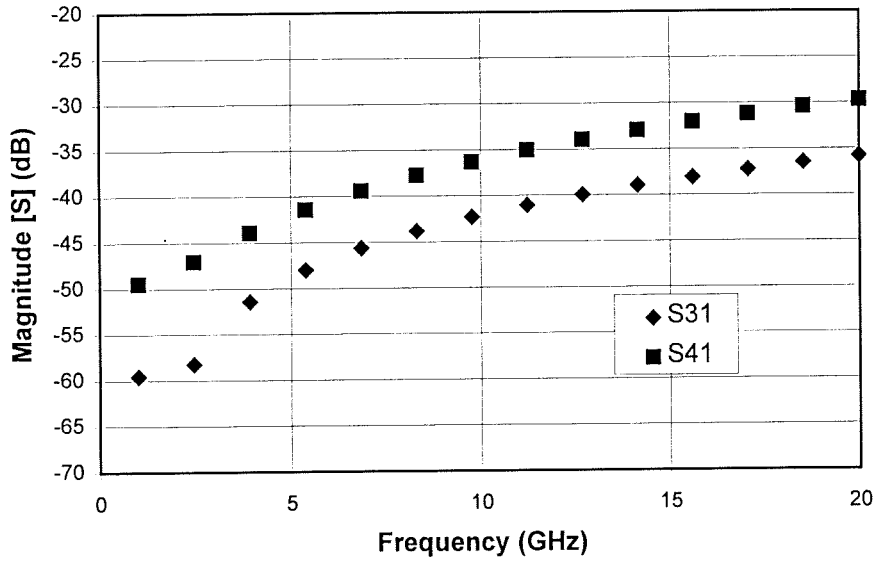


Figure 4.10 Crosstalk of coupled microstrip bends on adjacent levels

#### 4.2.5 Summary for simulation and modelling of microstrip bends

The work has shown that rigorous electromagnetic analysis is necessary to predict the behaviour of MCM and MMIC interconnects at high frequencies. In particular, the widely used circuit model for microstrip bends leads to significant errors when applied to the small dimensions necessary for MCM interconnects.



### **4.3 Interaction between vias in MCM interconnection in microwave frequencies**

The high density interconnection and high level of integration in MCMs and MICs are realised through multi-layer structures which are routed through by vias. From the point of view of wave propagation, a via can not be considered as a piece of transmission line. In fact its presence in the route of wave propagation behaves as an element of discontinuity to wave propagation. The parasitic characteristics of a via can be represented by an equivalent circuit with elements of inductance and capacitance, where the fringing field effects of a via lead to equivalent capacitive elements and the current flow disturbances, give rise to equivalent circuit inductance. For the purpose of rigorous electronic circuit design involving multi-layer structures and vias, the accurate characterisation and modelling of via and interaction among them is very important. For example, as a discontinuity in the interconnection structure of MCMs, a via can cause not only reflection of signal power but also excess phase which has already been addressed in chapter 3. Whilst the excess phase caused by a single via may not be big enough to create a detrimental effect, the combination of excess phase by multi-vias in the same route could cause bit errors.

In the following sections for vias, we will mainly investigate the interaction between vias in the same propagation route and crosstalk between vias in proximity. The effect due to the change in propagation direction from one transmission line to another through a via will also be simulated. The results obtained here can be used as a guideline for MCM design.

#### **4.3.1 Simulation of a standard cylindrical grounding via**

Before the simulation of interaction between vias, a standard grounding via, quoted from reference [7] was simulated using HP Momentum™ for the purpose of comparison between

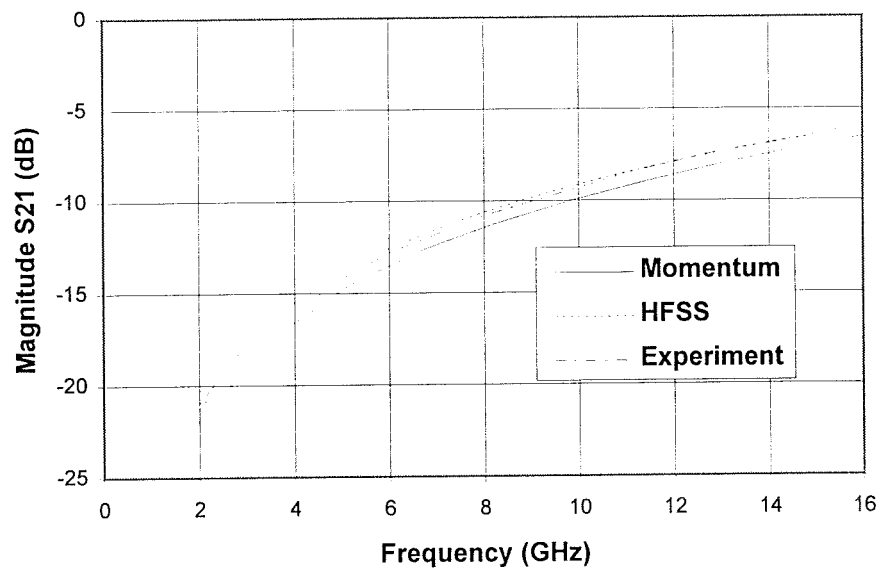


Figure 4.11 Simulated and experimental results for a standard grounding via.

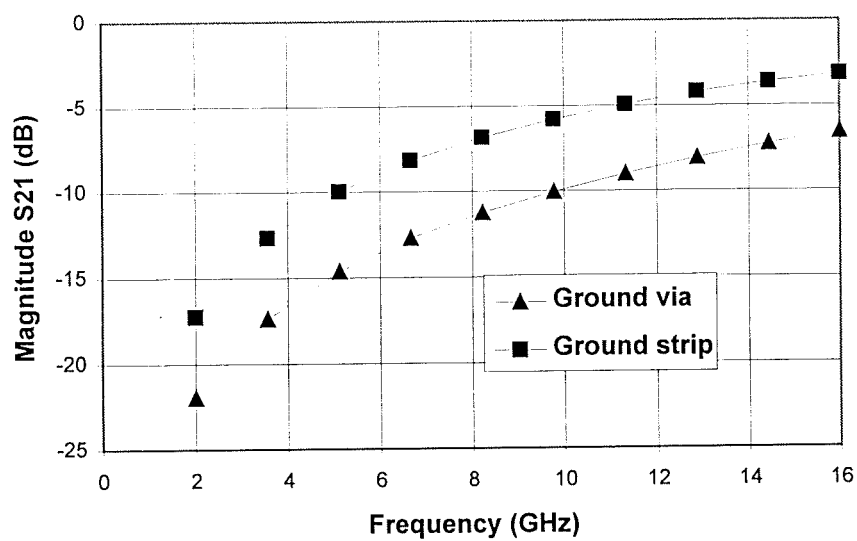


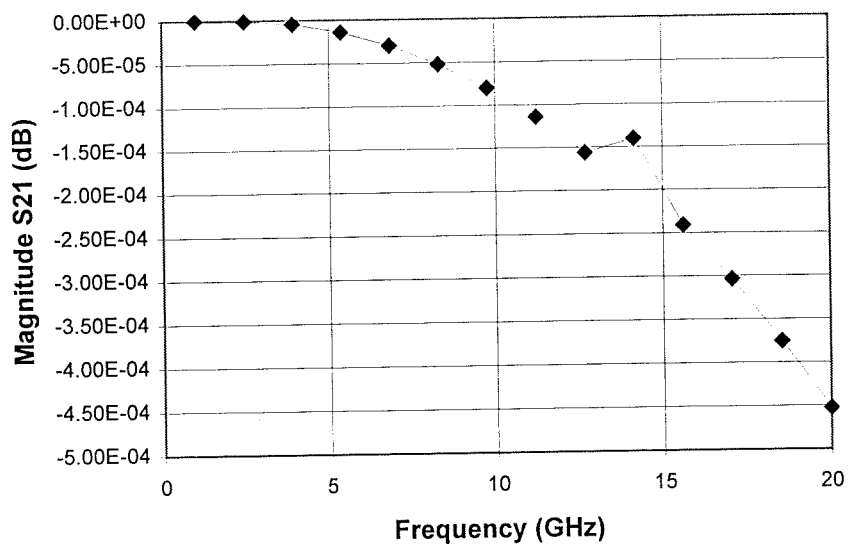
Figure 4.12 Comparison between results for a grounding via simulated either as a cylindrical via or as a simple strip.

experimental results and simulated ones. The diameter of the grounding via is 0.6 mm and the width of the microstrip line is 2.3 mm. The permittivity of the dielectric substrate is 2.32 with a thickness of 0.794 mm. The simulated and experimental results are shown in figure 4.11. The simulated results from HFSS<sup>TM</sup>, obtained in chapter 3, is also presented in figure 4.11. The comparison clearly indicates that the simulated results agree well with the experimental ones. However, the simulated result from Momentum<sup>TM</sup> is slightly less than the experimental result and the result from HFSS<sup>TM</sup> is a slightly larger. The comparison has demonstrated the accuracy in simulating vias using Momentum<sup>TM</sup>.

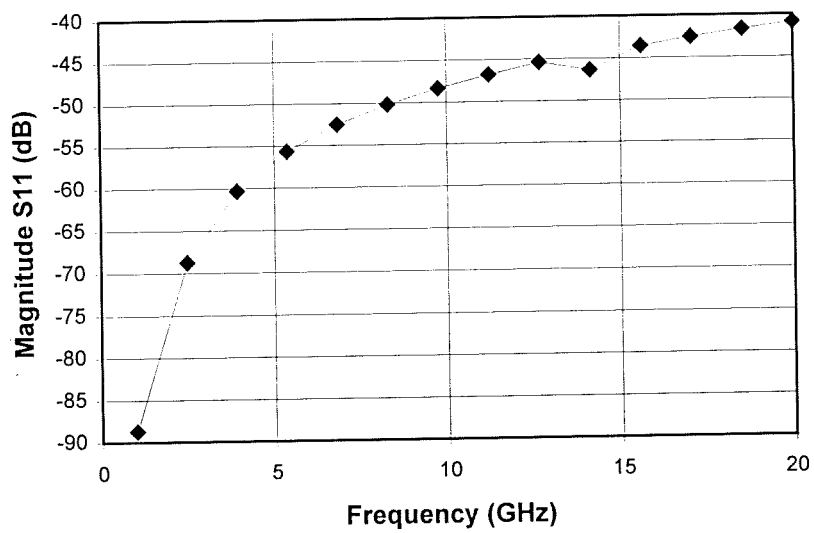
To examine how the geometric shape of the grounding via affects its behaviour, we have replaced the cylindrical grounding via by a conductor strip with size of 0.6×0.794 mm, which gives the same cross-sectional area facing the direction of wave propagation as a cylindrical grounding via. The simulated result for the grounding strip is shown in figure 4.12. The transmission loss of the strip via is about 4 dB less than that of the cylindrical via. According to the requirement for a grounding via, the transmitted energy should be as small as possible. We may thus conclude that, for the purpose of grounding connection, the performance of a cylindrical via is better than that of a strip via.

#### **4.3.2 Simulation of a 35 µm cylindrical via**

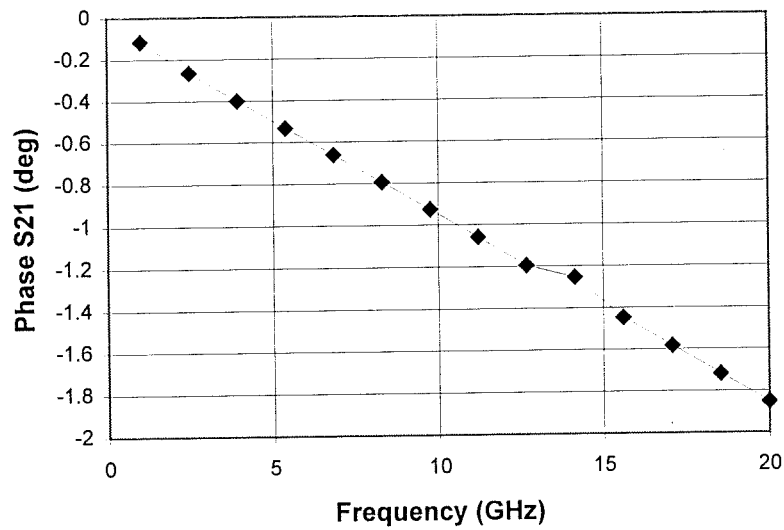
A 35 µm via has been selected because it is well compatible with the thick film and MCM technology of Heraeus. The standard thickness of a dielectric layer in Heraeus' KQ-technology is 20 µm with permittivity of 4. For a two layer structure, it can be easily confirmed by Momentum<sup>TM</sup> or HFSS<sup>TM</sup> that, in order to create 50 Ω characteristic impedance for the microstrip lines on both layers, the width of the microstrip lines on the lower and upper dielectric layers should be 35 µm and 81 µm respectively. A cylindrical via with a diameter of 35 µm can match well with the microstrip lines on the two layers. Shown in figure 4.13 is



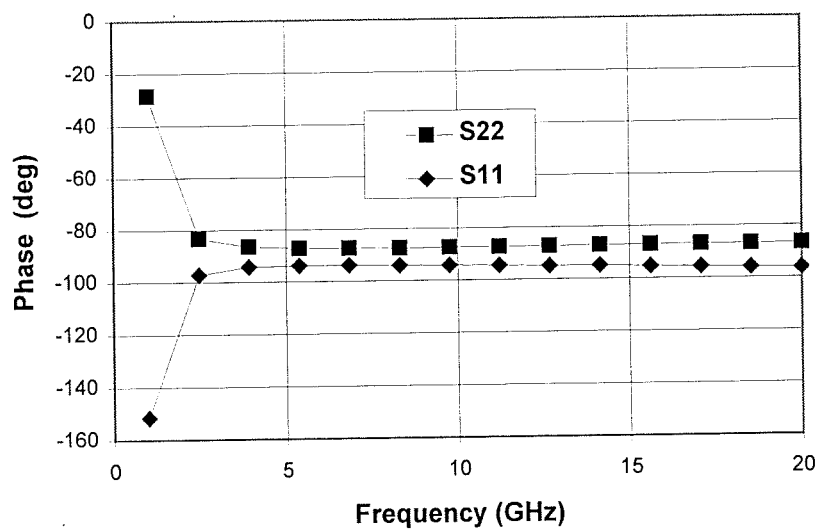
(a)



(b)



(c)



(d)

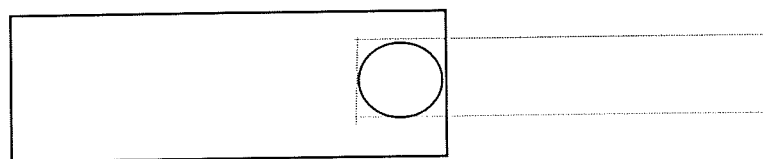
Figure 4.13 Simulated results for a 35  $\mu\text{m}$  cylindrical via. (a) Magnitude of transmission loss; (b) Magnitude of return loss (S11); (c) Phase change after transmission; (d) Phase change after reflection.

the simulated results for the 35  $\mu\text{m}$  cylindrical via. Both magnitude and phase of S-parameters are presented in the figure. Again in the simulation the dielectric loss and conductor loss is neglected to save CPU time for the computer. This is justified by the very low loss of the Heraeus materials used for the fabrication of vias and microstrip lines. Inspection of the results in figure 4.13 shows that in the frequency range investigated, the performance of the via is very good, i.e. very small transmission loss and big return loss. It should be noted that the magnitude of S21 equals magnitude S12 and the magnitude S11 equals that of S22. For the phase change after transmission,  $\text{Phase (S21)} = \text{Phase (S12)}$ . The only parameters which are not symmetrical are  $\text{Phase (S11)}$  and  $\text{Phase (S22)}$ . They just have a slight difference in the whole frequency range except at 1 GHz.

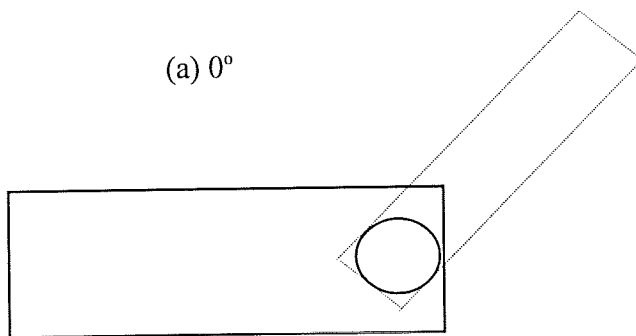
The explanation for the good performance of the via is from both the good electrical match between microstrip lines and the via and the properties of the materials involved in the construction of via. The permittivity of the dielectric substrate is very low compared with the traditional thick film materials which usually have permittivity values of around 8. The advantage of a low permittivity substrate is that the parasitic capacitance of the via is reduced. In addition the wave will travel faster in low permittivity material and thus reduce signal delay and enhance the system performance.

#### **4.3.3 Investigation of a 35 $\mu\text{m}$ cylindrical via connected by microstrip lines with different angles**

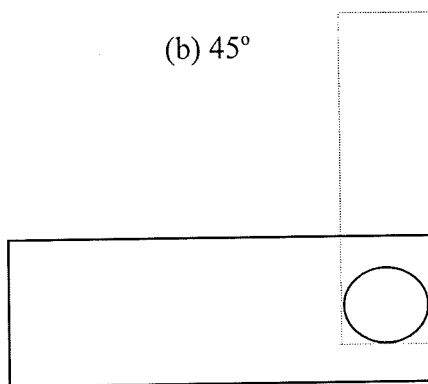
In real circuit design, for the flexibility and density of circuit layout the angle between the microstrip lines connecting via on the different dielectric layers is not necessarily  $0^\circ$ . Sometimes the angle could be  $45^\circ$  or  $90^\circ$ . Any angle bigger than  $0^\circ$  will introduce an extra parasitic effect which is mainly inductive because the current flow is disturbed by the change in direction of



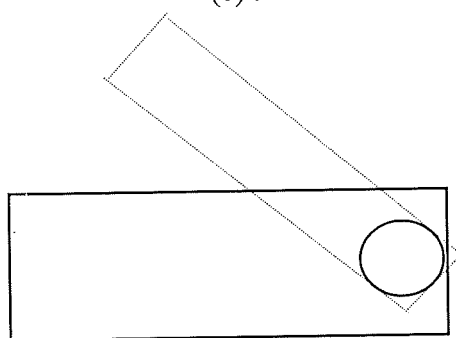
(a)  $0^\circ$



(b)  $45^\circ$

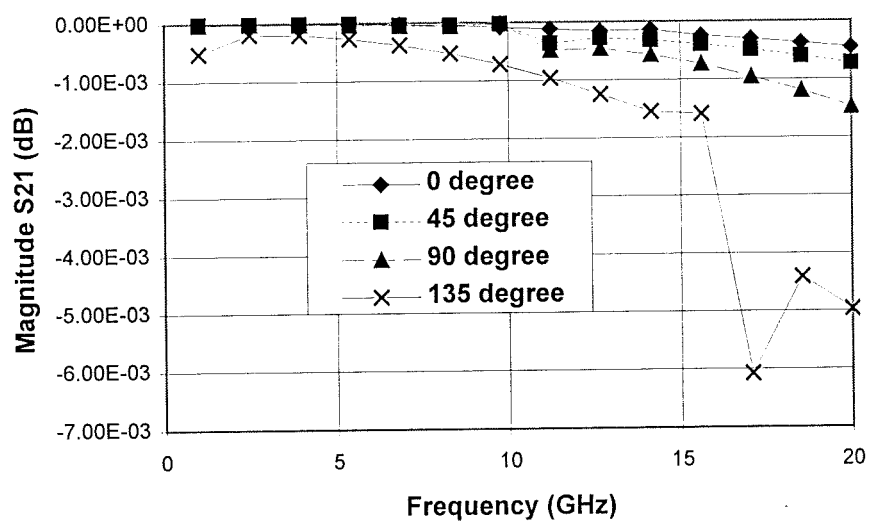


(c)  $90^\circ$

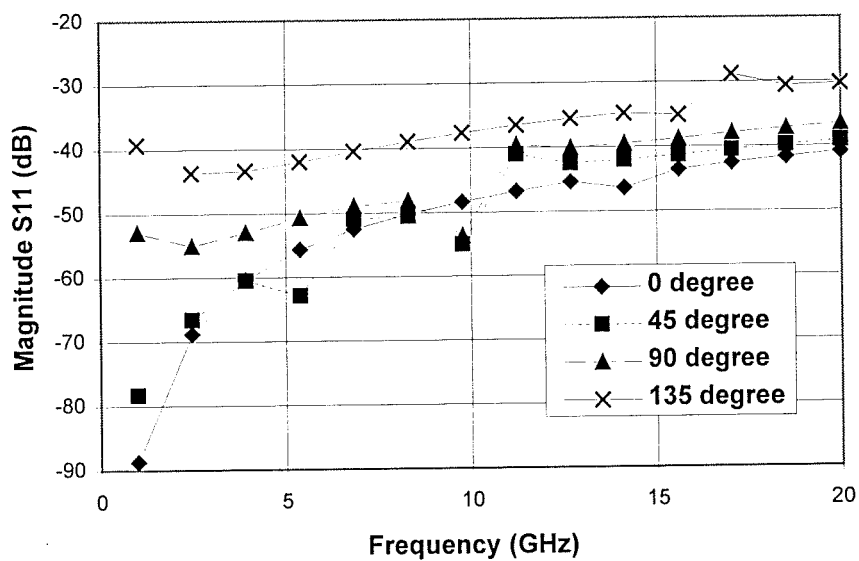


(d)  $135^\circ$

Figure 4.14 The diagrams showing the different angles between microstrip lines connecting via on different dielectric layers.



(a) Magnitude of S21



(b) Magnitude of S11

Figure 4.15 Magnitude of the simulated S-parameters for a 35  $\mu\text{m}$  cylindrical via connected by microstrip lines with different angles.



wave propagation. The top view of the via structures showing the different angles between microstrip lines connecting a via on different dielectric layers is given in figure 4.14. Four situations for the angles from  $0^\circ$  to  $135^\circ$  are considered.

The magnitudes of the simulated S-parameters for a  $35\text{ }\mu\text{m}$  cylindrical via connected by microstrip lines with different angles are presented in figure 4.15. The best performance was observed at  $0^\circ$  and the transmission loss ( magnitude(S21) ) increases with angle between microstrip lines. The extent of the deterioration in performance is not very big from  $0^\circ$  to  $90^\circ$ . However at  $135^\circ$  the transmission loss increases dramatically in comparison with other angles. The description can also be given from the change of reflection loss ( magnitude(S11) ). Because bigger reflection loss corresponds to better performance, the lowest reflection loss at  $135^\circ$  also indicates its worst performance. Figure 4.15 also demonstrates that, except  $0^\circ$  via, the S-parameter is not smoothly changing with frequency. This could be explained by the interactions between multi-discontinuities involved in a via.

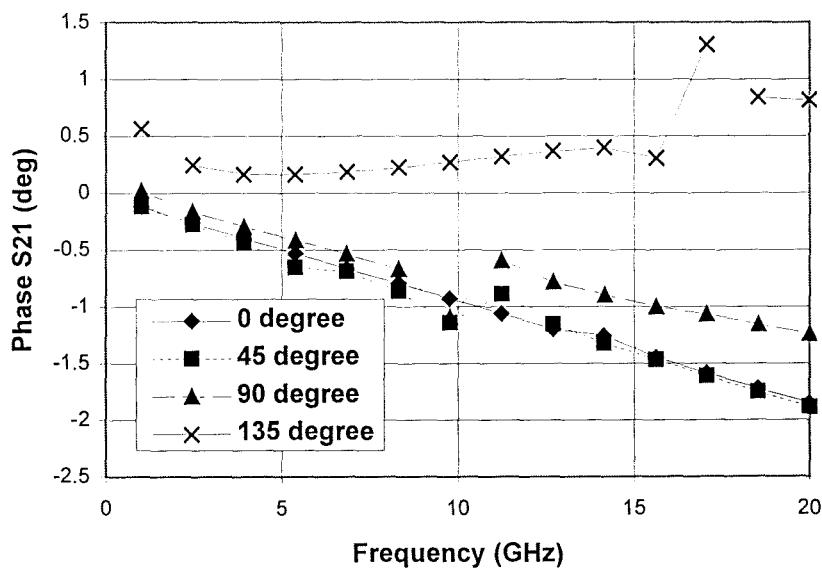


Figure 4.16 Phase change after transmission through a  $35\text{ }\mu\text{m}$  cylindrical via connected by microstrip lines with different angles.

Shown in figure 4.16 is the phase change after transmission through the  $35\text{ }\mu\text{m}$  cylindrical via connected by microstrip lines with different angles. At  $0^\circ$  and  $45^\circ$  the linear phase change against frequency is observed. At  $90^\circ$  from 1 to 10 GHz, the phase change after transmission is not far away from that for  $0^\circ$  and  $45^\circ$ . Nevertheless, in higher frequency range from 11 to 20 GHz, the phase delay at  $90^\circ$  is smaller than that for the situation at  $0^\circ$  and  $45^\circ$ . This can be attributed to the extra inductive effect introduced by the big change in the direction of current flow or wave propagation. At  $135^\circ$  the disturbance to the current flow due to the extremely big change in the direction of current flow causes advances of voltage phase. Again this is due to the large inductive effect.

#### 4.3.4 Two offset vias

In MCM structures the high density of interconnection is achieved through the combination of multi-layer and multi-via configuration. It is very common to have many vias in the same route for the transmission or processing of signals. It is therefore necessary to address the issue of interaction between vias in proximity. Shown in figure 4.17 is the top view of two offset vias

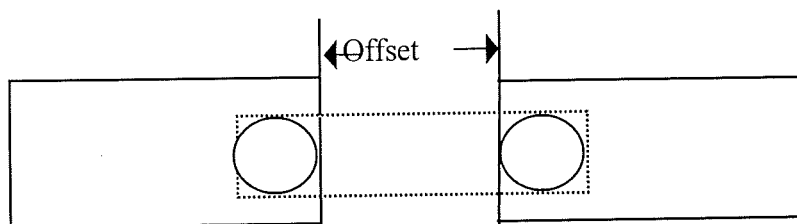
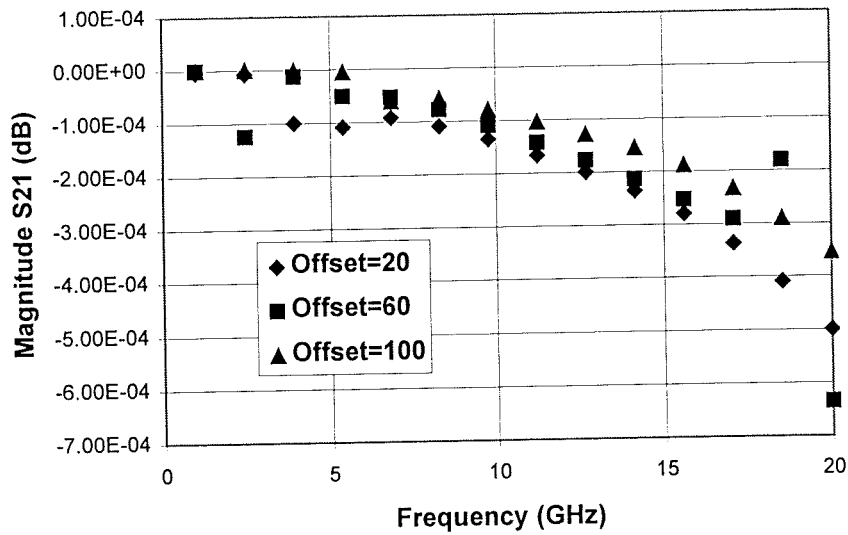
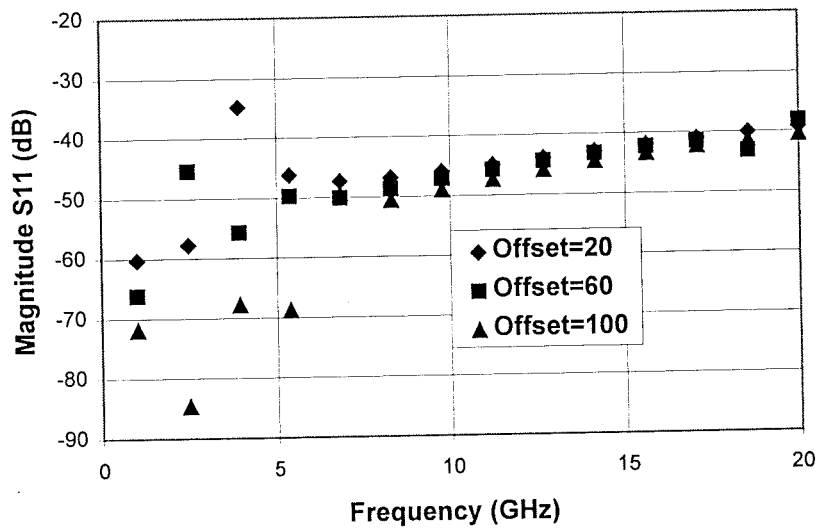


Figure 4. 17 Top view of two offset vias in the same propagation route



(a) Transmission loss



(b) Reflection loss

Figure 4.18 Simulated magnitude of transmission loss and reflection loss for two vias with different offset

vias in the same propagation route. The physical size of the via, microstrip width and substrate thickness is the same as in previous subsections. Shown in figure 4.18 is the simulated S-parameter in magnitude for a pair of offset vias with different offset values. The difference between each other for the three curves in either figure 4.18 (a) or 4.18 (b) is very small. The irregular behaviour at lower frequencies indicates the existence of significant electromagnetic interaction between the two vias. Figure 4.19 shows simulated phase change after transmission through two offset vias. The phase delay due to the offset length has been removed for comparison. There is almost no difference in phase change for three different offset values. This result also demonstrates the weak interaction between vias in the frequency range investigated. From the comparison between the result in figure 4.13 (c), where the phase change after transmission through a single via is given, and that in figure 6. 19 we can see that the values in the figure 4.13 (c) is nearly half of that in figure 4.19 at the respective frequency points.

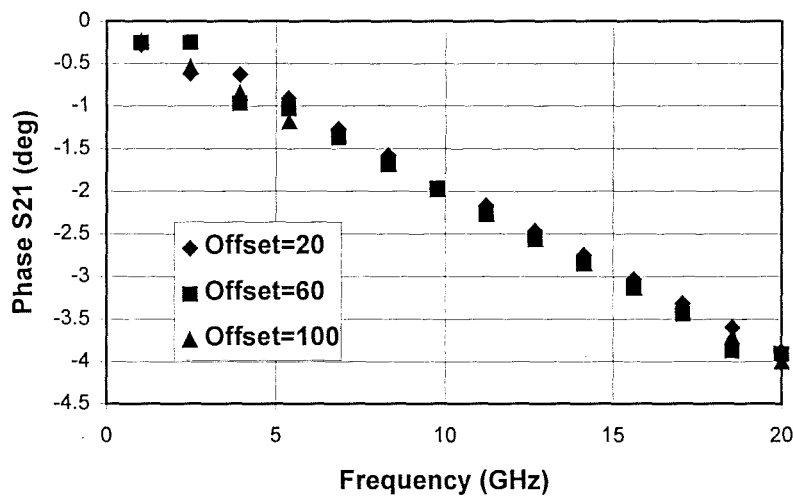


Figure 4.19 Simulated phase change after transmission through two offset vias. The phase delay due to the offset has been removed for comparison.

### 4.3.5 Crosstalk between two individual vias in proximity

The high density and high frequency MCM circuit layout often involves a via arrangement with two or more vias in proximity. It is very useful to understand the level of crosstalk between vias with respect to their separation for the electrical design of a MCM structure. Figure 4.20 shows the top view of two individual vias in proximity. The port numbers are also labelled in the figure. Figure 4.21 shows crosstalk between the two vias. The separation between them is defined as the distance from the edge of one via to the edge of another.

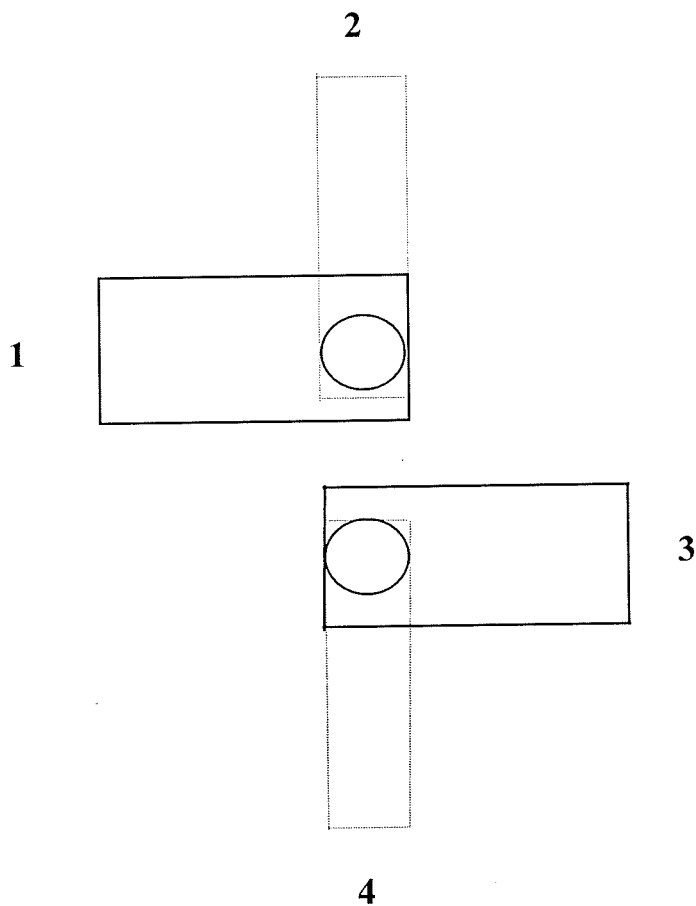
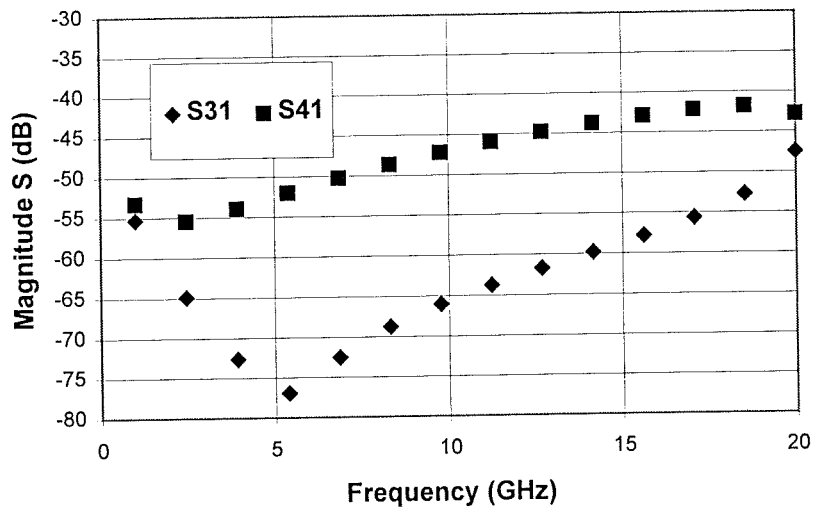
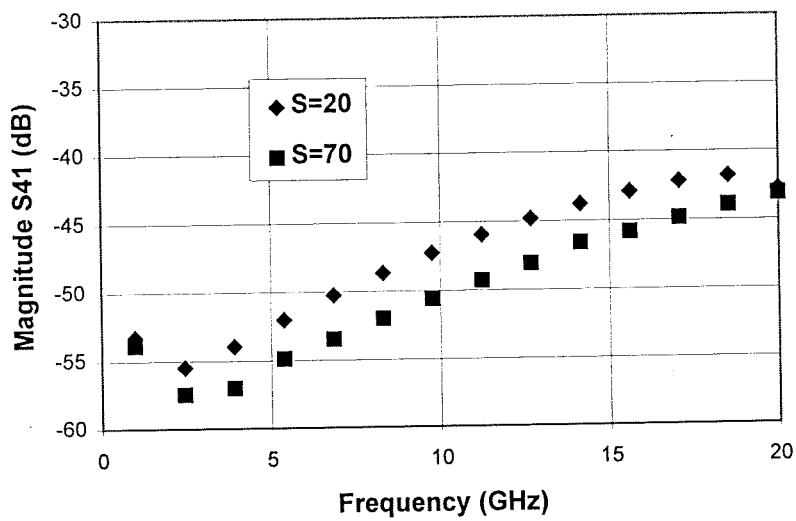


Figure 4.20 The top view of two individual via in proximity.



(a) Crosstalk between two vias with separation of 20  $\mu\text{m}$ .



(b) Crosstalk between two vias with separation of 70  $\mu\text{m}$ .

Figure 4.21 Crosstalk between two vias in proximity

It can be seen from figure 4.21(a) that the backward wave coupling S41 is bigger than forward wave coupling S31, which is consistent with the theory for electromagnetic coupling. Figure 4.21(b) compares the difference between crosstalk level between two vias with separation of 20 and 70  $\mu\text{m}$ . The general conclusion can be drawn from the results presented above that the crosstalk level between adjacent vias is very low in the frequency range investigated.

#### **4.3.6 Summary for simulation of interaction between vias**

Rigorous simulation has provided an insight into the understanding of electromagnetic interaction between vias in proximity. The low permittivity of the substrate material is the reason for the low level of crosstalk between vias. A single via can be simulated and modelled accurately. From the results in section 4.3.4 we can see that in the same propagation route even if the vias are positioned very closely, they can still be treated individually and the electromagnetic interaction between them can be neglected in the frequency range investigated. This is different from the situation for two bends in series where the interaction between two closely spaced bends causes extra phase delay. A convenience in circuit design can be adopted because of this result. That is in the case of multi-vias in the same propagation route, each via can be modelled individually, and their collective effect contributes little to the whole performance of the circuit. In a circuit simulator, such as Spice™ or MDST™, the lumped model of a single via can be inserted into the interconnection route between chips or transistors, where multi-vias are involved. This will allow the accurate simulation of the active circuit by taking all the passive elements into consideration.

## **4.4 Simulation of airbridge in high frequency, high density packaging**

Airbridges are frequently used in high density packaging as an interconnection component. The basic structure of it is given in figure 4.22. They are usually used to make connection between microstrip lines. As the airbridge is suspended over the substrate and surrounded by air, its transmission behaviour is quite different from that of microstrip lines. This difference will be more dramatic at higher frequencies. The presence of an airbridge in the route of wave propagation will cause a disturbance to the flowing current on the microstrip track and this disturbance will also increase with frequency. Using microwave terminology, the airbridge can be called a discontinuity to the propagation of wave. This discontinuity intrinsically results from the mismatch between microstrip line and airbridge. The electromagnetic behaviour of an airbridge can either be measured experimentally or simulated using an electromagnetic simulator, such as HP HFSS™ or HP Momentum™. The benefit of using an electromagnetic simulator is its flexibility in allowing us to change the parameters relevant to the airbridge. From the simulation we can have an in-depth understanding of the airbridge and find a way to realise a better match between the microstrip line and airbridge. In lumped terms we can minimise the inductive and capacitive parasitic behaviour of the airbridge. For a microstrip line, the energy is mainly propagated in the (dielectric) substrate area between line and its ground plane. The positioning of a bridge in air, however, will cause more energy to flow outside the substrate area. This may imply a bigger discontinuity and stronger crosstalk between airbridge lines. This needs to be addressed in circuit design.

### **4.4.1 The effect of airbridge height on transmission behaviour**

For a given substrate thickness, materials and a fixed characteristic impedance of the microstrip line (usually 50 ohms), the parameters which will influence the performance of the airbridge are its length, width and height above the substrate. As before, our investigation



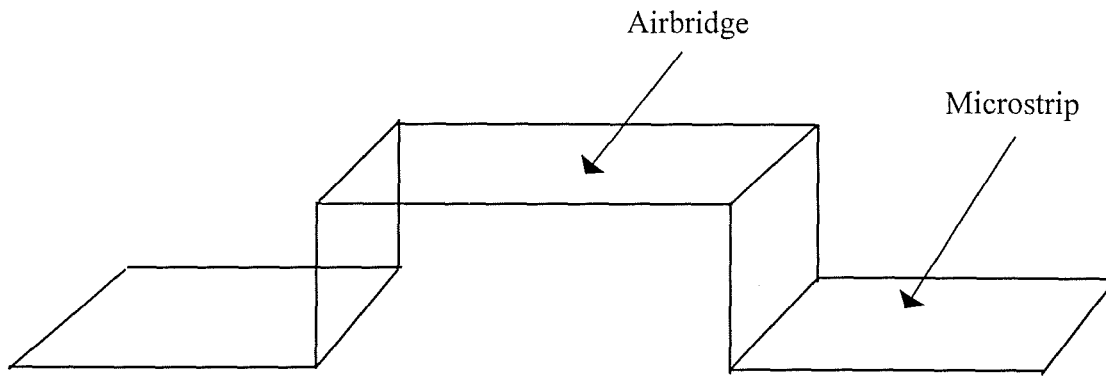
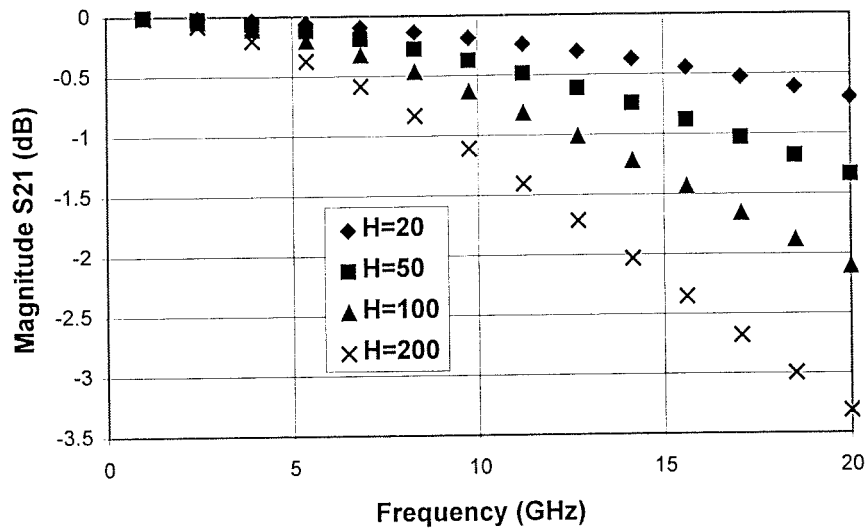


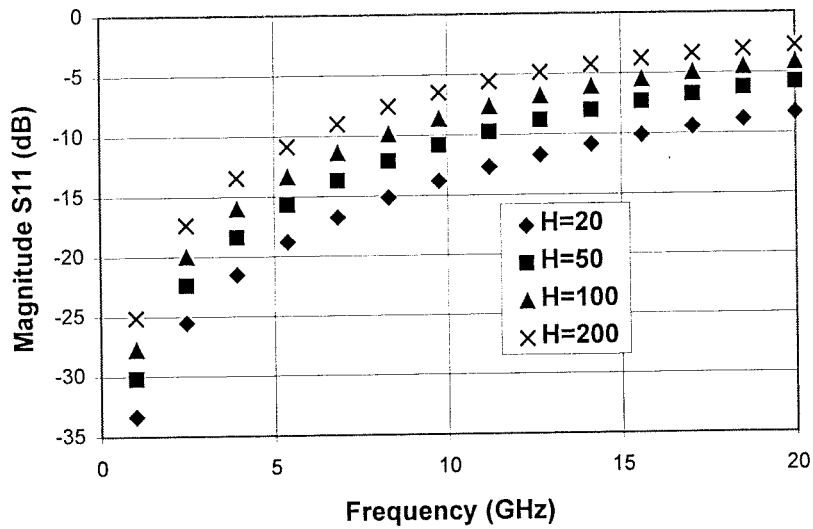
Figure 4.22 Diagram of an airbridge showing configuration(The substrate supporting the microstrip line is not drawn in the diagram).

will be concentrated on the Heraeus KQ material system and the substrate thickness in this section is always  $20\text{ }\mu\text{m}$  with a permittivity of 4, where the width of the microstrip line producing characteristic impedance of  $50\text{ }\Omega$  is  $41\text{ }\mu\text{m}$ . Throughout this section we assume that the vertical metal strip in the airbridge will have the same width as that of the airbridge part which is parallel to the microstrip line.

Initially, we study the effect of the airbridge height (the distance between the airbridge and the substrate) on its transmission behaviour. The width of the airbridge is fixed at  $41\text{ }\mu\text{m}$  which equals that of the microstrip line. The length of it is taken as  $1000\text{ }\mu\text{m}$ . The simulated results expressed in magnitude of transmission loss and reflection loss are given in figure 4.23. At a fixed airbridge width, the transmission loss increases with height over the substrate. This increase is more dramatic at higher frequencies. For example at  $20\text{ GHz}$  more than 50% of the incident energy to the airbridge will be reflected if the height over the substrate is  $200\text{ }\mu\text{m}$ . At the same frequency even for a height of  $50\text{ }\mu\text{m}$ , there is still nearly 30% of the energy being reflected back by the airbridge. For all the values of airbridge height investigated here, more than 90% of the incident energy can be transmitted through the

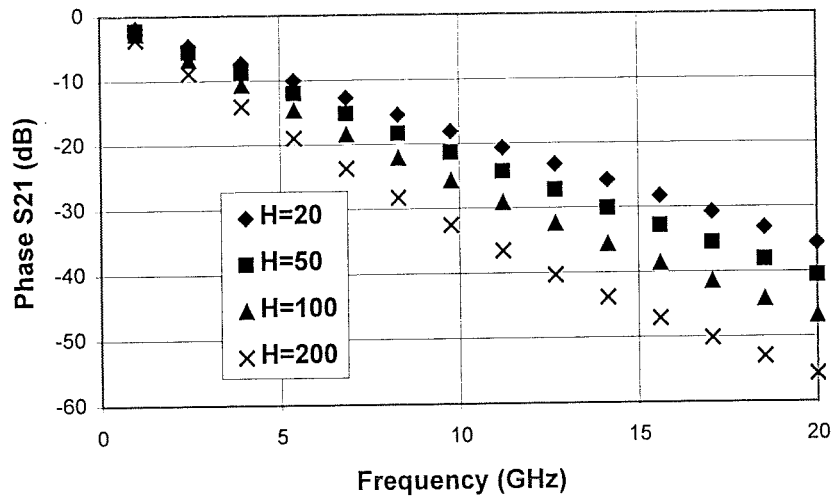


(a) Magnitude of transmission loss

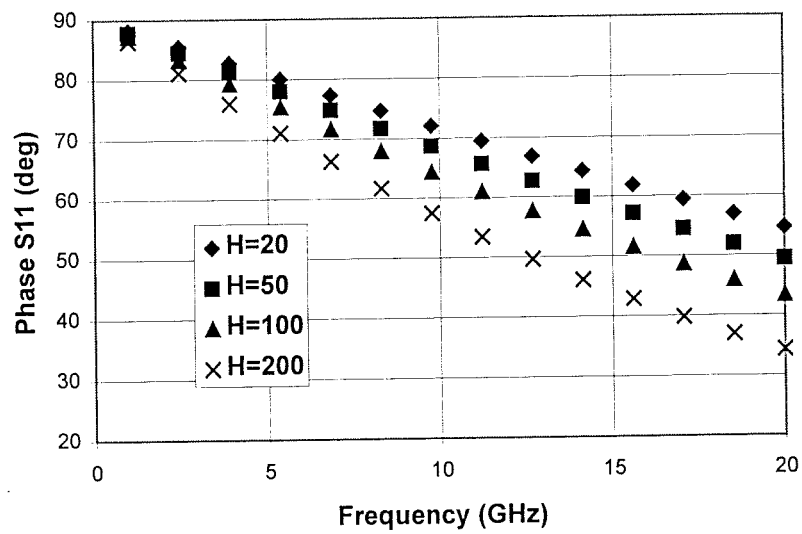


(b) Magnitude of reflection loss

Figure 4.23 Magnitude of transmission loss and reflection loss for a single airbridge with different values of height above substrate.



(a) Transmission phase change



(b) Reflection phase change

Figure 6.24 Phase change caused by airbridge after transmission or reflection of the incident wave.

airbridge under 5 GHz. As far as signal transmission is concerned, the transmission loss is sensitive to both the frequency and the airbridge height over the substrate, which indicates the necessity of rigorous characterisation of airbridges. In addition to transmission loss, the phase change after transmission through a certain element is always important and sometimes crucial in circuit design. Shown in figure 4.24 is the phase change after transmission through or reflection from an airbridge. The phase change is also strongly dependent on frequency and the height of the airbridge over the substrate.

#### **4.4.2 Characteristic impedance and phase propagation constant of airbridge line**

From the simulation presented above we can see that the airbridge is a severe discontinuity at high frequency, especially as its height increases. It is necessary to understand the reasons for the discontinuity and to find the way to reduce it. If we consider the section of the airbridge in parallel with the substrate as a piece of transmission line, the effective permittivity of it will be smaller than that of the microstrip line connected to it on the substrate because there is more fringing field in air for the airbridge than for the microstrip line. Effectively the characteristic impedance of the airbridge line is much higher than that of the microstrip line with the same width. Using HP Momentum™, the characteristic impedance of the airbridge line can be rigorously calculated at different values of its width and its height over the substrate. The calculated results for airbridge line at 100  $\mu\text{m}$  over substrate and with different values of width are presented in figure 4.25. It can be seen from the figure that a 60  $\mu\text{m}$  airbridge width will produce a characteristic impedance of 166  $\Omega$  creating very large mismatch between the microstrip line and the airbridge line. By increasing the width of the airbridge line, the characteristic impedance will be reduced. However, in order to produce an airbridge line with characteristic impedance of 50  $\Omega$ , the width of the

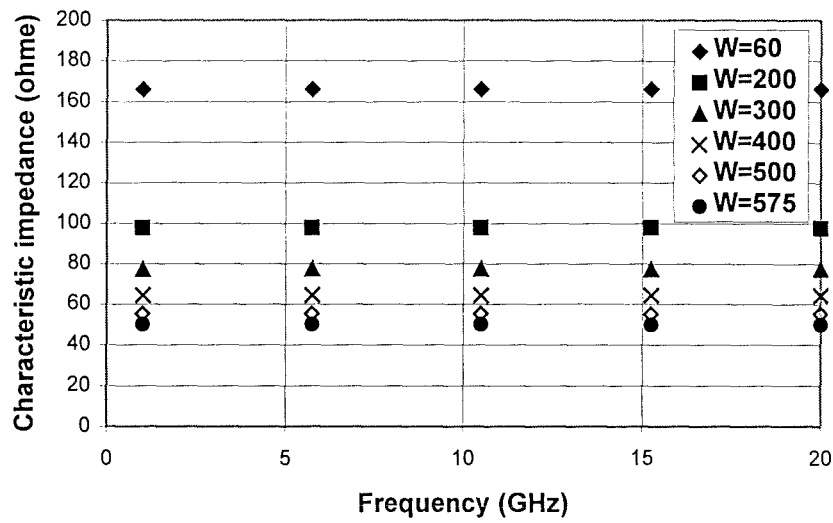


Figure 4.25 Characteristic impedance of airbridge lines at 100  $\mu\text{m}$  over substrate with different line widths

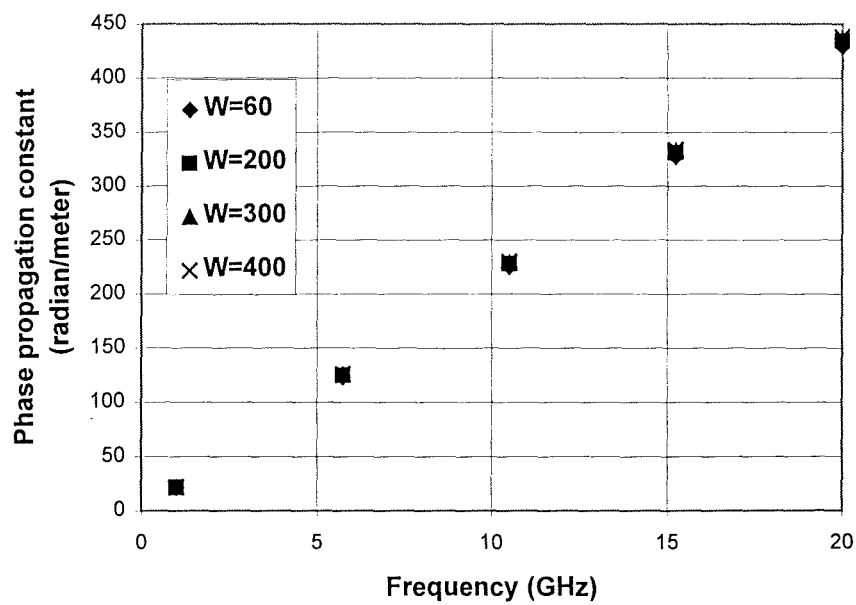


Figure 4.26 Phase propagation constant against airbridge width with airbridge line at 100  $\mu\text{m}$  over substrate.

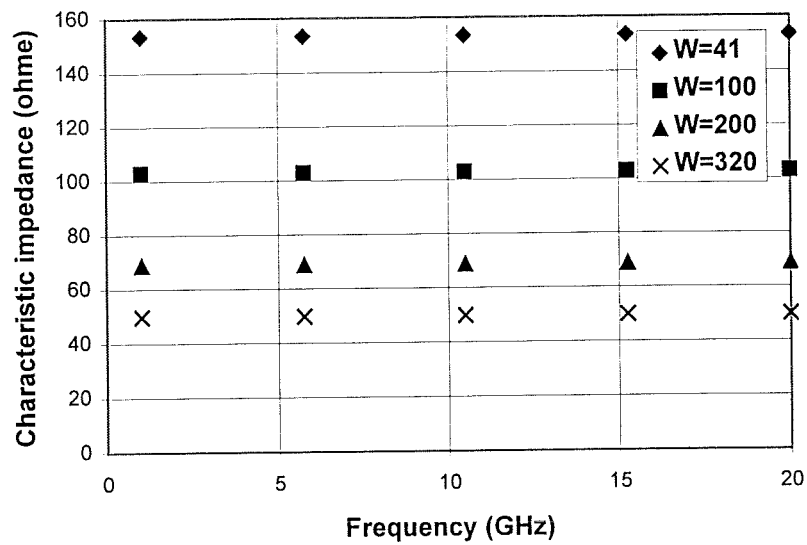


Figure 4.27 Characteristic impedance of airbridge line at 50  $\mu\text{m}$  over substrate with different line widths.

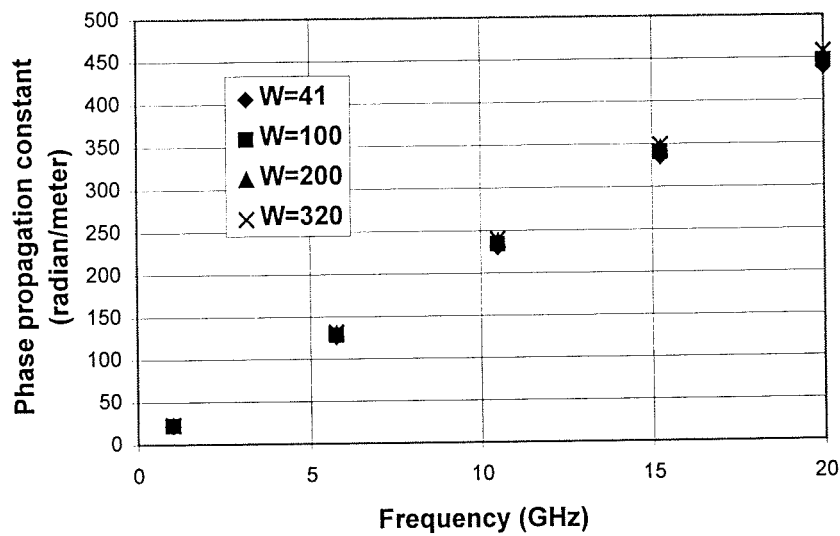


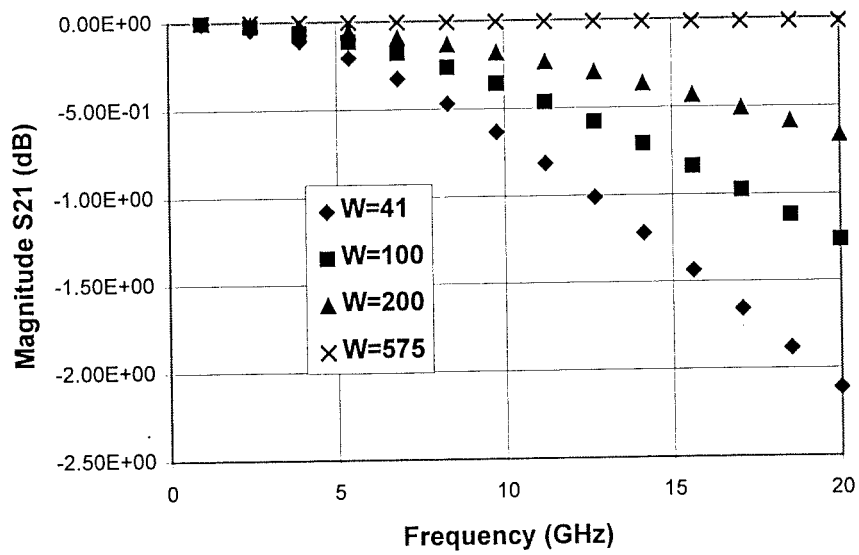
Figure 4.28 Variation of phase propagation constant with frequency showing effect of airbridge width with airbridge line at 50  $\mu\text{m}$  over substrate.

airbridge line needs to be as wide as 575  $\mu\text{m}$ . By examining phase propagation constant against airbridge width at different frequencies, which is presented in figure 4.26, it can be seen that although the characteristic impedance is strongly dependent on the airbridge width, the phase propagation constant is almost independent of it. Another set of simulations was carried out at a fixed airbridge height of 50  $\mu\text{m}$  over the substrate. The results of characteristic impedance and phase propagation constant are given in figure 4.27 and figure 4.28 respectively. As expected, the phase constant is also independent of airbridge width. Inspection of figure 4.27 shows that an airbridge line 41  $\mu\text{m}$  in width, which equals that of the microstrip lines connected to it, will produce a characteristic impedance of 153  $\Omega$ . This value is also far too large compared with a 50  $\Omega$  for microstrip line and the mismatch will cause a very large reflection of incident signal in the high frequency range. To create an airbridge line with characteristic impedance of 50  $\Omega$ , the width of airbridge line would have to be 320  $\mu\text{m}$  in width.

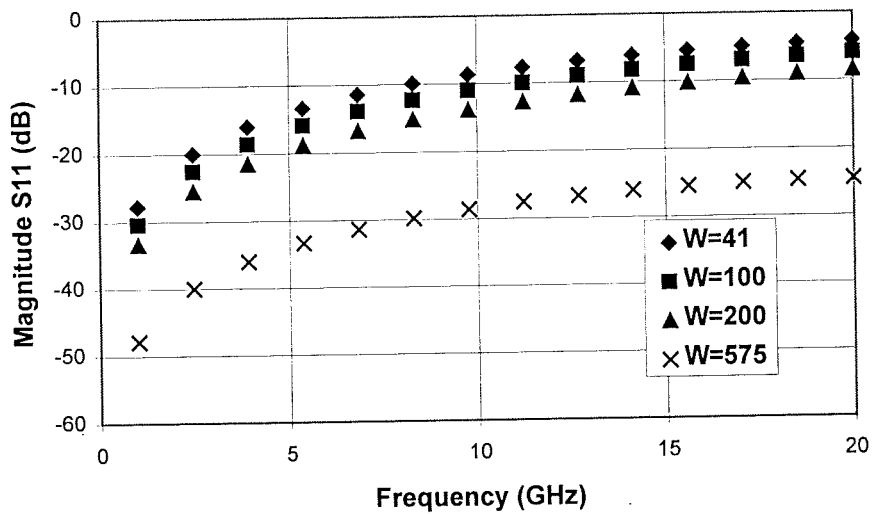
A general conclusion may be drawn that an airbridge line with the same width as microstrip lines connected to it will produce a much higher characteristic impedance. To match the characteristic impedances, the width of the airbridge line would have to be increased to an extent which is dependent on the height of airbridge line over the substrate.

#### 4.4.3 Simulated results for airbridge

From the simulated results of characteristic impedance for airbridge lines in the last section, we would naturally expect that an airbridge line with 50  $\Omega$  characteristic impedance would present the least discontinuity to the propagating wave. Figure 4.29 shows the simulated results for airbridge lines at 100  $\mu\text{m}$  over the substrate with different width. The length of the airbridge lines are 1000 $\mu\text{m}$ . The worst performance is observed for an airbridge line of 41  $\mu\text{m}$  in width. By increasing the width of the airbridge line, the transmission loss decreases and



(a) Transmission loss



(b) reflection loss

Figure 4.29 Simulated transmission and reflection behaviour of airbridge at 100  $\mu\text{m}$  over substrate with different width. (a) Transmission loss; (b) Reflection loss.



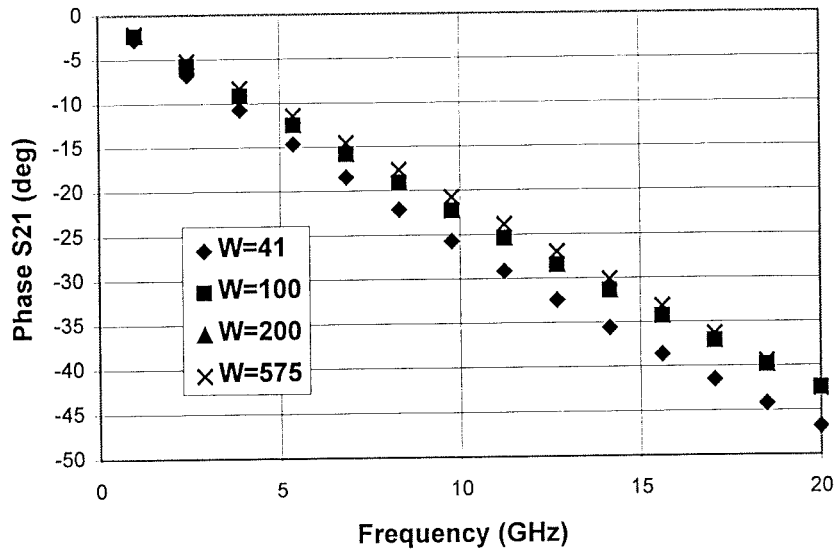
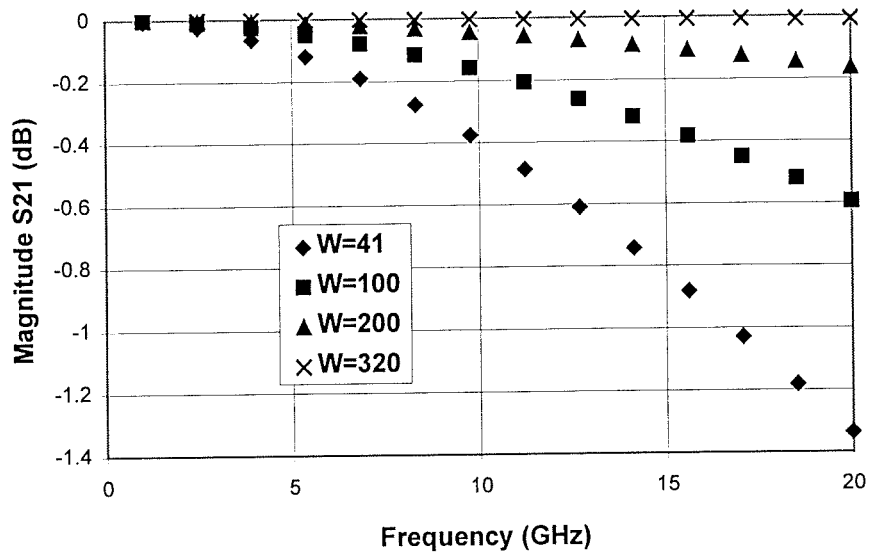


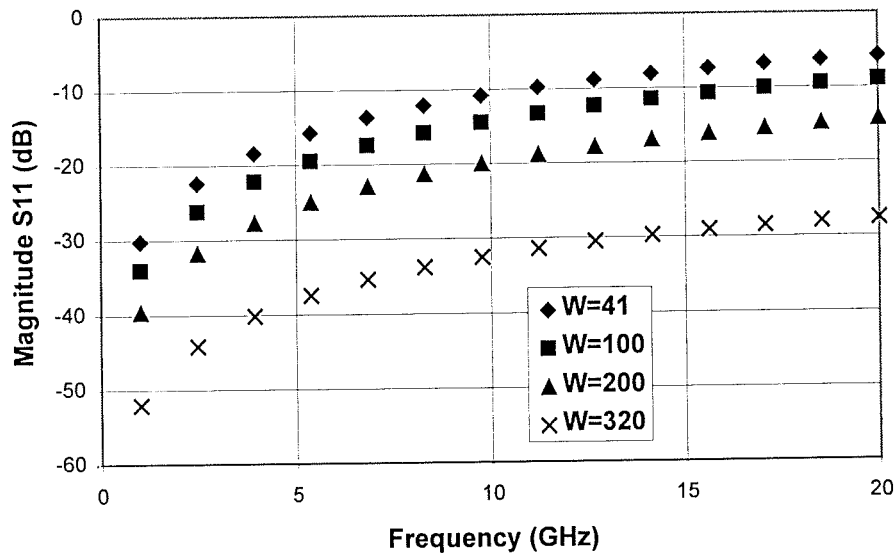
Figure 4.30 Phase change after transmission through an airbridge at 100  $\mu\text{m}$  over substrate with different values of width.

reflection loss increases. When the airbridge width reaches 575  $\mu\text{m}$ , the transmission loss is very small in the frequency range investigated. This is due to the match between the characteristic impedance of microstrip lines and that of the airbridge line. Figure 4.30 shows the phase change after transmission through an airbridge line at 100  $\mu\text{m}$  over substrate with different values of width. At 10 GHz the phase delay for an airbridge line of 575  $\mu\text{m}$  width is nearly 5 degrees less than that of a 41  $\mu\text{m}$  line. If several airbridge lines are connected in series, the phase delay may need to be addressed rigorously.

The simulation carried out for airbridge lines 50  $\mu\text{m}$  over a substrate with different values of width demonstrates a similar trend. The simulated results for transmission loss and reflection loss are presented in figure 4.31. The phase delay after transmission is given



(a) Transmission loss



(b) Reflection loss

Figure 4.31 Simulated transmission and reflection behaviour of airbridge at 50  $\mu\text{m}$  over substrate with different values of width. (a) Transmission loss; (b) Reflection loss.

in figure 4.32. At matched situation, where the airbridge line is 320  $\mu\text{m}$  in width, the transmission loss is minimum. By comparing the results in figure 4.32 and those in figure 4.29, it can be seen that the airbridge with a lower height over substrate performs better than that higher over substrate.

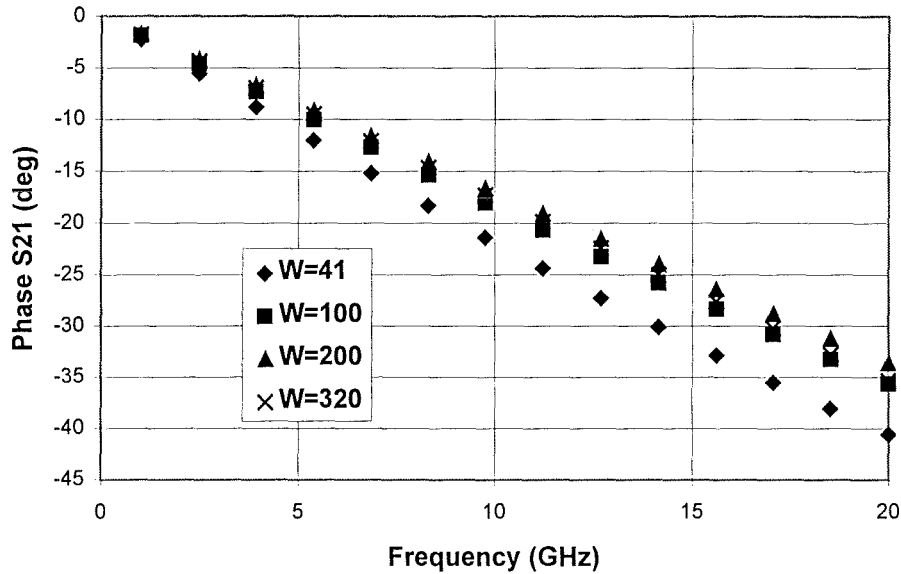


Figure 4.32 Phase change after transmission through an airbridge at 50  $\mu\text{m}$  over substrate with different values of width.

#### 4.4.4 Crosstalk between airbridge lines in proximity

In a tight layout where airbridge lines are closely placed, it is necessary to understand the crosstalk between them. In this study the crosstalk between airbridge lines positioned either at 100  $\mu\text{m}$  or 50  $\mu\text{m}$  over the substrate was investigated. The port numbers for coupled airbridge lines are labelled in figure 4.33. When the airbridge line is 100  $\mu\text{m}$  over

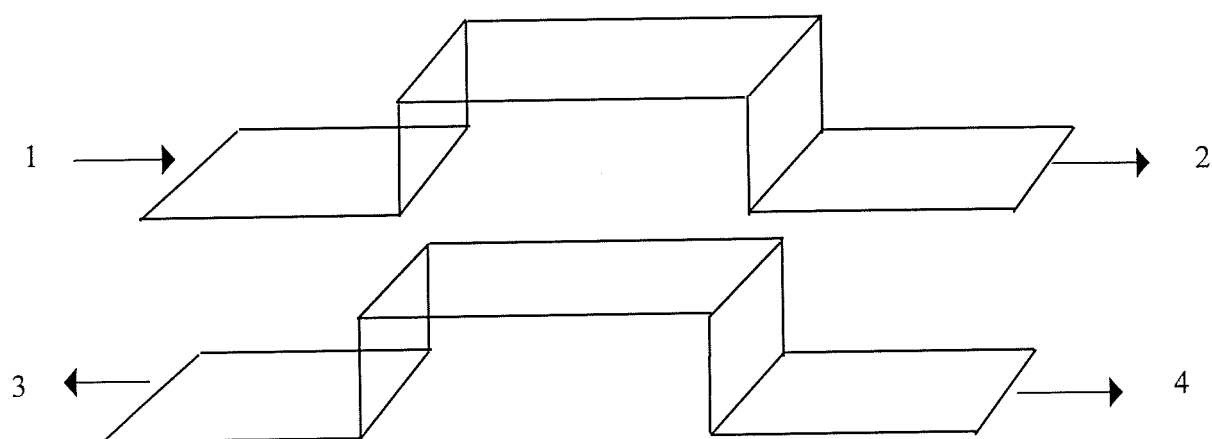


Figure 4.33 Two parallel placed airbridge lines with port number labelled on the structure.

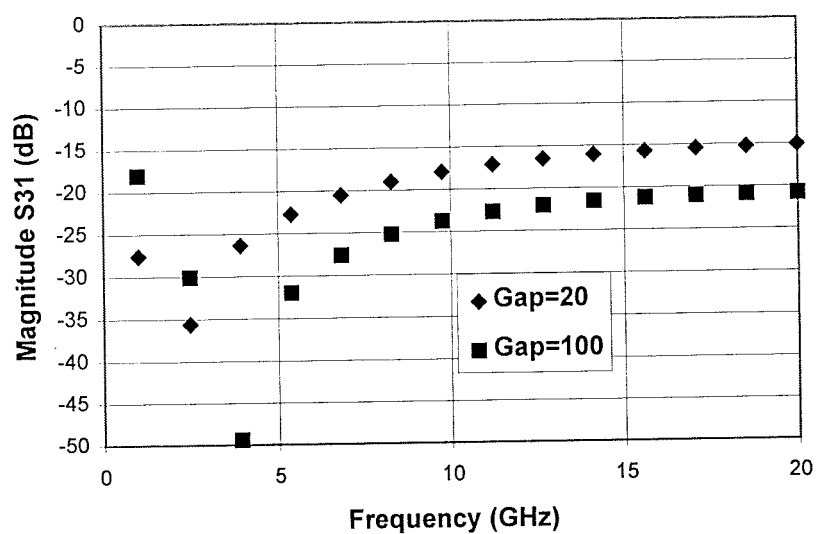


Figure 4.34 Crosstalk between airbridge lines 100  $\mu\text{m}$  over substrate and with width of 100  $\mu\text{m}$ .

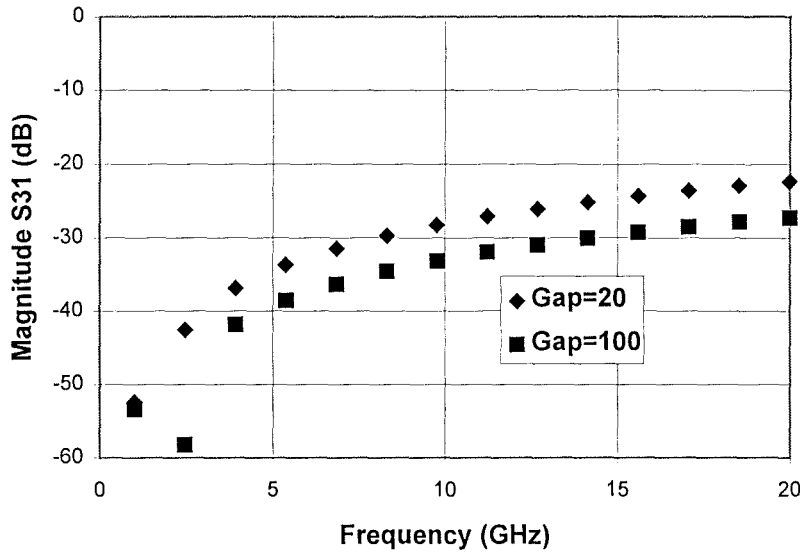


Figure 4.35 Crosstalk between airbridge lines 100  $\mu\text{m}$  over substrate and with width of 575  $\mu\text{m}$ .

substrate, the crosstalk between two parallel placed airbridge lines with width of 100  $\mu\text{m}$  is shown in figure 4.34 and the crosstalk between two airbridge lines with width of 575  $\mu\text{m}$ , which corresponds to a matched termination, is shown in figure 4.35 where the gaps between the two airbridge lines are chosen as 20 or 100  $\mu\text{m}$  and the S-parameter S31 means backward wave coupling. From comparison between figure 4.34 and figure 4.35, a general conclusion can be drawn that at a matched situation for a single airbridge line, the crosstalk level is less than that for an unmatched situation. In addition, a resonance is observed in the interaction between two unmatched airbridge lines. The upward shift in resonant frequency with respect to increase of the gap values between the lines can be explained by the reduction in the coupling capacitance between them.

When the airbridge lines are 50  $\mu\text{m}$  over substrate, the crosstalk between them is shown in figure 4.36 and figure 4.37, which correspond to 100  $\mu\text{m}$  and 320  $\mu\text{m}$  in width respectively. The crosstalk at a matched situation also exhibits a lower level. The same pattern of resonance is also observed when the airbridge lines are not matched. However the

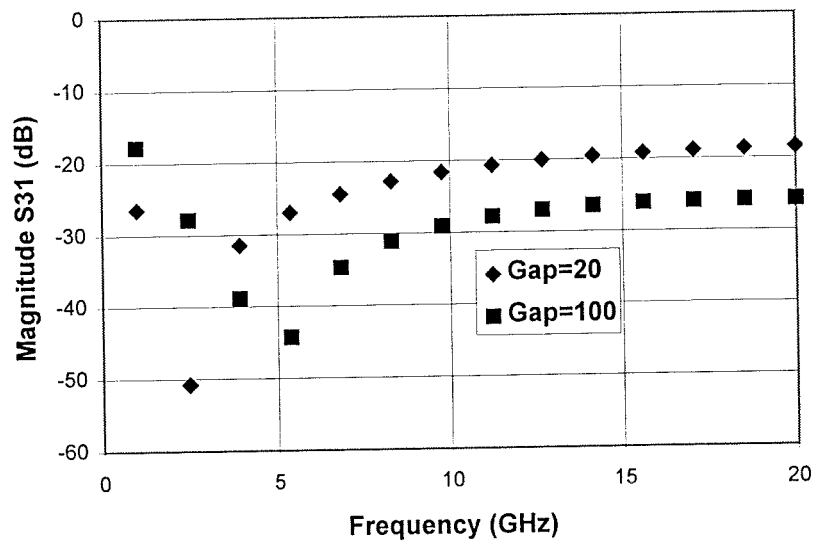


Figure 4.36 Crosstalk between airbridge lines 50  $\mu\text{m}$  over substrate and with width of 100  $\mu\text{m}$ .

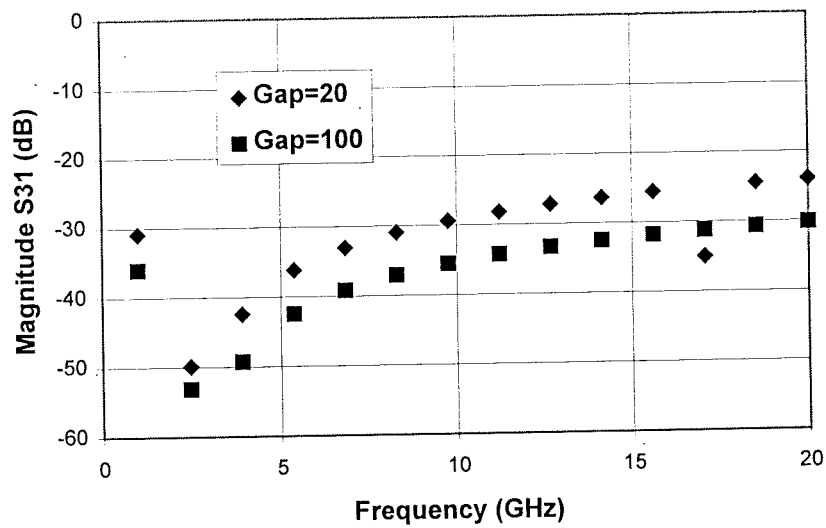


Figure 4.37 Crosstalk between airbridge lines 50  $\mu\text{m}$  over substrate and with width of 320  $\mu\text{m}$ .

comparison between figure 4.36 and figure 4.34 shows that the crosstalk is bigger between airbridge lines positioned at a higher level above substrate. This can be explained by bigger parasitic inductance introduced by airbridge lines at a high level above substrate.

#### **4.4.5 Summary for simulation of airbridge lines**

As an interconnection component in microwave circuits, airbridge lines inevitably introduce discontinuities to the propagation of the wave. In high packaging density and high frequency circuits, in order to realise optimum performance, it is necessary to employ a full wave electromagnetic method to rigorously simulate the behaviour of airbridge lines. This section has introduced the novel concept of considering airbridge lines as a piece of transmission line with a value of characteristic impedance which is dependent on both the width and the height of the line over the substrate. This concept can be applied in minimising the discontinuity introduced by an airbridge line. The implication of the work of this section is that the optimisation of airbridge interconnections can be realised with the aid of an electromagnetic simulator.

## References

- [1] C.E. Free, K.P. Tang, D. Li, K.E.G. Pitt, P.Barnwell, "High frequency interconnections and crosstalk on MCM structures", ISHM'96 microelectronics symposium, Proceedings, pp522-525, Minneapolis, Minnesota, USA, October, 1996
- [2] D. Li, C. E. Free, P. G. Barnwell, K. E. G. Pitt, "Simulated and practical behaviour of state-of-the-art MCM via structures", Proceedings of 6th International conference on MCMs, pp. 290-295, April, 1997, Denver, USA.
- [3] A. E. Ruehli, "Inductance calculations in a complex integrated circuit environment", IBM Journal of research development, vol.16, pp. 470-481,1972
- [4] A. E. Ruehli, "Efficient capacitance calculations for three-dimensional multiconductor systems", IEEE Transactions on Microwave Theory Techniques, vol. MTT-21, pp. 76-82, February 1973.
- [5] F. Grover, Inductance calculations: Working formulas and tables, Dover, New York, 1962.
- [6] K. C. Gupta, Ramesh Garg, Inder Bahl and Prakash, " Microstrip lines and slotlines", second edition, Artech House, Inc., 1996
- [7] R. Sorrentino, F. Alessandri, M. Mongiardo, G. Avitabile, and L. Roselli, "Full-wave modelling of via hole grounds in microstrip by three-dimensional mode matching technique", IEEE Trans. Microwave Theory Tech., Vol. 40, No. 12, pp 2228-2233, Dec., 1992.



## **Chapter 5 Design rules for interconnections in mutichip modules**

In this chapter the general design rules for MCM interconnections will be given, based on the electromagnetic simulation in chapter 2, 3 an 4.

### **5.1 Design rules for the minimisation of crosstalk between conductor lines**

#### **a. Avoid overlap in multi-layer structures**

The overlap between conductor tracks in different layers has to be avoided or at least the overlap area has to be minimised. This will reduce the coupling capacitance between conductors and consequently reduce the crosstalk noise between them.

#### **b. Cautions in parallel regions between adjacent conductors**

Two precautions need to be taken: firstly, the length of the coupling region should avoid the length of a quarter guide wavelength; secondly, the separation between conductors has to be carefully chosen to make a compromise between the crosstalk level and the packaging density.

#### **c. Calculation of crosstalk level between conductors in multi-layer MCM structures**

The microstrip theory for the calculation of crosstalk between conductors is only valid for two parallel placed microstrip lines on the same level without overlay. If the crosstalk between conductors on different levels or two conductors on the same level but with a dielectric overlay are considered, the electromagnetic simulation from first principles has to be employed to obtain accurate results. In addition, the collective effect of conductors, such as

the interference between the electromagnetic field from each conductor can only be addressed through rigorous electromagnetic simulation.

## **5.2 Design rules for interconnect vias in multi-layer MCM structures**

- Characteristic impedance match between conductor lines connecting the via on two different dielectric layers

The conductor lines connecting the via on two different levels should have the same characteristic impedance to avoid mismatch between them. For example, in a two-layer Heraeus KQ material system, the width of the conductor lines on the first and second layers should be 35 and 41  $\mu\text{m}$  respectively to match their characteristic impedance at 50 $\Omega$ . In general, the width of the conductor lines, producing 50 $\Omega$  characteristic impedance, on any dielectric layer can be found from rigorous electromagnetic simulation using either HFSS<sup>TM</sup> or Momentum<sup>TM</sup>.

- The effects of via pads

The via pads can be employed to provide the convenience for the connection between via and conductor lines. However, a via pad itself contributes to the discontinuity in the route of propagation wave. The performance of a via without via pads is better than that with a via pad. In addition, the presence of via pads also create more phase delay, which has to be counted especially when multi-vias are employed in an MCM interconnect route.

- Optimisation of via geometry

In practical MCM interconnections, cylindrical, square, wedge-shaped and rectangular vias may be used. When performance is a major concern, a cylindrical via is preferred.

- Modelling of via by its equivalent circuit

The vias can be modelled by their equivalent circuits. A single stage pi-type equivalent circuit can provide reasonable accuracy in modelling a via fabricated using Heraeus KQ technology. If high accuracy is needed, two or more stages of pi type equivalent circuit can be added together.

### **5.3 Design rules for airbridge line in MCM interconnections**

At microwave frequencies, an airbridge line could present a big discontinuity to the propagation wave. This can lead to severe losses of energy in the signals. The performance of an airbridge can be assessed through electromagnetic simulation. Most importantly, the geometry of an airbridge line can be optimised through the simulation. The approach in the optimisation is to consider the suspended part of the airbridge line as a piece of microstrip line on a dielectric layer with permittivity of 1. From electromagnetic simulation the width of the airbridge line can be found to give a characteristic impedance of  $50\ \Omega$ .

### **5.4 Design rules for interaction between discontinuities in proximity in multi-layer MCM interconnections**

- Microstrip bend

When two microstrip bends in the same wave propagation route are in proximity, the electromagnetic interaction between them will introduce extra phase change, which can not be modelled by the simple combination of models for individual microstrip bends. Extra elements have to be added between the models of individual microstrip bends.

- Vias

When two vias in the same wave propagation route are in proximity, no extra phase change is introduced and they can still be modelled individually. However, precautions have to be taken in producing the layout for vias. The interaction between vias could enhance the reflection of signals at specific frequency points. A large angle between the microstrip lines connecting the via on the two different dielectric layers should be avoided in order to reduce the discontinuity.

- Airbridge lines

The interaction between two airbridge lines is particularly significant if the airbridge lines are unmatched. At this situation, resonance could happen at a particular frequency. It is therefore recommended that airbridge lines should always be matched if possible. The design for the match can be realised through rigorous electromagnetic simulation.

In brief, electromagnetic simulation is a powerful tool in studying the passive behaviour of interconnect structures. After the accurate simulation, interconnect structures can be optimised to improve the performance of the designed high frequency circuits or subsystems. The availability of modern 2D and 3D electromagnetic simulators has enabled the interconnections in MMIC, MCM and other high frequency and high density packaging structures to be rigorously simulated, opening the door for sophisticated circuit design in a short time cycle to meet the demands of a competitive market.

## **Chapter 6 Characterisation of microwave conductive film materials using a microstrip ring resonator**

6.1 Theory of microstrip ring resonator

6.2 Optimisation of coupling gap for microstrip ring resonator

6.3 Test results for attenuation of microstrip line fabricated using a novel conductive paste

6.4 conclusions

---

### **6.1 Theory of microstrip ring resonator**

In microstrip or coplanar waveguide circuits the propagation of an electromagnetic wave is supported or guided by conductive track whose properties, such as conductivity and surface roughness, will determine the performance of the circuits. When the frequency reaches 10 GHz, the skin depth approaches  $1\mu\text{m}$  which is comparable with the surface roughness, and consequently the losses from conductor track will be significant. At frequencies higher than 10 GHz, due to the effect of skin depth, the line losses increase more dramatically with frequency. The characterisation of the conductive materials is therefore very important in microwave circuit design.

Microstrip resonant structures are widely used in determining the attenuation per unit length on the microstrip line [1-5]. A most commonly used method is the ring resonator method [1-4]. The top view of the ring resonator is shown in figure 6.1. For a 96% alumina substrate with thickness of 0.635 mm, the conductor width of 0.61 mm will produces  $50\ \Omega$  characteristic impedance of microstrip lines. The advantages of using a ring resonator for the measurement of attenuation along the conductor track and hence assessing the quality of

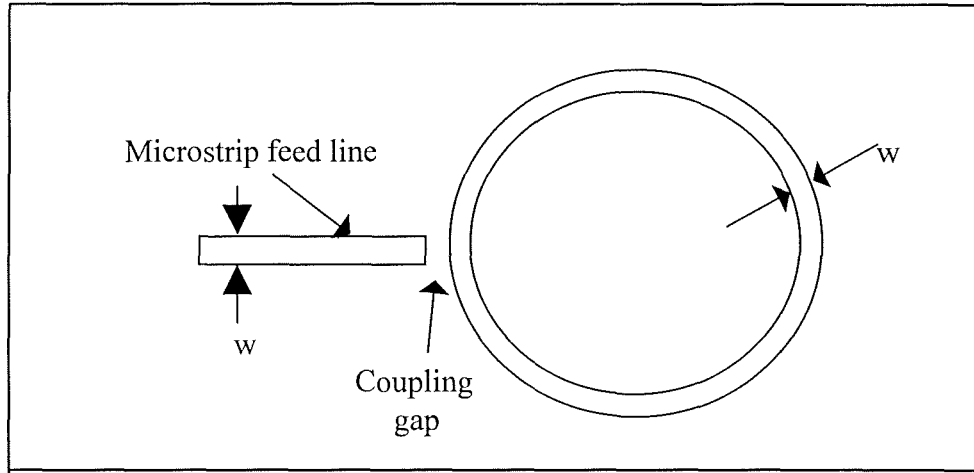


Figure 6.1 Top view of ring resonator.

the conductive material are the elimination of open-end effects and the minimisation of radiation. At resonance there is a basic relation between attenuation coefficient and measured Q factor, which is expressed as follows [1]

$$\alpha = \frac{\pi}{Q\lambda_g} \quad \text{Nepers/unit length} \quad (6-1)$$

Because 1 Neper = 8.686 dB, we have

$$\alpha = \frac{8.686\pi}{Q\lambda_g} \quad \text{dB/unit length} \quad (6-2)$$

where  $\alpha$  is the attenuation coefficient expressed in dB per unit length.  $\lambda_g$  is the guide wavelength for a specific resonant frequency, which can be calculated using microstrip theory.

The general approach in using the ring resonator method is to perform the Q value measurement first, and then employ formula (6-2) to calculate the attenuation coefficient.

The attenuation coefficient in (6-2) in fact consists of two parts; one is from conductor loss and the other is from dielectric loss [1]. According to Hammerstad and Bekkadal [5] the conductor loss of the microstrip line is

$$\alpha_c = 0.072 \frac{\sqrt{f}}{wZ_0} \lambda_g \left[ 1 + \frac{2}{\pi} \tan^{-1} \left\{ 1.4 \left( \frac{\Delta}{\delta_s} \right)^2 \right\} \right] \quad \text{dB/microstrip wavelength (6-3)}$$

where

$\Delta$  = r.m.s. surface roughness

$\delta_s = \frac{1}{(R_s \sigma)}$  is the skin depth at the appropriate operating frequency

$R_s$  = surface resistance

$\sigma$  = metal film conductivity of the microstrip track

$f$  = operating frequency in GHz

$Z_0$  = characteristic impedance in ohms

$w$  = width of microstrip line

The dielectric loss is derived by Gupta et al [6] and given as follows

$$\alpha_d = 27.3 \frac{\epsilon_r (\epsilon_{eff} - 1) \tan \delta}{\sqrt{\epsilon_{eff}} (\epsilon_r - 1) \lambda_0} \quad \text{dB/unit length} \quad (6-4)$$

where  $\tan \delta$  is the loss tangent for the substrate material and  $\lambda_0$  is wavelength in air.

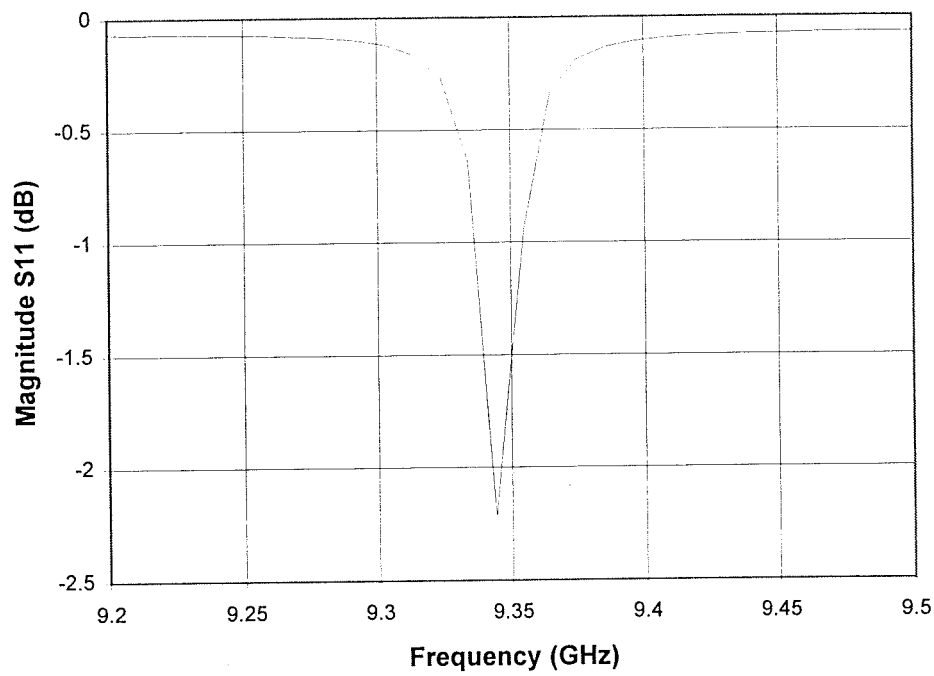
Regardless of the accuracy of (6-3) and (6-4), at least they indicate that the conductivity, surface roughness and loss tangent of the substrate material determine the attenuation coefficient or performance of the microstrip line. This tells us that improvement in

performance of microstrip lines can be achieved by addressing these three aspects. If a low loss substrate material, such as alumina, is used, it can be shown by using (6-3) and (6-4) that the conductor loss is the dominant one.

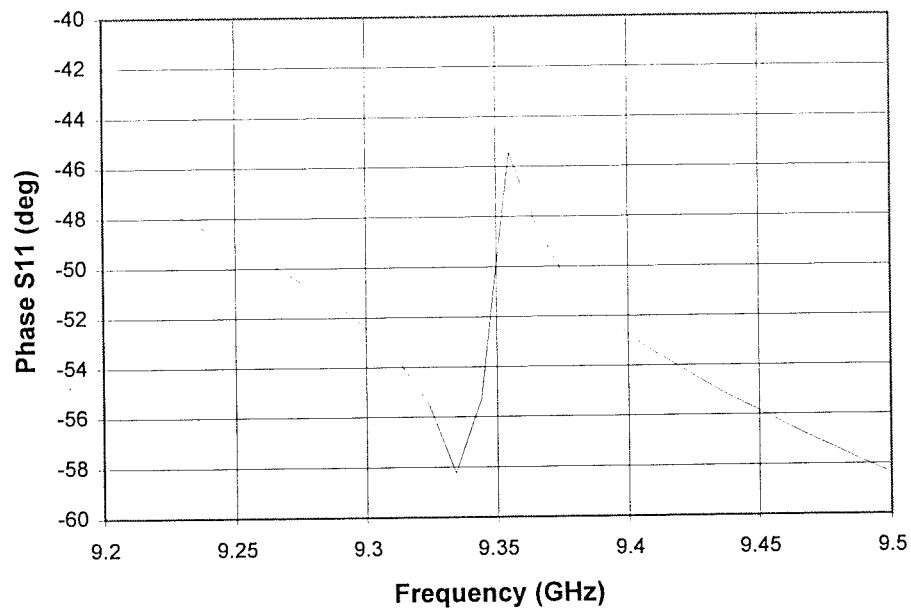
## 6.2 Optimisation of coupling gap for microstrip ring resonator

In the current study the aim of using a microstrip ring resonator is to characterise the quality of the newly developed KQ conductive material from Heraeus. The substrate is therefore chosen as low loss 96% alumina material. In (6-2), for the attenuation measurement, the Q factor is referred to as unloaded Q. However in a real situation the Q factor measured is the loaded one. If we try to minimise the loading effect of the feed line, the measured Q factor will approach the unloaded one and thus reasonable accuracy can be achieved if we use the loaded value of Q in (6-2). To reduce the loading effect of the feed line, the coupling gap has to be made large. However if the coupling gap is made too large, there may not be enough energy to be coupled into the ring resonator. Therefore, the dip in the reflected power curve may not be deep enough for an accurate determination of Q factor or even made a determination impossible. A compromise has to be made to achieve maximum measurable Q factor. We used simulation to determine the optimum coupling gap, instead of an experimental trial because it is more economical on both time and material. Since the ring resonator is a planar structure, it is justifiable to use a 2.5D electromagnetic simulator to simulate the coupling structure. A 3D electromagnetic simulator can also be used for this purpose, but it will take much longer simulation time. The simulator used here is HP Momentum™. The diameter of the ring resonator was 43.5 mm so that a wide frequency range of measurements could be made. In the simulation, the width of the conductor track was set at 0.61 mm and the alumina substrate used had a thickness of 0.635 mm and permittivity of 9.6. This is commensurate with practical materials and the actual ring structure to be tested. These pre-conditions leave only the coupling gap as a parameter to be investigated. As an example figure 6.2 shows the frequency dependence of magnitude and phase of the reflection coefficient from this one port structure of a ring resonator. The coupling gap is





(a)



(b)

Figure 6.2 Simulated S-parameter of ring resonator with coupling gap set as  $120\ \mu\text{m}$ .

(a) Magnitude of reflection coefficient (b) Phase of reflection coefficient

120 $\mu$ m and the simulated frequency range is from 9.2 to 9.5 GHz selected in order to capture one of the resonant peaks. From figure 6.2 (a) it can be seen that the resonance occurs at 9.34 GHz, which corresponds to the dip in the curve for the reflected wave. Inspection of figure 6.2 (b) shows that at resonance the phase of the reflected wave also has a dramatic change. In figure 6.3 a comparison was made of resonant curves with different coupling gaps. It

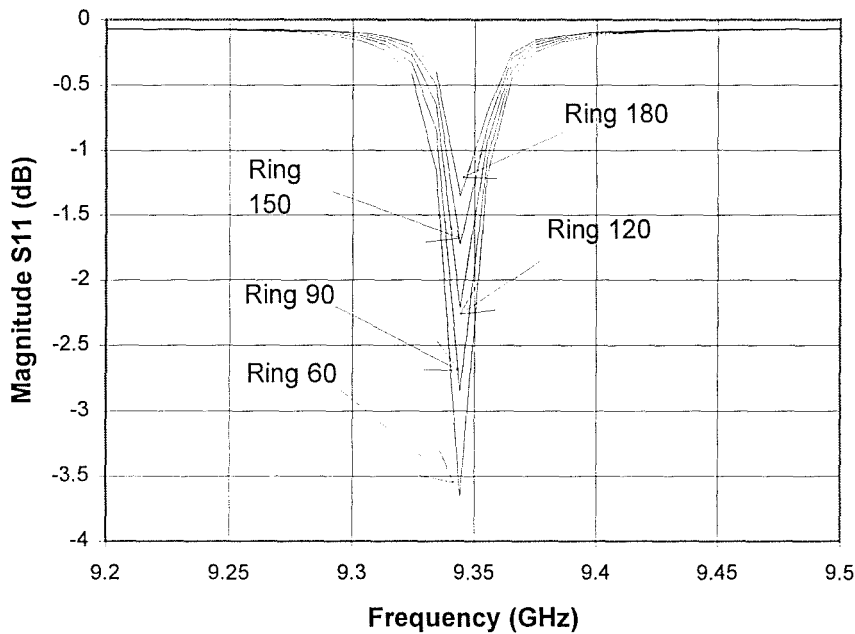


Figure 6.3 Comparison of resonant curves corresponding to different coupling gaps

is observed that the resonant curve becomes deeper with decreasing coupling gap. The dip is at -1.36 dB when the coupling gap is 180  $\mu$ m, the largest used. This dip value is not big enough since the resonant curve could be buried in the background noise of the test system. The general principle in choosing coupling gap is that the gap must be big enough to realise under-coupling. In this case, the losses in the measured Q factor are mainly from the resonant ring and the losses from the external circuit are small enough to be neglected. If the coupling

gap is too small, over-coupling will happen, and consequently the losses in the measured Q factor are mainly from external circuit. So the coupling gap can not be very small. On the other hand, at the condition of under-coupling, the resonant dip should be deep enough to have a clear distinction from background noise. Based on the simulation results in figure 6.3, a coupling gap of 120  $\mu\text{m}$  was chosen as optimum to give a dip value of -2.22 dB which can be properly recorded by the network analyser.

### **6.3 Test results for attenuation of microstrip line fabricated using a novel conductive paste**

The ring resonator test circuit used was fabricated by Heraeus Inc. using their KQ gold paste in order to characterise its microwave performance. It was first printed on 96% alumina substrate with thickness of 0.635 mm. After printing, the substrate was fired to remove the organic materials in the paste and obtain a layer of high quality gold film on the substrate, which has nearly the same conductivity as the bulk gold material. The realisation of high quality gold film is due to the novel technology which produces very small (0.1 to 0.5  $\mu\text{m}$ ), tightly distributed, spherical gold particles. These particles are combined with a novel vehicle system which allows printing and firing to give a very smooth surface with no agglomeration of particles. This is much smoother than conventional thick film golds. It is also designed for an optimum fired thickness of 4  $\mu\text{m}$ . This thickness is a good compromise between etched pattern accuracy and performance. It is large enough to avoid problems with skin depth at high frequency. The pattern of the ring resonator was etched to its predetermined size using well established photoresist and etching processes. The diameter of the ring was 43.5 mm and the width of the ring track, 0.6 mm. To minimise the loading effect due to the feeding line and external circuit, the coupling gap was chosen as 120  $\mu\text{m}$  to give loose coupling. This decision has been confirmed by our electromagnetic simulation. The test results for the ring resonator are shown in figure 6.4 in which the frequency dependence of the attenuation coefficient is presented. Because the substrate is alumina which is relatively low loss, the attenuation presented above can be considered as mainly coming from the conductor track of the ring.

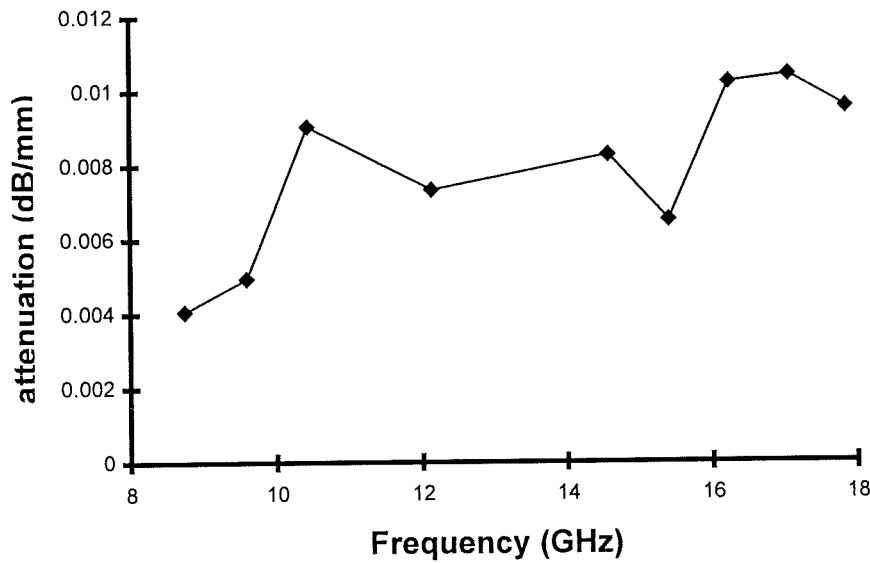


Figure 6.4 Frequency dependence of signal attenuation along ring track.

It can be seen from figure 6.4 that the attenuation of the signal increases with frequency and in the frequency range investigated, the values of the attenuation are quite low, indicating the great potential of the technology in the application of high frequency circuits. The expected increase of attenuation with frequency is due to the increased extent of skin effect. A large spread on measured data is also observed, which may come from the loading effect of the external circuit. In a rigorous way, the  $Q$  factors in (6-1) and (6-2) should be unloaded ones. Therefore, if the loaded  $Q$  is used in the two equations, the external loss will cause errors.

## 6.4 Conclusions

A ring resonator structure on an alumina substrate has been used to characterise Heraeus' high quality gold conductive paste. An electromagnetic simulator was used to optimise the design of the ring resonator for maximum measurement accuracy prior to the fabrication.

## References

- [1] Robert E. Collin, "Foundations for microwave engineering", McGraw-Hill, Inc., second edition, 1992.
- [2] K. R. Broome, "A low cost, multi-layer FR4 circuit board for the RF and microwave circuits in a fixed wireless access residential transceiver unit", IEE Colloquium on RF & Microwave circuits for commercial wireless applications, Savoy place, London, February 1997
- [3] P. Trought, "High-Q factor resonators in microstrip", Electronics Letters, vol4, no24, Nov. 1968, pp520-522
- [4] P. Trought, "Measurement techniques in microstrip", Electronics Letters, vol5, 1969, pp25-26
- [5] D. I. Amey and S. J. Horowitz, "Microwave material characterisation, " ISHM'96 Proceedings, pp. 494-499, October, 1996
- [6] E. O. Hammerstad, and F. Bekkadal, "A microstrip handbook", ELAB Report, STF 44 A74169, University of Trondheim, Norway, 1975, pp. 98-110
- [7] K. C. Gupta, Ramesh Garg, Inder Bahl and Prakash, " Microstrip lines and slotlines", second edition, Artech House, Inc., 1996

# **Chapter 7 Characterisation of microwave dielectric materials using resonant structures**

## **7.1 Introduction**

## **7.2 Advanced thick film technologies from Heraeus**

## **7.3 Permittivity measurement of film materials in a resonant cavity using transmission line theory**

## **7.4 Cavity perturbation method for the characterisation of dielectric film materials**

## **7.5 Further studies into the cavity perturbation method employing a circular waveguide and high Q mode**

## **7.6 Error investigation in the measurement of permittivity and loss tangent**

## **7.7 Conclusions**

---

Dielectric and conductive thick or thin film materials constitute the basis of MCM circuits, microwave integrated circuits (MIC) and other high density packaging circuits. Their accurate characterisation is vital to circuit design, especially at high frequencies. However, to date, although conductor characterisation is well understood, as discussed in chapter 6, there have been no satisfactory techniques for the accurate characterisation of dielectric film materials. This is due partly to the very small mass and volume of dielectric thick and thin films and partly to the fact that they need a carrier substrate which is of much greater mass than the former.

To meet this need, a novel technique has been developed using a cavity resonator to provide a reliable and accurate method to measure the intrinsic properties of the dielectric film. The basic principles of the new techniques are electromagnetic theory (Maxwell's equations) and transmission line equations. In the following sections of this chapter, both the measurement

techniques and the theoretical derivations will be described. Test results for Heraeus' state-of-the-art dielectric materials will be presented.

## 7.1 Introduction

The development of state-of-the-art hybrid and high density packaging technologies, such as multichip modules (MCMs), is increasingly in need of the accurate characterisation of dielectric film materials, especially at microwave frequencies because the permittivity values of the dielectric films play a crucial role in determining the geometric size of a high frequency circuit. In addition, the loss tangent of the dielectric film is also very important in determining the performance of a microwave circuit. Unlike the measurement of bulk materials, such as alumina substrates, for which standard microwave measurement techniques can be applied [1], the measurement of dielectric film materials is always a challenge because the dielectric film, whether deposited or printed, usually exists on a substrate and is very thin compared with the thickness of the supporting substrate, which makes the extraction of the electrical effects due to the dielectric film from the measured quantities, such as resonant frequency and loaded Q factor, very difficult.

Attempts have been made to characterise dielectric film materials. Amey and Horowitz have used a "T-pattern" microstrip resonator to measure the properties of the dielectric film materials [2]. This method has flexibility in covering a relatively wide frequency range. The disadvantage of it is that the effect of discontinuities and dispersion involved have to be corrected. It is difficult to measure the dielectric constant to high accuracy with this approach. They have also pointed out the difficulty in using this method to measure the loss tangent of the dielectric film materials because at the available thickness of the dielectric film materials, the width of the 50 $\Omega$  microstrip line is so narrow that the losses due to the microstrip line will dominate the total loss. Therefore it will be very difficult to separate the loss due to the dielectric film from the total loss. Janezic et al [3] initiated a novel method by loading a thin sample against a thick one in a circular cavity resonator. From the shift of the resonant frequency

introduced by the thin sample, its dielectric constant can be calculated. Since the field pattern inside the cavity resonator can be rigorously calculated, high accuracy of measurement can therefore be achieved with this method if the thickness of the substrate can be chosen to position the thin dielectric sample in the maximum electric field region. Huang et al [4] have developed this method to suit the measurement of dielectric films. In their methodology, the dielectric film is printed and fired on an alumina substrate and a rectangular waveguide cavity is used to ease sample preparation. Similar to Janezic's method, the sample is also loaded at the end of the cavity. By doing this, the theoretical treatment and sample loading are relatively easy. However, it suffers a disadvantage of positioning the sample under test in the weak electric field region. Examination of the standing wave pattern in a resonant cavity can prove that the electric field strength is very weak near the end of the cavity. To ensure the highest sensitivity of the measurement system, the dielectric film needs to be positioned in the area with the maximum electric field strength to enable the dielectric film material to have a maximum interaction with the electric field. However, limited by the thickness of the supporting alumina substrate, the dielectric film is usually located in a weak field region. This poses difficulty in measuring the very small shift of resonant frequency due to the dielectric film. The situation may even get worse if measurement over a wide frequency range is required. Again, Huang's method can not be used to measure the loss tangent of the dielectric film materials. To realise the optimum positioning of the dielectric sample inside the cavity resonator, a novel approach was developed in which a moveable short-circuit is introduced to accurately position the sample at a location away from the end of the cavity so that the dielectric film can always be loaded in the area of maximum electric field. This new positioning maximises the shift of resonant frequency caused by the dielectric film and consequently increases the accuracy of the measurements. The moveable short-circuit is realised by attaching a metal plate to a plunger and the accurate position of the plunger can be read out from the micrometer fitted to it. An additional advantage of using a moveable short-circuit is that the length of the cavity resonator can also be changed continuously to get test results over a wide frequency range. The inherent sharp Q curves for cavity resonators with different cavity lengths can ensure the accurate determination of resonant frequencies and dielectric constants as well. It should be noted that a good contact between the plunger on the moveable short-circuit and waveguide walls is necessary to ensure high Q factor.



The new sample loading scheme also requires a new derivation to account for what happens in the cavity. We have, from first principles, derived two sets of independent equations to correlate the physical parameters of the dielectric film sample and those of the cavity resonator with resonant frequency and Q factor when the cavity resonator is loaded with a two-layer test sample. The standard transmission line theory is used to derive the first set of equations from which the dielectric constant can be accurately deduced from the measured data. The general cavity perturbation theory is used to derive the second set of equations which can be used for the accurate measurement of both the dielectric constant and loss tangent of the dielectric film materials.

## **7.2 Advanced thick film technologies from Heraeus**

It has been generally understood that the performance of today's high speed electronic systems is often dominated by the interconnection and packaging external to the highly integrated chips or dice. The emergence of the packaging schemes of multi-chip modules is the response to the demand for higher levels of interconnection. Historically, thin film circuitry has been used for the majority of high density, high frequency applications, but several new technologies are now emerging. Thick film technology offers the appropriate costs for microwave applications, but does not provide suitable performance, due to limitations in conductivity, line definition and dielectric performance. Usually the circuit assemblies use two or more technologies, which require subcircuits to be separately manufactured, assembled and interconnected. This all adds to the cost of the assembly and reduces its reliability. To address these problems, Heraeus has developed a new thick-film material system, called 'thick film on ceramic technology', which provides the performance of thin film technology but at the same cost level of conventional thick film technologies [5-6]. This technology allows the fabrication of high performance microwave circuits together with appropriate high density interconnect, all on one substrate. Heraeus' new thick-film

technology consists of a novel gold-based conductive material used for the fabrication of conductor track, and photoimageable dielectric materials for substrate and overlay.

The gold-based material uses an innovative powder technology to provide extremely dense and smooth conductors. The key point in this technology is the small gold powder particles, ranging in size from 0.1 to 0.5  $\mu\text{m}$ . The powder particles can be blended into two forms: photoengrable gold material and screen printing gold material. The former is printed, fired, coated with photoresist and then etched to define the circuit pattern. The advantage of this material is that conductor track can be made as narrow as 10  $\mu\text{m}$  with excellent edge definition. The latter is formulated for fine line screen printing allowing 50  $\mu\text{m}$  line widths. The typical parameters for these two kinds of materials is as follows:

- Thickness of track conductor controllable from 3 to 10  $\mu\text{m}$
- Conductivity 2.6 milliohms per square at 10 microns in thickness compared with bulk gold at 2.4
- Excellent bondability with both gold or aluminum wire, both initial and aged.
- Excellent adhesion to substrates of various types

Examples of what can be achieved using this novel gold technology and a simple positive resist photoengraving process with an iodine/potassium iodide etchant are shown in Figure 7.1. The conductor pattern consists of 40 micron wide lines with a 10 micron wide gap patterned on a standard 96% alumina substrate. The sharp edge and smooth surface of the conductor track demonstrate the potential of the technology in high performance and high frequency circuits.

The companion photoimageable dielectric materials from Heraeus provide low loss, low permittivity and fine via resolution. This will match the high performance conductor technology. Historically, thick film dielectric materials have provided poor via resolution (250 microns), high loss and high dielectric constant. Poor via resolution is as a result of the

necessary rheological compromise made to avoid forming pinholes during printing, and the poor dielectric properties arise from the combination of fillers and low viscosity glasses used to form the fired layer. Although certain commercially available photoimageable dielectric systems largely address the via resolution problems of thick film dielectrics, they do not

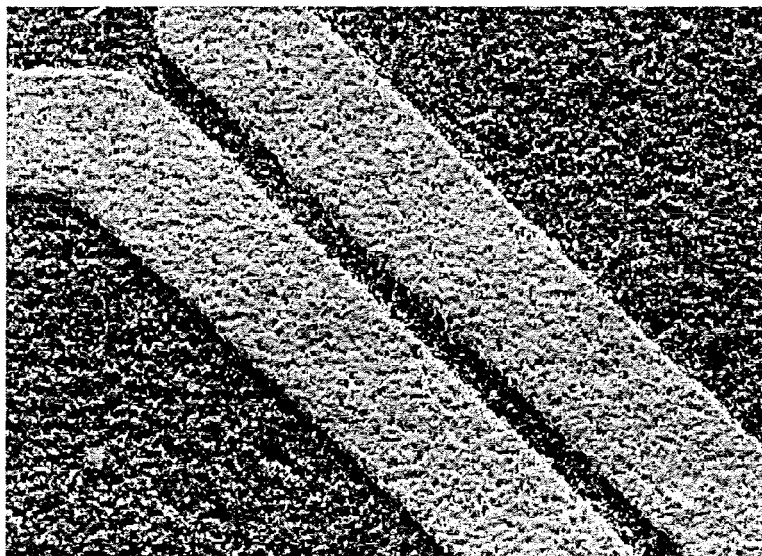


Figure 7.1 Fine line conductor tracks fabricated on alumina substrate using Heraeus novel gold technology. The line width and spacing are 40 and 10 $\mu$ m respectively.

(Source: Heraeus Inc.)

address the problem of high dielectric constant and high loss. The new dielectric material system uses a radically different technology to overcome all these problems. The dielectric material consists of inorganic powders manufactured using boro-silicate technology in combination with a photosensitive vehicle. The powders are produced by the hydrolysis and condensation of various metal alkoxides, to form a polymeric structure that, depending on reaction conditions, is either precipitated as a solid or forms a gel from which the solvent is subsequently removed. After additional treatments, highly reactive powders are formed which will sinter to give fully dense films at temperatures hundreds of degrees lower than conventionally produced materials of the same composition. It is important to note that

sintering is achieved without the addition of the usual alkali metal fluxing components necessary in other thick film dielectrics. The removal of these mobile constituents in combination with the use of very pure starting materials is the reason for the unprecedentedly low levels of dielectric loss. The resultant dielectric thick film material provides the following performance characteristics:

- Via resolution better than 50 microns with 25 microns achievable
- Permittivity 3.9 - measured to 12 GHz
- Extremely low dielectric loss (loss tangent around 0.00005)
- Layer thickness 10 microns
- Fully dense and hermetic

An example of a via formed using this material is shown in Figure 7.2 which shows a 50 micron via prior to firing. It can be seen that the via structure is well defined with clear edges. Shown in figure 7.3 is an array of vias after firing fabricated using Heraeus new dielectric material system. It demonstrates the capacity of the new material system for high density packaging involving multi-layer interconnections.

In order to provide a suitable structure for fabricating circuits offering a range of applications, it is vital that the new material system is compatible with appropriate substrates and other thick film materials. Tests carried out with a variety of solderable thick film conductors, as well as conventional resistor and dielectric materials have shown the outstanding performance of the new material system. This performance is further enhanced by compatibility with a wide range of substrate materials including alumina, aluminum nitride, glass and beryllia.

In figure 7.4 surface profiles show conductors on dielectric film fabricated using the Heraeus novel gold and dielectric material system. A wide conductor track is shown in figure 7.4 (a) and a narrow conductor track is shown in figure 7.4 (b). The scanning curves clearly

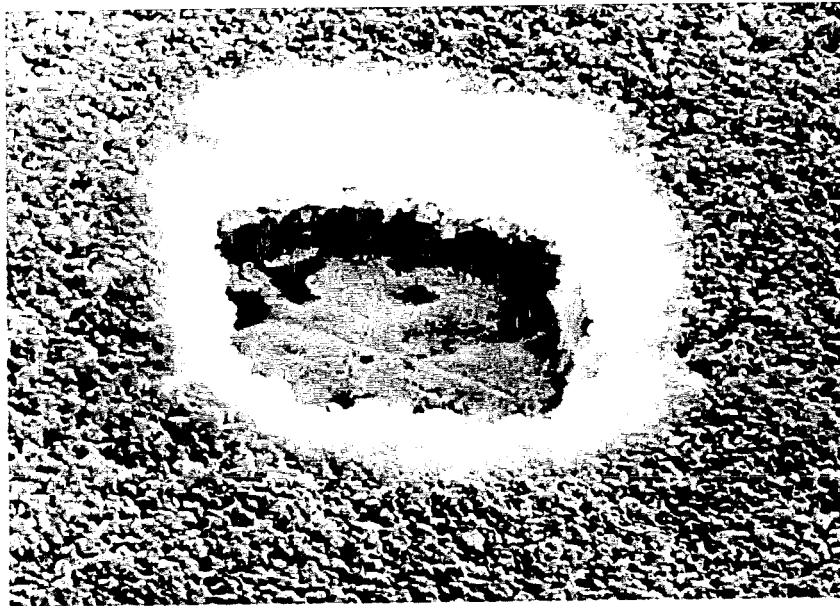


Figure 7.2 SEM picture for a 50  $\mu\text{m}$  square via prior to firing. (Heraeus Inc.)

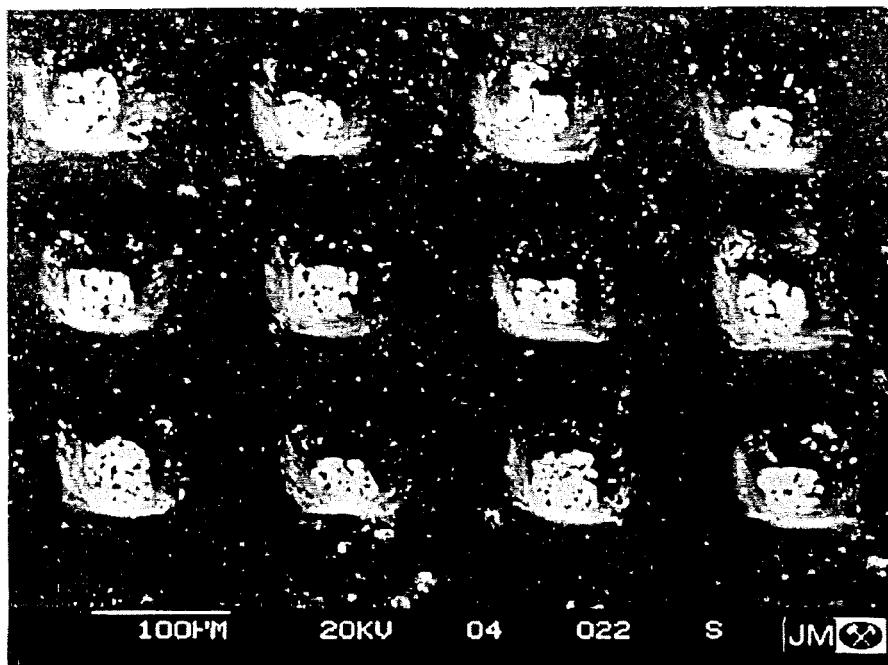
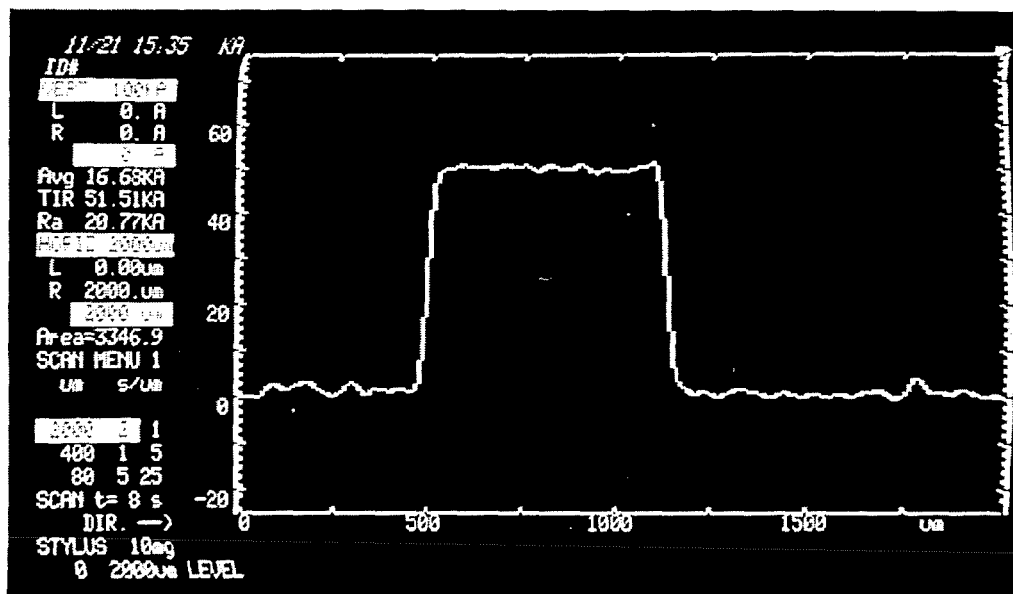
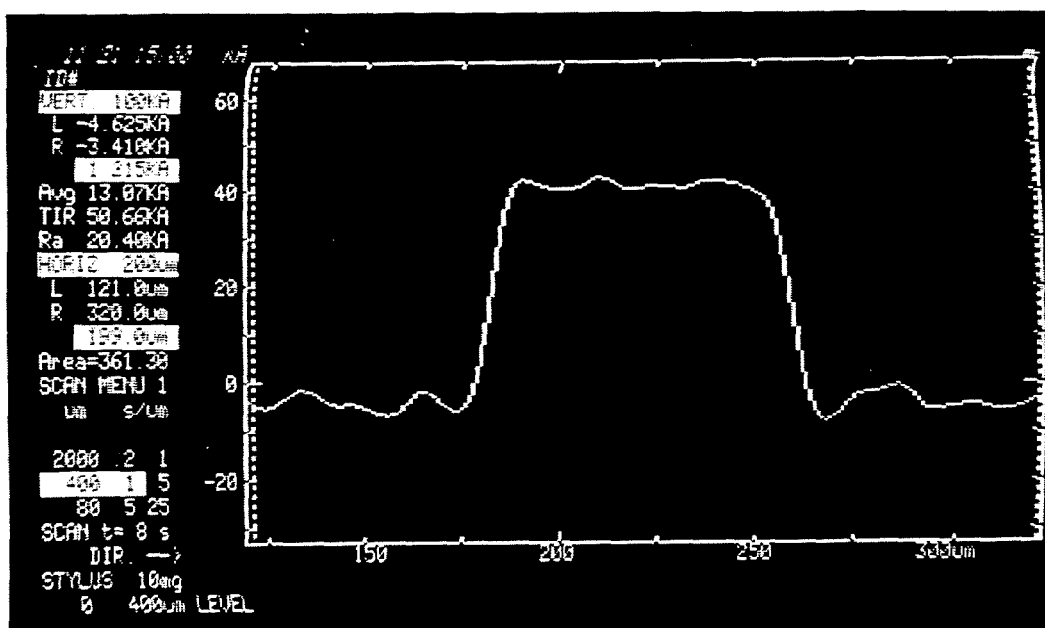


Figure 7.3 SEM picture of a via array fabricated using Heraeus' new dielectric material system. (Heraeus Inc.)



(a)



(b)

Figure 7.4 Alphastep (Tencor Instruments) scanned profiles for microstrip lines fabricated using Heraeus' new conductive and dielectric materials. (a) A wide track (about 600  $\mu\text{m}$ ) (b) A narrow track (about 80  $\mu\text{m}$ ) (Middlesex University microelectronics Lab)

indicate the smoothness of both the dielectric surface and conductor surface. The almost constant width of the conductor track also demonstrates its high quality which imply that the material system can be used for the fabrication of high frequency and high performance circuits. The equipment used for the scans was a Tencor Alphastep Model-200.

Table 7.1 Summary of Heraeus novel conductive and dielectric material system. (Heraeus Inc.)

Property	Conventional Thick Film	Heraeus Material System
Conductor spacing	125 $\mu\text{m}$ line & space	25 $\mu\text{m}$ line & space
Conductor thickness	10 $\mu\text{m}$	3 to 5 $\mu\text{m}$
Dielectric thickness	50 $\mu\text{m}$	20 $\mu\text{m}$
Via resolution	250 to 300 $\mu\text{m}$	25 to 50 $\mu\text{m}$
Permittivity	8 to 14	3.8 to 4.2
Dielectric loss tangent	0.001 to 0.003	0.00005
Leakage current ( $\mu\text{A}$ )	1 to 20	0.00002 to 0.00005

It can be seen that the new materials system offers an outstanding technology which addresses the disparate requirements of microwave, MCM and general purpose interconnect technology. In combination with conventional thick film materials it opens up many new application areas in growing industries. The materials offer excellent microwave characteristics, which in turn leads to outstanding performance in MCMs. The general summary of the new material system and its comparison with conventional thick film technology is given in table 7.1.

## 7.3 Permittivity measurement of film materials in a resonant cavity using transmission line theory

### 7.3.1 Basic relations in a rectangular waveguide

The cross-section of a metal cavity resonator to be used could be either circular or rectangular. For convenience of sample preparation, a metal rectangular waveguide was chosen to form the cavity resonator in our measurement. It is therefore necessary to give the basic relationships governing wavelength and frequency in a rectangular waveguide.

The wavelengths inside the rectangular waveguide are related by the following equation,

$$\frac{1}{\lambda^2} = \frac{1}{\lambda_g^2} + \frac{1}{\lambda_c^2} \quad (7-1)$$

where

$\lambda_g$  is guide wavelength of the field pattern.

$\lambda$  is wavelength of the wave in the medium filling the waveguide.

$\lambda_c$  is the cut-off wavelength.

If  $\lambda$  is bigger than  $\lambda_c$ , the wave can not propagate in the waveguide. Using the relation between guide wavelength  $\lambda_g$  and phase constant  $\beta$ , we can find

$$\beta = \frac{2\pi}{\lambda_g} = \frac{2\pi}{\lambda_0} \sqrt{\epsilon_r - \left(\frac{\lambda_0}{\lambda_c}\right)^2} \quad (7-2)$$



where  $\epsilon_r$  is the relative permittivity of the material filling the waveguide and  $\lambda_0$  is the wavelength in air.

For  $TE_{mn}$  mode in waveguide,

$$\frac{1}{\lambda_c^2} = \left(\frac{m}{2a}\right)^2 + \left(\frac{n}{2b}\right)^2 \quad (7-3)$$

where  $m, n$  are integers, and  $a$  and  $b$  are the cross-section dimensions of the rectangular waveguide as indicated in figure 7.5. In a rectangular waveguide  $TE_{10}$  mode is the dominant one. It follows from equation (7-3)

$$\lambda_c \Big|_{TE_{10}} = 2a \quad (7-4)$$

For the dominant mode, equation (7-2) can therefore be rewritten as

$$\beta = \frac{2\pi}{\lambda_0} \sqrt{\epsilon_r - \left(\frac{\lambda_0}{2a}\right)^2} = \frac{2\pi f_0}{c} \sqrt{\epsilon_r - \left(\frac{c}{2af_0}\right)^2} \quad (7-5)$$

where  $c$  is the velocity of the light in air and  $f_0$  is the frequency of the propagation wave.

Another important quantity in waveguide is its characteristic impedance,  $Z_0$ , or admittance,  $Y_0$ , which is mode dependent [7] and can be expressed as

$$Z_0 = \frac{1}{Y_0} = \sqrt{\frac{\mu}{\epsilon}} \frac{\lambda_g}{\lambda} \quad \text{for } TE \text{ modes} \quad (7-6a)$$

$$Z_0 = \frac{1}{Y_0} = \sqrt{\frac{\mu}{\epsilon}} \frac{\lambda}{\lambda_g} \quad \text{for } TH \text{ modes} \quad (7-6b)$$

where  $\epsilon = \epsilon_0 \epsilon_r$ ,  $\mu = \mu_0 \mu_r$  and  $\lambda = \lambda_0 / \sqrt{\epsilon_r}$ .

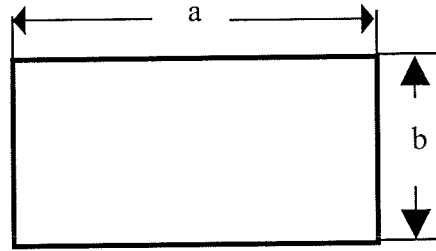
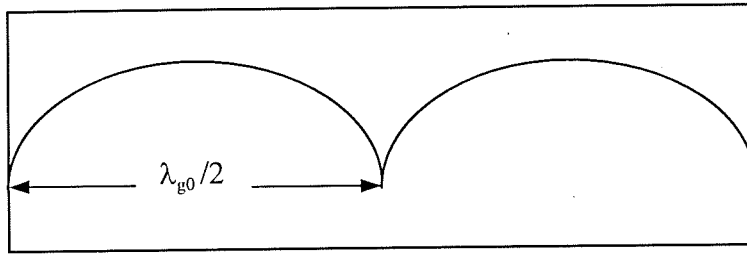


Figure 7.5. Internal cross-section dimensions of rectangular waveguide.

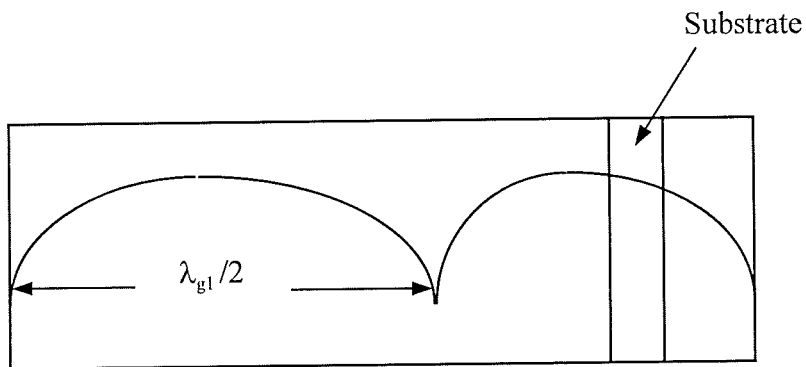
### 7.3.2 Theoretical treatment of a resonant cavity loaded with dielectric samples

As stated previously, the two-layer specimen has to be loaded in the cavity resonator away from the cavity end in making the permittivity measurement of the dielectric film. Since, for this novel approach, there are no existing formulae to relate the resonant frequency and loaded Q factor to the physical sizes and properties of the dielectric materials inside it, a derivation has to be made from first principles.

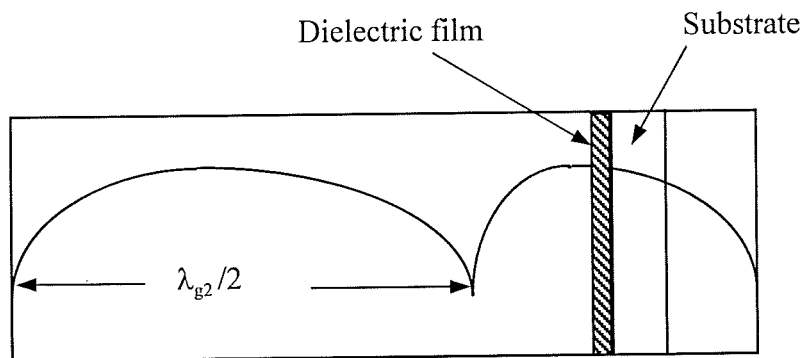
A visualisation of the operation of the cavity resonator loaded with dielectric material is important. Before we proceed with our derivation, let us first establish the physical picture of what will happen during measurement using cavity resonator method. It is well known that in a cavity resonator formed by rectangular waveguide, when the cavity length equals integer



(a)



(b)

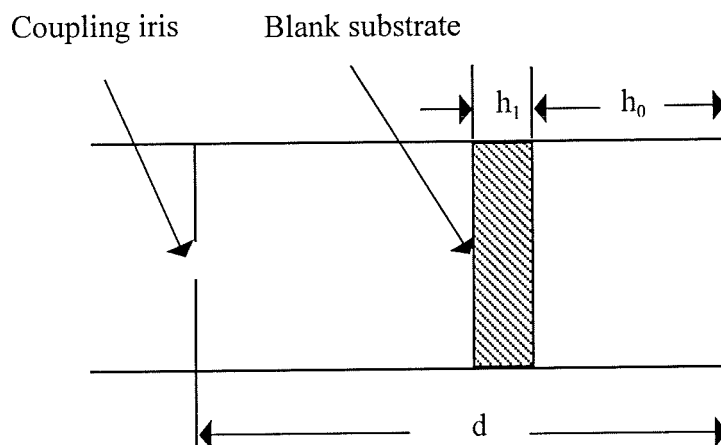


(c)

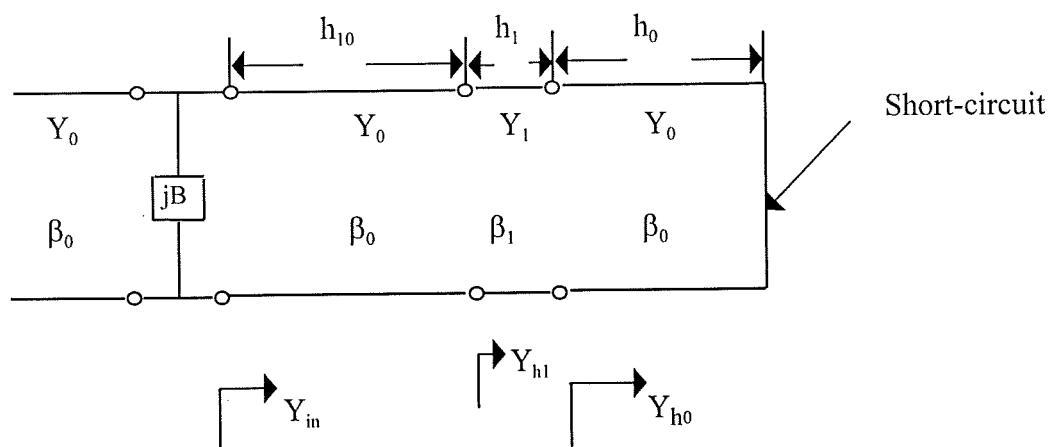
Figure 7.6 Standing wave pattern of E field in a resonant cavity formed by rectangular waveguide. (a) Empty cavity; (b) Cavity loaded with substrate only; (c) Cavity loaded with two-layer sample.

number of half guide wavelength, the cavity will be in resonance. As an example, figure 7.6 (a) shows the resonant situation when the length of the empty resonant cavity equals two half guide wavelength. For dominant  $TE_{10}$  mode this resonance can be marked as  $TE_{102}$ , where the number, 2, in subscript represents the number of half guide wavelengths in the cavity at resonance. When a piece of dielectric substrate is inserted in a cavity resonator like the situation in figure 7.6 (b), the dielectric substrate will effectively introduce extra electrical length. Only if the physical length of the cavity plus this extra electrical length introduced by the dielectric substrate equals the integer number of half guide wavelength can the cavity resonate. In other words, the effective length of the substrate loaded cavity is longer than the empty cavity. This will cause a downwards shift of resonant frequency. The picture of resonance in a substrate loaded cavity can also be understood from the phase change taking place in the cavity. At resonance, the incoming wave in the cavity should have integral number of  $\pi$  in phase change before its reflection from short-circuit end. For the situation in figure 7.6 (b), because there is more phase change in the substrate area than in the air region with the same length which equals the substrate thickness, the wave in the air region should travel a longer route to make the total  $2\pi$  phase change in the cavity. Therefore  $\lambda_{g1}$  is bigger than  $\lambda_{g0}$  as shown in figure 7.6 (a) and (b). If the inserted sample is in a two-layer structure, shown in figure 7.6 (c), and for the convenience of theoretical derivation and measurement we assume that the substrate supporting the dielectric film material is exactly the same as that in figure 7.6 (b), the resonant frequency of the cavity will have a further downwards shift in respect to the situation in figure 7.6 (b). The frequency shifts due to the substrate material and film material can be employed to extract the permittivity value of the dielectric film supported by the substrate. This idea is developed in detail in this chapter. For the purpose of measuring permittivity of film material to high accuracy, the most important thing is that the shift in resonant frequency must be big enough. This can be ensured by positioning the dielectric film in the strong field region. Later we will derive a formula used to determine the optimum position of the two-layer sample in a cavity resonator, where the maximum shift of resonant frequency due to the dielectric film can be realised.

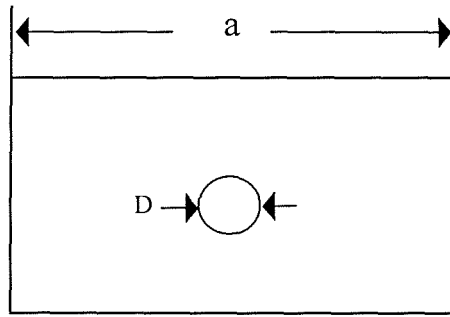
The derivation will start from the reference cavity, i.e. the cavity loaded only with a blank substrate. The formulae derived from substrate loaded cavity will be used to calculate the permittivity of the blank substrate on which the dielectric film is printed. The diagram for reference cavity and its distributed equivalent circuit are shown in figure 7.7. To simplify the



(a)



(b)



(c)

Figure 7.7 Structures of the cavity resonator loaded with blank substrate. (a) Physical structure; (b) distributed equivalent circuit; (c) side view of coupling end of the cavity resonator.

derivation we have neglected the losses on the waveguide walls since they have very little effect on the resonant frequency of the cavity [8]. Based on the waveguide formulae given in reference [7], we have also verified that the shift of the resonant frequency due to the losses of the dielectric substrate and film can be neglected. It is also assumed that only the dominant mode is excited in the resonant cavity. In the frequency range where the higher order modes exist, the present theory will cease to be valid because we can hardly tell to which mode a resonant peak can be attributed. For the present circuit structure it would be more convenient to derive the resonant condition by using the input admittance as given in equation (7-7)

$$Y_m = Y_0 \left[ \frac{Y_L + jY_0 \tan(\beta l)}{Y_0 + jY_L \tan(\beta l)} \right] \quad (7-7)$$

In the cavity loaded with a blank substrate, the input admittance  $Y_{in}$ , looking from the coupling end of the cavity towards the other end of the cavity, is given as follows according to figure (7-7),

$$Y_{in} = Y_0 \left( \frac{Y_{h1} + jY_0 \tan(\beta_0 h_{10})}{Y_0 + jY_{h1} \tan(\beta_0 h_{10})} \right) \quad (7-8)$$

in which

$$Y_{h1} = Y_1 \left( \frac{Y_{h0} + jY_1 \tan(\beta_1 h_1)}{Y_1 + jY_{h0} \tan(\beta_1 h_1)} \right) \quad (7-9)$$

$$Y_{h0} = -jY_0 \cot(\beta_0 h_0) \quad (7-10)$$

$Y_{h1}$  and  $Y_{h0}$  are the admittances looking from the left and right interfaces respectively between the substrate and the air towards the short-circuit end of the resonant cavity, which are indicated in figure 7.7(b). In writing up equation (7-10),  $Y_L = \infty$  is used which corresponds to the short-circuit of the cavity resonator at the termination end.  $h_1$  is the thickness of the blank substrate,  $h_0$  is the distance from the right interface between the blank substrate and air to the short-circuit end as indicated in figure 7.7(a) and  $h_{10} = d - h_1 - h_0$ ,  $d$  is the total length of the cavity resonator. In equations (7-8), (7-9) and (7-10)  $Y_0$  and  $Y_1$  are characteristic admittances of the waveguide filled with air and blank substrate respectively, and  $\beta_0$  and  $\beta_1$  are phase constants in air and substrate region inside resonant cavity respectively. According to equation (7-6) the characteristic admittance of the waveguide for TE modes can be expressed as

$$Y_0 = \frac{\lambda_0 \beta_0}{2\pi} \sqrt{\frac{\epsilon_0}{\mu_0}} \quad (7-11)$$

$$Y_1 = \frac{\lambda_0 \beta_1}{2\pi} \sqrt{\frac{\epsilon_0}{\mu_0}} \quad (7-12)$$

where

$$\beta_n = \frac{2\pi}{\lambda_0} \sqrt{\epsilon_n' - \left(\frac{\lambda_0}{\lambda_c}\right)^2} \quad (7-13)$$

$n = 0, 1, 2$  corresponds to air, substrate and dielectric film region respectively inside the cavity space (the case of the dielectric film region will be dealt with later for a cavity loaded with a two-layer specimen).  $\epsilon_0$  and  $\mu_0$  are the permittivity and permeability of free space.  $\beta_n$  denotes phase constant while  $\epsilon_n'$  is the relative permittivity of the medium in corresponding region inside the cavity.  $\lambda_0$  is the free space wavelength and  $\lambda_c$  is the cut-off wavelength which equals  $2a$  for the dominant mode considered here ( $a$  is the cross-section dimension of the rectangular waveguide as shown in figure 7.7 (c))

At resonance of the cavity, if the external circuit is assumed to be matched, we have

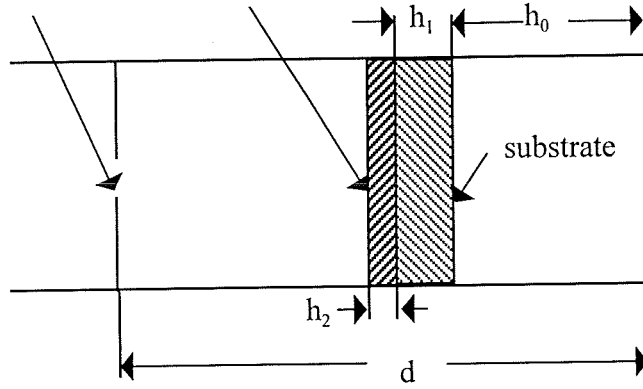
$$\text{Im}(Y_0 + Y_m + jB) = 0 \quad (7-14)$$

Where  $Y_0$  is the admittance looking towards external circuit, which is real and equals to characteristic admittances of the waveguide.  $B$  is the susceptance of the coupling iris that behaves like a pure inductance, and  $B$  is therefore negative [9]. Combining equations (7-8)-(7-12), after rearrangement, the resonant condition can be rewritten as

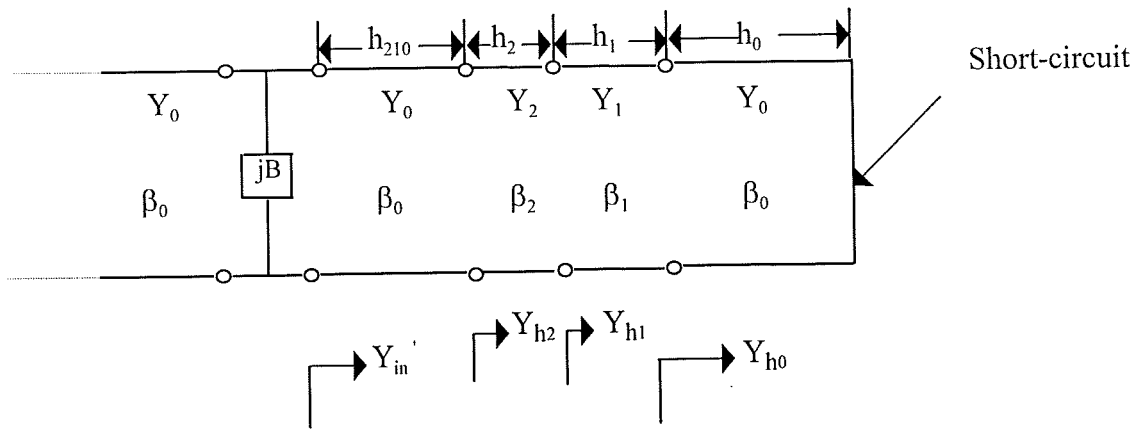


$$\frac{\beta_1(\beta_1 E_1 - \beta_0 E_0) + \beta_0(\beta_1 + \beta_0 E_0 E_1) \tan(\beta_0 h_{10})}{\beta_0(\beta_1 + \beta_0 E_0 E_1) - \beta_1(\beta_1 E_1 - \beta_0 E_0) \tan(\beta_0 h_{10})} = -\frac{B}{Y_0} = -b \quad (7-15)$$

Coupling iris      Dielectric film



(a)



(b)

Figure 7.8 (a) Cavity resonator loaded with two-layer specimen; (b) the distributed equivalent circuit of (a).

in which  $E_0 = \cot(\beta_0 h_0)$  ,  $E_1 = \tan(\beta_1 h_1)$  and  $b$  is the normalised susceptance which will be calculated later using a three dimensional electromagnetic software package.

The resonant condition for a cavity loaded with a two-layer specimen can also be derived in a similar way. Figure 7.8 shows a cavity resonator loaded with a two-layer sample and its distributed equivalent circuit. The admittance looking from the coupling end towards the termination end is

$$Y_m' = Y_0 \left( \frac{Y_{h2} + jY_0 \tan(\beta_0 h_{210})}{Y_0 + jY_{h2} \tan(\beta_0 h_{210})} \right) \quad (7-16)$$

where

$$Y_{h2} = Y_2 \left( \frac{Y_{h1} + jY_2 \tan(\beta_2 h_2)}{Y_2 + jY_{h1} \tan(\beta_2 h_2)} \right) \quad (7-17)$$

$Y_{h2}$  is admittance looking from the interface between the dielectric film material to be measured and air towards the short-circuit end of the cavity.  $h_{210} = d - h_2 - h_1 - h_0$ ,  $h_2$  is the thickness of the dielectric film, the meaning of  $d$ ,  $h_1$ ,  $h_0$  and  $Y_{h1}$  is the same as that in the situation of blank substrate loaded cavity. Similar to (7-11) and (7-12),  $Y_2$  is given as:

$$Y_2 = \frac{\lambda_0 \beta_2}{2\pi} \sqrt{\frac{\epsilon_0}{\mu_0}} \quad (7-18)$$

At resonance,

$$\text{Im}(Y_0 + Y_m' + jB) = 0 \quad (7-19)$$

Substituting equation (7-16) into equation (7-19), finally the resonant condition can be reduced to the form of

$$\frac{\beta_2 C_1 + \beta_0 \tan(\beta_0 h_{210})}{\beta_0 - C_1 \beta_2 \tan(\beta_0 h_{210})} = -\frac{B}{Y_0} = -b \quad (7-20)$$

where

$$C_1 = \frac{\beta_1(\beta_1 E_1 - \beta_0 E_0) + \beta_2(\beta_1 + \beta_0 E_0 E_1) \tan(\beta_2 h_2)}{\beta_2(\beta_1 + \beta_0 E_0 E_1) - \beta_1(\beta_1 E_1 - \beta_0 E_0) \tan(\beta_2 h_2)} \quad (7-21)$$

After mechanical and electrical measurement, the resonant frequencies for the resonant cavities loaded with i) a blank substrate and ii) a two-layer specimen, and the relevant physical sizes will be obtained. By solving two main transcendental equations (7-15) and (7-20), the relative permittivity (or dielectric constant) of the dielectric film material can be found.

As mentioned before, we need to maximise the difference between the resonant cavity loaded with a blank substrate and that loaded with a two-layer specimen in order to increase the accuracy and sensitivity of the measurement system. To realise this, let us first consider a simple situation, i.e. a cavity resonator loaded with only a blank substrate against the short-circuit end as shown in figure 7.9. If the phase change inside the substrate equals  $90^\circ$ , the dielectric film printed on it will be located in the maximum electric field region. Therefore

$$\beta_1 h_1 = \frac{\pi}{2} \quad (7-22)$$

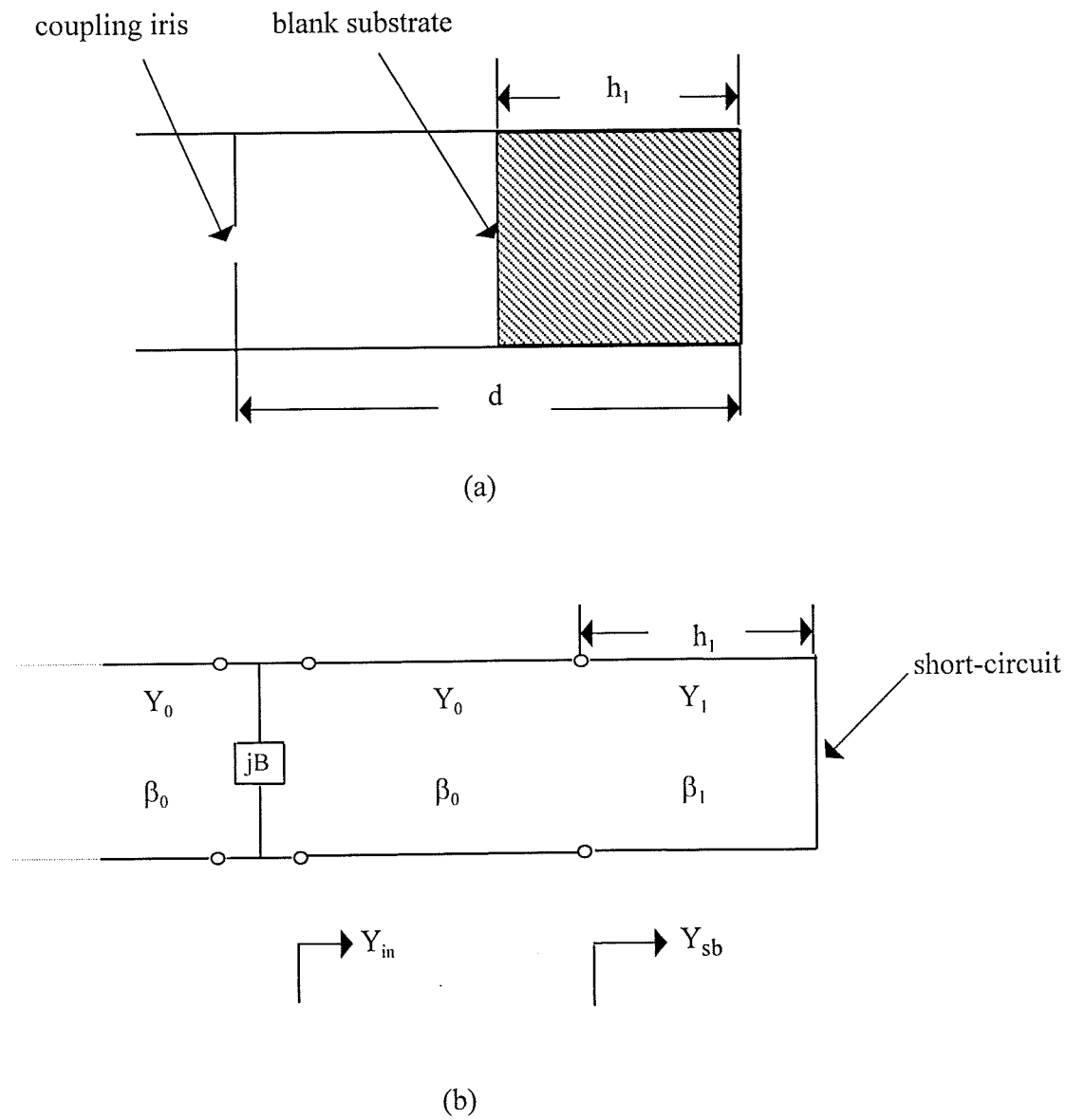


Figure 7.9 Cavity resonator loaded with blank substrate at the short-circuit end. (a) physical structure of the cavity; (b) the distributed equivalent circuit of (a).

For the situation where the sample is loaded at a position away from the short-circuit end, shown in figure 7.8, the phase change in the air region between substrate and short-circuit end has to be taken into account. It follows

$$\beta_0 h_0 + \beta_1 h_1 = \frac{\pi}{2} \quad (7-23)$$

$$h_0 = \frac{(\frac{\pi}{2} - \beta_1 h_1)}{\beta_0} \quad (7-24)$$

Equation (7-24) can be used to determine the optimum loading position of the samples to ensure maximum interaction between electric field and dielectric film material to create a maximum shift of resonant frequency due to the dielectric film.

To ensure the accurate calculation of the relative permittivity from the measured data, the coupling iris needs to be rigorously modelled. To this end HP HFSS™ [10] was used. This package employs the finite element method to simulate the electromagnetic behaviour of the coupling iris at different frequencies. During the simulation a thin plate with a hole at its centre was placed in a waveguide which is matched on both sides. The simulated results are presented as S-parameters from which the equivalent shunt susceptance can be calculated. To establish the relation between the S-parameters and the equivalent shunt susceptance of the coupling iris, let us consider the equivalent circuit of the simulated structure which is shown in figure 7.10. In figure 7.10,  $a_1$  is the voltage of the incident wave and  $a_1'$  is the voltage of the reflected wave at the same port. Furthermore,  $a_2'$  is the voltage of the transmitted wave through the coupling iris and  $a_2$  is the voltage of the wave due to the reflection of the transmitted wave.  $Y_m$  is the admittance looking from the input side towards the output side at the coupling iris which equals

$$Y_m = Y_0 + jB \quad (7-25)$$

Because the output port is matched,  $a_2 = 0$ . Then the reflection coefficient on the input side is

$$S_{11} = \Gamma = \frac{Y_0 - Y_m}{Y_0 + Y_m} \quad (7-26)$$

Substituting  $Y_m$  in equation (7-25) for that in equation (7-26), we have

$$S_{11} = \frac{-jB}{2Y_0 + jB} \quad (7-27)$$

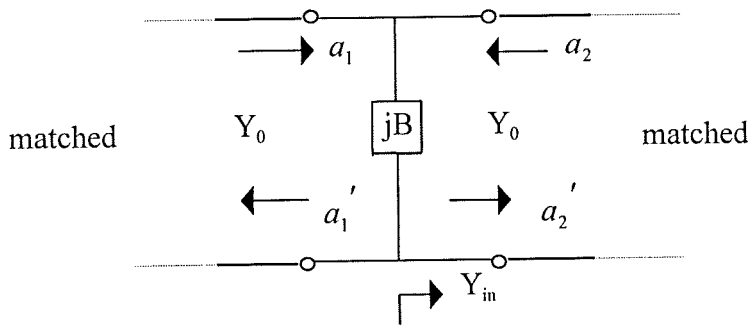


Figure 7.10 Equivalent circuit of the coupling iris for the extraction of shunt susceptance

If we consider the voltage relation on the coupling iris, we must have

$$a_2' = a_1 + a_1' = a_1(1 + S_{11}) \quad (7-28)$$

Thus

$$\frac{a_2'}{a_1} = S_{21} = 1 + S_{11} = \frac{2Y_0}{2Y_0 + jB} \quad (7-29)$$

It follows

$$b = \frac{B}{Y_0} = \frac{2jS_{11}}{1 + S_{11}} = 2j \left| \frac{S_{11}}{S_{21}} \right| \exp(j(\theta_{11} - \theta_{21})) \quad (7-30)$$

Because the coupling iris behaves like an shunt inductance, the phase difference  $\theta_{11} - \theta_{21}$  between  $S_{11}$  and  $S_{21}$  must be  $90^\circ$ . Our simulation in fact also confirms this. Therefore

$$b = -2 \frac{|S_{11}|}{|S_{21}|} \quad (7-31)$$

Equation (7-31) was used to obtain the reduced shunt susceptance  $b$  after simulation.  $b$  can also be obtained directly from (7-30) using only  $S_{11}$ . The reduced shunt susceptance  $b$  in figure 7.11 was compared with that in [7] and 6% difference was identified. Since the results in [7] have 10% error, it is justifiable to obtain  $b$  from rigorous electromagnetic simulation. In the simulation, the number of adaptives for mesh generation can be increased to reach an accuracy specified by users. In our measurement an X-band waveguide was used and the diameter of the coupling iris was chosen as 6 mm. The simulated results for the coupling iris are presented in figure 7.11, which will be used in the calculation of the relative permittivity of the dielectric film after measurement.

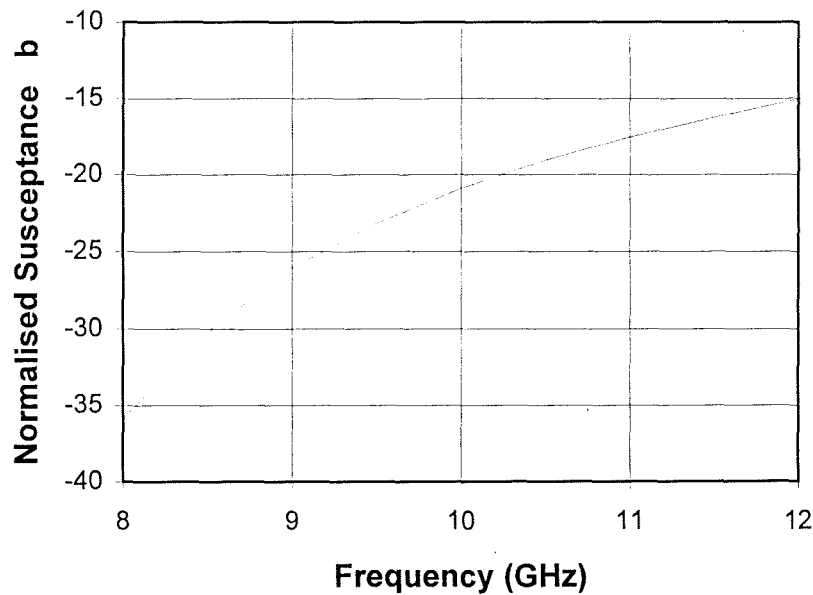


Figure 7.11 Frequency dependence of the reduced shunt susceptance for the coupling iris simulated by HP HFSS™.

### 7.3.3 Experimental details of the measurements

To demonstrate how to use the formulae we have derived above, an X-band rectangular waveguide (22.86×10.16mm) was chosen to form the cavity resonator which comprises two parts. One part is a piece of standard rectangular waveguide and the other part is a moveable short-circuit for waveguide that is a standard microwave component. The two parts are joined together by coupling rings to enclose the cavity. The microwave energy is coupled into the cavity through a coupling iris which is a hole of 6 mm in diameter on a brass plate. The equivalent circuit of the coupling iris is a shunt inductance whose values are obtained here through a rigorous electromagnetic simulation using HP HFSS™ as described in the previous section and is used in solving the transcendental equations to find the permittivity of the dielectric film materials.

Although the previously presented formulae are quite general in application for any  $TE_{10m}$  resonant mode ( $m$  is the number of half guide wavelengths in the cavity resonator at resonance), in order to determine the exact mode for a resonant frequency, the resonant frequencies in the empty cavity without sample are usually calculated first before measurement. The resonant frequency for  $TE_{10m}$  is

$$f_{10m} = \frac{c}{2} \left\{ \left( \frac{1}{a} \right)^2 + \left( \frac{m}{d} \right)^2 \right\}^{1/2} \quad (7-32)$$

in which  $c$  is the velocity of light,  $a$  is cross-dimension of the waveguide and  $d$  is the total length of the cavity. Equation (7-32) seems to indicate that, just by increasing  $m$ , a very wide frequency range can be covered by a given cavity length with a certain cross-section size. However, once the resonant frequency  $f_{10m}$  extends upward to a value which is out of the



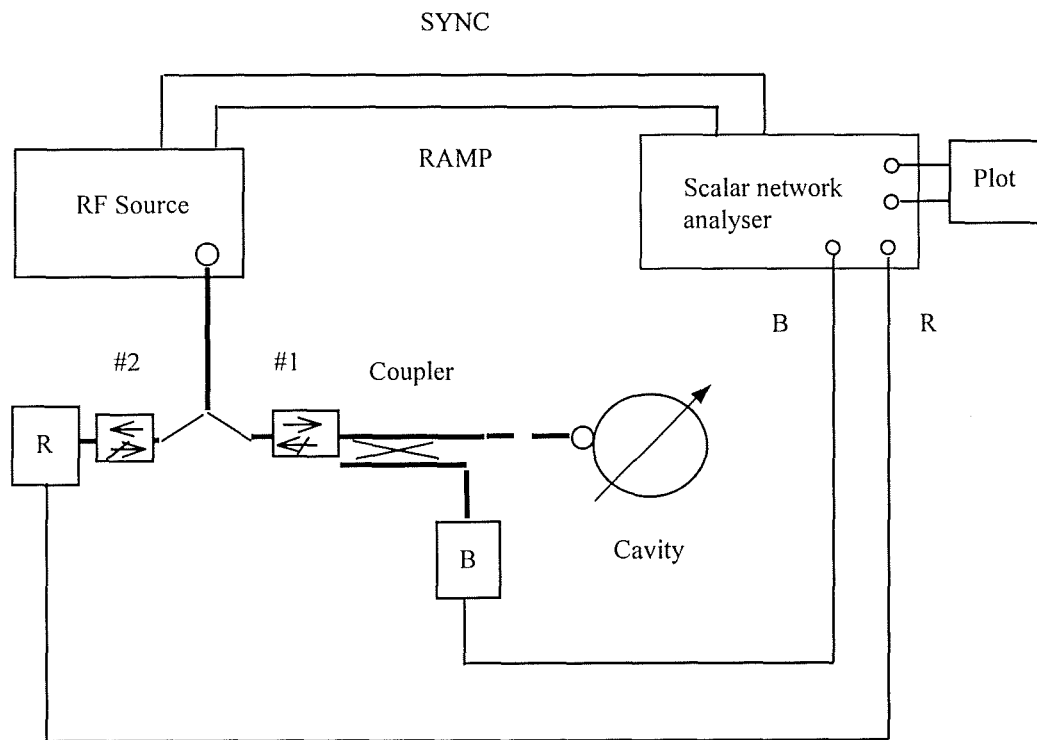
frequency band for which the waveguide cross-section applies, the higher order modes will be excited which invalidate the present theory. Caution has to be taken in determining the valid frequency range for a specific waveguide.

Using equations (7-32), (7-13) and (7-24), an estimated optimum sample position,  $h_0$ , can be found. By adjusting the sample position around  $h_0$  so that the difference in resonant frequency between the cavity loaded with a blank substrate and that loaded with the two-layer sample is maximum, the optimum position for sample loading can be found for final measurement. In finding the optimum position for sample loading, the blank substrate and the two-layer sample should always be loaded at exactly the same distance away from the short-circuit end of the cavity. To load the sample accurately, firstly, the plunger should be screwed so as to move the short-circuit to the pre-determined sample position and the sample placed against the short-circuit; secondly the two pieces of waveguide are joined together and the cavity is connected to a microwave network analyser. Finally, the short-circuit is moved away from the sample to leave a gap between the sample and the short-circuit.

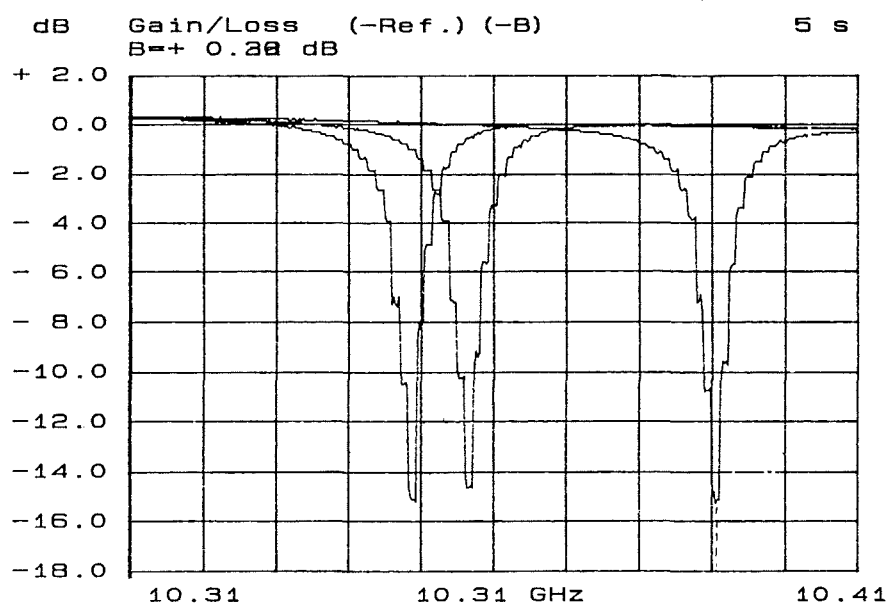
In order to prepare two-layer samples, the dielectric films are printed and then fired on a 99.5% lapped alumina substrate with the thickness of 0.635 mm. The film thickness after firing is about 140 $\mu$ m. The samples measured were provided by Heraeus Inc. for this project. Compared with a circular waveguide, the rectangular waveguide allows a easier sample preparation because the sample can be cut to shape using a ceramic cutting wafer saw. After cutting, the samples are ground to size on their edges to have a friction fit with the waveguide walls. This friction fit is important because it will not only eliminate the error from the sample size (the width is more critical than the length due to the field distribution of the dominant mode), but also ensure that the sample will stay at the optimised position after the removal of the short-circuit.

A scalar network analyser has been used to measure the resonant frequency of the cavity resonator. Since one end of the cavity is terminated by a short-circuit, for this one port device, we only need to measure the return loss of the cavity. The reflected signal is

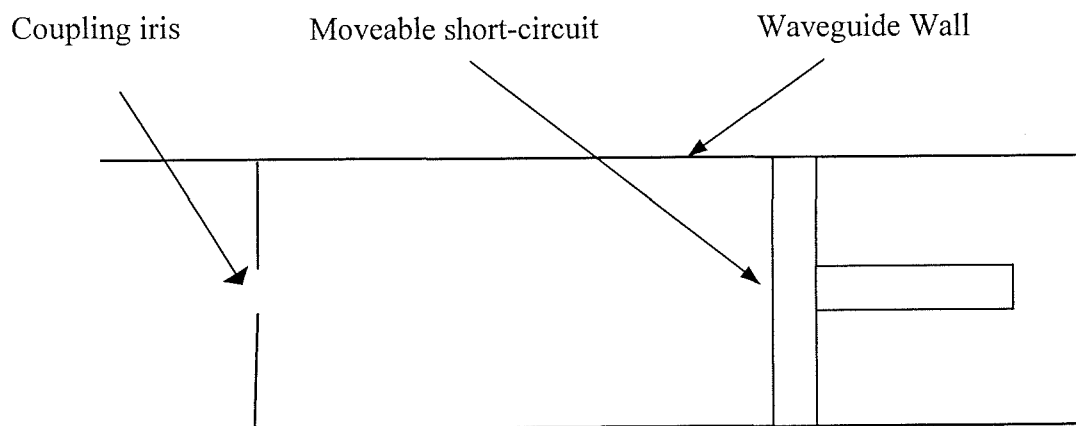
displayed in frequency-domain and at resonant frequency the reflected signal will have a dip. The basic setup of the test system is shown in figure 7.12 (a) in which the power splitter is connected to the RF signal source with the reference channel (R) detector connected to one arm of the splitter and a high directivity coupler connected to the other arm. The directional coupler allow the reflected power from the device under test to be sampled. (In our situation the device under test is a cavity resonator). The use of a reference channel allows any variation in the output from the RF source to be taken into account in the display of the reflected signal. The function of the isolator #1 is to prevent frequency pulling of the source by the reactive input impedance of the cavity. In addition, both suppressing isolators have the effect of suppressing multiple reflections in the measurement system. The measurement method is to first perform a calibration for return loss measurement. The average value of



(a) Scalar network analyser



(b) Resonant curves



(c) Resonant cavity and moveable short-circuit

Figure 7.12 Arrangement of scalar network analyser for return loss measurement of cavity resonator (a), typical resonant curves (b) and resonant cavity with moveable short-circuit (c).

reflections from an open circuit and a short-circuit over the frequency range of interest is stored in memory B of scalar network analyser. When the cavity is connected to the test port the resultant return loss is displayed by subtracting memory B and subtracting the variation from RF signal source from reference channel. The frequency stability of the RF signal source is important. An X-band Marconi 6158A (8-12.4 GHz) signal source was used in our measurement. Using a frequency meter we checked its stability which has a variation within  $\pm 0.2$  MHz. Compared with the frequency shift caused by the dielectric film, which is usually between 40 and 100 MHz, the error introduced by this variation is virtually negligible. Figure 7.12 (b) shows the typical spectrum recorded from the test system. In the spectrum three resonant curves corresponding to blank alumina substrate and two-layer specimens are displayed. The resonant frequencies can be accurately read from the spectrum. The diagram of resonant cavity and moveable short-circuit is shown in figure 7.12 (c).

After the measurement of the all of the physical dimensions of the cavity and samples, and of the resonant frequencies for cavities loaded with blank substrate and two-layer sample, the final task is to solve the transcendental equations (7-15) and (7-20) to find the permittivity of the dielectric film. From equation (7-15) the permittivity of the substrate can be found and that value will then be put into equation (7-20) to calculate the permittivity of dielectric film. There are many mathematical methods for solving a transcendental equation. Here a "searching in a region" method was used because it is easy to design a computer programme using this method. The basic principle of the method is first to change the transcendental equation to be solved into the form

$$f(x) = 0$$

If we plot a curve for  $f(x)$  versus  $x$  as shown in figure 7.13, the crossing point between the curve and X-axis, at  $x_0$ , will be the solution of the transcendental equation. In order to find this crossing point, a searching region  $(x_1, x_2)$  has to be given first. The computer calculates the values of  $f(x_1)$  and  $f(x_2)$  and then compare the signs of them. If  $f(x_1)$  and  $f(x_2)$  have the same sign, that indicates that there is no solution between  $x_1$  and  $x_2$ . In this case another

searching region has to be defined. On the contrary if  $f(x_1)$  and  $f(x_2)$  have opposite signs, the solution must be somewhere between  $x_1$  and  $x_2$ . Then the middle point  $x_3$  between  $x_1$  and  $x_2$  will be picked up. If  $f(x_3)$  has the same sign as  $f(x_1)$ , the solution will not be in the region between  $x_1$  and  $x_3$ . That will eliminate the searching region in  $(x_1, x_3)$  and the solution must be in the region between  $x_3$  and  $x_2$ . If  $f(x_3)$  has the opposite sign to  $f(x_1)$ , then the searching can be concentrated in  $(x_1, x_3)$ . Using this principle for solution searching, the solution can be finally found at a given accuracy which is defined by the user. Normally if the searching region is less than  $10^{-5}$  or if  $f(x)$  is less than  $10^{-6}$ , we can assume that the accuracy is acceptable. Sometimes if the slope for the function  $f(x)$  around solution point is very large, i.e. if the rate of change of the function  $f(x)$  at the solution point is very great, caution has to be taken in setting the initial searching region. Ideally the searching region should include the solution in it and, at the same time be as narrow as possible.

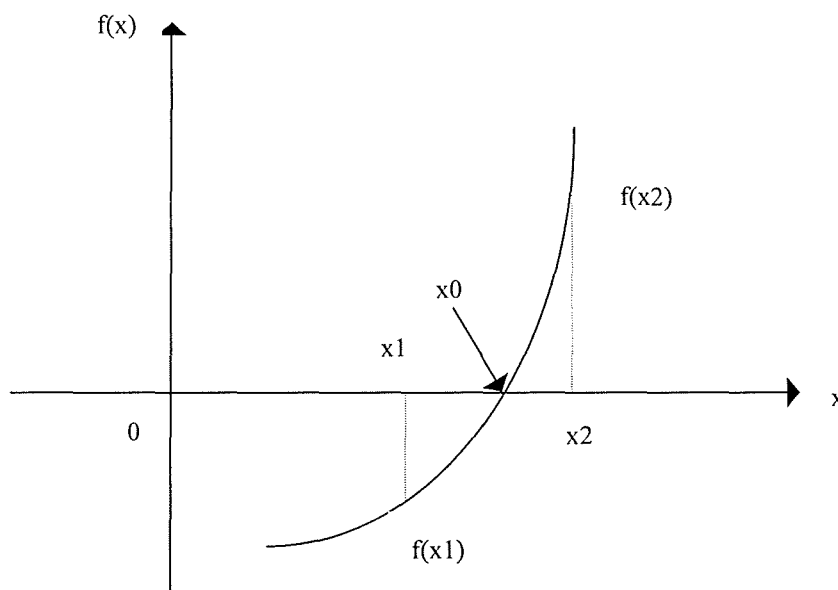


Figure 7.13 Diagram showing the principle of finding a solution for the equation  $f(x) = 0$ .

This can be realised by approaching from one side of the solution point. In a FORTRAN programme for this purpose, a sentence can be added for printing out the function values in a specified region. Then the searching region can be defined as narrowly as desired which will

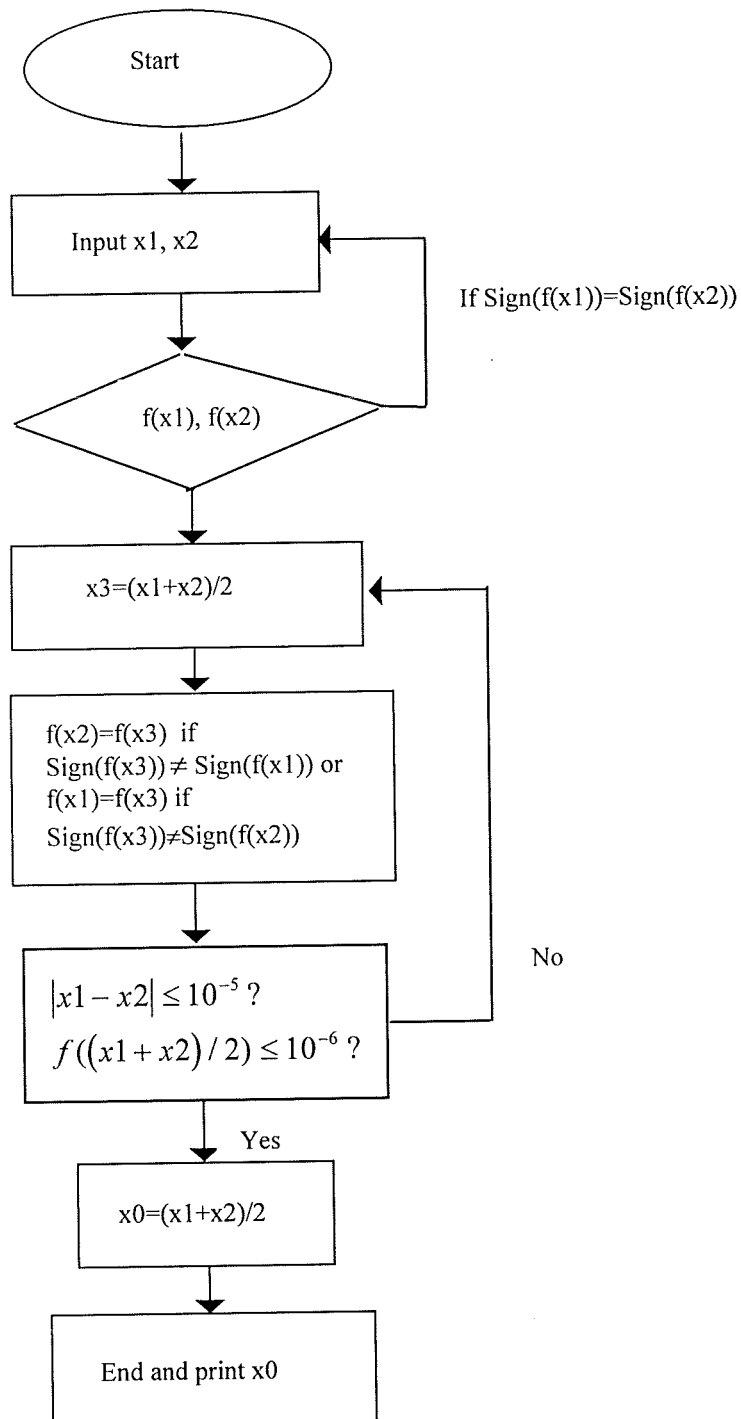


Figure 7.14 Flow chart for the process of solving the transcendental equation.

allow the transcendental equation to be accurately solved. A flow chart for the process of solving the transcendental equation is shown in figure 7.14.

Shown in Table 7.2 is the cavity set-ups and the measured resonant frequencies for cavities loaded either with two-layer sample (for KQ-type 1) or with blank substrate. The sample positions have been optimised to give maximum frequency shift due to the dielectric film. The resonant modes were determined from a simple calculation and presented here to make a clear picture. In fact, for the purpose of permittivity calculation using equations (7-15) and (7-20), we do not need to know the exact resonant mode. We only need to make sure that the resonance is not built up from higher order modes, such as  $TE_{201}$  and  $TE_{312}$  etc.

Table 7.2 Cavity set-up and measured resonant frequencies for cavities loaded either with two-layer sample ( for KQ-type 1) or with alumina substrate only.

Resonant frequency for cavity loaded with two-layer sample (GHz)	Resonant frequency for cavity loaded with substrate (GHz)	Cavity length (mm)	Sample position from cavity end (mm)	Resonant mode
8.2085	8.2506	47.5	7	$TE_{103}$
9.0254	9.0754	37.95	6.5	$TE_{102}$
10.3495	10.3909	47.95	5	$TE_{103}$
11.9818	12.0334	37.95	4	$TE_{103}$

Table 7.3 shows relative permittivity values for KQ-type 1 and KQ-type 2 dielectric films. The results are quite consistent and almost frequency independent which is important for microwave applications. The relative permittivity values obtained here are also in the range expected for this kind of film material produced using boro-silicate technology [5]. It should be noted that in the frequency range for our measurement, many more data points

Table 7.3 Measured permittivity values for KQ-type 1 and KQ-type 2 dielectric films

Frequency (GHz)	KQ-type1	KQ-type2
8.21	3.88	3.91
8.41	3.91	3.90
8.72	3.88	3.94
9.02	3.90	3.95
9.26	3.90	3.94
9.65	3.90	3.93
10.35	3.88	3.91
10.75	3.92	3.96
11.35	3.89	3.92
11.98	3.94	3.95

can be obtained by just continuously changing the length of the cavity resonator using the moveable short-circuit. The cavity length can be measured to the accuracy of better than  $2\mu\text{m}$ . Compared with the total waveguide length, this accuracy is good enough and the resulting error is negligible. On the other hand, because what is significant is the difference in resonant frequencies between the resonant cavity loaded with blank substrate and that loaded with two-layer specimen, this will dramatically reduce the errors in dielectric measurement caused by the signal source, directional coupler and other components in the external circuit. To improve the measurement, the sample should be made as flat as possible. If the dielectric film is relatively thin, a high quality substrate is recommended. This will reduce the uncertainty in the geometrical sizes of the samples. In addition the microwave signal source should be extremely stable to avoid error introduced by unwanted shift of the resonant frequency. The film thickness used here was of the order of  $140\mu\text{m}$ , however, if this is halved to  $70\mu\text{m}$ , this method still allows the permittivity to be accurately measured. The minimum thickness for the dielectric film materials of KQ series, where an accurate measurement for permittivity values can be carried out, is about  $20\mu\text{m}$ . If the dielectric film is quite thin, a cavity resonator with a shorter length will be desirable and, for the resonant mode,  $\text{TE}_{10m}$ ,  $m$  should be less than 3. This will increase the shift of resonant frequency due to the dielectric film. The examples presented here are in the X-band frequency range (8-12GHz). However the measurement can



be carried out at much higher frequency ranges such as 30-40 GHz by using a waveguide of smaller cross-sectional dimension.

## **7.4 Cavity perturbation method for the characterisation of dielectric film materials**

### **7.4.1 Introduction**

It can be seen from the last section that the cavity measurement techniques are based on rigorous solutions of the electromagnetic environment of the cavity. Although the change in resonant frequency due to the insertion of dielectric materials into a cavity can enable us to measure the permittivity value of the dielectric material, the loss tangent or imaginary part of permittivity can only be measured from accurate measurement of the Q-factor of the cavity. The theory presented in the previous section allows us to measure the permittivity of both single layer and double layer dielectric samples with arbitrary thickness. To measure the loss tangent of the dielectric material, we need to take all sources of losses into account and establish a link between the loss tangent of the dielectric material and the measured Q-factor. For a single layer sample with a specific loading position, the theory for this link already exists [1]. However, for a two-layer sample and a one-layer sample at an arbitrary position, this link does not exist. In this section we will adopt the cavity perturbation principle [1,11] for the loss tangent measurement of a dielectric film supported by a dielectric substrate. This new method can also be used for a one-layer sample at an arbitrary position in the cavity. Permittivity values can also be obtained with this method. As the name “perturbation” implies, the cavity with and without a test sample must be very much alike. To ensure this, the sample must be small compared with the cavity itself so that the difference in resonant frequency between empty cavity and sample loaded cavity is also very small. The advantage of the cavity perturbation method is its accuracy and simplicity. It avoids the necessity to account for many of the details of the cavity, since these are the same for the cavity with and without sample, and therefore the effects due to them are cancelled out. Perturbation

techniques are also quite flexible, which allows the measurement of dielectric samples with various shapes, such as discs, spheres and rods etc.

#### 7.4.2 Quality factors: basic relationships and measurement

Typical resonant structures at microwave frequencies are resonant transmission lines and cavities with conductive walls. Dielectric materials can be encased by the conductive walls creating a change to the resonant structures, which can be employed for the measurement of the properties of dielectric materials. The measurement of relative permittivity and loss tangent of the dielectric samples by means of a cavity technique generally takes the form of frequency and Q factor measurements. Before we proceed further, it is necessary to clarify the concept of Q factor and to give some basic relations relevant to it and its measurement. Q-factor or Quality factor is a basic parameter used to characterise the extent of losses in a circuit at resonance. It describes how sharply the cavity or a resonant circuit resonates. The Q-factor of any circuit at resonance is defined as

$$Q = 2\pi \frac{\text{Total energy stored}}{\text{Energy dissipated per cycle}} = \omega_r \frac{\text{Total energy stored}}{\text{Average power loss}} \quad (7-33)$$

Here,  $\frac{\omega_r}{2\pi}$  is the resonant frequency of the cavity, and “Total stored energy” is referred as total energy stored in the cavity, i.e., the sum of instantaneous electric and magnetic energies. Because at a certain instant in a cycle the energy resides entirely in the electric field and a quarter cycle later entirely in the magnetic field, the “Total energy stored” also equals the maximum electric or magnetic energy stored in the cavity.

Practical cavities must have means of coupling power into them and sometimes also means of coupling power out. If we look at the sources of energy dissipation in a practical situation, we may find that in addition to the energy losses inside the cavity, which are from the metal

walls and the medium filling it, there also exist losses of stored energy through the cavity coupling (iris or loop) from input and output circuits, known as external losses. It follows naturally that there are three type of Q-factors

$$Q_U = 2\pi \frac{\text{Energy stored}}{\text{Energy lost per cycle in the resonant cavity}} \quad (7-34)$$

$$Q_E = 2\pi \frac{\text{Energy stored}}{\text{Energy lost per cycle into the input and output circuits}} \quad (7-35)$$

$$Q_L = 2\pi \frac{\text{Energy stored}}{\text{Total energy lost per cycle to the circuit}} \quad (7-36)$$

where  $Q_U$ ,  $Q_E$  and  $Q_L$  are defined as unloaded Q, external Q and loaded Q respectively. For  $Q_U$ , only the loss in the cavity is taken into account; for  $Q_E$ , only the loss through the coupling; for  $Q_L$ , the loss in the cavity as well as that through the cavity coupling. From the relationship,

$$\text{Total energy lost per cycle to the circuit} = \text{Energy lost per cycle in the resonant cavity} + \text{Energy lost per cycle into the input and output circuit}$$

these three Q factors must be related by:

$$\frac{1}{Q_L} = \frac{1}{Q_U} + \frac{1}{Q_E} \quad (7-37)$$

In a real test system the loaded Q factor,  $Q_L$ , is usually directly measured. The other Q factors can be calculated through relationship which can be derived. Since many formulae involving various Q factors simply assume that the energy leaking out through the coupling

mechanism enters a matched transmission line, it is usually wise to provide conditions closely corresponding to a match in situations where such formulae may need to be used.

The accurate measurement of Q factors for a cavity resonator is vital if the cavity is to be used for the purpose of loss tangent measurement of dielectric materials. If the cavity is a two-port structure, it is customary to measure the resonant frequency,  $f_0$ , and bandwidth,  $\Delta f$ , between half power (or 3dB) points of the transmission characteristic. Then the loaded Q value would be

$$Q_L = \frac{f_0}{\Delta f} \quad (7-38)$$

from which the unloaded Q can be determined with the aid of additional data. For a single ended cavity, which is the set-up used in our test, the Q factor has to be measured by reflected power. Figure 7.15 is the diagram of the test system used for Q factor measurement. RF signal is generated from Hewlett Packard 8673M synthesised signal

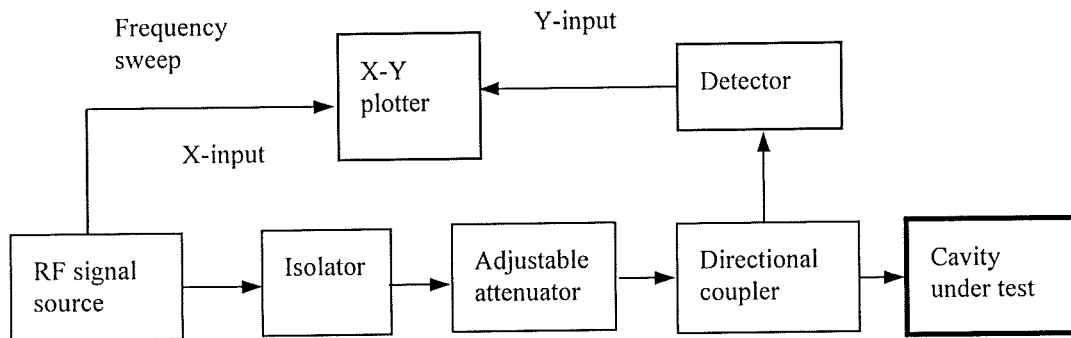
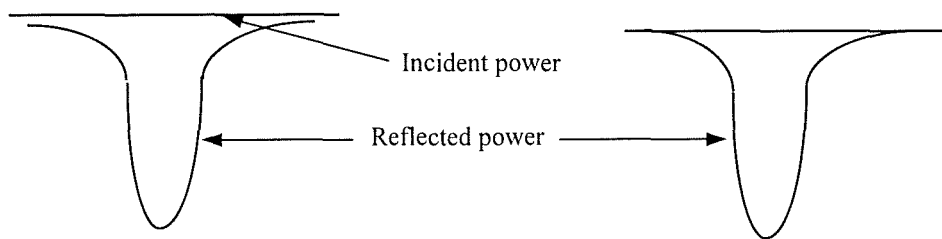


Figure 7.15 Block diagram for Q factor measurement of single-ended cavity.

generator operating in the range 2.0-18.0 GHz. This provides a stable power output. The frequency stability of the RF generator is also excellent. The reason for our concern over the

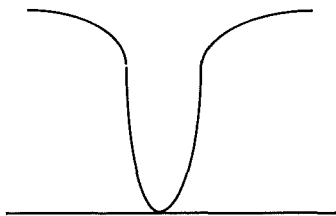
output power and frequency stability is because they are so vital in an accurate Q factor measurement. The procedure of measuring loaded Q factor using the set-up in figure 7.15 is illustrated in figure 7.16 and given as follows

1. Plot the reflected power trace with the cavity under test connected to the test system.
2. Replace the cavity by a short-circuit plate to plot the incident power trace then adjust the calibrated attenuator to lower the incident power trace so as to touch the shoulder of the reflected power trace ( shown in figure 7.16b). Record  $\Gamma_1$  , the reflection coefficient off resonance, in dB.
3. Adjust the attenuator to let the incident power trace touch the bottom of the reflected power trace and record  $\Gamma_0$  , the reflection coefficient at resonance, in dB (shown in figure 7.16c).

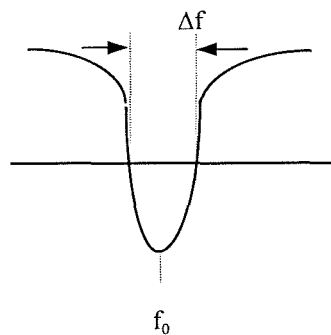


(a) Incident and reflected power traces

(b) Incident power trace lowered for the determination of reflection coefficient off resonance



(c) Incident power trace lowered for determination of reflection coefficient at resonance



(d) Incident power trace for bandwidth measurement

Figure 7.16 Reflected power traces and the method to measure the necessary parameters for the determination of loaded Q factor,  $Q_L$

4. Set attenuator at a value,  $\Gamma_2$ , where the incident power trace can intersect the reflected power trace or resonant curve like that in figure 7.16(d).
5. Manually sweep the incident power trace and record  $\Delta f$  when the incident power trace intersects the reflected power trace. The resonant frequency,  $f_o$ , can also be recorded at the same time (shown in figure 7.16d).

After the measurement the loaded Q factor can be calculated from the following formula

[1]

$$Q_L = \alpha \left( \frac{f_o}{\Delta f} \right) \quad (7-39)$$

where

$$\alpha = \left( \frac{\left| \text{anti log}(\Gamma_2/10) \right|^2 - \left| \text{anti log}(\Gamma_0/10) \right|^2}{\left| \text{anti log}(\Gamma_1/10) \right|^2 - \left| \text{anti log}(\Gamma_2/10) \right|^2} \right)^{\frac{1}{2}} \quad (7-40)$$

For the current study, we are only interested in the loaded Q factor. The unloaded Q factor can also be calculated using the formulae given in reference [1].

### 7.4.3 General principles of the cavity perturbation method

In a dissipative cavity system at resonance the angular frequency  $\omega$  can be expressed in complex form [1]

$$\omega = \omega_R + j\omega_i \quad (7-41)$$

where the real part,  $\omega_R$ , is related to the real resonant frequency  $f_r$  by

$$\omega_R = 2\pi f_r \quad (7-42)$$

From electromagnetic theory we know that the field quantities are dependent on  $e^{j\omega t}$ , and energy involves the square of field quantities, therefore  $e^{2j\omega t}$  will be associated with energy. Because  $e^{2j\omega t} = e^{2j\omega_R t} e^{-2\omega_i t}$ , we can see that energy decreases as  $e^{-2\omega_i t}$ . Therefore,  $\omega_i$  reflects the losses of an electromagnetic system. If we assume that  $U_T$  is the total energy stored in the cavity, then the energy dissipated in a short interval  $\Delta t$  would be

$$U_T - U_T e^{-2\omega_i \Delta t} \approx U_T - U_T (1 - 2\omega_i \Delta t) = 2\omega_i \Delta t U_T \quad (7-43)$$

Hence the average power loss is  $2\omega_i U_T$ . In the cavity system considered here, all losses, including leakage through the coupling mechanism, are included. Therefore the loaded  $Q$  factor,  $Q_L$ , can be written as

$$Q_L = \frac{\omega_R U_T}{2\omega_i U_T} = \frac{\omega_R}{2\omega_i} \quad (7-44)$$

Consider the following expression after a minute change ( or perturbation ) of the resonant cavity ( due to the insertion of the sample or size change of the cavity )

$$\frac{\delta\omega}{\omega} = \frac{\omega_2 - \omega_1}{\omega_2} \quad (7-45)$$

where  $\omega_1$  and  $\omega_2$  are complex,  $\omega_{R1} \cong \omega_{R2}$  and  $\omega_i \ll \omega_R$ . On expanding  $\delta\omega/\omega$  and employing the indicated approximations, we have

$$\frac{\delta\omega}{\omega} = \frac{(\omega_{R2} - \omega_{R1}) + j(\omega_{i2} - \omega_{i1})}{\omega_{R2} \left(1 + j \frac{\omega_{i2}}{\omega_{R2}}\right)} \cong \left[ \left( \frac{f_{r2} - f_{r1}}{f_{r2}} \right) + j \left( \frac{1}{2Q_{L2}} - \frac{1}{2Q_{L1}} \right) \right] \left[ 1 - j \frac{1}{2Q_{L2}} \right]$$

(7-46)

Here  $f_{r2}$  and  $f_{r1}$  are resonant frequencies of the cavities before and after the minute change.

Since  $1/(2Q_{L2})$  can be neglected compared with unity, it follows

$$\frac{\delta\omega}{\omega} \cong \frac{f_{r2} - f_{r1}}{f_{r2}} + \frac{j}{2} \left( \frac{1}{Q_{L2}} - \frac{1}{Q_{L1}} \right) \quad (7-47)$$

Equation (7-47) provides a link between the measured quantities ( $f_r$  and  $Q_L$ , the resonant frequency and loaded quality factor) and the theoretical expression  $\delta\omega/\omega$ .

In order to establish further the link between the measured quantities and the permittivity properties of the dielectric materials under test, we must approach the problem from electromagnetic theory. If we define the initial cavity as cavity 1 and the cavity after the perturbation as cavity 2, then both cavities are almost alike. The only difference is assumed to be in the dielectric constant (or the magnetic permeability) of the material the cavities contain. The cavity walls are assumed to be lossless; then Maxwell's equations for the two cavities are

$$\nabla \times \mathbf{E}_i = -j\omega_i \mu_i \mathbf{H}_i \quad (7-48a)$$

$$\nabla \times \mathbf{H}_i = j\omega_i \varepsilon_i \mathbf{E}_i \quad (7-48b)$$

$$i = 1, 2$$

where the subscripts 1 and 2 denote cavity 1 and 2 respectively. The angular frequency  $\omega_i$  is complex and all the losses, including those through coupling mechanism, are reflected in it. By taking suitable dot products with the four equations in (7-48), subtracting and integrating over the cavity volume,  $\Psi_C$ , one obtains



$$\begin{aligned}
& \int_{\Psi_c} \left\{ \left[ \mathbf{E}_2 \cdot (\nabla \times \mathbf{H}_1) - \mathbf{E}_1 \cdot (\nabla \times \mathbf{H}_2) \right] + \left[ \mathbf{H}_2 \cdot (\nabla \times \mathbf{E}_1) - \mathbf{H}_1 \cdot (\nabla \times \mathbf{E}_2) \right] \right\} d\Psi \\
& = j \int_{\Psi_c} \left[ (\omega_1 \varepsilon_1 - \omega_2 \varepsilon_2) \mathbf{E}_1 \cdot \mathbf{E}_2 - (\omega_1 \mu_1 - \omega_2 \mu_2) \mathbf{H}_1 \cdot \mathbf{H}_2 \right] d\Psi \quad (7-49)
\end{aligned}$$

The left-hand side can be rearranged to the form of

$$\int_{\Psi_c} \nabla \cdot (\mathbf{H}_1 \times \mathbf{E}_2) d\Psi - \int_{\Psi_c} \nabla \cdot (\mathbf{H}_2 \times \mathbf{E}_1) d\Psi \quad (7-50)$$

Using divergence or Gauss's theorem, equation (7-50) can be rewritten as

$$\int_{S_c} (\mathbf{H}_1 \times \mathbf{E}_2) d\mathbf{S} - \int_{S_c} (\mathbf{H}_2 \times \mathbf{E}_1) d\mathbf{S} \quad (7-51)$$

Here  $\int_{S_c}$  means the integration is carried out on the inner surface of the cavity,  $S_c$ . Since the cavity walls are assumed to be perfectly conducting,  $\mathbf{E}_1$  and  $\mathbf{E}_2$  have only components normal to the cavity surface. It follows that  $(\mathbf{H}_1 \times \mathbf{E}_2)$  and  $(\mathbf{H}_2 \times \mathbf{E}_1)$  have no components normal to the cavity surface. Expression (7-51) therefore equals to zero. Equation (7-49) can then be changed to the form of

$$\omega_1 \int_{\Psi_c} (\varepsilon_1 \mathbf{E}_1 \cdot \mathbf{E}_2 - \mu_1 \mathbf{H}_1 \cdot \mathbf{H}_2) d\Psi = \omega_2 \int_{\Psi_c} (\varepsilon_2 \mathbf{E}_1 \cdot \mathbf{E}_2 - \mu_2 \mathbf{H}_1 \cdot \mathbf{H}_2) d\Psi \quad (7-52)$$

When each side of equation (7-52) is subtracted from the integral

$\omega_2 \int_{\Psi_c} (\varepsilon_1 \mathbf{E}_1 \cdot \mathbf{E}_2 - \mu_1 \mathbf{H}_1 \cdot \mathbf{H}_2) d\Psi$  and after the rearrangement, one has

$$\frac{\omega_2 - \omega_1}{\omega_2} = \frac{\int_{\Psi_c} [(\mu_2 - \mu_1) \mathbf{H}_1 \cdot \mathbf{H}_2 - (\varepsilon_2 - \varepsilon_1) \mathbf{E}_1 \cdot \mathbf{E}_2] d\Psi}{\int_{\Psi_c} (\varepsilon_1 \mathbf{E}_1 \cdot \mathbf{E}_2 - \mu_1 \mathbf{H}_1 \cdot \mathbf{H}_2) d\Psi} \quad (7-53)$$

Equation (7-53) is the basic cavity perturbation formula from which further derivations can be made to suit the specific cavity and sample shapes. If the samples are assumed to be nonmagnetic we have  $\mu_2 = \mu_1$  and the first term in the numerator can be removed. In the denominator, if  $\mathbf{E}$  is taken as real,  $\mathbf{H}$  is imaginary, then  $\mathbf{H} \cdot \mathbf{H} = -|\mathbf{H}|^2$ . Since the sample considered here is small and can consequently be assumed to change the field in the cavity as a whole only slightly, only a small error is introduced by assuming  $\mathbf{E}_2 = \mathbf{E}_1$  and  $\mathbf{H}_2 = \mathbf{H}_1$  in the integrals in the denominator. The two terms in the denominator can be added to equal 2 times the total energy stored in the cavity. Equation (7-53) can be reduced to

$$\frac{\omega_2 - \omega_1}{\omega_2} = -\frac{1}{2} \frac{\int_{\Psi_s} (\varepsilon_2 - \varepsilon_1) \mathbf{E}_1 \cdot \mathbf{E}_2 d\Psi}{\int_{\Psi_c} \varepsilon_1 |\mathbf{E}_1|^2 d\Psi} \quad (7-54)$$

In equation (7-54)  $\int_{\Psi_s}$  means the integration is only carried out in the sample region,  $\Psi_s$ . In the other region of  $\Psi_c - \Psi_s$ , because  $\varepsilon_2 - \varepsilon_1 \equiv 0$ , the integration is also zero. Here  $\varepsilon_2$  and  $\varepsilon_1$  are complex. Combining equations (7-54) and (7-47), we have

$$2\left(\frac{f_{r1} - f_{r2}}{f_{r2}}\right) + j\left(\frac{1}{Q_{L1}} - \frac{1}{Q_{L2}}\right) = \frac{\int_{\Psi_s} (\varepsilon_2 - \varepsilon_1) \mathbf{E}_1 \cdot \mathbf{E}_2 d\Psi}{\int_{\Psi_c} \varepsilon_1 |\mathbf{E}_1|^2 d\Psi} \quad (7-55)$$

where  $(\varepsilon_2 - \varepsilon_1)$  are the complex permittivity differences in the area  $\Psi_s$  between sample loaded cavity 2 and cavity 1.  $\varepsilon_1$  is the complex permittivity for the medium in cavity 1.  $\varepsilon_2$  is the complex permittivity for sample under test in cavity 2 and can be expressed as

$$\varepsilon_2 = \varepsilon_0 \varepsilon_{r2} = \varepsilon_0 (\varepsilon'_2 - j\varepsilon''_2) \quad (7-56a)$$

where  $\epsilon_{r2}$  is complex relative permittivity of the sample under test and  $\epsilon'_2$ ,  $\epsilon''_2$  are relative permittivity and loss factor respectively. The loss tangent of the sample under test is

$$\tan \delta = \frac{\epsilon''_2}{\epsilon'_2} \quad (7-56b)$$

Equation (7-55) is basic cavity perturbation formula from which further derivations can be made to suit the specific cavity and sample shapes. That will be carried out in the following sections.

#### **7.4.4 Application of the perturbation method in rectangular-shaped resonant cavity loaded with a two-layer specimen**

Now we want to use this general perturbation method to carry out the measurement of dielectric film materials. The cross-section of the cavity is chosen as rectangular because it will allow easy sample preparation. Since the dielectric films, printed or deposited, can only exist on a supportive substrate, they can not be inserted into a cavity without the support of the substrate. We therefore define the blank substrate loaded cavity as cavity 1, and the two-layer sample loaded cavity as cavity 2, which are shown in figure 7.17. The former is a reference cavity which will be used to calculate the field pattern and stored energy in it. The difference in resonant frequency and Q factor between the two cavities are assumed to be caused by the dielectric film, and this difference will be used to calculate the relative permittivity and loss tangent of the dielectric film material.

In electromagnetic theory we know that the following boundary condition is always satisfied

$$\mathbf{n} \times (\mathbf{E}_2 - \mathbf{E}_1) = 0 \quad (7-57a)$$

or

$$\mathbf{E}_{1t} = \mathbf{E}_{2t} \quad (7-57b)$$

where  $\mathbf{E}_1, \mathbf{E}_2$  are electric-field intensity in two mediums respectively at an interface between them.  $\mathbf{n}$  is a unit vector normal to the interface between the two mediums. The subscript  $t$  represents the direction tangential to the interface. If we apply this boundary condition to the interface between air and dielectric film in cavity 2, we can find that for the dominant mode, the electric-field intensities on both sides of the air-film interface are equal. The numerator on the right-hand side of the equation (7-55) can therefore be written as  $\int_{\Psi_s} |\mathbf{E}_1|^2 d\Psi$ . Then

equation (7-55) can be changed to

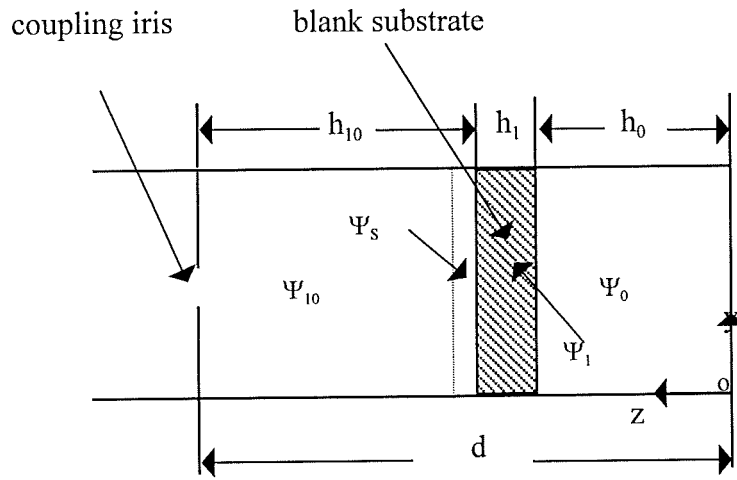
$$2\left(\frac{f_{r1} - f_{r2}}{f_{r2}}\right) + j\left(\frac{1}{Q_{L1}} - \frac{1}{Q_{L2}}\right) = (\varepsilon_{r2} - 1) \frac{\int_{\Psi_s} |\mathbf{E}_1|^2 d\Psi}{\int_{\Psi_c} \varepsilon_{r1} |\mathbf{E}_1|^2 d\Psi} \quad (7-58)$$

where

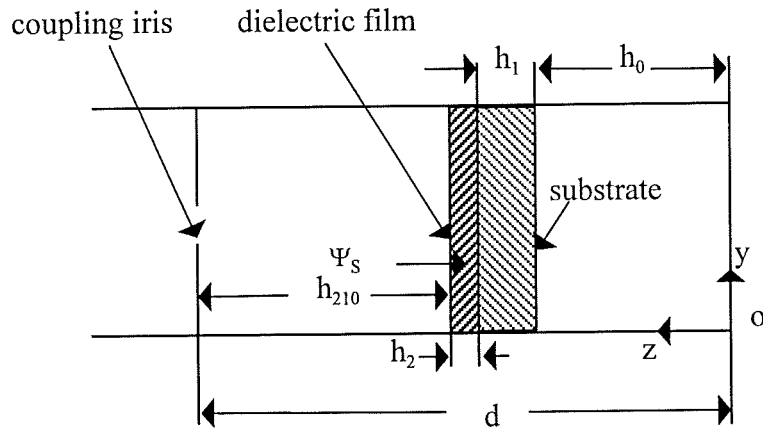
$$\varepsilon_{r1} = \begin{cases} \varepsilon_1' & \text{in substrate area} \\ 1 & \text{in air region} \end{cases} \quad (7-59)$$

$\varepsilon_{r1}$  is the relative permittivity of the medium filling the cavity 1. It has two values: in air region its value is 1 and in the substrate area its value equals  $\varepsilon_1'$  of the substrate relative permittivity. Because the cavity 1 is mainly filled with air, if the substrate is low loss material, the effect of the loss factor of the substrate on the whole cavity can be neglected. Therefore  $\varepsilon_{r1}$  can be treated as real value. To simplify equation (7-58), we assume

$$E_{\Psi_c} = \int_{\Psi_c} \epsilon_{r1} |\mathbf{E}_1|^2 dV = E_{\Psi_0} + E_{\Psi_1} + E_{\Psi_{10}} \quad (7-60)$$



(a) cavity 1



(b) cavity 2

Figure 7.17 Physical structure and co-ordinate system for (a) reference cavity 1 and (b) sample loaded cavity 2. The cross-section of the cavities are rectangular.

Where

$$E_{\Psi_0} = \int_{\Psi_0} |\mathbf{E}_1|^2 d\Psi \quad (7-61)$$

$$E_{\Psi_1} = \int_{\Psi_1} \epsilon_1' |\mathbf{E}_1|^2 d\Psi \quad (7-62)$$

$$E_{\Psi_{10}} = \int_{\Psi_{10}} |\mathbf{E}_1|^2 d\Psi \quad (7-63)$$

with

$$\Psi_C = \Psi_0 + \Psi_1 + \Psi_{10} \quad (7-64)$$

If the right hand side of (7-60-7-63) is multiplied by  $\epsilon_0$ , the permittivity of air, then each expression will represent energy stored in the respective regions. As indicated in figure 7.17(a),  $\Psi_0, \Psi_{10}$  are the air regions in cavity 1 and  $\Psi_1$  is the substrate area in cavity 1.  $\Psi_C$  therefore is the total area enclosed in cavity 1. In equation (7-62)  $\epsilon_1'$  is the relative permittivity of the blank substrate. If we further assume

$$E_S = \int_{\Psi_S} |\mathbf{E}_1|^2 d\Psi \quad (7-65)$$

and

$$\Gamma = \frac{E_S}{E_{\Psi_C}} = \frac{E_S}{E_{\Psi_0} + E_{\Psi_1} + E_{\Psi_{10}}} \quad (7-66)$$

then the complex relative permittivity and loss tangent of the dielectric film can be expressed as

$$\varepsilon_{r2} = \frac{2}{\Gamma} \left( \frac{f_{r1} - f_{r2}}{f_{r2}} \right) + 1 - j \frac{1}{\Gamma} \left( \frac{1}{Q_{L2}} - \frac{1}{Q_{L1}} \right) \quad (7-67)$$

$$\tan \delta = \frac{\frac{1}{\Gamma} \left( \frac{1}{Q_{L2}} - \frac{1}{Q_{L1}} \right)}{\frac{2}{\Gamma} \left( \frac{f_{r1} - f_{r2}}{f_{r2}} \right) + 1} \quad (7-68)$$

Equation (7-67) and (7-68) clearly establish a link between the property of the dielectric film and the measurable quantities,  $f_r$  and  $Q_L$ .

In order to use equations (7-67) and (7-68) for an experimental purpose,  $\Gamma$  has to be found. From the definition of  $\Gamma$  in equation (7-66), we can see that  $\Gamma$  represents in cavity 1 the ratio of the energy stored in air layer,  $\Psi_s$ , as indicated in figure 7.17(a), to that stored in the whole cavity. To calculate  $\Gamma$ , the voltage distribution in cavity 1 has to be found first. Then the voltage distribution multiplied by a sine function would be the distribution of the electric-field intensity. It has been well understood that on an arbitrary transmission line (shown in figure 7.18) the voltage and current distribution is given as follows [7]

$$V(z) = V(z_0) \cos \beta(z - z_0) - j \frac{1}{Y_0} I(z_0) \sin \beta(z - z_0) \quad (7-69a)$$

$$I(z) = I(z_0) \cos \beta(z - z_0) - j Y_0 V(z_0) \sin \beta(z - z_0) \quad (7-69b)$$

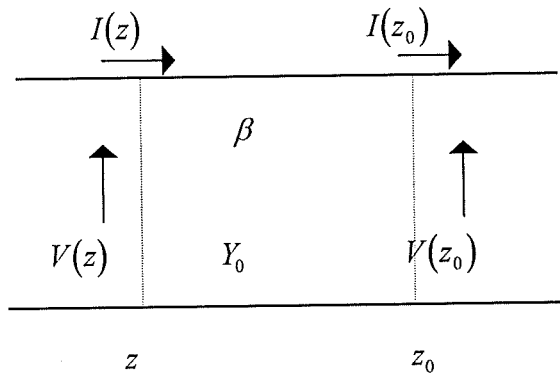


Figure 7.18 Diagram for voltage and current distribution on transmission lines

Equations (7-69) represents the voltage and current everywhere in terms of the voltage and current at a single point  $z_0$ . At resonance in cavity 1 at the short-circuit end,  $V(0) = 0$  and  $I(0)$  is a fixed arbitrary number depending on incoming power. In region  $\Psi_0$  inside cavity 1 (shown in figure 7.17),  $0 < z \leq h_0$  one has

$$V(z) = -j \frac{1}{Y_0} I(0) \sin \beta_0 z \quad (7-70a)$$

$$I(z) = I(0) \cos \beta_0 z \quad (7-70b)$$

where  $\beta_0$  is propagation constant in air region given in equation (7-13). At the right interface between air and substrate,  $z = h_0$ , the voltage and current is

$$V(h_0) = -j \frac{1}{Y_0} I(0) \sin \beta_0 h_0 \quad (7-71a)$$

$$I(h_0) = I(0) \cos(\beta_0 h_0) \quad (7-71b)$$

In the region  $\Psi_1$ , i.e. the substrate area,  $h_0 < z \leq h_0 + h_1$ , one has

$$V(z) = V(h_0) \cos \beta_1 (z - h_0) - j \frac{1}{Y_1} I(h_0) \sin \beta_1 (z - h_0) \quad (7-72a)$$

$$I(z) = I(h_0) \cos \beta_1 (z - h_0) - j Y_1 V(h_0) \sin \beta_1 (z - h_0) \quad (7-72b)$$

where  $\beta_1$  is propagation constant in substrate region which can also be calculated from (7-13). At the left interface between air and substrate,  $z = z_1 = h_0 + h_1$ , one has

$$V(z_1) = V(h_0) \cos \beta_1 h_1 - j \frac{1}{Y_1} I(h_0) \sin \beta_1 h_1 \quad (7-73a)$$

$$I(z_1) = I(h_0) \cos \beta_1 h_1 - j Y_1 V(h_0) \sin \beta_1 h_1 \quad (7-73b)$$



In the region  $\Psi_{10}$ ,  $h_1 + h_0 < z \leq d$ , we have

$$V(z) = V(z_1) \cos \beta_0(z - z_1) - j \frac{1}{Y_0} I(z_1) \sin \beta_0(z - z_1) \quad (7-74a)$$

$$I(z) = I(z_1) \cos \beta_0(z - z_1) - j Y_0 V(z_1) \sin \beta_0(z - z_1) \quad (7-74b)$$

Substituting equation (7-71) into equation (7-72a) gives

$$V(z) = -j \frac{1}{Y_0} I(0) \left( \sin \beta_0 h_0 \cos \beta_1(z - h_1) + \frac{\beta_0}{\beta_1} \cos \beta_0 h_0 \sin \beta_1(z - h_0) \right) \quad (7-75)$$

$$(h_0 < z \leq h_0 + h_1)$$

Combining equation (7-73) and equation (7-74a), we have

$$V(z) = -j \frac{1}{Y_0} I(0) \{ [\sin \beta_0 h_0 \cos \beta_1 h_1 + \frac{\beta_0}{\beta_1} \cos \beta_0 h_0 \sin \beta_1 h_1] \cos \beta_0(z - z_1) \\ + [\cos \beta_0 h_0 \cos \beta_1 h_1 - \frac{\beta_1}{\beta_0} \sin \beta_0 h_0 \sin \beta_1 h_1] \sin \beta_0(z - z_1) \} \quad (7-76)$$

$$(h_1 + h_0 < z \leq d)$$

For  $TE_{10}$  mode in a rectangular waveguide, since the vector of electric-field intensity has only  $y$  component, we have

$$|E_y| = E_y = \sqrt{\frac{2}{ab}} V(z) \sin \frac{\pi x}{a} \quad (7-77)$$

It follows by combining equation (7-70)-(7-76) with equation (7-77), when  $0 < z \leq h_0$ , one has

$$E_y = j \sqrt{\frac{2}{ab}} \frac{1}{Y_0} I(0) \sin(\beta_0 z) \sin \frac{\pi x}{a} \quad (7-78a)$$

If the substitution  $E_0 = \sqrt{\frac{2}{ab}} \frac{1}{Y_0} I(0)$  is made, then equation (7-80a) can be changed to

$$E_y = jE_0 \sin(\beta_0 z) \sin \frac{\pi x}{a} \quad (7-78b)$$

Similarly, when  $h_0 < z \leq h_0 + h_1$ , one has

$$E_y = jE_0 (C_1 \cos \beta_1 (z - h_0) + C_2 \sin \beta_1 (z - h_0)) \sin \frac{\pi x}{a} \quad (7-79)$$

where

$$C_1 = \sin \beta_0 h_0 \quad (7-80a)$$

$$C_2 = \frac{\beta_0}{\beta_1} \cos \beta_0 h_0 \quad (7-80b)$$

When  $h_1 + h_0 < z \leq d$ , the electric field is

$$E_y = jE_0 (C_3 \cos \beta_0 (z - z_1) + C_4 \sin \beta_0 (z - z_1)) \sin \frac{\pi x}{a} \quad (7-81)$$

where

$$C_3 = \sin \beta_0 h_0 \cos \beta_1 h_1 + \frac{\beta_0}{\beta_1} \cos \beta_0 h_0 \sin \beta_1 h_1 \quad (7-82a)$$

$$C_4 = \cos \beta_0 h_0 \cos \beta_1 h_1 - \frac{\beta_1}{\beta_0} \sin \beta_0 h_0 \sin \beta_1 h_1 \quad (7-82b)$$

Since the electric field pattern in cavity 1 has been found analytically, the integration in equation (7-61)-(7-65) can be readily obtained as follows

$$\begin{aligned}
E_{\Psi_0} &= \int_{\Psi_0} |\mathbf{E}_1|^2 d\Psi = \int_0^a \int_0^b \int_0^{h_0} |E_y|^2 dx dy dz \\
&= \frac{ab}{2} E_0^2 \left( \frac{h_0}{2} - \frac{1}{4\beta_0} \sin 2\beta_0 h_0 \right)
\end{aligned} \tag{7-83}$$

$$\begin{aligned}
E_{\Psi_1} &= \int_{\Psi_1} \varepsilon_1' |\mathbf{E}_1|^2 d\Psi = \varepsilon_1' \int_0^a \int_0^b \int_{h_0}^{h_0+h_1} |E_y|^2 dx dy dz \\
&= \frac{abE_0^2}{2} \varepsilon_1' \left[ \frac{h_1}{2} (C_1^2 + C_2^2) + \frac{1}{4\beta_1} \sin(2\beta_1 h_1) (C_1^2 - C_2^2) + \frac{1}{\beta_1} C_1 C_2 \sin^2 \beta_1 h_1 \right]
\end{aligned} \tag{7-84}$$

$$\begin{aligned}
E_{\Psi_{10}} &= \int_{\Psi_{10}} |\mathbf{E}_1|^2 d\Psi = \int_0^a \int_0^b \int_{h_0+h_1}^{h_0+h_1+h_2} |E_y|^2 dx dy dz \\
&= \frac{abE_0^2}{2} \left[ \frac{h_{10}}{2} (C_3^2 + C_4^2) + \frac{1}{4\beta_0} \sin(2\beta_0 h_{10}) (C_3^2 - C_4^2) + \frac{C_3 C_4}{\beta_0} \sin^2 \beta_0 h_{10} \right]
\end{aligned} \tag{7-85}$$

$$\begin{aligned}
E_s &= \int_{\Psi_s} |\mathbf{E}_1|^2 d\Psi = \int_0^a \int_0^b \int_{h_0+h_1}^{h_0+h_1+h_2} |E_y|^2 dx dy dz \\
&= \frac{abE_0^2}{2} \left[ \frac{h_2}{2} (C_3^2 + C_4^2) + \frac{1}{4\beta_0} \sin(2\beta_0 h_2) (C_3^2 - C_4^2) + \frac{C_3 C_4}{\beta_0} \sin^2 \beta_0 h_2 \right]
\end{aligned} \tag{7-86}$$

In (7-84)  $\varepsilon_1'$  is the permittivity of the substrate material. From equation (7-83)-(7-86) and (7-66),  $\Gamma$  can be calculated. Then from equation (7-67) and (7-68), the relative permittivity and loss tangent of the dielectric film materials can be found.

#### 7.4.5 Measurement results using the perturbation method

Using the algorithm established above, permittivity measurements were made on the same samples of dielectric film materials as those discussed in section 7.3 where the standard

Table 7.4 Measured values of relative permittivity for KQ-type 1 and KQ-type 2 dielectric films using cavity perturbation method.

Frequency (GHz)	KQ-type1	KQ-type2
8.21	3.88	3.91
8.41	3.90	3.91
8.72	3.89	3.96
9.02	3.93	3.95
9.26	3.92	3.97
9.65	3.88	3.92
10.35	3.91	3.94
10.75	3.92	3.97
11.35	3.88	3.92
11.98	3.95	3.97

transmission line theory was used to derive the formulae for the measurement of relative permittivity. The test results are shown in table 7.4. Comparing the results in table 7.3 with those in table 7.4, we find that the two methods give nearly the same results, which confirms the correctness of our derivation and test procedure. The advantage of the perturbation method is that it is more straightforward. Because what is fundamentally important is to compare the difference between the two resonant cavities, if the coupling irises in two cavities have the same geometric size, there is no need to consider or simulate their frequency-dependent behaviour. In addition, depending on the thickness of the dielectric film, samples can either be loaded in the strong field region like that in section 7.3 or loaded in the weak field region. In general the perturbation method is quite flexible.

If the cavity perturbation method is only used for the measurement of relative permittivity, there is no need to measure the loaded Q factor. In that situation, things would be much easier and the physical size of the coupling iris would not be critical as long as a clear resonant curve can be observed to ensure an accurate measurement of resonant frequency. While the accurate

measurement of the relative permittivity of the dielectric film only relies on the accurate measurement of resonant frequencies, the accurate Q value measurement is critical for an accurate loss tangent measurement. Therefore if we want to measure the loss tangent of the dielectric film, the size of the coupling iris has to be optimised. The aim for the optimisation of the coupling iris is to try to get the maximum measurable loaded Q factor. In another word, the size of the coupling iris has to be as small as possible in order to realize low return loss which should be as small as possible if a clear resonant curve can be displayed for the accurate measurement of Q-factor. In that situation the whole test system would be at its most sensitive state to the losses introduced by dielectric film. Generally speaking, if the coupling iris is too big then the energy leaking from the iris would greatly lower the loaded Q factor. On the contrary if the coupling iris is too small, the energy coupled into the cavity from the incident power would be very small. The resonant peak on the trace of the reflected power will be too small to ensure an accurate determination of Q factor. Compromise has to be made to have a reasonably small coupling iris. The optimum size of the coupling iris could be determined in two way: the first is from the simulation by a 3-D electromagnetic solver and the second is

Table 7.5 Optimised size of coupling iris giving maximum measurable loaded Q factor

Resonant frequency (GHz)	Diameter of the coupling iris (mm)
8	6
9	5.5
10	5
12	4.5

through practical trials. Because the latter is straightforward, we used the second method by fabricating a series of coupling irises ranging from 8 mm to 3 mm. Finally, we found that in X-band (8-12 GHz) , the optimum size of the coupling iris is dependent on the resonant frequency of the cavity whose length is fixed at 48 mm. The optimised results are listed in Table 7.5. In doing iris optimisation, it was found that the return loss has to be optimised to a value less than 10dB.

Using appropriate coupling irises for different resonant frequencies, the loaded Q factor for a substrate loaded cavity and a two-layer sample loaded cavity can be measured. Then from equation (7-68) the loss tangent of the dielectric film can be calculated. The results for KQ-type 1 and KQ-type 2 dielectric film materials are presented in table 7.6. From the table we can see that the dielectric film materials of KQ series have extremely low loss which is achieved by their novel material system. The losses found in KQ-type 1 are even comparable to alumina bulk material indicating its potential for application as a thin substrate or dielectric overlay in the fabrication of microwave or millimetre wave circuits. The losses of dielectric materials are almost independent of frequency. This is due to the narrow frequency range investigated in the current study. The increase in losses can be expected if the measurement is extended to millimetre frequency range.

Table 7.6 Loss tangent of KQ-type 1 and KQ-type 2 dielectric film materials measured using the cavity perturbation method

Frequency (GHz)	KQ-type 1	KQ-type 2
8.21	$4.88 \times 10^{-4}$	$2.4 \times 10^{-3}$
10.35	$4.20 \times 10^{-4}$	$2.5 \times 10^{-3}$
11.98	$4.62 \times 10^{-4}$	$2.2 \times 10^{-3}$

## 7.5 Further studies into the cavity perturbation method employing a circular waveguide and high Q mode

The cavity perturbation formulae in section 7.4 for the measurement of dielectric constant and loss tangent were derived from the cavity structure formed by a rectangular waveguide. In this part, we will extend the previous theory to suit the cavity structure formed by a circular waveguide. It has been well understood that the  $TE_{01}$  mode in a circular waveguide has extremely low attenuation to the propagation wave inside it and, in contrary to other modes in circular waveguide or any mode in rectangular waveguide, the attenuation in a circular waveguide for  $TE_{01}$  mode decreases with frequency. It can thus be visualised that if a cavity is

built up from a circular waveguide and only  $TE_{01}$  mode exists in the cavity, then the Q factor of the cavity would be very high at resonance. Consequently, the loss tangent of the dielectric sample inserted in the cavity can be measured more accurately.

Figure 7-19 shows the cross-section of cavities loaded with a blank substrate and a two-layer sample. For a circular-shaped waveguide cavity, the basic cavity perturbation equation (see 7-55) is still valid and it is repeated here,

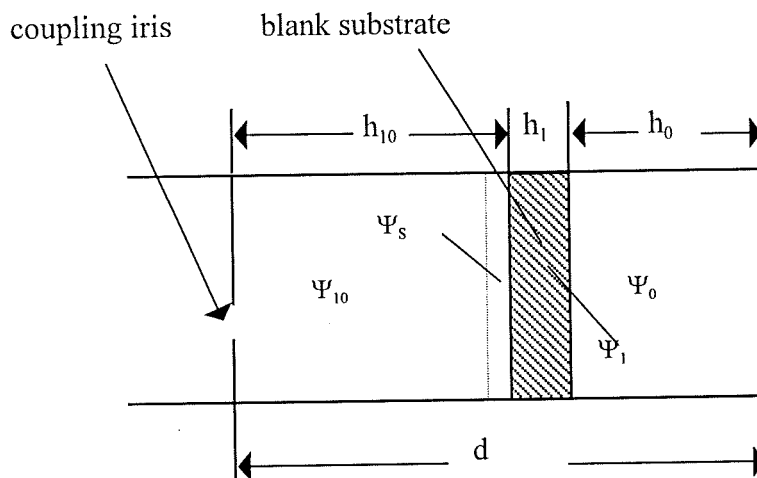
$$2\left(\frac{f_{r1} - f_{r2}}{f_{r2}}\right) + j\left(\frac{1}{Q_{L1}} - \frac{1}{Q_{L2}}\right) = \frac{\int_{\Psi_s} (\epsilon_2 - \epsilon_1) \mathbf{E}_1 \cdot \mathbf{E}_2 d\Psi}{\int_{\Psi_c} \epsilon_1 |\mathbf{E}_1|^2 d\Psi} \quad (7-87)$$

If  $TE_{01}$  is the mode to be launched in the circular waveguide, the electric field in the waveguide is [1]

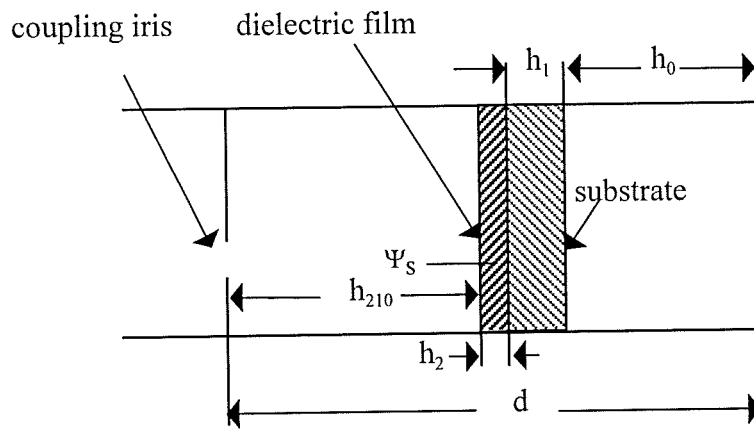
$$E_r = 0 \quad (7-88a)$$

$$E_z = 0 \quad (7-88b)$$

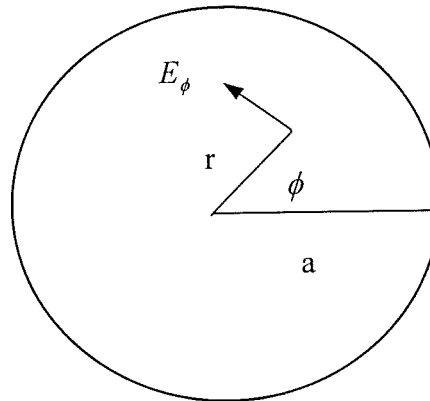
$$E_\phi = V(z) \sqrt{\frac{\chi_{01}'}{\pi}} \frac{J_0' \left( \frac{\chi_{01}'}{a} \right)}{a J_0'(\chi_{01}')} \quad (7-88c)$$



(a) Circular cavity loaded with alumina substrate (Cavity 1)



(b) Circular cavity loaded with two-layer sample (Cavity 2)



(c) Cross-section of circular waveguide

Figure 7-19 Cross-sections of a circular cavity loaded with blank substrate and two-layer sample

where  $J_0$  is the 0th order Bessel function,  $J_0'$  is the derivative of 0th order Bessel function and  $\chi_{01}' = 3.832$  is the first nonvanishing root of the derivative of the 0th order Bessel function.  $V(z)$  is the voltage amplitude distribution along waveguide. At resonant condition of



the circular-shaped cavity, there will be a fixed standing wave pattern of  $V(z)$  in the cavity. In circular waveguide, the phase propagation constant for  $TE_{01}$  mode is

$$\beta_n = \frac{2\pi}{\lambda_0} \sqrt{\epsilon_{nr} - \left(\frac{\lambda_0}{1.64a}\right)^2} \quad (7-89)$$

where  $n = 0, 1$  correspond to air and dielectric substrate regions respectively.  $\lambda_0$  is the wavelength in free space and  $a$  is diameter of the cross-section of circular waveguide.

The boundary condition for the electric field at the interface between the supporting substrate and the dielectric film is similar to the situation in a rectangular waveguide, i.e.  $|\mathbf{E}_1| = |\mathbf{E}_2|$  in  $\Psi_s$  region in figure 7.19. If we assume

$$E_{\Psi_c}' = \int_{\Psi_c} \epsilon_{r1} |\mathbf{E}_1|^2 d\Psi = E_{\Psi_0}' + E_{\Psi_1}' + E_{\Psi_{10}}' \quad (7-90)$$

$$E_s' = \int_{\Psi_s} |\mathbf{E}_1|^2 d\Psi \quad (7-91)$$

$$\Gamma' = \frac{E_s'}{E_{\Psi_c}'} = \frac{E_s'}{E_{\Psi_0}' + E_{\Psi_1}' + E_{\Psi_{10}}'} \quad (7-92)$$

where

$$E_{\Psi_0}' = \int_{\Psi_0} |\mathbf{E}_1|^2 d\Psi \quad (7-93)$$

$$E_{\Psi_1}' = \int_{\Psi_1} \epsilon_{r1} |\mathbf{E}_1|^2 d\Psi \quad (7-94)$$

$$E_{\Psi_{10}}' = \int_{\Psi_{10}} |\mathbf{E}_1|^2 d\Psi \quad (7-95)$$

with

$$\Psi_C = \Psi_0 + \Psi_1 + \Psi_{10} \quad (7-96)$$

where  $\Psi_C$  is the total area enclosed in the cavity loaded with blank substrate and  $\varepsilon_1'$  is the relative permittivity of the blank substrate, then the complex relative permittivity and loss tangent of the dielectric film can be expressed as

$$\varepsilon_{r2} = \frac{2}{\Gamma'} \left( \frac{f_{r1} - f_{r2}}{f_{r2}} \right) + 1 - j \frac{1}{\Gamma'} \left( \frac{1}{Q_{L2}} - \frac{1}{Q_{L1}} \right) \quad (7-97)$$

$$\tan \delta = \frac{\frac{1}{\Gamma'} \left( \frac{1}{Q_{L2}} - \frac{1}{Q_{L1}} \right)}{\frac{2}{\Gamma'} \left( \frac{f_{r1} - f_{r2}}{f_{r2}} \right) + 1} \quad (7-98)$$

The substitution of electric field in (7-88) into (7-91), (7-93), (7-94) and (7-95) gives

$$\begin{aligned} E_{\Psi_0} &= \int_{\Psi_0} |\mathbf{E}_1|^2 d\Psi = \int_0^{2\pi} \int_0^a \int_0^{h_0} |E_\phi|^2 r d\phi dr dz \\ &= \frac{3.832}{\pi a^2} \frac{2\pi}{J_0^2(3.832)} \int_0^a \left( J_0' \left( \frac{3.832}{a} r \right) \right)^2 dr \int_0^{h_0} V^2(z) dz \\ &= C_0 \int_0^{h_0} V^2(z) dz \end{aligned} \quad (7-99)$$

where

$$C_0 = \frac{7.664}{a^2 J_0^2(3.832)} \int_0^a \left( J_0' \left( \frac{3.832}{a} r \right) \right)^2 dr \quad (7-100)$$

$$\begin{aligned} E_{\Psi_1} &= \int_{\Psi_1} \varepsilon_1' |\mathbf{E}_1|^2 d\Psi = \varepsilon_1' \int_0^{2\pi} \int_0^a \int_{h_0}^{h_0+h_1} |E_\phi|^2 r d\phi dr dz \\ &= \varepsilon_1' C_0 \int_{h_0}^{h_0+h_1} V^2(z) dz \end{aligned} \quad (7-101)$$

$$\begin{aligned}
E_{\Psi_{10}} &= \int_{\Psi_{10}} |\mathbf{E}_1|^2 d\Psi = \int_0^{2\pi a} \int_0^d \int_{h_0+h_1}^d |E_\phi|^2 r d\phi dr dz \\
&= C_0 \int_{h_0+h_1}^d V^2(z) dz
\end{aligned} \tag{7-102}$$

$$\begin{aligned}
E_s &= \int_{\Psi_s} |\mathbf{E}_1|^2 d\Psi = \int_0^{2\pi a} \int_0^{h_0+h_1+h_2} \int_{h_0+h_1}^d |E_\phi|^2 r d\phi dr dz \\
&= C_0 \int_{h_0+h_1}^{h_0+h_1+h_2} V^2(z) dz
\end{aligned} \tag{7-103}$$

It can be clearly seen that  $\Gamma'$  is only determined by the voltage amplitude distribution in the circular resonant cavity, which is also the case for rectangular resonant cavity. Therefore, all of the cavity perturbation formulae developed for rectangular cavity are still valid for circular cavity except that the phase propagation constant has to be replaced by those in (7-89). If we have a further examination of the boundary condition for electric field in the resonant cavity, we may find that all of the TE modes have the similar boundary condition due to the fact that the electric field only has a component in the transverse plane of the waveguide. This may lead to another conclusion that all of the cavity perturbation formulae for a rectangular cavity can still be used for any other TE modes as long as the phase propagation constant for TE mode launched in the cavity is used in the formulae.

In this part of the study for a circular cavity, only the theory is given. No practical measurement was made due to the limitation in available time.

## 7.6 Error investigation in the measurement of permittivity and loss tangent

In the previous sections of this chapter, we have developed two independent theories for the measurement of dielectric constant and loss tangent. The measurements using the theories have also produced consistent results with reasonable accuracy. However, there are still two remaining questions which have not been answered yet: what is the exact accuracy we have

achieved and what is the achievable accuracy for the two new methods?; is there any correction algorithm to improve the measurement accuracy? In the following sections we will firstly identify the error sources in the measurement and then make the estimation of the error range in our current measurement. At the same time, based on the rigorous mathematical calculation, a correction algorithm for the measured results will also be given to improve the measurement accuracy.

### 7.6.1 Identification of error sources for permittivity measurement

If the theory and techniques developed in section 7.3 are called method 1, the factors which contribute to the total error range in this method can be identified as follows

1. The accuracy in modelling the shunting susceptance of the coupling iris,  $b$
2. The uncertainty in the total length of the resonant cavity,  $d$
3. The uncertainty in measuring the thickness of substrate,  $h_1$
4. The uncertainty in determining the thickness of the dielectric film,  $h_2$
5. The uncertainty in reading the loading position of the substrate,  $h_0$
6. The clearance gap between samples and waveguide walls, and difference in geometric size between the blank reference substrate and the two-layer sample
7. The stability of signal source, leading to uncertainty in reading resonant frequencies
8. Permittivity difference between the blank reference substrate and the supporting substrate in the two-layer sample
9. Changes in environment temperature
- 10 Discontinuities in the microwave components in the whole test system

In the case when cavity perturbation method (method 2) is used for the permittivity measurement, the error sources in method one still remain except for the first one because there is no need for modelling the coupling iris in method 2. In all of the factors listed here, the sixth one is probably the most significant one and yet there is no available theory to predict the effect of gap clearance on the shift of resonant frequency. Before we proceed further for the estimation of total error range, we have to develop a theory to calculate the

effect of clearance gap. It seems that discontinuities in the test system will have a big influence on the test result. However, because what matters is the difference between the tests from two waveguides loaded with blank and two-layer samples, the error due to discontinuities is very small.

### 7.6.2 The effect of the clearance gap between the dielectric sample and waveguide walls on the shift of resonant frequency

Figure 7-20 shows the clearance gaps between the sample and waveguide walls. There are two types of gaps: the clearance gap between the broad side of sample and waveguide wall and that between the narrow side of the sample and waveguide wall. Obviously the former has a much bigger effect on the resonant frequency than the latter due to the electric field distribution. The cavity perturbation method will be used again in this part to calculate the effect of two kinds of clearance gaps on the resonant frequencies.

#### A. The clearance gap between the broad side of sample and waveguide wall

Figure 7.21 shows reference cavity (cavity 1) and cavity with clearance gap (cavity 2). In cavity 1 it is imagined that the dielectric sample (blank substrate) completely fills the cross-section of the cavity, while in cavity 2 there is a clearance gap between the sample and waveguide wall. If the losses in the dielectric sample are neglected, then the basic cavity perturbation formula in (7-55) can be changed to the following form

$$2\left(\frac{f_{r1} - f_{r2}}{f_{r2}}\right) = \frac{\int_{\Psi_s} (\epsilon_2 - \epsilon_1) \mathbf{E}_1 \cdot \mathbf{E}_2 d\Psi}{\int_{\Psi_c} \epsilon_1 |\mathbf{E}_1|^2 d\Psi} \quad (7-104)$$

At the interface between the dielectric sample and air in the region of clearance gap in cavity 2, the boundary condition for the electric field is

$$\mathbf{n} \cdot (\mathbf{D}_1 - \mathbf{D}_2) = 0 \quad (7-105a)$$

or

$$\varepsilon_1 \mathbf{E}_{n1} = \varepsilon_2 \mathbf{E}_{n2} \quad (7-105b)$$

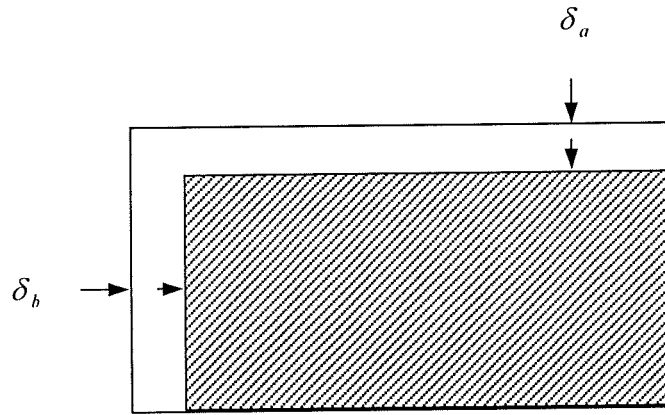
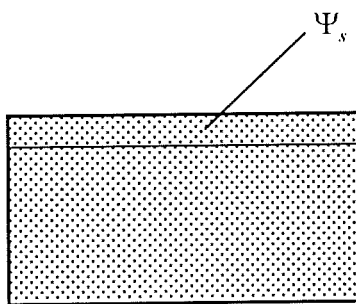
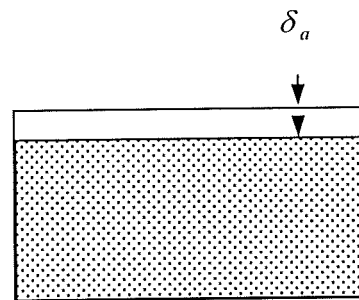


Figure 7-20 Clearance gaps between sample and waveguide walls.



a. Cavity 1



b. Cavity 2

Figure 7.21 Reference cavity (cavity 1) and cavity with clearance gap at broad side (cavity 2).

For the dominant mode in a rectangular waveguide, the electric field is perpendicular to the interface, then it follows

$$\varepsilon_1' \mathbf{E}_1 = \mathbf{E}_2 \quad (7-106)$$

where  $\varepsilon_1'$  is the relative permittivity of blank dielectric substrate. It should be noted that  $\mathbf{E}_1$  in (7-106) also equals the electric field strength in the corresponding region in cavity 1. Therefore, (7-104) can be changed into

$$2 \left( \frac{f_{r2} - f_{r1}}{f_{r2}} \right) = \frac{\varepsilon_1' (\varepsilon_1' - 1) \int_{\Psi_s} |\mathbf{E}_1|^2 d\Psi}{\int_{\Psi_c} \varepsilon_{r1} |\mathbf{E}_1|^2 d\Psi} \quad (7-107)$$

where

$$\int_{\Psi_c} \varepsilon_{r1} |\mathbf{E}_1|^2 d\Psi = E_{\Psi_0} + E_{\Psi_1} + E_{\Psi_{10}} \quad (7-108)$$

has already been defined in (7-60) in section 7.3. The remaining work is to calculate

$E_g = \int_{\Psi_s} |\mathbf{E}_1|^2 d\Psi$  in the numerator in cavity 1. The calculation of  $E_g$  is given as follows

$$\begin{aligned} E_g &= \int_{\Psi_s} |\mathbf{E}_1|^2 d\Psi = \int_0^a \int_{h-\delta_a}^b \int_{h_0}^{h_0+h_1} |E_y|^2 dx dy dz \\ &= \frac{abE_0^2}{2} \left( \frac{\delta_a}{b} \right) \left[ \frac{h_1}{2} (C_1^2 + C_2^2) + \frac{1}{4\beta_1} \sin(2\beta_1 h_1) (C_1^2 - C_2^2) + \frac{1}{\beta_1} C_1 C_2 \sin^2 \beta_1 h_1 \right] \\ &= \left( \frac{\delta_a}{b} \right) \frac{1}{\varepsilon_1} E_{\Psi_1} \end{aligned} \quad (7-109)$$

where

$C_1$ ,  $C_2$  and  $E_{\Psi_1}$  were given in (7-80) and (7-84). Therefore (7-107) can be changed to the form of

$$\Delta f = f_{r2} - f_{r1} = \left( \frac{\delta_a}{b} \right) (\epsilon_1' - 1) \frac{f_{r2}}{2} \left( \frac{E_{\psi_1}}{E_{\psi_0} + E_{\psi_1} + E_{\psi_{10}}} \right) \quad (7-110)$$

where  $\Delta f$  is the change in resonant frequency due to the clearance gap. As an example, (7-110) was used to calculate the shift of resonant frequency with respect to clearance gap, resonant frequencies and resonant modes. The respective parameters of the resonant cavities for the calculation are listed in table 7.7 and the calculated results are given in figure 7.22. The substrate loaded in the cavity is alumina which has a thickness of 0.635 mm and permittivity of 9.8. The resonant frequencies in table 7.7 were obtained from our measurement. The diameter of the coupling iris is 6 mm in the measurement. Alternatively the resonant frequencies can also be obtained from rigorous calculation. The change in resonant frequency caused by per  $\mu\text{m}$  of the clearance gap is also listed in the table. Inspection of figure 7.22 shows that the change in resonant frequency is linear to the clearance gap and this change is significant, which can not be neglected in the permittivity measurement. At 10.39 GHz, 10  $\mu\text{m}$  clearance gap will create 6.97 MHz in the change of resonant frequency. In the

Table 7.7 Set-up and resonant state of X-band (8-12 GHz) cavity

Resonant frequency (GHz)	Resonant mode	Cavity length (mm)	Sample position (mm)	$\Delta f$ (MHz)/ $\mu\text{m}$
8.2506	TE <sub>102</sub>	47.95	7	0.689
9.0754	TE <sub>102</sub>	37.95	6.5	0.822
10.3909	TE <sub>103</sub>	47.95	5	0.697
12.0334	TE <sub>103</sub>	37.95	4	0.885



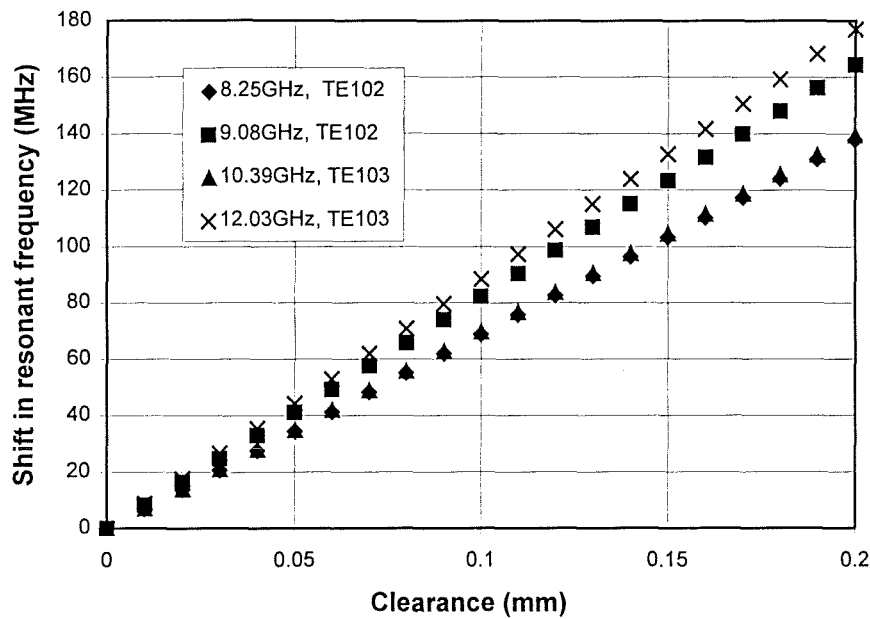


Figure 7.22 The effect of clearance gap at broad side of waveguide walls on the shift of resonant frequency.

practical measurement, if there is a  $10\ \mu\text{m}$  difference in the narrow side width between the blank substrate and two-layer sample, this 6.97 MHz will contribute to more than 10% error in the measured relative permittivity. It can also be observed from figure 7.22 that the change in resonant frequency due to the gap is not only dependent on the resonant frequency but also on the resonant mode. The clearance gap has a bigger effect on the change of resonant frequency at lower resonant mode  $\text{TE}_{102}$  than at higher resonant mode  $\text{TE}_{103}$ . If the resonant mode is fixed, the clearance gap would have a bigger effect on the change of resonant frequency at higher resonant frequency than at lower resonant frequency.

#### B. The clearance gap between the narrow side of sample and waveguide wall

Figure 7.23 shows the reference cavity (cavity 1) and cavity with clearance gap at the narrow side of waveguide wall (cavity 2). Following a similar derivation procedure to that for

the clearance gap at the broad side, the change in resonant frequency due to the clearance gap at narrow side can be obtained as

$$\Delta f' = f_{r2} - f_{r1} = \left( \frac{\varepsilon_1' - 1}{\varepsilon_1'} \right) \frac{f_{r2}}{2} \left( \frac{\delta_b}{a} - \frac{1}{2\pi} \sin\left(\frac{2\pi}{a} \delta_b\right) \right) \left( \frac{E_{\Psi_1}}{E_{\Psi_0} + E_{\Psi_1} + E_{\Psi_{10}}} \right) \quad (7-111)$$

Figure 7.24 shows the effect of clearance gap at narrow side on the shift of resonant frequency, which is calculated using (7-111). The cavity set-up is exactly the same to that used in the calculation for clearance gap at broad side of the waveguide. A similar trend for the shift in resonant frequency in respective to resonant mode and resonant frequency can be observed. However, this shift is very small. For example, the shift in resonant frequency is still in the order of KHz even the gap is as big as 200  $\mu\text{m}$ . Therefore, it is justifiable in permittivity measurement to neglect the effect from the clearance gap along the narrow side.

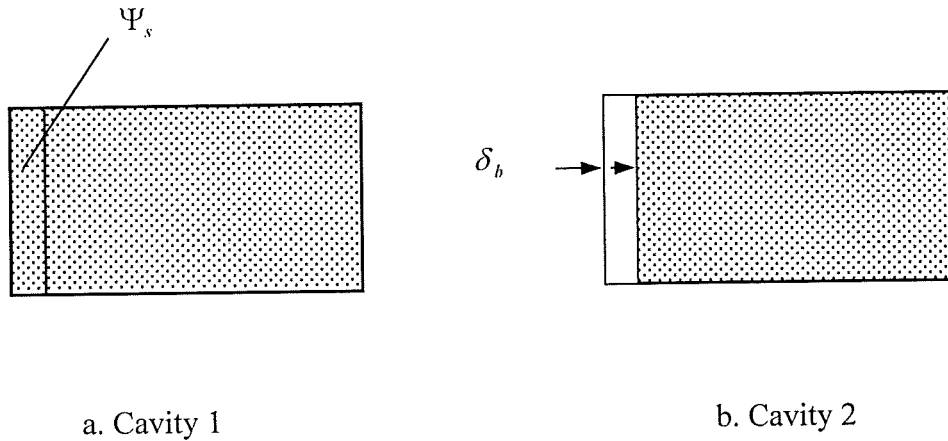


Figure 7.23 Reference cavity (cavity 1) and cavity with clearance gap at narrow side (cavity 2).

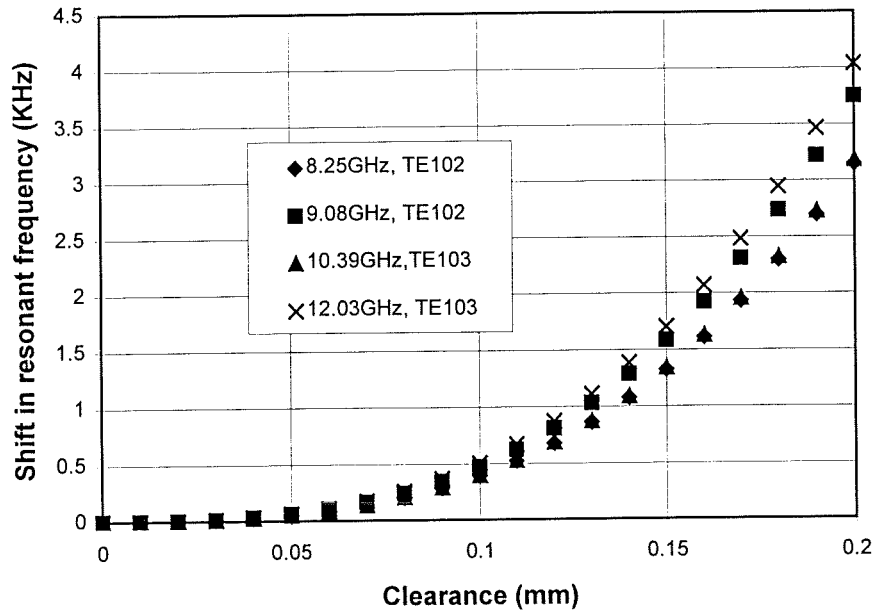


Figure 7.24 The effect of clearance gap at narrow side between sample and waveguide walls on the shift of resonant frequency.

### 7.6.3 Correction algorithm for the clearance gap between broad side of sample and waveguide wall

The calculation in last section for the clearance gaps clearly indicates that the accuracy of the measurement would to a large extent depend on the tight fit of the sample in the waveguide if the shift in the resonant frequency due to the clearance gap is not corrected. It is also easy to see that the smaller the cross-section of the waveguide and the higher the substrate permittivity, the more critically the accuracy of measurement will depend on the tight fit. However, in a practical measurement, it is very difficult to ensure that both the blank substrate and two-layer sample have the same width at their narrow sides. A correction algorithm is necessary to take into account the difference in geometric size between them.

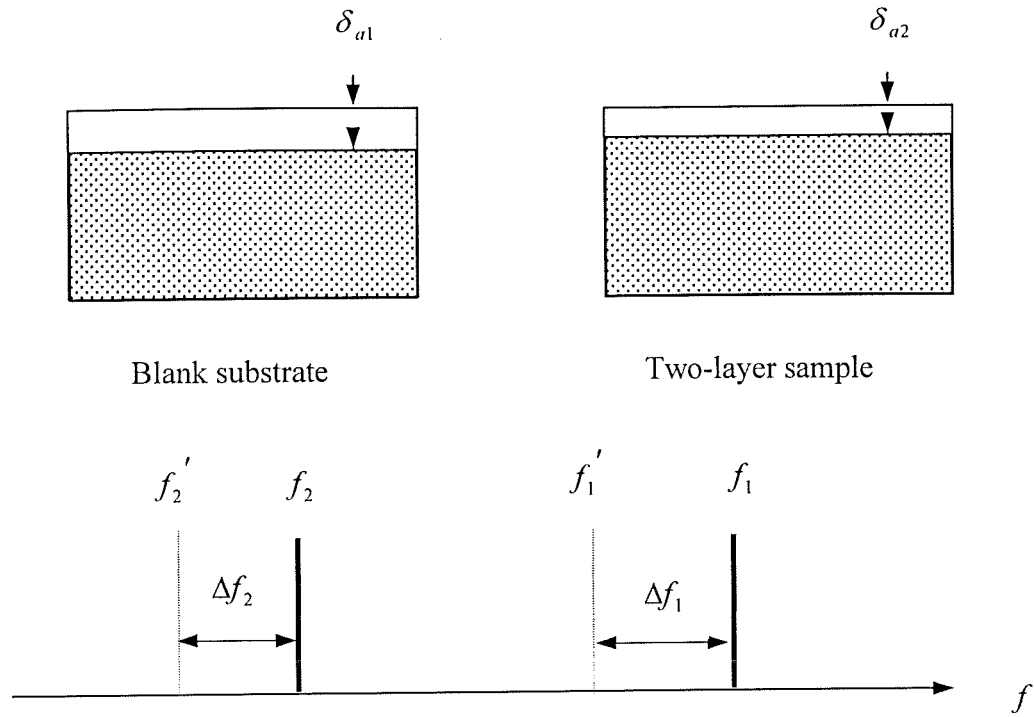


Figure 7.25 Correction algorithm for clearance gap at broad side of waveguide

A proposed correction algorithm is shown in figure 7.25, where  $f_1$  and  $f_2$  are assumed to be the measured resonant frequencies for blank substrate and two-layer sample respectively. The clearance gap for the blank substrate is  $\delta_{a1}$  and  $\delta_{a2}$  for the two-layer sample. If  $\delta_{a1} = \delta_{a2}$ , the direct use of  $f_1$  and  $f_2$  for the calculation of relative permittivity of the dielectric film would not yield much error. However, if  $\delta_{a1} \neq \delta_{a2}$ , as indicated in section 7.6.2, a significant error would occur and the error increases almost linearly with the difference between  $\delta_{a1}$  and  $\delta_{a2}$ . Therefore,  $f_1$  and  $f_2$  have to be corrected to  $f_1'$  and  $f_2'$ , which corresponds to the situation without clearance gaps. If we assume

$$\Delta f_1 = f_1 - f_1' \quad (7-112a)$$

$$\Delta f_2 = f_2 - f_2' \quad (7-112b)$$

then

$$\Delta f_2 = \left( \frac{\delta_{a2}}{\delta_{a1}} \right) \Delta f_1 = \left( \frac{b - w_2}{b - w_1} \right) \Delta f_1 \quad (7-113)$$

where  $b$  is the narrow side width of the rectangular waveguide (10.16 mm for X-band waveguide) and  $w_1$  and  $w_2$  are the measured width of the blank substrate and two-layer sample respectively.  $\Delta f_1$  can be calculated from (7-110). Table 7.8 shows an example of how the correction algorithm is used. In this example, the narrow side width of the blank substrate and two-layer sample are 10.143 and 10.132 mm respectively. The difference between them is 11  $\mu\text{m}$ . The cavity perturbation method is used in the measurement of relative permittivity. It can be seen from the table that the clearance gap can contribute to more than 10% of error if the correction is not made. The correction can significantly increase the accuracy of the cavity technique for the measurement of relative permittivity.

Table 7.8 Measured and corrected resonant frequencies and relative permittivity ( $w_1 = 10.143$  mm,  $w_2 = 10.132$  mm)

Two-layer sample (KQ-type1)		Blank substrate (Alumina)		Relative permittivity	
Resonant frequency (GHz)		Resonant frequency (GHz)		As- calculated	After correction
Measured	Corrected	Measured	Corrected		
8.2085	8.1892	8.2506	8.2389	3.43	3.88
9.0254	9.0024	9.0754	9.0614	3.53	3.93
10.3495	10.3299	10.3909	10.3791	3.45	3.91
11.9818	11.9570	12.0334	12.0183	3.48	3.95

#### 7.6.4 Numerical calculation of error range in permittivity measurement

The total error range in permittivity measurement can be obtained by adding together the errors from each error source. According to the error sources identified in section 7.6.1, the relative permittivity of the dielectric film can be expressed as

$$\varepsilon_2 = F(b, d, h_1, h_2, h_0, \delta_b, \delta_a, f, \varepsilon_1) \quad (7-114)$$

where  $b, d, h_1, h_2, h_0, \delta_b, \delta_a, f$  and  $\varepsilon_1$  have been defined previously. The error source from the environmental temperature is neglected because every time before measurement, sufficient time has been allowed to make sure the whole test system is thermally stabilised. The total error range or maximum absolute error in the measured permittivity can be mathematically calculated as follows

$$\begin{aligned} \Delta_{\varepsilon_2} = \sum_i \left| \frac{\partial F}{\partial x_i} \right| \Delta_{x_i} = & \left| \frac{\partial F}{\partial b} \right| \Delta_b + \left| \frac{\partial F}{\partial d} \right| \Delta_d + \left| \frac{\partial F}{\partial h_1} \right| \Delta_{h_1} + \left| \frac{\partial F}{\partial h_2} \right| \Delta_{h_2} + \left| \frac{\partial F}{\partial h_0} \right| \Delta_{h_0} + \left| \frac{\partial F}{\partial \delta_b} \right| \Delta_{\delta_b} \\ & + \left| \frac{\partial F}{\partial \delta_a} \right| \Delta_{\delta_a} + \left| \frac{\partial F}{\partial f} \right| \Delta_f + \left| \frac{\partial F}{\partial \varepsilon_1} \right| \Delta_{\varepsilon_1} \end{aligned} \quad (7-115)$$

where  $\frac{\partial F}{\partial x_i}$  is the derivative of  $\varepsilon_2$  in respect to the parameter  $x_i$  and  $\Delta_{x_i}$  is the error range of  $x_i$ . The derivatives in (7-115) can not be obtained analytically due to the complex relationship between  $\varepsilon_2$  and  $x_i$ . A numerical method has to be used to calculate the respective derivatives. Table 7.9 shows the numerical results for the derivatives in method 1 where the coupling iris is simulated. The error range for each measured parameter is also given in the table. At the bottom of the table the total error ranges in the measured permittivity are obtained by adding together the individual terms in (7-115). The set-ups of the cavity for the calculation are the same as those listed in table 7.7. It can be seen that in the

Table 7.9 Contribution of each measured parameter to the total error range in the measured relative permittivity using method 1

Parameters	$\frac{\partial \varepsilon_2}{\partial x_i}$	8.21 (GHz)	9.02 ( GHz)	10.35 (GHz)	11.98 (GHz)	$\Delta_{x_i}$
Shunting susceptance	$\frac{\partial \varepsilon_2}{\partial b}$	$2.031 \times 10^{-3}$	$6.694 \times 10^{-3}$	$11.13 \times 10^{-3}$	$22.38 \times 10^{-3}$	0.5
Cavity length	$\frac{\partial \varepsilon_2}{\partial d}$	$3.415 \times 10^{-3}$ ( $\mu\text{m}^{-1}$ )	$5.536 \times 10^{-3}$ ( $\mu\text{m}^{-1}$ )	$7.455 \times 10^{-3}$ ( $\mu\text{m}^{-1}$ )	$10.28 \times 10^{-3}$ ( $\mu\text{m}^{-1}$ )	2 $\mu\text{m}$
Substrate thickness	$\frac{\partial \varepsilon_2}{\partial t_1}$	$5.851 \times 10^{-2}$ ( $\mu\text{m}^{-1}$ )	$5.991 \times 10^{-2}$ ( $\mu\text{m}^{-1}$ )	$6.039 \times 10^{-2}$ ( $\mu\text{m}^{-1}$ )	$6.056 \times 10^{-2}$ ( $\mu\text{m}^{-1}$ )	1 $\mu\text{m}$
Film thickness	$\frac{\partial \varepsilon_2}{\partial t_2}$	$1.682 \times 10^{-2}$ ( $\mu\text{m}^{-1}$ )	$1.757 \times 10^{-2}$ ( $\mu\text{m}^{-1}$ )	$1.689 \times 10^{-2}$ ( $\mu\text{m}^{-1}$ )	$1.682 \times 10^{-2}$ ( $\mu\text{m}^{-1}$ )	1 $\mu\text{m}$
Sample position	$\frac{\partial \varepsilon_2}{\partial t_0}$	$39.79 \times 10^{-4}$ ( $\mu\text{m}^{-1}$ )	$4.725 \times 10^{-4}$ ( $\mu\text{m}^{-1}$ )	$2.915 \times 10^{-4}$ ( $\mu\text{m}^{-1}$ )	$10.14 \times 10^{-4}$ ( $\mu\text{m}^{-1}$ )	1 $\mu\text{m}$
Sample length	$\frac{\partial \varepsilon_2}{\partial \delta_b}$	$<10^{-5}$ ( $\mu\text{m}^{-1}$ )	$<10^{-5}$ ( $\mu\text{m}^{-1}$ )	$<10^{-5}$ ( $\mu\text{m}^{-1}$ )	$<10^{-5}$ ( $\mu\text{m}^{-1}$ )	1 $\mu\text{m}$
Sample width	$\frac{\partial \varepsilon_2}{\partial \delta_a}$	$3.937 \times 10^{-2}$ ( $\mu\text{m}^{-1}$ )	$4.098 \times 10^{-2}$ ( $\mu\text{m}^{-1}$ )	$4.158 \times 10^{-2}$ ( $\mu\text{m}^{-1}$ )	$4.271 \times 10^{-2}$ ( $\mu\text{m}^{-1}$ )	1 $\mu\text{m}$
Resonant frequency	$\frac{\partial \varepsilon_2}{\partial f}$	$5.686 \times 10^{-2}$ (MHz $^{-1}$ )	$4.984 \times 10^{-2}$ (MHz $^{-1}$ )	$5.958 \times 10^{-2}$ (MHz $^{-1}$ )	$5.041 \times 10^{-2}$ (MHz $^{-1}$ )	0.05 MHz
Substrate permittivity	$\frac{\partial \varepsilon_2}{\partial \varepsilon_1}$	4.619	4.733	4.794	4.927	<0.01 %
Total error range	$\Delta_{\varepsilon_2} = \sum_i \left  \frac{\partial \varepsilon_2}{\partial x_i} \right  \Delta_{x_i}$	0.1339	0.1406	0.1474	0.1603	—

nine terms listed in table 7.9, the uncertainty in substrate thickness, film thickness and clearance gap have far more significant contribution to the total error range than any other terms. The total error range increases with frequency. The worst case in the chosen frequency band is observed at 11.98 GHz, where the total error range of 0.1603 is equivalent to 4% in the uncertainty of the measured relative permittivity of the dielectric film. Table 7.10 shows the contribution of each measured parameter to the total error range in the cavity perturbation method (method 2). In this method, there is no need to simulate the coupling iris. The major contribution to the total error range is also from substrate thickness, film thickness and

Table 7.10 Contribution of each measured parameter to the total error range in the measured relative permittivity using method 2 (cavity perturbation method)

Parameters	$\frac{\partial \epsilon_2}{\partial x_i}$	8.21 (GHz)	9.02 ( GHz)	10.35 (GHz)	11.98 (GHz)	$\Delta_{x_i}$
Cavity length	$\frac{\partial \epsilon_2}{\partial l}$	$<10^{-7}$ ( $\mu\text{m}^{-1}$ )	$<10^{-7}$ ( $\mu\text{m}^{-1}$ )	$<10^{-7}$ ( $\mu\text{m}^{-1}$ )	$<10^{-7}$ ( $\mu\text{m}^{-1}$ )	2 $\mu\text{m}$
Substrate thickness	$\frac{\partial \epsilon_2}{\partial h_1}$	$3.349 \times 10^{-2}$ ( $\mu\text{m}^{-1}$ )	$4.300 \times 10^{-2}$ ( $\mu\text{m}^{-1}$ )	$4.938 \times 10^{-2}$ ( $\mu\text{m}^{-1}$ )	$5.728 \times 10^{-2}$ ( $\mu\text{m}^{-1}$ )	1 $\mu\text{m}$
Film thickness	$\frac{\partial \epsilon_2}{\partial h_2}$	$1.747 \times 10^{-2}$ ( $\mu\text{m}^{-1}$ )	$1.808 \times 10^{-2}$ ( $\mu\text{m}^{-1}$ )	$1.742 \times 10^{-2}$ ( $\mu\text{m}^{-1}$ )	$1.743 \times 10^{-2}$ ( $\mu\text{m}^{-1}$ )	1 $\mu\text{m}$
Sample position	$\frac{\partial \epsilon_2}{\partial h_0}$	$2.891 \times 10^{-4}$ ( $\mu\text{m}^{-1}$ )	$3.822 \times 10^{-4}$ ( $\mu\text{m}^{-1}$ )	$5.841 \times 10^{-4}$ ( $\mu\text{m}^{-1}$ )	$7.831 \times 10^{-4}$ ( $\mu\text{m}^{-1}$ )	1 $\mu\text{m}$
Sample length	$\frac{\partial \epsilon_2}{\partial \delta_h}$	$<10^{-8}$ ( $\mu\text{m}^{-1}$ )	$<10^{-8}$ ( $\mu\text{m}^{-1}$ )	$<10^{-8}$ ( $\mu\text{m}^{-1}$ )	$<10^{-8}$ ( $\mu\text{m}^{-1}$ )	1 $\mu\text{m}$
Sample width	$\frac{\partial \epsilon_2}{\partial \delta_w}$	$4.004 \times 10^{-2}$ ( $\mu\text{m}^{-1}$ )	$4.106 \times 10^{-2}$ ( $\mu\text{m}^{-1}$ )	$4.142 \times 10^{-2}$ ( $\mu\text{m}^{-1}$ )	$6.699 \times 10^{-2}$ ( $\mu\text{m}^{-1}$ )	1 $\mu\text{m}$
Resonant frequency	$\frac{\partial \epsilon_2}{\partial f}$	$5.807 \times 10^{-2}$ (MHz $^{-1}$ )	$4.996 \times 10^{-2}$ (MHz $^{-1}$ )	$5.944 \times 10^{-2}$ (MHz $^{-1}$ )	$4.832 \times 10^{-2}$ (MHz $^{-1}$ )	0.05 MHz
Substrate permittivity	$\frac{\partial \epsilon_2}{\partial \epsilon_1}$	4.902	5.000	5.108	5.310	<0.01%
Total error range	$\Delta_{\epsilon_2} = \sum_i \left  \frac{\partial \epsilon_2}{\partial x_i} \right  \Delta_{x_i}$	0.09909	0.1100	0.1169	0.1502	—

clearance gap. The total error range for method 2 is slightly smaller than that for method 1. Further improvement in measurement accuracy is possible. This can be achieved by using a better technique, an optical method for example, in measuring the physical size of the dielectric samples. Using a more stable signal source can also significantly improve the accuracy in permittivity measurement.

### 7.6.5 Error range calculation for loss tangent measurement

In loss tangent measurement, in addition to the previous parameters encountered in permittivity measurement, the uncertainty in measuring the width of the Q-curve and the



uncertainty in the reading of the attenuator have to be considered. The signal source used in the loss tangent measurement is very stable (the frequency drift in the measurement period is less than 0.3 KHz). The contribution of each parameter to the total error range in the

Table 7.11 Contribution of each measured parameter to the total error range in loss tangent measurement

Parameters	$\frac{\partial(\tan\delta)}{\partial x_i}$	8.20 (GHz)	10.35 (GHz)	12.02 (GHz)	$\Delta_{x_i}$
Cavity length	$\frac{\partial(\tan\delta)}{\partial l}$	$<10^{-10}$ ( $\mu\text{m}^{-1}$ )	$<10^{-10}$ ( $\mu\text{m}^{-1}$ )	$<10^{-10}$ ( $\mu\text{m}^{-1}$ )	2 $\mu\text{m}$
Substrate thickness	$\frac{\partial(\tan\delta)}{\partial t_1}$	$4.977 \times 10^{-7}$ ( $\mu\text{m}^{-1}$ )	$8.373 \times 10^{-7}$ ( $\mu\text{m}^{-1}$ )	$3.310 \times 10^{-7}$ ( $\mu\text{m}^{-1}$ )	1 $\mu\text{m}$
Film thickness	$\frac{\partial(\tan\delta)}{\partial t_2}$	$11.42 \times 10^{-7}$ ( $\mu\text{m}^{-1}$ )	$8.863 \times 10^{-7}$ ( $\mu\text{m}^{-1}$ )	$8.520 \times 10^{-7}$ ( $\mu\text{m}^{-1}$ )	1 $\mu\text{m}$
Sample position	$\frac{\partial(\tan\delta)}{\partial t_0}$	$1.936 \times 10^{-8}$ ( $\mu\text{m}^{-1}$ )	$3.389 \times 10^{-8}$ ( $\mu\text{m}^{-1}$ )	$3.897 \times 10^{-8}$ ( $\mu\text{m}^{-1}$ )	1 $\mu\text{m}$
Sample length	$\frac{\partial(\tan\delta)}{\partial \delta_b}$	$<10^{-12}$ ( $\mu\text{m}^{-1}$ )	$<10^{-12}$ ( $\mu\text{m}^{-1}$ )	$<10^{-12}$ ( $\mu\text{m}^{-1}$ )	1 $\mu\text{m}$
Sample width	$\frac{\partial(\tan\delta)}{\partial \delta_a}$	$6.680 \times 10^{-6}$ ( $\mu\text{m}^{-1}$ )	$5.382 \times 10^{-6}$ ( $\mu\text{m}^{-1}$ )	$5.890 \times 10^{-6}$ ( $\mu\text{m}^{-1}$ )	1 $\mu\text{m}$
Resonant peak width	$\frac{\partial(\tan\delta)}{\partial(\Delta f)}$	$8.836 \times 10^{-6}$ (KHz $^{-1}$ )	$9.351 \times 10^{-6}$ (KHz $^{-1}$ )	$9.749 \times 10^{-6}$ (KHz $^{-1}$ )	2.5 KHz
Resonant frequency	$\frac{\partial(\tan\delta)}{\partial f_0}$	$<10^{-8}$ (KHz $^{-1}$ )	$<10^{-8}$ (KHz $^{-1}$ )	$<10^{-8}$ (KHz $^{-1}$ )	0.3 KHz
Attenuator	$\frac{\partial(\tan\delta)}{\partial(x_{att})}$	$1.995 \times 10^{-3}$ (dB $^{-1}$ )	$2.332 \times 10^{-3}$ (dB $^{-1}$ )	$2.535 \times 10^{-3}$ (dB $^{-1}$ )	0.005 dB
Substrate permittivity	$\frac{\partial(\tan\delta)}{\partial \epsilon_1}$	$1.669 \times 10^{-5}$	$2.218 \times 10^{-5}$	$1.885 \times 10^{-5}$	<0.01%
Total error range	$\Delta_{\tan\delta} = \sum_i \left  \frac{\partial(\tan\delta)}{\partial x_i} \right  \Delta_{x_i}$	$4.091 \times 10^{-5}$	$4.301 \times 10^{-5}$	$4.449 \times 10^{-5}$	—

measured loss tangent is given in table 7.11. From table 7.11 it can be seen that the total error range in the measured loss tangent is mainly contributed by the uncertainties in the measured width of the Q-curve and in the reading of the attenuator. The quoted uncertainty for attenuator is based on the accuracy with which the dial on the attenuator can be set. The

total error range in table 7.11 represents about 10% of uncertainty in the measured values of loss tangent. Further improvement in measurement accuracy can be made by using a more accurate attenuator and interfacing the test system with a computer to enable more accurate reading of the Q-curve width.

## **7.7 Conclusions**

A novel cavity perturbation method was developed to accurately measure both the relative permittivity and loss tangent of the dielectric films deposited on a supporting substrate. An additional independent technique, derived from transmission line theory, for measuring the relative permittivity of dielectric film was also established. A particular feature of the new techniques, which led to high accuracy in measuring relative permittivity and loss tangent was the positioning of the dielectric film, realised through a moveable short-circuit, in the region of maximum electric field strength, thereby ensuring maximum interaction between the electric field and the film material. A rigorous error analysis was performed on the new techniques, which led to the establishment of practical measurement corrections. The correction of the effect of clearance gaps between samples and waveguide walls is particularly important in improving the measurement accuracy.

## References

- [1] M. Sucher and J. Fox, Handbook of Microwave Measurements. Polytechnic Press of the Polytechnic Institute of Brooklyn, Vol.II, 1963
- [2] D. I. Amey and S. J. Horowitz, "Microwave material characterisation," ISHM'96 Proceedings, pp. 494-499, October, 1996.
- [3] M. D. Janezic and J. H. Grosvenor, "Improved technique for measuring permittivity of thin dielectrics with a cylindrical resonant cavity," IEEE Int. Conf. Instrument and Measurement, pp. 580-584, 1991.
- [4] H. Huang, C. E. Free, K. E. G. Pitt, A. R. Berzins and G. P. Shorthouse, "Relative permittivity measurement of thick-film dielectrics at microwave frequencies," Electronics Lett., pp. 1812-1814, 1995.
- [5] Peter G. Barnwell, "A thick film technology combining microwave and MCM applications", ISHM'96 microelectronics symposium, Proceedings, pp340-343, Minneapolis, Minnesota, USA, October, 1996
- [6] Peter G. Barnwell and Jim Wood, "Advanced thick film technology-the new generation", 11th European Microelectronics Conference, Proceeding, pp221-226, Venice, 1997
- [7] N. Marcuvitz, Waveguide Handbook, Dover Publication, Inc., pp.18-20, 1965.
- [8] E. V. D. Glazier, H. R. Lamont, The Services' Textbook of Radio, Vol.5 (Transmission and Propagation), Her Majesty's Stationary Office, pp. 231-255, 1958
- [9] H. Mooijweer, Microwave Techniques, Macmillan, pp. 182-187, 1971.
- [10] High Frequency Structure Simulator, Trademarks of Hewlett-Packard, Santa Rosa, CA
- [11] H.A. Bethe and J. Schwinger, "Perturbation theory of resonant cavities," NDRC Report DI-117, Radiation Laboratory, MIT, March, 1943

## **Chapter 8 Further advances in the dielectric characterisation techniques at microwave frequencies**

### **8.1 Introduction**

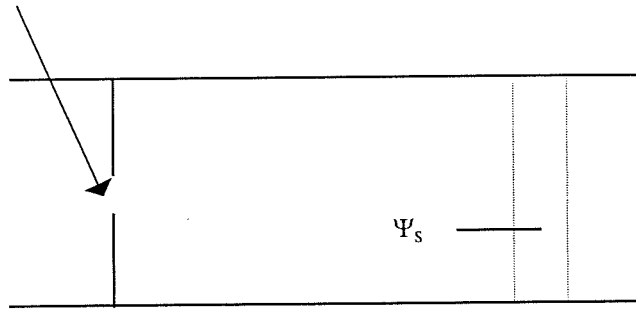
The fast development of wireless communication has resulted in the ever increasing interest in the accurate characterisation of dielectric materials which lay foundation for the high frequency components, microwave integrated circuits (MICs) and multi-chip modules (MCMs) [1-4]. Of the two major properties of the dielectric material, dielectric constant and loss tangent, it has been well understood that the former is almost independent of frequency and relatively easy to measure while the latter is dependent on the frequency and its measurement is much more difficult. In the available methods for the loss tangent measurement, the resonant cavity technique is probably the most accurate one [5].

In this chapter, the cavity perturbation method has been extended for the loss tangent measurement of the dielectric material at a specific situation where the dielectric constant is already known. It was proved that at this situation both the calculation of field pattern inside the cavity and the physical measurement of cavity and dielectric sample can be avoided thus greatly simplifying the theoretical formula and increasing the accuracy of the measurement.

### **8.2 Theory**

Figure 1 shows the empty cavity (reference cavity ) and cavity with sample under test (perturbed cavity). According to cavity perturbation theory, the following equation exists [5],

coupling iris

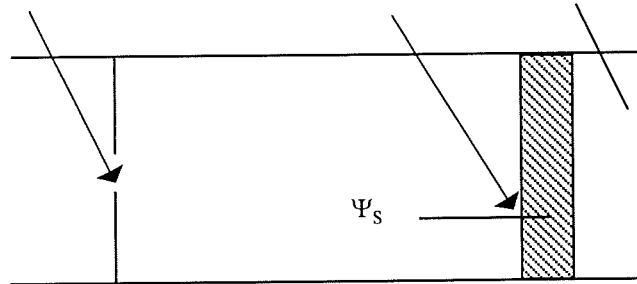


(a) Empty cavity (reference cavity)

coupling iris

dielectric sample

Air gap



(b) Cavity loaded with dielectric sample (perturbed cavity)

Figure 1. Configuration of resonant cavity for loss tangent measurement

$$2\left(\frac{f_{r1}-f_{r2}}{f_{r2}}\right) + j\left(\frac{1}{Q_{L1}} - \frac{1}{Q_{L2}}\right) = \frac{\int_{\Psi_s} (\varepsilon_r - 1) \mathbf{E}_1 \cdot \mathbf{E}_2 d\Psi}{\int_{\Psi_c} |\mathbf{E}_1|^2 d\Psi} \quad (8-1)$$

where  $f_{r1}, Q_{L1}, \mathbf{E}_1$  and  $f_{r2}, Q_{L2}, \mathbf{E}_2$  are resonant frequencies, loaded Q-factors and electric field strength for the reference cavity and perturbed cavity respectively.  $\varepsilon_r$  is the complex relative permittivity for the dielectric material under test.  $\Psi_s$  is the region occupied by the sample indicated in figure 1 and  $\Psi_c$  is referred to the whole region in the reference cavity. After rearrangement, (8-1) can be changed to the form of

$$\varepsilon_r = \frac{2}{\eta} \left( \frac{f_{r1}-f_{r2}}{f_{r2}} \right) + 1 - j \frac{1}{\eta} \left( \frac{1}{Q_{L2}} - \frac{1}{Q_{L1}} \right) = \varepsilon' - j\varepsilon'' \quad (8-2)$$

thus the loss tangent is

$$\tan \delta = \frac{\varepsilon''}{\varepsilon'} = \frac{\frac{1}{\eta} \left( \frac{1}{Q_{L2}} - \frac{1}{Q_{L1}} \right)}{\frac{2}{\eta} \left( \frac{f_{r1}-f_{r2}}{f_{r2}} \right) + 1} \quad (8-3)$$

where

$$\eta = \frac{\int_{\Psi_s} \mathbf{E}_1 \cdot \mathbf{E}_2 d\Psi}{\int_{\Psi_c} |\mathbf{E}_1|^2 d\Psi} \quad (8-4)$$

For the purpose of loss tangent measurement, if the dielectric constant, i.e. the real part of  $\varepsilon_r$  in (8-2) is unknown, the electric field pattern in the resonant cavity has to be calculated to find  $\eta$  in (8-4). This will necessitate the accurate physical measurement of both the cavity and the dielectric sample under test. In current study the dielectric constant,  $\varepsilon'$ , is assumed to be a

known quantity before loss tangent measurement, which is usually true for most of the situations. Consequently, from (8-2),  $\Gamma$  can be directly obtained as

$$\eta = \frac{2}{(\varepsilon' - 1)} \left( \frac{f_{r1} - f_{r2}}{f_{r2}} \right) \quad (8-5)$$

Therefore, (8-3) can be rewritten as

$$\tan \delta = \frac{(\varepsilon' - 1)}{2\varepsilon'} \frac{f_{r2}}{(f_{r1} - f_{r2})} \left( \frac{1}{Q_{L2}} - \frac{1}{Q_{L1}} \right) \quad (8-6)$$

(8-6) clearly indicates that only the resonant frequencies and loaded Q-factors for the reference cavity and perturbed cavity need to be measured. Actually the physical information for the cavity and dielectric sample has already been reflected in the change of the resonant frequencies.

### 8.3 Experimental results and discussion

As a demonstration of the new technique, 99.6% standard alumina and two kinds of new dielectric substrate from Heraeus Inc. have been tested in X-band (8-12 GHz). The test procedures have already been detailed in chapter 7. The cavity length, sample loading position and the diameter of the coupling iris were shown in table 8-1 as a reference. The resonant frequencies for the cavity in the table are only used as an indication to show the frequency region where the resonance of the cavity occurs. The selection of the iris diameter is to

Table 8-1 Set-ups of resonant cavities for loss tangent measurement

Frequency (GHz)	Cavity length (mm)	Iris diameter (mm)	Air gap (mm)
8.2	29.95	6	1.5
9.2	44.95	6	2
10.0	37.95	5.5	2
11.5	29.95	5.5	1.5

increase the loaded Q-factor of the reference cavity and hence increase the sensitivity of the test system. The air gap between the sample and the cavity end is needed to create sufficient perturbation to the cavity. It should be noted that none of the physical data in table 8-1 will be used for the calculation of the loss tangent. After the accurate measurement of resonant frequencies and loaded Q factors, the loss tangent of the dielectric sample can be easily obtained from (8-6).

Table 8-2 shows the measured results for the three dielectric materials. The dielectric constant for alumina is taken as 9.8. For sample 1 and sample 2 from Heraeus Inc., the dielectric constants are 7.9 and 5.1 respectively, which were obtained from our own measurement using standard cavity technique before loss tangent measurement. The examination of the loss tangent for alumina shows that the measured values consistently converge at around  $7.1 \times 10^{-4}$ . In the previously published data for 96% alumina, the loss tangent increases by a factor of 3 from  $3 \times 10^{-4}$  to  $9 \times 10^{-4}$  when the frequency increases from 1MHz to 10 GHz [6]. According to the data provided by Coors, the loss tangent of 99.6% alumina at 1KHz and 1MHz are  $2 \times 10^{-4}$  and  $3 \times 10^{-4}$  respectively. Although the loss tangent data for 99.6% alumina at high frequency region is not available from the manufacturer, we can accept that the values obtained here are realistic. To confirm the validity of the new technique, we have also carried out accurate physical measurement of the resonant cavity and dielectric samples, and the physical data were used in the standard cavity technique given in [5] for loss tangent calculation. The same results were also obtained. A systematic analysis of the test system has been made to analyse the error sources in the measurement. The uncertainty for the measured loss tangent is less than 5%.



Table 8-2 Measured loss tangent of three dielectric materials

Frequency (GHz)	Alumina (99.6%)	Sample 1	Sample 2
8.2	$7.4 \times 10^{-4}$	$5.8 \times 10^{-3}$	$6.2 \times 10^{-3}$
9.2	$6.9 \times 10^{-4}$	$5.5 \times 10^{-3}$	$6.3 \times 10^{-3}$
10.0	$7.1 \times 10^{-4}$	$5.6 \times 10^{-3}$	$6.2 \times 10^{-3}$
11.5	$7.2 \times 10^{-4}$	$5.6 \times 10^{-3}$	$6.1 \times 10^{-3}$

## 8.4 Conclusions

A novel technique has been established for accurately measuring the loss tangent of the dielectric material with known dielectric constant. In the previous techniques and theories for dielectric measurement, the dielectric constant and loss tangent are usually measured at the same time. The loss tangent measurement is always much more difficult than dielectric constant measurement. The key aspect of the new technique is that the theory for loss tangent determination can be significantly simplified if the dielectric material has a known dielectric constant. The simplification of the theory leads to the elimination of physical measurement of the resonant cavity and dielectric sample and hence to the high accuracy of the loss tangent measurement. The new technique opens the door for the accurate characterisation of dielectric material at very high frequency region, such as millimetre wave.

## References

- [1] D. Li, C. E. Free, P. G. Barnwell, K. E. G. Pitt, "Perturbation method for dielectric constant measurement of thick-film dielectric materials", *Electronics Lett.*, 1998, 34, (21) pp. 2042-2044
- [2] Barnwell, P., and Wood, J., 'Advanced thick film technology-the new generation'. Proceedings of 11th European Microelectronics Conference, Venice, May, 1997. pp.221-228
- [3] Amey, D. I., and Horowitz, S. J., 'Microwave material characterisation'. ISHM'96 Proceedings, Minneapolis, October, 1996, pp. 494-499
- [4] Huang, H., Free, C. E., Pitt, K. E. G., Berzins, A. R., and Shorthouse, G. P., 'Relative permittivity measurement of thick-film dielectrics at microwave frequencies'. *Electronics Lett.*, 1995, 31, (21) pp. 1812-1814
- [5] Sucher, M., and Fox, J.: 'Handbook of Microwave Measurements'. Polytechnic Press of the Polytechnic Institute of Brooklyn, 1963, Vol.II
- [6] Holmes, P. J., Loasby, R. J.: 'Handbook of thick film technology'. Electrochemical Publications Ltd, 1976

## **Chapter 9 Conclusions and suggestions for future work**

### **9.1 Summary and conclusions**

In this study the interconnections in multi-chip modules have been investigated at microwave frequencies. Two areas were addressed: firstly, the simulation and modelling of interconnections in MCM structures, and, secondly, the characterisation of the materials used for interconnections in multi-chip modules. The simulation was carried out using electromagnetic simulators which perform numerical calculations from first-principles, i.e. fundamental electromagnetic theory. The models chosen for simulation were described using appropriate parameters for the Heraeus KQ novel MCM technology. Support from Heraeus Inc. provided samples and material data to enable us to use realistic structures. Typical elements which have a parasitic effect in MCM interconnections have been investigated using commercially available modern CAD software, HP HFSS™, HP MDS™ and HP Momentum™. The elements studied include vias, bends and airbridges. The simulated results were obtained in the form of S-parameters, from which the elements were modelled by their equivalent circuits which can be used in circuit simulators for more rigorous circuit design. The crosstalk between microstrip conductors in multi-layer MCM structures was also simulated. The newly generated data from simulation were also used to produce general design rules for MCM interconnections.

The materials developed by Heraeus used for ceramic MCM interconnections fall into two categories: conductive and dielectric thick film materials. These newly developed materials have the advantages of high performance and low cost. Their accurate characterisation is essential prior to their wide use in MCM interconnections and microwave devices. For the characterisation of the conductive thick film gold material, the standard microstrip ring resonator method was used to measure the transmission loss of microstrip lines made from it. However it became necessary to develop a novel algorithm for the characterisation of the dielectric film materials because in the previous methods for the measurement of dielectric films, the accuracy in measuring the relative permittivity is limited and there is no available

technique to measure the loss tangent. A novel cavity perturbation method was developed to accurately measure both the relative permittivity and loss tangent of the films deposited on a supporting substrate. An additional independent technique, derived from transmission line theory, for measuring the relative permittivity of dielectric films was also established. A particular feature of the new techniques, which led to high accuracy in measuring dielectric constant and loss tangent was the positioning of the dielectric film in the region of maximum electric field strength, thereby ensuring maximum interaction between the electric field and the film material. A rigorous error analysis was performed on the new measurement techniques, which led to the establishment of practical measurement corrections. The correction of the effect of clearance gaps between samples and waveguide walls and the accurate characterisation of the physical dimensions of the samples are particularly important in improving the measurement accuracy.

Further advances in the characterisation of dielectrics have also been made, where a simple and rigorous method was developed to accurately measure the loss tangent of dielectrics with known dielectric constant using resonant cavity. The novel method eliminates the need for any physical measurement of the resonant cavity and dielectric sample leading to very high accuracy.

The work in this study has shown that a field theory simulation based on first principles can provide accurate information on crosstalk between conductors and performance of interconnect components, such as vias, bends and airbridges etc., in multi-layer interconnection of multichip modules at high frequencies. After the rigorous electromagnetic simulation, optimisation of circuit layout and geometric sizes of interconnect components can be made to ensure a successful circuit design.

Both the dielectric constant and loss tangent of thick dielectric film can be accurately measured using the novel techniques developed in this study. Although all of the measurements were carried out in X-band (8-12 GHz), there are no inherent frequency limitations to the new methods. The measurement can be implemented in much higher

frequency range, such as millimetre frequencies. The current techniques are also accurate for the characterisation of bulk dielectric materials.

## **9.2 Implications of this study**

The competitive market in wireless communication, main frame computers, military and medical equipment etc. is putting increasing pressure on manufacturers for high performance of their products but at reduced cost, size and weight. Under these pressures the manufacturers often need to modify or update the architectures of their products. First-pass design strategy is always favoured because this will greatly reduce the idea-to-market time. To ensure first pass and avoid any redesign, rigorous simulation of both the microwave circuit and the whole system are necessary. In an MMIC power amplifier circuit as an example, although transistor models and the models of microstrip discontinuities are available in most microwave simulation packages, these are intended to be available for as many applications as possible and are, therefore, very generic. For a first pass design, they are not accurate enough [1,2]. The transistor model for the power amplifier can be obtained by measuring S-parameters at different load values and by doing so, the optimum input and output impedance values for matching can thus be obtained at the same time. The matching network involving discontinuities can be simulated and modified using an electromagnetic simulator, such as HP Momentum™ or HFSS™, to provide optimum matching. Upon accurate simulation of the whole circuit, the chance of first pass success for the design of power amplifier will be greatly enhanced.

In general the availability of modern 2.5D and 3D electromagnetic simulators has enabled the interconnections in MMIC, MCM and other high density packaging structures to be rigorously simulated, which opens the door for sophisticated circuit design in a short cycle to meet market demand.

The ever developing electronic circuits and systems are underpinned by the development of electronic materials which are usually chosen to suit different needs for either performance or cost. In today's communication market, in particular, new conductive and dielectric materials are always emerging to meet the market need. This will inevitably create a need for accurate characterisation of new electronic materials. In some circumstances, new theories and techniques have to be developed for the characterisation. In this study an extension of traditional cavity theory and techniques has been made for the characterisation of dielectric film materials, previous techniques not applying to film dielectrics. Although only printed dielectric thick films are characterised in this study, the newly developed theory and technique is not restricted to this particular application. The deposited dielectric thin film materials can also be characterised using the techniques developed in this study provided the film is thick enough to ensure an adequate perturbation to the resonant cavity. The potential of this new cavity technique is that it can be used as a powerful tool in the research and development of new dielectric film materials by providing accurate data on both losses and permittivities. There are no inherent frequency limitations for the measurement technique. It can also be implemented at millimetre wavelengths where there is significant current interest in characterising thin dielectric films, such films being needed for fabrication of advanced microwave circuits for an increasing range of applications. The principles used here could be automated to provide quick and convenient data in a laboratory which is actually developing or using dielectric films.

### **9.3 Suggestions for future work**

The current study offers potential for further research. The possible areas to be addressed are:

- Interconnections using coplanar waveguide structures
- Packaging effects in microwave circuit design
- Other options for cavity techniques-for example, the samples can be loaded differently and a circular waveguide can also be used to form the resonant cavity with higher Q values.

- Development of a novel jig for the test of MCM structures at microwave frequencies
- Extension of conductive loss studies and dielectric measurements to much higher frequencies.

### 9.3.1 Interconnections using coplanar waveguide structures

Throughout this study the interconnect structures in MCM or MMIC structures were based on microstrip lines. For monolithic circuits operating at millimetre-wave frequencies, coplanar waveguide (CPW) transmission lines are an alternative for microstrip lines and, under some circumstances, offer even better performance and lower fabrication cost. The geometric structure of a CPW is shown in figure 9.1. The advantages of these structures are:

- ◇ Low dispersion-an important feature for broadband applications [3].
- ◇ Both signal and ground conductors are placed on the same side of the wafer or substrate- this unique structure saves effort of wafer thinning, via hole drilling and backside metallisation and thus reduce the process cost.
- ◇ Easy access to ground plane-passive and active components can be surface mounted on the same side of the wafer. For FETs, this is especially advantageous at very high frequencies, where a higher gain can be obtained due to the absence of a via-hole inductance at the source.
- ◇ Reduced crosstalk-the presence of the ground plane results in reduced coupling between adjacent signal lines, which enables a further miniaturisation of MMIC circuits [4].
- ◇ Convenience for accurate measurement-on-wafer measurement techniques are well established, based on coplanar probe tips which are commercially available.

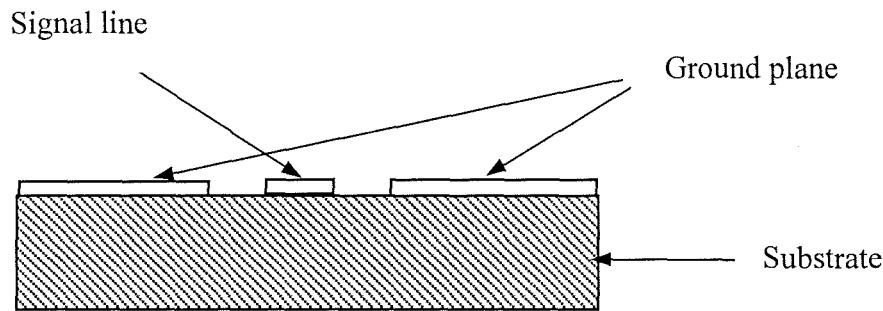


Figure 9.1 Geometric structure of coplanar waveguide

The impedance of a CPW structure is determined by the width to ground spacing ratio and is almost insensitive to the substrate height. While most of the coplanar mm-wave amplifiers use a ground spacing of  $50\text{ }\mu\text{m}$ , MMIC circuits can be considerably miniaturised. The small ground spacing also means reduced parasitic packaging effects [5]. These promising CPW interconnections have already attracted considerable research effort and industrial interest. The current research can be readily extended to this area. Using the electromagnetic simulator, the effect of the finite width of the ground plane(s) can be studied. The matching CPW network, including its discontinuities, for an amplifier can also be addressed in a similar way to its microstrip counterpart. In addition, some CPW passive structures, such as single-loop coplanar meander lines which are used as inductive transmission line elements, and have no standard model for use in a circuit simulator, can also be investigated by this simulation technique.

### 9.3.2 Packaging effects in microwave circuit design

Most of the RF ICs in commercial wireless applications are packaged in low cost plastic packages which are compatible with high volume surface mount assembly processes.



Because the packaging of RF components can seriously degrade performance, the effects of the package must be considered as an integral part of the design. Accurate models are necessary to precisely determine the ultimate packaged performance [6].

The packaging issues mainly involve coupling between package leads, series inductance to the input/output of the RF circuit, common lead inductance between the RF ground of the die and that of the PCB or substrate, dielectric loading and loss loading as a result of the plastic encapsulation, and thermal management. Electromagnetic simulation can play a crucial role in this area. From the results of a rigorous simulation, package models can be extracted in the frequency range of interest. Problems in the packaging structure or the materials used can also be spotted and optimised through simulation.

### 9.3.3 Other options for cavity techniques

In general, for the purpose of dielectric material characterisation using cavity techniques, the cavity could be any geometric shape and the samples could be loaded anywhere inside the cavity as long as the distribution of electromagnetic field inside the cavity can be obtained either analytically or numerically. In this study, for the convenience of sample preparation and theoretical derivation, the cavity resonator

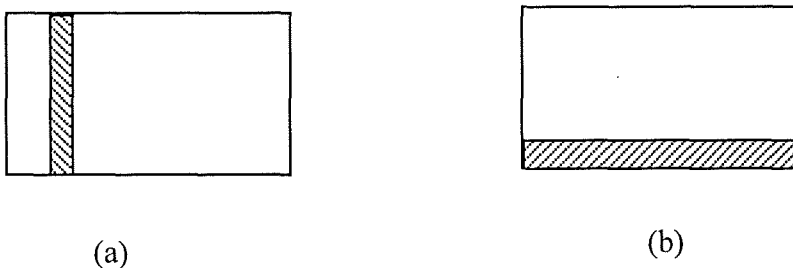


Figure 9.2 Other possible methods for sample loading in rectangular cavity

consists of a rectangular waveguide with the sample filling the whole cross-section of the waveguide.

Other options are available with regard to the positioning of a sample in the cavity and the geometric shape of the cavity resonator. The sample can be loaded in possible ways like those in figure 9.2. Appropriate derivations can be made to relate the test parameters to the electrical parameters of the material in these set-ups in a similar way to that used in chapter 7. The geometry of the cavity can also be chosen as circular in order to employ the advantages of low attenuation and high  $Q$  of the  $TE_{01}$  mode. Since this cavity structure can provide extremely high  $Q$ , the sensitivity of the test system in measuring loss tangent of the dielectric film is expected to be high. The theory for a circular-shaped cavity has already been developed in chapter 7, which provides a foundation for further investigation into the more accurate characterisation of dielectric films.

## References

- [1] F.L.M. van den Bogaart, A.P. de Hek, "First-pass design strategy for high-power amplifier at X-band", Colloquium on design of RFIC's and MMIC's, Savoy place, London, 1997.
- [2] A. P. de Hek, "An accurate scaleable microstrip T-junction discontinuity model valid up to 50 GHz", Microwave and RF Conference 1997.
- [3] W. Heinrich, "Full-wave analysis of conductor losses on MMIC transmission lines", IEEE Trans. Microwave theory Technology, Vol. MTT-38, No.10, pp1468-1472, 1990.
- [4] G. Ghione and C. U. Naldi, "Coplanar waveguides for MMIC applications: effect of upper shielding, conductor backing, finite-extent ground planes, and line-to-line coupling", IEEE Trans. Microwave Theory Technology, Vol. MTT-35, No.3, pp.260-267, 1987.
- [5] T. Krems, W. Haydl, H. Massler and J. Rüdiger, " Millimeter-wave performance of flip-chip interconnections using wire bonding and flip chip", Proceedings of the 1996 IEEE MTT-S International Microwave Symposium, pp.247-250, San Francisco, 1996.
- [6] M. Kamon and S. S. Majors, "Package and interconnect modeling of the HFA3624, a 2.4GHz RF to IF converter", Proceedings of the 33rd Design Automation Conferences, IEEE, 1996, pp2-7.

# Appendices

- **Appendix A: Integrals used in the derivation of cavity perturbation formulae in chapter 7**
- **Appendix B: Definition of S, Y and Z parameters**
- **Appendix C: Standard rectangular waveguide data**
- **Appendix D: Publications resulting from this study**

## Appendix A: Integrals used in derivation of cavity perturbation formulae

$$\int_0^a \sin^2 \frac{\pi x}{a} dx = \frac{a}{2}$$

$$\int_0^a \cos^2 \frac{\pi x}{a} dx = \frac{a}{2}$$

$$\int \sin^2 ax dx = \frac{x}{2} - \frac{1}{4a} \sin(2ax) + C$$

$$\int \cos^2 ax dx = \frac{x}{2} + \frac{1}{4a} \sin(2ax) + C$$

$$\int \sin ax dx = -\frac{1}{a} \cos ax + C$$

## Appendix B: Definition of S, Y and Z matrices

At the  $n$ th port on a specific point (called terminal plane) for an arbitrary N-port microwave network,  $(V_n^+, I_n^+)$  and  $(V_n^-, I_n^-)$  are defined as incident and reflected voltage and current respectively as indicated in figure B1. The total current and voltage at the  $n$ th port are given by

$$V_n = V_n^+ + V_n^- \quad \text{B-1a}$$

$$I_n = I_n^+ + I_n^- \quad \text{B-1b}$$

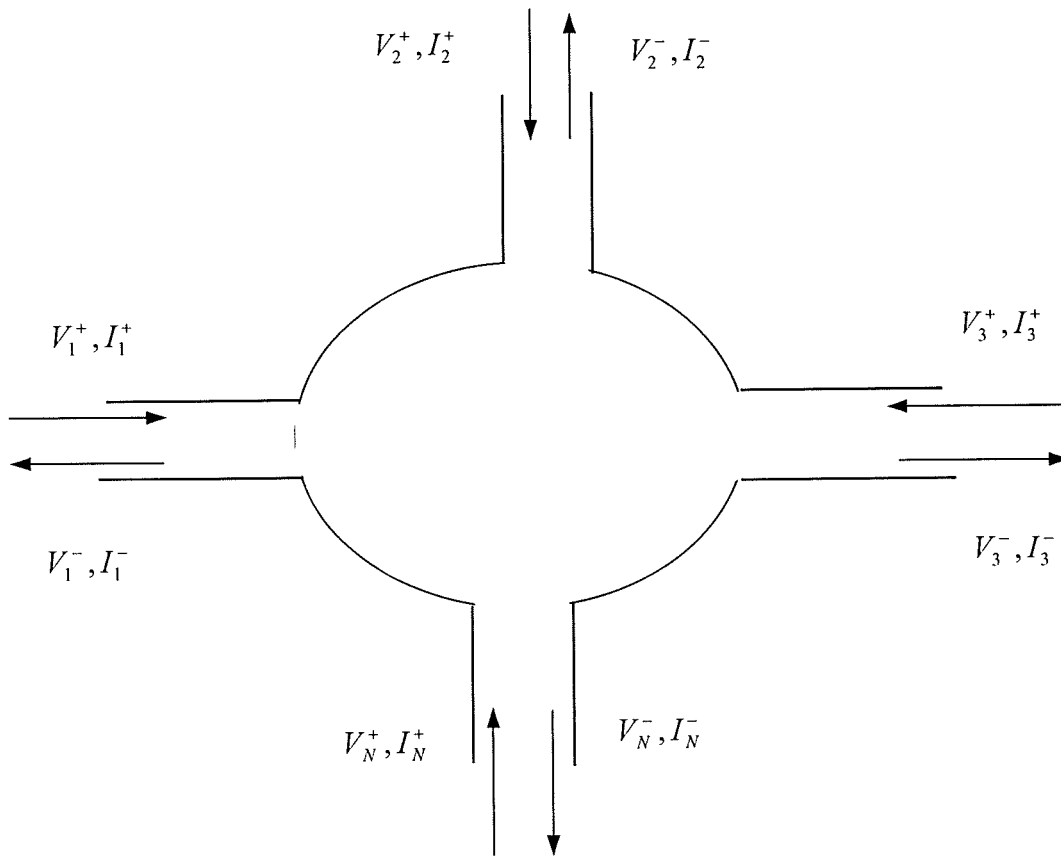


Figure B1 An arbitrary N-port microwave network

For all of the ports in the microwave network, the matrix relating these voltages and currents are defined as impedance or admittance matrix. Mathematically there are two ways to express this relation:

$$\begin{bmatrix} V_1 \\ V_2 \\ \vdots \\ V_N \end{bmatrix} = \begin{bmatrix} Z_{11} & Z_{12} & \dots & Z_{1N} \\ \vdots & \vdots & & \vdots \\ Z_{N1} & \dots & \dots & Z_{NN} \end{bmatrix} \begin{bmatrix} I_1 \\ I_2 \\ \vdots \\ I_N \end{bmatrix} \quad \text{B-2a}$$

and

$$\begin{bmatrix} I_1 \\ I_2 \\ \vdots \\ I_N \end{bmatrix} = \begin{bmatrix} Y_{11} & Y_{12} & \dots & Y_{1N} \\ \vdots & & & \vdots \\ \vdots & & & \vdots \\ Y_{N1} & \dots & \dots & Y_{NN} \end{bmatrix} \begin{bmatrix} V_1 \\ V_2 \\ \vdots \\ V_N \end{bmatrix} \quad \text{B-2b}$$

or alternatively in a more concise form as

$$[V] = [Z][I] \quad \text{B-3a}$$

$$[I] = [Y][V] \quad \text{B-3b}$$

where  $[Z]$  is defined as impedance matrix and  $[Y]$  as admittance matrix. Note that both the  $[Z]$  and  $[Y]$  matrices relate the total port voltages and currents, and they are the inverses of each other, i.e.

$$[Y] = [Z]^{-1} \quad \text{B-4}$$

From C-2a the element of  $[Z]$  can be found as

$$Z_{ij} = \left. \frac{V_i}{I_j} \right|_{I_k=0 \text{ for } k \neq j} \quad \text{B-5}$$

C-5 indicates that  $Z_{ij}$  can be found by driving port  $j$  with the current  $I_j$ , open-circuiting all other ports (so  $I_k = 0$  for  $k \neq j$ ), and measuring the open-circuit voltage at port  $i$ .

Similarly, from C-2b the element of  $[Y]$  can be found as

$$Y_{ij} = \left. \frac{I_i}{V_j} \right|_{V_k=0 \text{ for } k \neq j} \quad \text{B-6}$$

which states that  $Y_{ij}$  can be determined by driving port  $j$  with the voltage  $V_j$ , short-circuiting all other ports (so  $V_k = 0$  for  $k \neq j$ ), and measuring the short-circuit current at port  $i$ .

The S-parameters or scattering matrix is defined in a similar way as that for  $Z$  and  $Y$  matrices. The scattering matrix relates the voltage waves incident on the ports to those reflected from the ports, as follows

$$\begin{bmatrix} V_1^- \\ V_2^- \\ \vdots \\ \vdots \\ V_N^- \end{bmatrix} = \begin{bmatrix} S_{11} & S_{12} & \dots & S_{1N} \\ \cdot & & & \cdot \\ \cdot & & & \cdot \\ S_{N1} & \dots & \dots & S_{NN} \end{bmatrix} \begin{bmatrix} V_1^+ \\ V_2^+ \\ \vdots \\ \vdots \\ V_N^+ \end{bmatrix} \quad \text{B-7}$$

or

$$[V^-] = [S][V^+] \quad \text{B-8}$$

where  $[S]$  is called scattering matrix. The element of the  $[S]$  matrix can be determined as

$$S_{ij} = \left. \frac{V_i^-}{V_j^+} \right|_{V_k^+ = 0 \text{ for } k \neq j} \quad \text{B-9}$$

which states that  $S_{ij}$  is found by driving port  $j$  with an incident wave of voltage  $V_j^+$ , and measuring the voltage of reflected wave,  $V_i^-$ , coming out of port  $i$ . The incident waves on all ports except the  $j$ th port are set to zero. The termination for all ports should be matched to avoid reflections.



## Appendix C: Standard rectangular waveguide data

Band	Recommended frequency range (GHz)	TE <sub>10</sub> Cutoff frequency (GHz)	Internal dimensions Inches (cm)
L	1.12-1.70	0.908	6.500×3.250 (16.51×8.225)
R	1.70-2.60	1.372	4.300×2.150 (10.922×5.461)
S	2.60-3.95	2.078	2.840×1.340 (7.214×3.404)
H (or G)	3.95-5.85	3.152	1.872×0.872 (4.755×2.215)
C (or J)	5.85-8.20	4.301	1.372×0.622 (3.485×1.580)
W (or H)	7.05-10.0	5.259	1.122×0.497 (2.850×1.262)
X	8.20-12.4	6.557	0.900×0.400 (2.286×1.016)
Ku (P)	12.4-18.0	9.486	0.622×0.311 (1.580×0.790)
K	18.0-26.5	14.047	0.420×0.170 (1.07×0.43)
Ka (R)	26.5-40	21.081	0.280×0.140 (0.711×0.356)
Q	33.0-50.5	26.342	0.224×0.112 (0.57×0.28)
U	40.0-60.0	31.357	0.188×0.094 (0.48×0.24)
V	50.0-75.0	39.863	0.148×0.074 (0.38×0.19)
E	60.0-90.0	48.350	0.122×0.061 (0.31×0.15)
W	75.0-110.0	59.010	0.100×0.050 (0.254×0.127)
F	90.0-140.0	73.840	0.080×0.040 (0.203×0.102)
D	110.0-170.0	90.854	0.065×0.0325 (0.170×0.083)
G	140.0-220.0	115.750	0.051×0.0255 (0.130×0.0648)

## Appendix D: Publications resulting from this study

- [1] C. E. Free, K. P. Tang, D. Li, P. Barnwell, K. E. G. Pitt, "High frequency interconnections and crosstalk on MCM structures", Proceedings of International Symposium on Microelectronics, pp522-525, October, 1996, Minneapolis, USA.
- [2] C. E. Free, K. P. Tang, D. Li, P. G. Barnwell, K. E. G. Pitt, "Analysis of crosstalk in multi-layer structures", Proceedings of European MCM conference, Jan., 1997, London, UK.
- [3] D. Li, C. E. Free, P. G. Barnwell, K. E. G. Pitt, "Simulated and practical behavior of state-of-the-art MCM via structures", Proceedings of 6th International conference on MCMs, pp290-295, April, 1997, Denver, USA.
- [4] C. E. Free, D. Li, P. Barnwell, K. E. G. Pitt, "High frequency modelling of vias in 3D interconnect structures", Proceedings of 11th European Microelectronics Conference, pp84-91, May, 1997, Venice, Italy.
- [5] P. G. Barnwell, J. Wood, C. E. Free, D. Li, "Microwave frequency characterization of an advanced thick-film material system", Proceedings of 30th International Symposium on Microelectronics, October, 1997, Philadelphia, USA.
- [6] D. Li, C. E. Free, P. G. Barnwell, K. E. G. Pitt, "High frequency implications of modern MCM interconnections", Proceedings of European MCM conference, Jan., 1998, London, UK.
- [7] K. E. G. Pitt, C. E. Free, D. Li, P. G. Barnwell, "Influence of materials properties on the design of MCM and microstrip structures", Proceedings of European MCM conference, Jan., 1998, London, UK.
- [8] D. Li, C. E. Free, P. G. Barnwell, K. E. G. Pitt, "Perturbation method for dielectric constant measurement of thick-film dielectric materials", Electronics Letters, Vol. 34, No. 21, pp.2042-2044, 1998.
- [9] D. Li, C. E. Free, P. G. Barnwell, K. E. G. Pitt, "Permittivity measurement of dielectric film materials in high frequency range using resonant cavity", submitted to IEEE Trans. MTT.

- [10] D. Li, C. E. Free, P. G. Barnwell, K. E. G. Pitt, "A simple method for accurate loss tangent measurement of dielectrics using resonant cavity", to be submitted to Electronics Letters.
- [11] D. Li, C. E. Free, P. G. Barnwell, K. E. G. Pitt, "Characterization of printed dielectric thick-film using cavity resonator", to be submitted to IEEE Trans. MTT.
- [12] D. Li, C. E. Free, P. G. Barnwell, K. E. G. Pitt, "Correction algorithm for clearance gaps between dielectric sample and resonant cavity walls for the accurate characterisation of dielectric film at high frequencies", to be submitted to IEEE Trans. MTT.